J. E. Tillman
Atmospheric Sciences
3-4586

Many sensor design &
test criteria are developed & explained
here. Please guard this one carefully,
as well as others. You should
copy this in case we need to
refer to it.

TRW®
SYSTEMS GROUP
ONE SPACE PARK • REDONDO BEACH • CALIFORNIA 90278

TRW
SYSTEMS GROUP
ONE SPACE PARK • REDONDO BEACH, CALIFORNIA

CODE IDENT 11982

TITLE

SENSOR DESIGN ANALYSIS REPORT

DATE : 12 September 1973 NO. METC-021

SUPERSEDING: _____

This report is an update of the original Sensor Design Analysis Report issued 26 January 1973 under the report number METC-013.

PREPARED BY: R. Davey/T. Chamberlain/L. Harnett

APPROVAL SIGNATURES:

S. Rocklin 9-13-73 DATE
S. Rocklin

E. Erickson 9/20/73 DATE
E. Erickson
MMA Engineering

M. Kolpin DATE
M. Kolpin

D. Zook 9/20/73 DATE
D. Zook
MMA Quality Assurance

DATE

DATE

SYSTEMS 1391 REV. 3-67

NO. METC-021

TRW
SYSTEMS GROUP
ONE SPACE PARK • REDONDO BEACH, CALIFORNIA

REVISION RECORD

REV	DATE	AUTHORIZATION	CHANGE	PAGES AFFECTED
N/C	9/12/73	See Title Page		

SYSTEMS 1392 REV. 10-67

(FILE DIRECTLY AFTER COVER SHEET)

INTRODUCTION

This document presents the analyses supporting the Viking Meteorology Instrument Sensor design, and compares the system capabilities with the requirements of PD 7400090.

The report has been arranged in three independent sections covering the wind sensor, temperature sensor and quadrant sensor.

SECTION I

TEMPERATURE SENSOR

TABLE OF CONTENTS

	Page
1. DESIGN CRITERIA	1
1.1 Performance Specifications	1
1.2 Environmental Conditions	1
2. SENSOR SYSTEM DESCRIPTION	1
2.1 MSA Elements	1
2.1.1 Sensing Thermocouples and Frame	2
2.1.2 Reference Module	3
2.2 MEA Elements	3
3. PRINCIPLE OF OPERATION	4
4. PERFORMANCE ANALYSIS	5
4.1 Operating Range	5
4.2 Accuracy	6
4.2.1 Accuracy of Electronics	6
4.2.2 Sensor Calibration Accuracy	7
4.2.3 Temperature Difference Compensation Accuracies	8
4.2.4 Total System Uncertainty	16
4.3 Stability	17
4.4 Resolution	17
4.5 Response Time	17
4.6 Warm-Up Time	24
4.7 Attitude	24
4.8 Hysteresis	24
REFERENCES	24

NOMENCLATURE

C_w	Thermocouple wire heat capacity
d	Thermocouple wire diameter
F	View factor
K_g	Atmosphere thermal conductivity
K_w	Thermocouple wire thermal conductivity
L	Thermocouple wire length
M_∞	Wind Mach number
Nu	Nusselt number
$\dot{Q}_s$	Solar radiation energy density
Re	Reynolds number
T_R	Recovery temperature
T_T	Total temperature
T_w	Thermocouple wire temperature
T_∞	Ambient atmosphere temperature
u_∞	Wind velocity
x	Distance from junction along thermocouple wire
α	Thermocouple wire low temperature absorptivity
α_s	Thermocouple wire solar absorptivity
γ	Atmospheric specific heat ratio
ϵ	Thermocouple wire emissivity ($= \alpha$)
ρ_w	Thermocouple wire density
σ	Stefan-Boltzmann constant
τ	Thermocouple time constant

1. DESIGN CRITERIA

1.1 Performance Specifications

The sensor is designed to measure the temperature of the Martian atmosphere in accordance with the requirements given below.

Range	130°K to 350°K
Accuracy	3°K Absolute 1.5°K Relative
Hysteresis	±.8°K
Stability	±.8°K
Resolution	±.8°K
Response Time	≤ 3 sec
Warm-up Time	≤ 4 sec
Attitude	Operate in any attitude

1.2 ENVIRONMENTAL CONDITIONS

The sensor design reflects the severe environmental conditions which will be encountered during the transit to Mars and on the Martian surface. Of particular concern are the following:

Martian Atmospheric Pressure	2.1 torr to 15.2 torr
Martian Wind Speed	2 m/sec to 70 m/sec

2. SENSOR SYSTEM DESCRIPTION

The sensor system is composed of three subsystems: 1) a set of sensing thermocouples exposed to the Martian atmosphere, 2) an isothermal module housing the reference thermocouple junction, and 3) the supporting electronics.

2.1 MSA Elements

The sensing thermocouples and reference module are mounted as part of the MSA at the end of the MBA. The configuration is shown in Figure 1.

2.1.1 Sensing Thermocouples and Frame

Three sensing thermocouples are mounted vertically in an open fork frame. The frame design was chosen to minimize the influence of the frame's thermal wake on the junction temperature. With the sensor mounted so that the plane of the fork lies in the center of the lander's thermal wake, the influence of the wake can be neglected entirely. Of course, the greater influence from the lander can be significant when the wind direction places the sensor in its thermal wake, and some consequent error will be introduced. The region of influence is expected to be about 70 degrees wide.

The frame is machined from polyimide which provides electrical insulation and a minimum of thermal expansion problems as well as the necessary strength and rigidity. Thermocouple extension wires (.020 inch diameter) are mounted in slots in the frame and the sensing thermocouple wires are welded to them. The connection area is filled with silicone rubber to provide shock and vibration protection.

The sensing thermocouples are fabricated by butt-welding .003 inch diameter Chromel-P and Constantan wires. The butt-welding was chosen to provide a cylindrical sensor. This simple geometry allowed a reasonably accurate heat transfer analysis to be made despite the complexity of the operating conditions which cover the transitional region from free-molecular to continuum flow. The materials were selected to best satisfy the following desired characteristics.

- Low thermal conductivity
- High loop EMF
- Adequate structural characteristics over the operating range
- Corrosion resistance
- Adequately documented properties
- Low specific heat
- Low specific mass

A very thin (1000 Å) gold plate is applied to the thermocouple wires to stabilize the radiation properties by increasing the corrosion resistance.

2.1.2 Reference Module

The reference thermocouple junction is housed in an isothermal module together with parasitic junctions, a platinum resistance thermometer and a bridge reference resistor. The module is mounted just below the temperature sensor inside the MSA housing. A cross section of the module is included in Figure 1.

The primary purpose of the reference module is to minimize the temperature difference between the reference thermocouple and the platinum resistance thermometer and make the difference independent of variations in the module temperature. In addition, the module thermally connects the two parasitic junctions (Chromel-P/copper) so that the total parasitic EMF is zero.

2.2 MEA Elements

The sensor is connected to its associated electronics package through junctions at the MSA/MBA and MBA/lander interfaces. Connections are made between the thermocouple loop and the platinum and bridge reference resistors to the input circuits of signal amplifiers.

The temperature sensor electronics consist of four elements: 1) the thermocouple loop EMF amplifier, 2) the platinum thermometer amplifier, 3) the chopper oscillator, and 4) the supply voltage circuits. Both amplifiers are chopper stabilized.

The thermocouple loop EMF is fed directly to the amplifier and the amplified signal is digitized and stored in a memory, ready for transmission. The transmitted signal is, therefore, a direct analog of the loop EMF.

The platinum resistance thermometer is connected in a bridge circuit and the bridge unbalance voltage is amplified and transmitted in digital form. Its value, together with the bridge supply voltage, which is also transmitted, is used to determine the platinum thermometer resistance.

3. PRINCIPLE OF OPERATION

The temperature of the Martian atmosphere is measured in two stages: the difference between the atmosphere temperature and reference module temperature is measured by the thermocouple loop and the module temperature is measured by the platinum resistance thermometer.

The .003 inch diameter sensing thermocouples provide the rapid time response. They are wired in parallel to provide redundancy and thereby offset the risk of breakage from excessive shock or vibration, impact by sand particles, etc. The reference junction, housed in the isothermal module, has a very long time constant and provides a stable relative reference. The platinum resistance thermometer then provides the absolute temperature standard.

The operation of the sensor system relies upon the application of calibration data. A block diagram showing the functional relationships is given in Figure 2. Two sets of calibration data are required to characterize the sensor. The first relates the sensor temperature to the inputs to the sensor electronics (i.e., the loop EMF and platinum thermometer resistance). The second relates the electronic subsystem inputs to the transmitted digital data.

The first calibration consists of measuring the loop EMF and platinum thermometer resistance while the temperatures of the sensing thermocouples and the reference module are varied over the operating range. The bridge current used to measure the platinum thermometer resistance is maintained at the same value used in the MEA in order to match the self-heating. The

calibration provides a unique relation between the temperature of the sensing thermocouples and the loop EMF and platinum resistance. Note in particular that it is not necessary to determine the module temperature, thereby eliminating the errors due to uncertainties in subordinate computations. The MSA components are treated as a unit where two output values characterize the temperature measurement.

The calibration of the sensor electronics involves the determination of conversion factors used to compute the characteristic sensor outputs from the transmitted digital data.

The calibration data are used to convert measured voltages to atmospheric temperature values. The entire data reduction scheme is shown diagrammatically in Figure 3. Note that it is divided into two phases, the first being a relatively simple application of the calibration tables to provide a preliminary estimate of the ambient temperature. Corrections are then made to account for differences between the sensor and ambient temperatures due to conduction along the thermocouple wires, radiation, and directed kinetic energy. The preliminary estimate can be recovered very quickly and can provide relatively accurate information for near-real-time monitoring.

4. PERFORMANCE ANALYSIS

4.1 Operating Range

The operating range of the sensor system was verified by extending the calibration to the specified temperature extremes. The results of a typical calibration are given in Table 1. Note that the signal sensitivity is relatively uniform over the temperature range. Values at significant points are listed below.

Signal Sensitivity

	130°K	230°K	330°K	350°K
Loop EMF	.038 mv/°K			.066 mv/°K
Pt. Thermometer Resistance		.606 Ω/°K	.597 Ω/°K	

4.2 Accuracy

Errors in the measurements made by the temperature sensor system are introduced at three points. First, a difference in temperature will exist between the ambient atmosphere and the thermocouple junction due to conduction along the thermocouple wires, the conversion of directed kinetic energy into heat, and radiation. Inaccuracies in correcting for these factors will lead to perceived temperature errors. Calibration inaccuracies are the second source of error. These will be manifested as a difference between the thermocouple junction temperature and the temperature calculated from the loop EMF and platinum resistance values. Finally, errors will be introduced by the sensing electronics and data transmission systems as evidenced by differences between the actual and received EMF and platinum resistance measurements.

4.2.1 Accuracy of Electronics

The accuracy of the signal handling electronics and digital data transmission systems is discussed in the Worst Case Analysis for the Meteorology Electronics Assembly (METC-013, 29 September 1972). The three sigma uncertainties listed in the report correspond to temperature measurement errors of .59°K for the thermocouple electronics and 1.07°K for the platinum thermometer electronics giving a total expected error of 1.22°K for the two independent measurements.

4.2.2 Sensor Calibration Accuracy

The accuracy of the sensor calibrations was determined by making repeated calibrations of the same system. A statistical analysis of the calibration data was performed to establish uncertainty intervals and determine the most accurate interpolation scheme. The three sigma accuracy was established as 1.50°K. As calibration experience is gained, this is expected to decrease.

Sensor calibrations are carried out by the TRW Metrology Department. Precise temperature control is obtained by using a Rosemount 913 calibration bath and associated precision platinum resistance thermometers, sensing bridges and control circuits. The overall accuracy of the system is ±.02°C. Freon 12 and Freon E-4 are used as calibration liquids. The fluids are relatively inert and will not react with any material in the sensor system. at the point where it is calibrated. Potting compounds and paint, which do react with Freon 12, are applied after calibration.

The sensor frame is placed in the calibration bath and its temperature is varied over the operating range. The reference module is placed in an auxiliary facility and its temperature is varied from about 230°K to 330°K, the highest temperature expected in the MSA housing. Readings of the output parameters (loop EMF and platinum thermometer resistance) are taken at 30 calibration points (see Table 1). The resistance of the bridge reference resistor is also measured to verify its zero thermal coefficient of resistivity. Bridge circuits are used to measure both the loop EMF and the resistances. The bridge current is maintained at the same value used in the temperature sensor electronics (about 1 ma) during resistance measurements to reproduce

the self-heating which will occur during actual operation. The platinum thermometer resistance is measured to .01 ohms while the loop EMF is measured to one microvolt.

4.2.3 Temperature Difference Compensation Accuracies

4.2.3.1 Conduction Induced Errors

If the temperature of the sensor frame is different from the ambient temperature, heat flow to or away from the thermocouple junction will lead to a difference between the junction and ambient temperatures. This difference can be evaluated using the equilibrium relation:

$$k_w \pi \frac{d^2}{4} \frac{d^2 T_w}{dx^2} - \pi k_g Nu (T_w - T_\infty) = 0$$

or, with $\Delta T = T_w - T_\infty$

$$\frac{d^2 \Delta T}{dx^2} - 4 \frac{k_g}{k_w} \frac{Nu}{d^2} \Delta T = 0; \quad \Delta T = \Delta T_o = T_{frame} - T_\infty \quad \text{at} \quad x = \pm \frac{L}{2}$$

Since the thermal conductivities of Chromel and Constantan are nearly equal, we can take k_w = const. Then, solving for ΔT:

$$\Delta T = \Delta T_o \frac{\cosh 2 \sqrt{\frac{k_g}{k_w} Nu} \frac{x}{d}}{\cosh \sqrt{\frac{k_g}{k_w} Nu} \frac{L}{d}}$$

and, at the thermocouple junctions (x = 0):

$$\Delta T \Big|_{T.C.} = \Delta T_o \frac{1}{\cosh \sqrt{\frac{k_g}{k_w} Nu} \frac{L}{d}}$$

Worst case conditions will occur at minimum pressure, wind speed and temperature since the k_g Nu product will be minimum. With:

$$L = 2 \text{ cm}$$
$$d = .003 \text{ in} = .00762 \text{ cm}$$
$$k_g = 12.79 \times 10^{-6} \text{ cal/cm-sec-°K}$$
$$Nu = .557$$
$$k_w = 4.83 \times 10^{-2} \text{ cal/cm-sec-°K}$$

we have:

$$\Delta T\Big|_{T.C.} = \frac{\Delta T_o}{12.3}$$

The temperature measurement uncertainty due to conduction can be expressed as

$$\delta\Delta T = \left[\sum_i \left(\frac{\partial \Delta T}{\partial V_i}\,\delta\, V_i\right)^2\right]^{1/2}$$

where the V_i are the variables in $\Delta T = \Delta T(V_i)$, namely k_g, k_w, Nu, L/D and ΔT_o.

Assuming the following uncertainties for the independent variables:

$$\frac{\delta k_g}{k_g} = .05$$

$$\frac{\delta k_w}{k_w} = .1$$

$$\frac{\delta Nu}{Nu} = .2$$

$$\frac{\delta\ L/D}{L/D} = .03$$

$$\delta\Delta T_o = \text{Unknown}$$

we have:

$$\delta\Delta T = [(.0815\ \delta\Delta T_o)^2 + (.0308\ \Delta T_o)^2]^{1/2}$$

Therefore, a difference in frame and ambient temperature of 23.6 ± 8.7°K will lead to a one degree measurement uncertainty.

4.2.3.2 Radiation Induced Errors

An appreciable radiative heat exchange will take place between the sensing thermocouple wires and the Martian environment. The following components make up the radiative effect:

Emission from wires: $-\pi\, d\, \sigma\, \varepsilon\, T_w^4$; ε = emissivity = α

Absorption from surface: $\pi\, d\, F_{sur}\, \varepsilon_{sur}\, \alpha\, \sigma\, T_{sur}^4$; F_{sur} = view factor;

ε_{sur} = surface emissivity; α = wire absorptivity

Absorption from space: $\pi\, d\, F_{sky}\, \varepsilon_{sky}\, \alpha\, \sigma\, T_{sky}^4$

Solar radiation: $\dot{Q}_s\, d\, \alpha_s$; $\dot{Q}$ = solar energy; α_s = wire solar absorptivity

The equilibrium relation is, therefore:

$$-\pi\, k_g\, Nu\, (T_w - T_\infty) + \pi\, d\, F_{sky}\, \varepsilon_{sky}\, \alpha\, \sigma\, T_{sky}^4 + \pi\, d\, F_{sur}\, \varepsilon_{sur}\, \alpha\, \sigma\, T_{sur}^4 + \dot{Q}_s\, d\, \alpha_s - \pi\, d\, \sigma\, \alpha\, T_w^4 = 0$$

Values used in calculations:

$d = .00762$ cm	$\delta d/d = .03$
$\sigma = 5.67 \times 10^{-12}$ watt/cm^2 °K^4	$\delta\sigma/\sigma = .01$
$\alpha = .1$	$\delta\alpha/\alpha = 1.$
$F_{sky} = .5$	$\delta F_{sky}/F_{sky} = .1$
$\varepsilon_{sky} = .95$	$\delta\varepsilon_{sky}/\varepsilon_{sky} = .05$
$T_{sky} = 144$°K	$\delta T_{sky}/T_{sky} = .15$
$F_{sur} = .5$	$\delta F_{sur}/F_{sur} = .1$
$\varepsilon_{sur} = .7$	$\delta\varepsilon_{sur}/\varepsilon_{sur} = .3$
$T_{sur} = T_\infty$	Unknown accuracy

$\dot{Q}_s = .0734$ watts/cm^2	$\delta\dot{Q}_s/\dot{Q}_s = .068$
$\alpha_s = .2$	$\delta\alpha_s/\alpha_s = .5$
k_g (130°K) = 12.79×10^{-6} cal/sec cm °K	$\delta k_g/k_g = .05$
k_g (350°K) = 49.0×10^{-6} cal/sec cm °K	$\delta k_g/k_g = .02$
Nu_{min} (130°K) = .557	$\delta Nu/Nu = .2$
Nu_{min} (350°K) = .254	$\delta Nu/Nu = .2$

Defining $\Delta T = T_w - T_\infty$, and substituting $T_w^4 \doteq T_\infty^4 - 4\,T_\infty^3\,\Delta T$ for $\Delta T << T_\infty$, we have:

$$\Delta T = \frac{\pi\, d\, F_{sky}\, \varepsilon_{sky}\, \alpha\, \sigma\, T_{sky}^4 + \pi\, d\, F_{sur}\, \varepsilon_{sur}\, \alpha\, \sigma\, T_\infty^4 + \dot{Q}_s\, d\, \alpha_s - \pi\, d\, \alpha\, \sigma\, T_\infty^4}{\pi\, k_g\, Nu + 4\pi\, d\, \alpha\, \sigma\, T_\infty^3}$$

Worst Case Conditions

Maximum temperature differences will be generated at minimum pressure and wind velocity. The worst case temperature is not immediately apparent and the following calculations are required:

1. Minimum Temperature Case: $T_\infty = 130°K$
   a. Solar Radiation Absent: $\dot{Q}_s = 0$
      $\Delta T = .003°K$
   b. Solar Radiation Maximum
      $\Delta T = 1.19°K$
2. Maximum Temperature Case: $T_\infty = 350°K$
   a. Solar Radiation Absent: $\dot{Q}_s = 0$
      $\Delta T = -.79°K$
   b. Solar Radiation Maximum
      $\Delta T = -.113°K$

The greatest temperature difference occurs at minimum temperature conditions with maximum solar radiation. Since the uncertainties are linear in most of the temperature difference variables, the greatest error should occur at the same worst case conditions.

Uncertainty Analysis

With $\Delta T = \Delta T(V_i)$, we evaluate the uncertainty after compensation for radiation effects as:

$$\delta\Delta T = \left[\sum_i \left(\frac{\partial \Delta T}{\partial V_i}\,\delta V_i\right)^2\right]^{1/2}$$

where the V_i are the independent variables

$$\left\{d,\ F_{sky},\ \varepsilon_{sky},\ \alpha,\ \sigma,\ T_{sky},\ \varepsilon_{sur},\ \dot{Q}_s,\ \alpha_s,\ k_g,\ Nu\right\}.$$

For $T_\infty = 130°K$ and $\dot{Q}_s = .0734$ watts/cm^2, the component values are:

$$\frac{\partial \Delta T}{\partial d} = \delta d = .035°K$$

$$\frac{\partial \Delta T}{\partial F_{sky}}\,\delta F_{sky} = .003°K$$

$$\frac{\partial \Delta T}{\partial \varepsilon_{sky}}\,\delta \varepsilon_{sky} = .002°K$$

$$\frac{\partial \Delta T}{\partial \alpha}\,\delta \alpha = .003°K$$

$$\frac{\partial \Delta T}{\partial \sigma}\,\delta \sigma = .0001°K$$

$$\frac{\partial \Delta T}{\partial T_{sky}}\,\delta T_{sky} = .018°K$$

$$\frac{\partial \Delta T}{\partial \varepsilon_{sur}}\,\delta \varepsilon_{sur} = .004°K$$

$$\frac{\partial \Delta T}{\partial \dot{Q}_s}\,\delta \dot{Q}_s = .081°K$$

$$\frac{\partial \Delta T}{\partial \alpha_s}\,\delta \alpha_s = .595°K$$

$$\frac{\partial \Delta T}{\partial k_g}\,\delta k_g = .060°K$$

$$\frac{\partial \Delta T}{\partial Nu}\,\delta Nu = .238°K$$

The uncertainty is dominated by the solar absorptivity component with the Nusselt number contribution being the only other significant term.

The total (RSS) uncertainty is:

$$\underline{\delta T = .65°K \text{ at } 130°K}$$

With $T_\infty = 350°K$ and $\dot{Q}_s = 0$, the component values are:

$$\frac{\partial \Delta T}{\partial d} \delta d = .023°K$$

$$\frac{\partial \Delta T}{\partial F_{sky}} \delta F_{sky} = .003°K$$

$$\frac{\partial \Delta T}{\partial \varepsilon_{sky}} \delta \varepsilon_{sky} = .002°K$$

$$\frac{\partial \Delta T}{\partial \alpha} \delta \alpha = .246°K$$

$$\frac{\partial \Delta T}{\partial \sigma} \delta \sigma = .008°K$$

$$\frac{\partial \Delta T}{\partial T_{sky}} \delta T_{sky} = .018°K$$

$$\frac{\partial \Delta T}{\partial \varepsilon_{sur}} \delta \varepsilon_{sur} = .130°K$$

$$\frac{\partial \Delta T}{\partial k_g} \delta k_g = .016°K$$

$$\frac{\partial \Delta T}{\partial Nu} \delta Nu = .156°K$$

Here, the error is largely due to the uncertainty in the low temperature absorptivity. The total (RSS) uncertainty is:

$$\delta T = .32°K$$

4.2.3.3 Velocity Induced Errors

The sensor as designed will measure the recovery temperature, T_R. At low wind speeds, this will be very close to the ambient temperature, T_∞; however, at the highest predicted wind speeds, compressibility heating will be significant and compensation will be necessary. The governing relation is:

$$T_\infty = \frac{T_R}{1 + \alpha \frac{\gamma - 1}{2} M_\infty^{\ 2}}$$

α = recovery factor = $(T_R - T_\infty)/(T_T - T_\infty)$

T_T = total temperature

γ = specific heat ratio = 1.337 for .91 CO_2 + .09 A

$M_\infty = u_\infty/\sqrt{\gamma R T_\infty}$

u_∞ = wind velocity

The recovery factor is a function of the Knudsen number in the region of transition from free molecular to continuum flow. Values associated with the sensor operating range, $.0072 < Kn < .232$, are shown in Figure 4. The data used in the graph were derived from values published by Atassi[1], Moffet[2], and Vrebalovich.[3]

Worst Case Analysis

Solving for the difference between the recovery and ambient temperatures gives:

$$\Delta T = T_R - T_\infty = \alpha \frac{\gamma - 1}{2} \frac{u^2}{\gamma R}$$

The compressibility effect will, therefore, be greatest at the highest wind speed, 70 m/sec, and the highest Knudsen number (i.e., highest α). Maximum Knudsen number conditions occur with minimum pressure (2 torr) and maximum temperature (350°K). With α = 1.04:

Worst
CASE GROWTHS

M

$$\Delta T = 3.0°K$$

The magnitude of this temperature difference makes analytic compensation essential. The error induced in the recovered ambient temperature will then be due to uncertainties in the compensation.

Uncertainty Analysis

The total uncertainty is again given by:

$$\delta\Delta T = \left[\sum_i \left(\frac{\partial T}{\partial V_i}\,\delta V_i\right)^2\right]^{1/2}$$

since the variables $V_i = \{u, \alpha, \gamma\}$ are independent. The component values are:

$$\frac{\partial\Delta T}{\partial u}\,\delta u = 1.20°K \text{ with } \delta u/u = .2$$

$$\frac{\partial\Delta T}{\partial \alpha}\,\delta \alpha = .45°K \text{ with } \delta\alpha/\alpha = .15$$

$$\frac{\partial\Delta T}{\partial \gamma}\,\delta \gamma = .14°K \text{ with an assumed argon concenctration of } 9\% \pm 5\%$$

The total (RSS) uncertainty is, therefore:

$$\delta\Delta T = 1.29°K$$

4.2.3.4 Total Compensation Uncertainty

Since the largest uncertainties do not occur at the same conditions for each of the three compensation terms, the total uncertainty is not the sum or RSS of the components. Worst case conditions for the radiation and conduction effects occur at the minimum wind speed where compressibility effects are negligible. Similarly, at the highest wind speeds where the

compressibility effect is greatest, the Nusselt number is relatively large and the convective heat transfer dominates conduction and radiation. Since the magnitude of all the compensation terms decreases at least linearly as conditions vary from worst case, at intermediate values of the temperature, pressure and wind velocity , the total compensation uncertainty will be relatively small. Thus the overall worst case lies at whichever extreme condition yields the largest uncertainty.

Worst case conduction effects have not been determined because the difference between the frame and ambient temperatures has not been accurately predicted for all combinations of ambient conditions. However, an engineering analysis based upon the best estimate daily temperature and pressure cycle showed that the frame stayed within a few degrees of the ambient temperature. Therefore, an assumed worst case uncertainty of one degree (corresponding to a frame temperature difference of 23.6 ± 8.7°K) should be an adequately conservative conduction error estimate. With the radiation uncertainty, this makes the low wind speed error 1.19°K. Thus, the high speed error, 1.29°K, is the worst case.

4.2.4 Total System Uncertainty

The errors due to all postulated contributors can now be combined and compared with the accuracy requirements. The resulting error budget is given below.

Error Budget

Electronics and Data Transmission	1.22°K
Calibration, Repeatability and Drift	1.50°K
Compensation Uncertainty	1.29°K
RSS	2.33°K
Unassigned Latitude	1.90°K
Specification	3.00°K

4.3 Stability

The stability of the sensing elements was verified by monitoring the output over a period of time during a calibration while the temperature was held constant. There was no discernible variation. The long term stability was inferred from the repeated calibrations. The stability of the electronics was established independently, as discussed in the Worst Case Analysis Report for the Meteorology Electronics Assembly (METC-013, 29 September 1972).

4.4 Resolution

The resolution of the thermocouple loop and platinum resistance thermometer is almost infinitely small and the system resolution is determined by the characteristics of the electronics and data transmission elements. These are discussed in the Worst Case Analysis Report.

4.5 Response Time

The response time of the temperature sensor was determined by a test conducted in the Viking Wind Tunnel on 15 August 1972. The response time is defined as the time required for the sensor to transition 63.2 percent towards a step change in temperature. After adjusting the test results to worst case operating conditions, the response time was found to be 1.8 seconds.

Test Description

The sensor was mounted in the wind tunnel with the open portion of the frame facing upstream and the thermocouple junctions at the approximate

Temp
Worst case
1.8 sec

center of the test section. A step change in temperature was simulated by heating the thermocouple wires with a current until a stabilized overheat was achieved. The current source was then disconnected and the colder fluid flowing through the tunnel provided the incremental temperature change. The response of the sensor to the temperature difference was then monitored to determine the response time.

Since the test objective was to evaluate the response time under worst case conditions, the wind tunnel was operated at the lowest measurable flow rate. The resulting test conditions are compared with worst case operating conditions in Table 2.

Table 2. Comparison of Test and Worst Case Operating Conditions

Parameter	Test Conditions	Worst Case Operating Conditions
Fluid	Air	CO_2 + < 18% Argon
Pressure	2.17 mm Hg	2.1 mm Hg
Velocity	2.62 m/sec	2 m/sec
Temperature	296.3°K	130 to 350°K

The sensor thermocouple triad was wired in a loop with a Chromel-P/Constantan reference junction placed in a distilled water ice bath. Secondary junctions to copper leads were also located in the ice bath to minimize residual voltages.

A 200 ma heating current was applied to the thermocouple wires through the copper leads. The diameter of the leads and the reference junction thermocouple wire (.020 inch minimum) was sufficiently in excess of the .003 inch diameter sensor wires to make the lead overheat negligible. A Harrison 6111A DC Power Supply was used to supply the heating current. The resulting sensor wire overheat was about 17°C.

After a stabilization period of about one minute, the heating current was disconnected and the thermocouple loop leads were connected to a voltage recording system made up of a Hewlett Packard 467A DC stable power amplifier and a Moseley Autograf X-Y plotter. The plotter was started as soon as the thermocouple loop was connected to the DC amplifier. The plot of EMF vs. time was then used to determine the response time. A schematic of the test configuration is given in Figure 5.

The temperature sensor response was measured only after the wind tunnel flow conditions had stabilized and had been verified at the desired pressure and velocity. Final readings of total pressure, dynamic pressure and total temperature were made simultaneously with the sensor output recordings. The wind tunnel and its recording equipment were operated in accordance with published operating procedures.

Analysis of Results

A plot of the thermocouple EMF vs. time is shown in Figure 6. Values from this plot were used to prepare the exponential plot shown in Figure 7. The linearity demonstrates the anticipated exponential character of the thermal response and the slope of the line yields the response time for the test, .91 seconds. Adjustments to this value were necessary to obtain the response time corresponding to worst case operating conditions.

The sensor response time can be equated to the ratio of the thermal inertia and the rate of heat transfer:

$$\tau = \frac{\rho_w \, c_w \, d^2}{4 \, K_g \, Nu}$$

where

ρ_w = thermocouple wire density
c_w = thermocouple heat capacity
d = wire diameter
K_g = gas thermal conductivity
Nu = Nusselt number

Therefore,

$$\tau_{worst\ case} = \tau_{test} \frac{(K_g \, Nu)_{test}}{(K_g \, Nu)_{worst\ case}}$$

Since the worst case temperature is not immediately evident, the K_g Nu product must be evaluated for both temperature extremes.

Thermal Conductivities:

$K_{g(Air,\ 296.3°K)}$	62.09×10^{-6} cal/sec cm °C
$K_{g(CO_2,\ 130°K)}$	12.79×10^{-6} cal/sec cm °C
$K_{g(CO_2,\ 350°K)}$	49.0×10^{-6} cal/sec cm °C

Nusselt Numbers:

The test and worst case conditions lie in the near-free-molecular flow regime and, therefore, Nu = Nu (M, Re).

Mach Numbers: $M = u/\sqrt{\gamma RT}$

M_{test}	.00756	
$M_{worst\ case,\ 130°K}$	.01122	21 mm, 2m/s
$M_{worst\ case,\ 350°K}$	.00681	21 mm, 2m/s

Reynolds Numbers: $Re = \rho\ u\ d/\mu$

Re_{test}	.0332
$Re_{worst\ case,\ 130°K}$	.281
$Re_{worst\ case,\ 350°K}$	.0374

The variation of Nusselt number in the Mach and Reynolds number ranges of interest has been discussed by Baldwin, Sanborn and Laurence[4]. Figure 8 shows their results over the range of interest. The figure gives the Nusselt number as a function of Reynolds number only for M = 0 and M = .1 (above Re = .8, data for M = .05 is also given). Therefore, an interpolation scheme was used based on the relation:

$$\frac{1}{Nu} = \frac{1}{Nu_{cont}} + k\ \frac{M}{Re}$$

where Nu_{cont} is the M = 0 Nusselt number, and the factor k was determined from several values at M = .05 and M = .1. A representative value of k = 10.3 ± .3 was established. The resulting Nusselt numbers were:

$$Nu\ (M = .00756,\ Re = .0332) = .226$$

$$Nu\ (M = .01122,\ Re = .281) = .557$$ .01c chart

$$Nu\ (M = .00681,\ Re = .0374) = .254$$ roughly 0.2

The ratios of the thermal conductivity-Nusselt number products are then:

$$\frac{(K_g\ Nu)_{test}}{(K_g\ Nu)_{worst\ case,\ 130°K}} = 1.963$$ 1.963

$$\frac{(K_g\ Nu)_{test}}{(K_g\ Nu)_{worst\ case,\ 350°K}} = 1.128$$ ✓

The worst case temperature is, therefore, 130°K and the adjusted time constant is:

$$\tau_{worst\ case} = 1.963\ \tau_{test} = 1.8 \text{ seconds}$$

Evaluation of Uncertainty

1. Test Uncertainties

a. Measured Time Constant

The aggregate error from electronics and plotter inaccuracies is less than 3 percent. Thus:

$$\frac{\delta\ \tau_{test}}{\tau_{test}} \doteq .03$$

b. Measured Quantities

Temperature	±	.02 mv = ± .5°C
Total Pressure	±	.005 mm Hg
Dynamic Pressure	±	.00001 mm Hg

Met paper calculations
Assume 6.8 mb not 2.1
∴ Re = 3* Re (worst case)
From Sanborn & Baldwin
Nu (M = 0.01122, Re = .281) = 0.6
Nu (M = 0.011 [illegible]) ≈ 0.8
∴ τ ≈ τw · 0.6/0.8 = 1.8 · 0.6/0.8 = 1.35
3x speed next
Nu (M = 0.033, Re 2.529) = 1.1
∴ τ = 1.8* 0.6/1.1 = 0.98

c. Mach Number Uncertainty

$$M_\infty = \left\{ \frac{2}{\gamma - 1} \left[\left(\frac{P_o}{P_o - \Delta P} \right)^{\frac{\gamma-1}{\gamma}} - 1 \right] \right\}^{1/2} \doteq 1.195 \left(\frac{\Delta P}{P_o} \right)^{1/2}$$

and

$$\frac{\delta M_\infty}{M_\infty} = \frac{1}{2} \left[\left(\frac{\delta \Delta P}{\Delta P} \right)^2 + \left(\frac{\delta P_o}{P_o} \right)^2 \right]^{1/2}$$

$$\frac{\delta M_\infty}{M_\infty} = .058$$

d. Reynolds Number Uncertainty

$$Re = \frac{\rho \; u \; d}{\mu}$$

$$\frac{\delta Re}{Re} = \left[\left(\frac{\delta \rho}{\rho} \right)^2 + \left(\frac{\delta u}{u} \right)^2 + \left(\frac{\delta d}{d} \right)^2 + \left(\frac{\delta \mu}{\mu} \right)^2 \right]^{1/2}$$

$$\frac{\delta \rho}{\rho} = .0029 \quad \text{from} \quad \left[\left(\frac{\delta P_o}{P_o} \right)^2 + \left(\frac{\delta T_o}{T_o} \right)^2 \right]^{1/2}$$

$$\frac{\delta u}{u} = .058 \quad \text{from} \quad \frac{\delta M_\infty}{M_\infty}$$

$$\frac{\delta d}{d} = .1$$

$$\frac{\delta \mu}{\mu} = .02 \quad \text{for air at ambient temperature}$$

Then

$$\frac{Re}{Re} = .118$$

e. Nusselt Number Uncertainty

$$\frac{1}{Nu} = \frac{1}{Nu_{cont}} + k \frac{M}{Re}$$

$$\frac{\delta Nu}{Nu} = \frac{kM}{Re + kM}\left[\left(\frac{\delta Re}{Re}\right)^2 + \left(\frac{\delta M}{M}\right)^2\right]$$

$$\left(\frac{\delta Nu}{Nu}\right)_{test} = .087$$

f. Thermal Conductivity Uncertainty

$$\left(\frac{\delta K_g}{K_g}\right)_{test} = .02$$

2. Worst Case Uncertainties

a. Mach Number Uncertainty

$$\frac{\delta M_\infty}{M_\infty} = 0 \quad \text{defined value}$$

b. Reynolds Number Uncertainty

$$\frac{\delta R}{R} = \frac{\delta \mu}{\mu} = .05 \quad \begin{cases} \text{d correlated with test uncertainty} \\ \text{other values defined} \end{cases}$$

c. Nusselt Number Uncertainty

$$\frac{\delta Nu}{Nu} = \frac{kM}{Re + kM}\frac{\delta Re}{Re} = .029$$

3. Total Uncertainty

$$\frac{\delta \tau}{\tau} = \left[\left(\frac{\delta K_g}{K_g}\right)^2_{test} + \left(\frac{\delta K_g}{K_g}\right)^2_{worst\ case} + \left(\frac{\delta Nu}{Nu}\right)^2_{test} + \left(\frac{\delta Nu}{Nu}\right)^2_{worst\ case} + \left(\frac{\delta \tau_{test}}{\tau_{test}}\right)^2\right]^{1/2}$$

$$= .107$$

Thus, $\underline{\tau = 1.8 \pm .2 \text{ sec}}$

4.6 Warm-up Time

The sensing elements have an insignificant warm-up time and meeting this specification involves the electronics package only. This is discussed in the Worst Case Analysis Report.

4.7 Attitude

The design of the sensing element makes the system inherently insensitive to attitude changes. It is, however, sensitive to orientation in one respect. When the wind direction is such that the sensor lies in the thermal wake of the lander, an error of unknown magnitude will be introduced by the change in air temperature over the sensing thermocouples. The affected directions are expected to cover a sector of about seventy degrees.

4.8 Hysteresis

The hysteresis of the sensing elements was determined during a calibration by approaching a calibration point temperature from above and below. The measured output difference was within the limitations of the test equipment (i.e., equivalently less than .2°K). Similar tests were performed on the electronics package, as discussed in the Worst Case Analysis Report.

References

1. Atassi, H. and Brun, E., "Heat Transfer from Wires in a Rarefied Low Speed Flow," Rarefied Gas Dynamics, Vol. II, pp. 1221-1234, Academic Press (1967).

2. Moffat, R., "Gas Temperature Measurement," Temperature, Its Measurement and Control in Science and Industry, Vol. III, Part 2, pp. 553-571 (1962).

3. Vrebalovich, T., "Heat Loss and Recovery Temperature of Fine Wires in Transonic Transition Flow," Rarefied Gas Dynamics, Vol. II, pp. 1205-1219, Academic Press (1967).

4. Baldwin, L., Sandborn, V., and Laurence, J., "Heat Transfer from Transverse and Yawed Cylinders in Continuum, Slip, and Free Molecule Air Flows," Journal of Heat Transfer, Vol. 82, No. 2, May 1960.

Table 1. Temperature Sensor Calibration Schedule

Frame Temp. (°K)	Rosemount Fluid	Module Temp. (°K)	Voltage Pin 4-Pin 3	Resistance Pins 1, 2	Resistance Top Pins
130	FREON 12	230	- 4.542	124.41	121.01
		255	- 5.911	139.24	121.00
		280	- 7.358	154.05	121.01
		305	- 8.864	168.86	121.01
		330	-10.421	183.64	121.01
180	FREON 12	230	- 2.366	124.47	121.01
		255	- 3.730	139.22	121.01
		280	- 5.179	154.08	121.01
		305	- 6.682	168.88	121.01
		330	- 8.247	183.59	121.01
230	FREON 12	230	0.003	124.51	121.01
		255	- 1.375	139.31	121.01
		280	- 2.816	154.09	121.01
		305	- 4.324	168.84	121.01
		330	- 5.880	183.58	121.01
270	FREON E-4	230	2.222	124.39	121.01
		255	0.858	139.20	121.02
		280	- 0.591	154.01	121.01
		305	- 2.101	168.78	121.01
		330	- 3.664	183.70	121.01
310	FREON E-4	230	4.639	124.43	121.00
		255	3.267	139.31	121.01
		280	1.823	154.35	121.01
		305	0.315	168.92	121.01
		330	- 1.256	183.72	121.01
350	FREON E-4	230	7.200	124.50	121.02
		255	5.839	139.27	121.01
		280	4.392	154.21	121.01
		305	2.887	168.81	121.01
		330	1.324	183.63	121.01

NOTES

1. Frame temperatures accurate to ±.05°K
2. Module temperatures accurate to ±1°K
3. Voltage measured accurate to ±.002 mv
4. Resistances measured accurate to ±.01 ohm

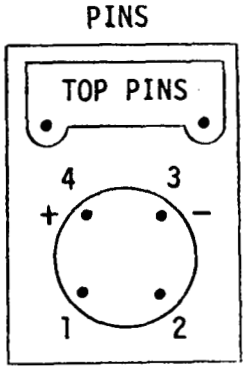

Figure 1
Temperature Sensor System Configuration

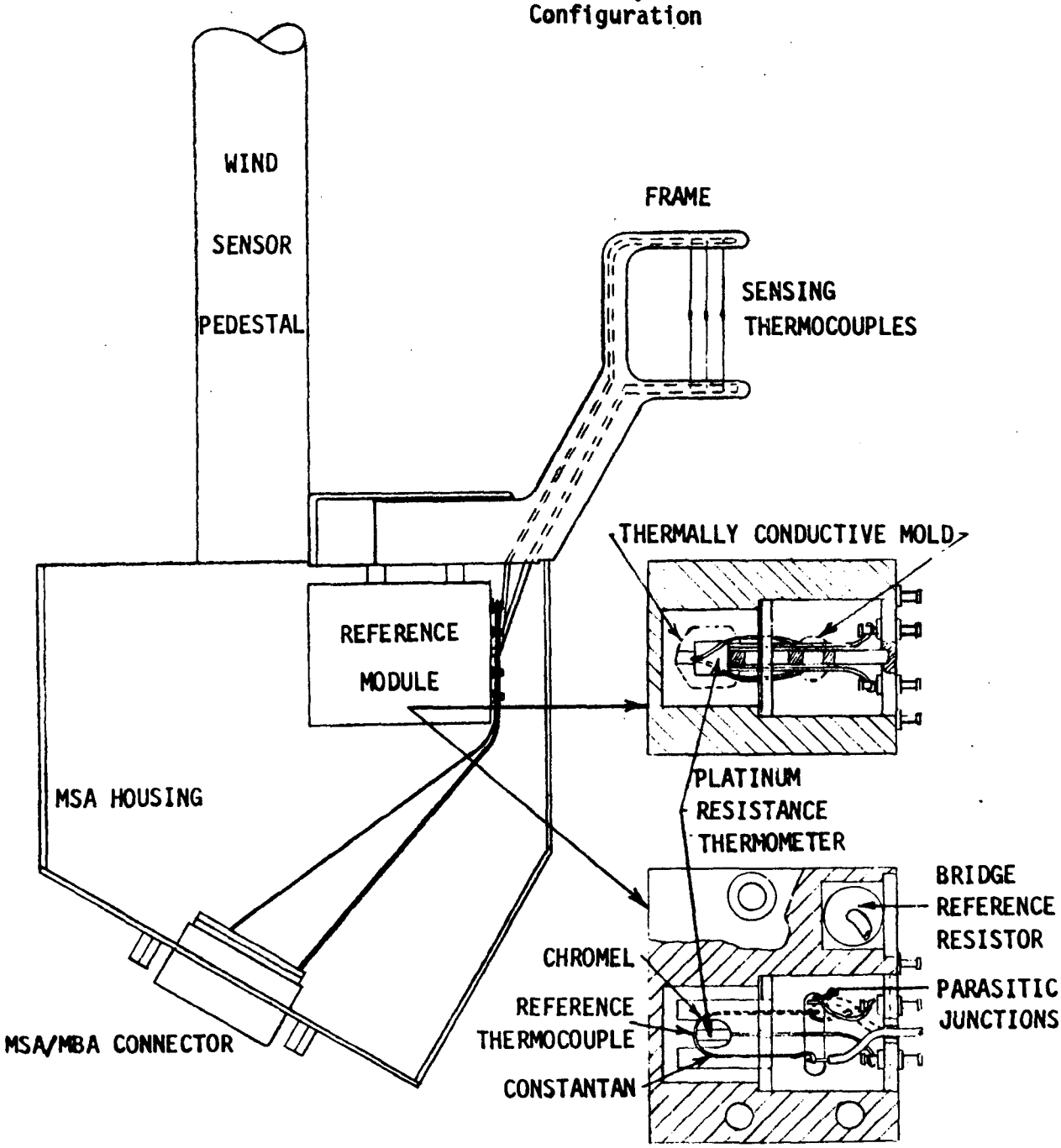

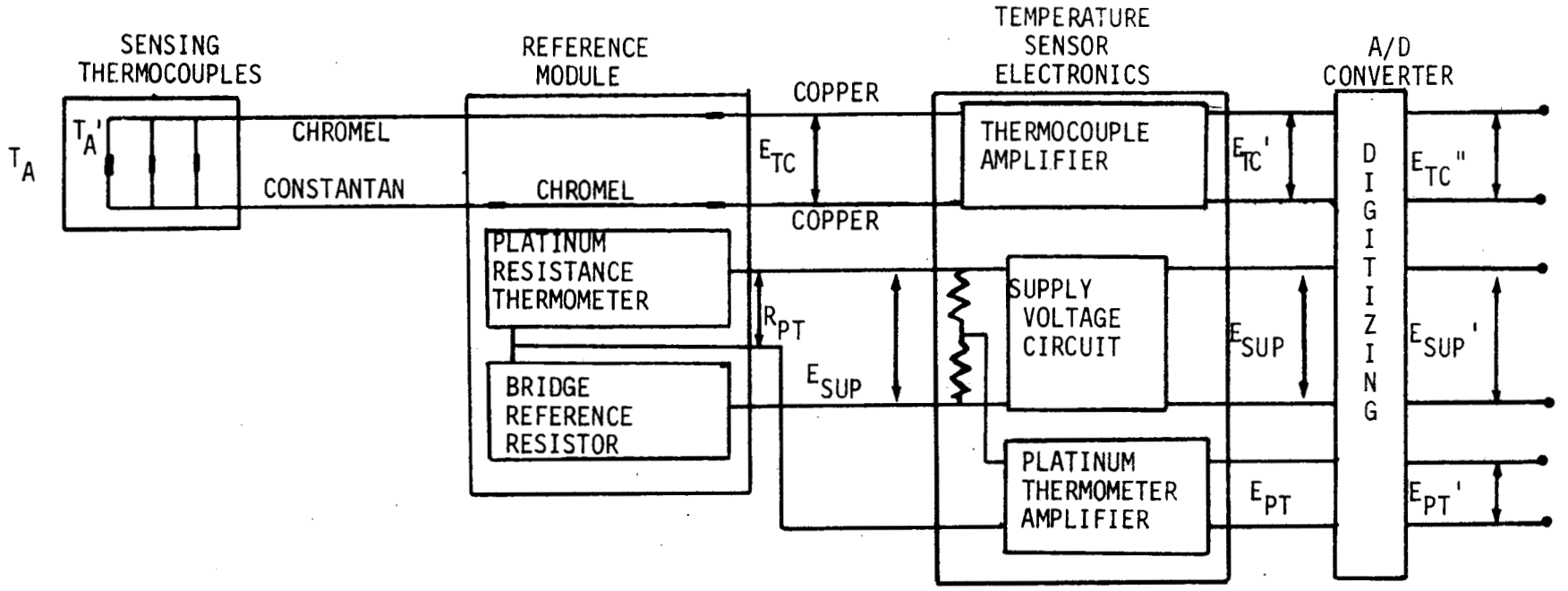

CALIBRATION RELATIONS

$$\{E_{TC};\ R_{PT}\} = f_1(\ T_A',\ T_M\ )$$

$$E_{TC}'' = f_2(E_{TC})$$

$$E_{PT}' = f_3(R_{PT},\ E_{SUP})$$

$$E_{SUP}' = f_4(E_{SUP})$$

OPERATIONAL RELATIONS

$$E_{TC} = g_1(E_{TC}'') = f_2^{-1}(E_{TC}'')$$

$$E_{SUP} = g_2(E_{SUP}') = f_4^{-1}(E_{SUP}')$$

$$R_{PT} = g_3(E_{PT}',\ E_{SUP})$$

$$T_A' = g_5(E_{TC},\ R_{PT})$$

Figure 2. Temperature Sensor Operation

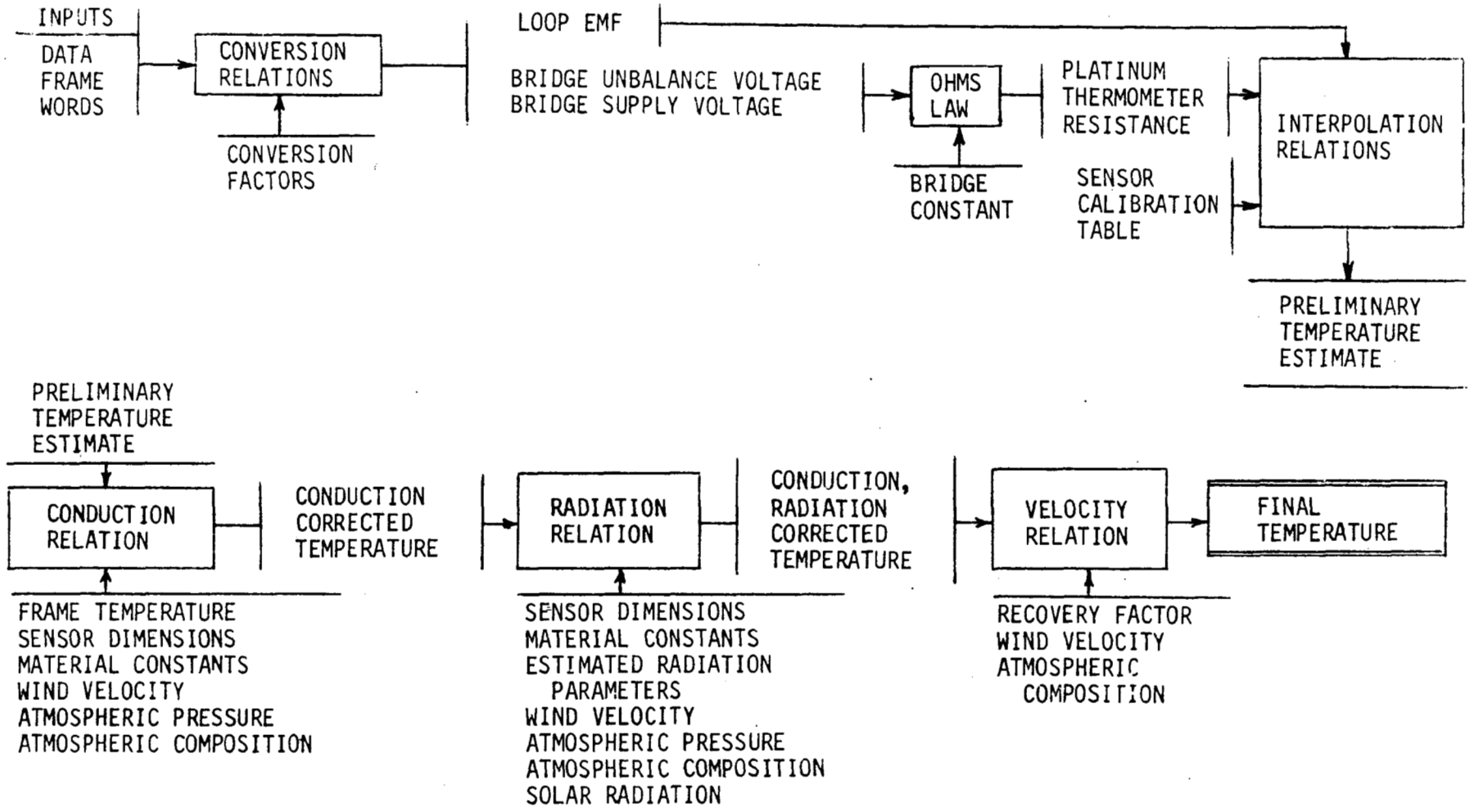

Figure 3. Data Reduction Procedure

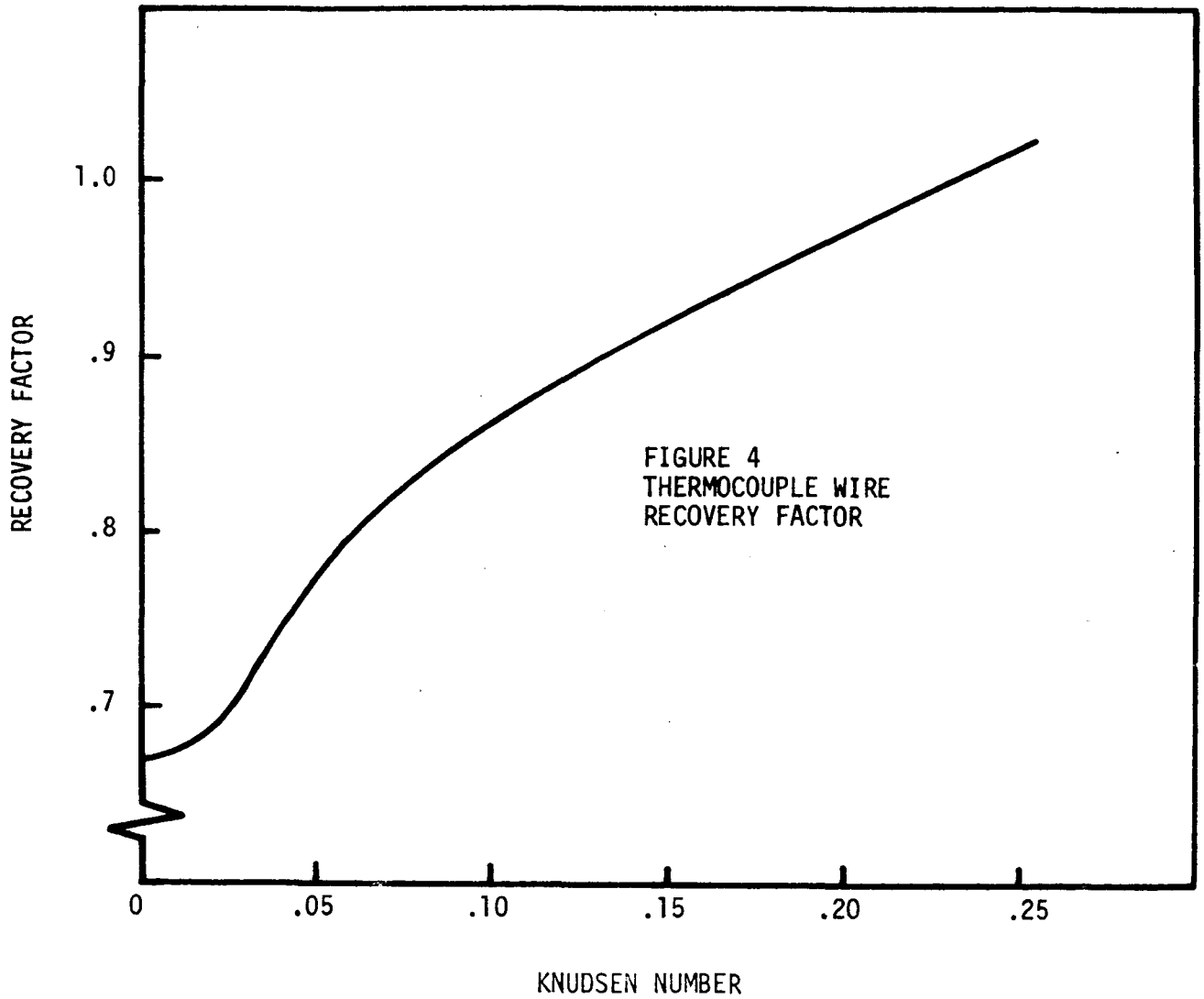

FIGURE 4
THERMOCOUPLE WIRE
RECOVERY FACTOR

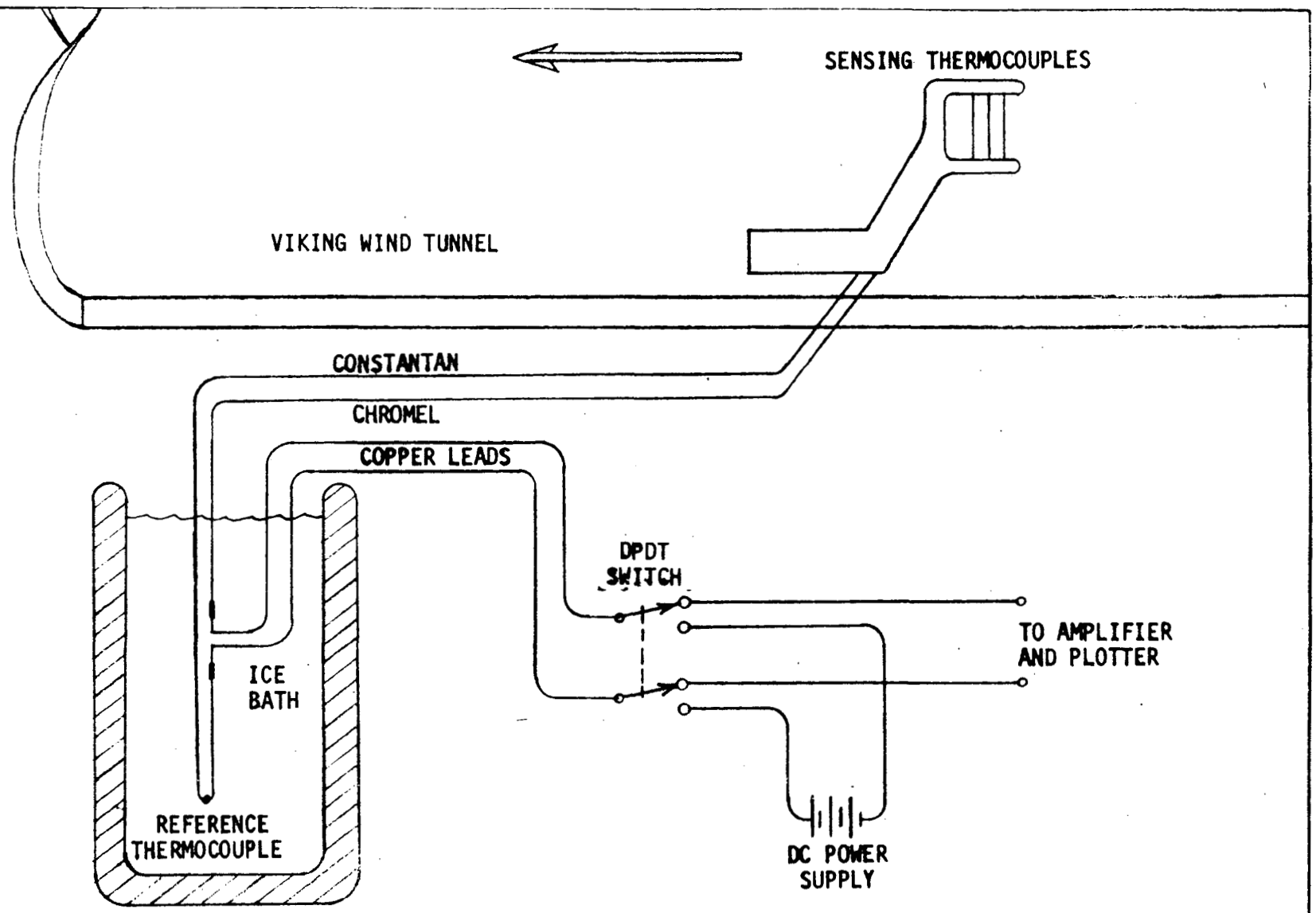

FIGURE 5

TEMPERATURE SENSOR TIME RESPONSE TEST
EXPERIMENT CONFIGURATION

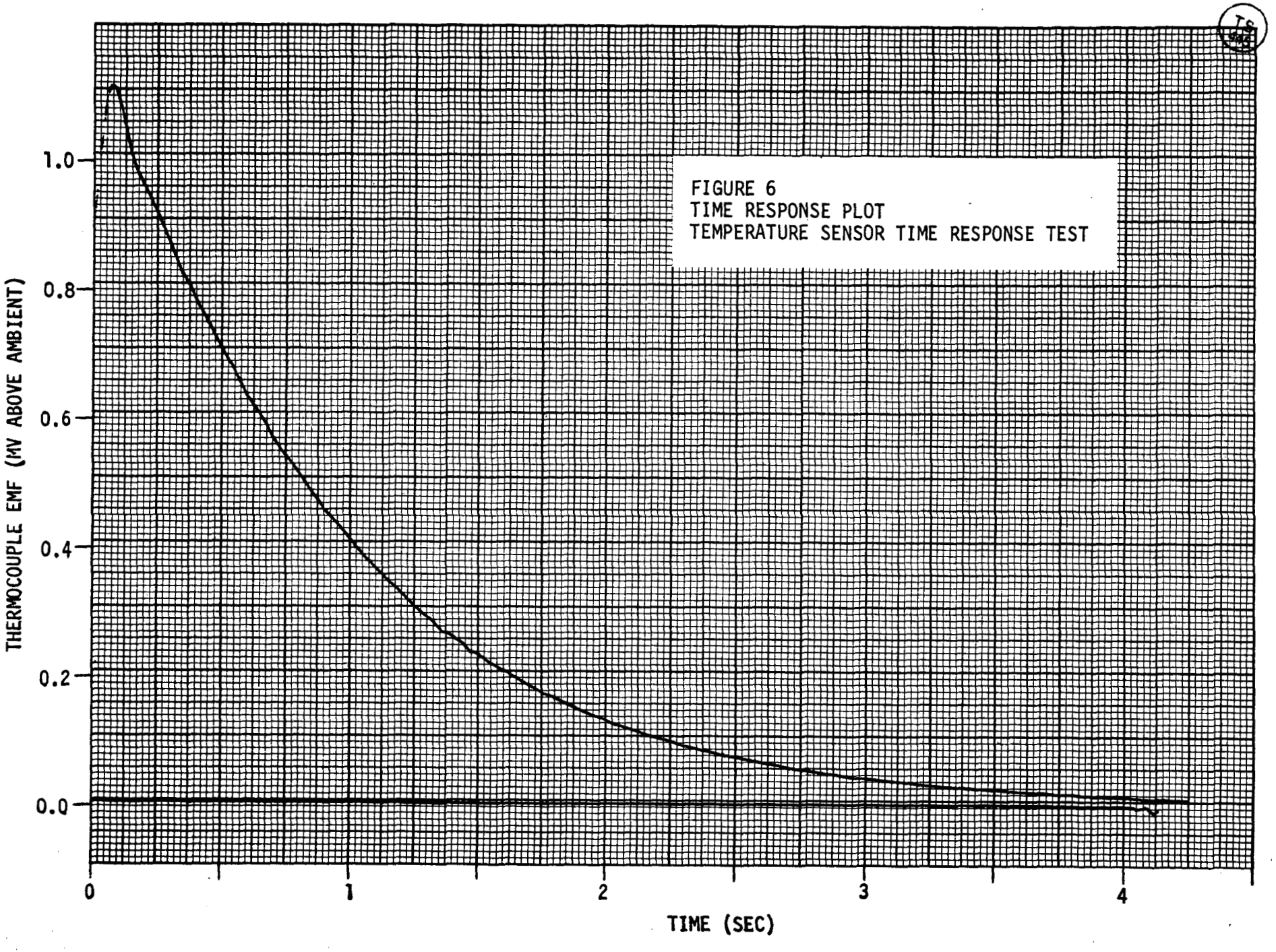

FIGURE 6
TIME RESPONSE PLOT
TEMPERATURE SENSOR TIME RESPONSE TEST

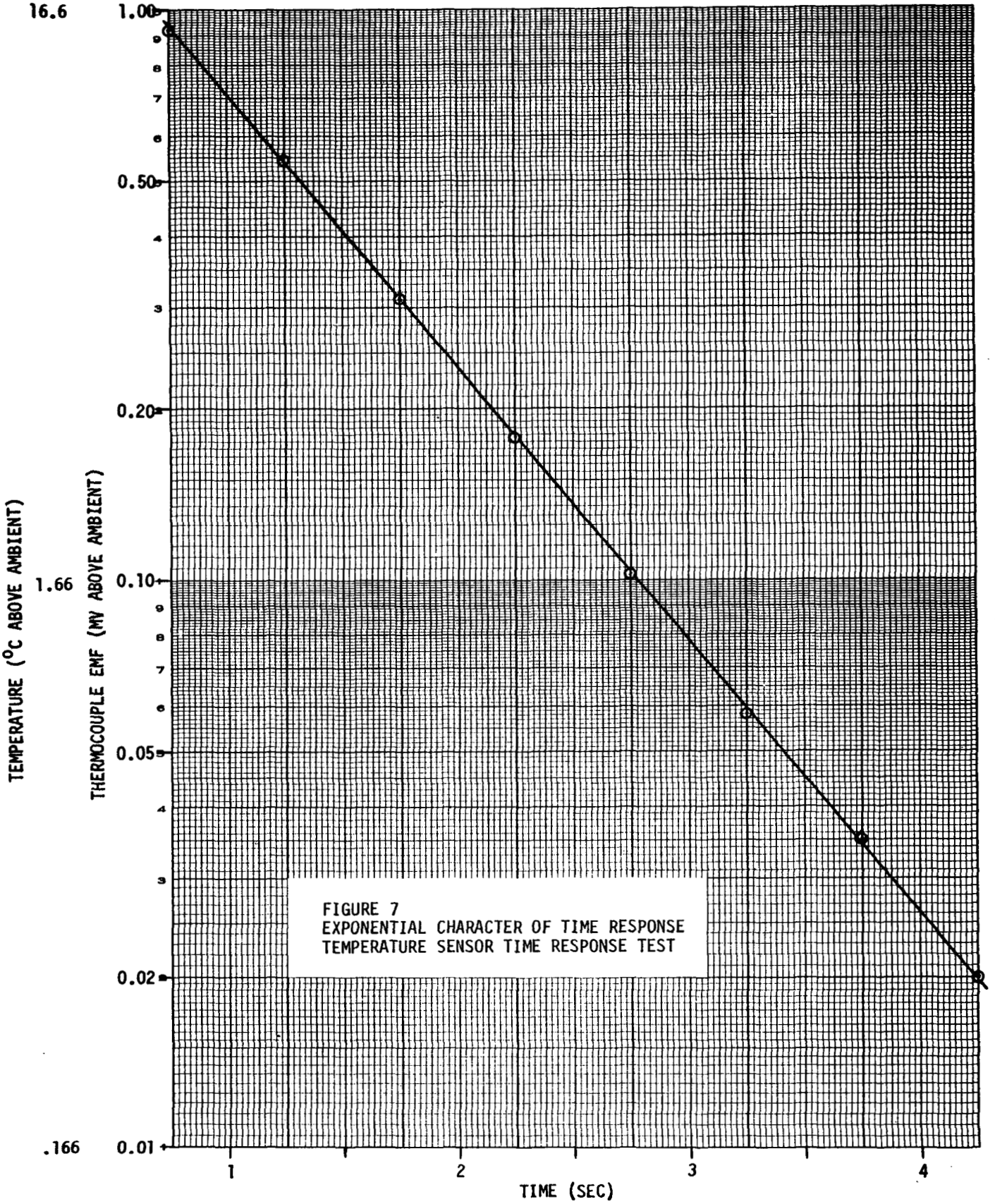

FIGURE 7
EXPONENTIAL CHARACTER OF TIME RESPONSE
TEMPERATURE SENSOR TIME RESPONSE TEST

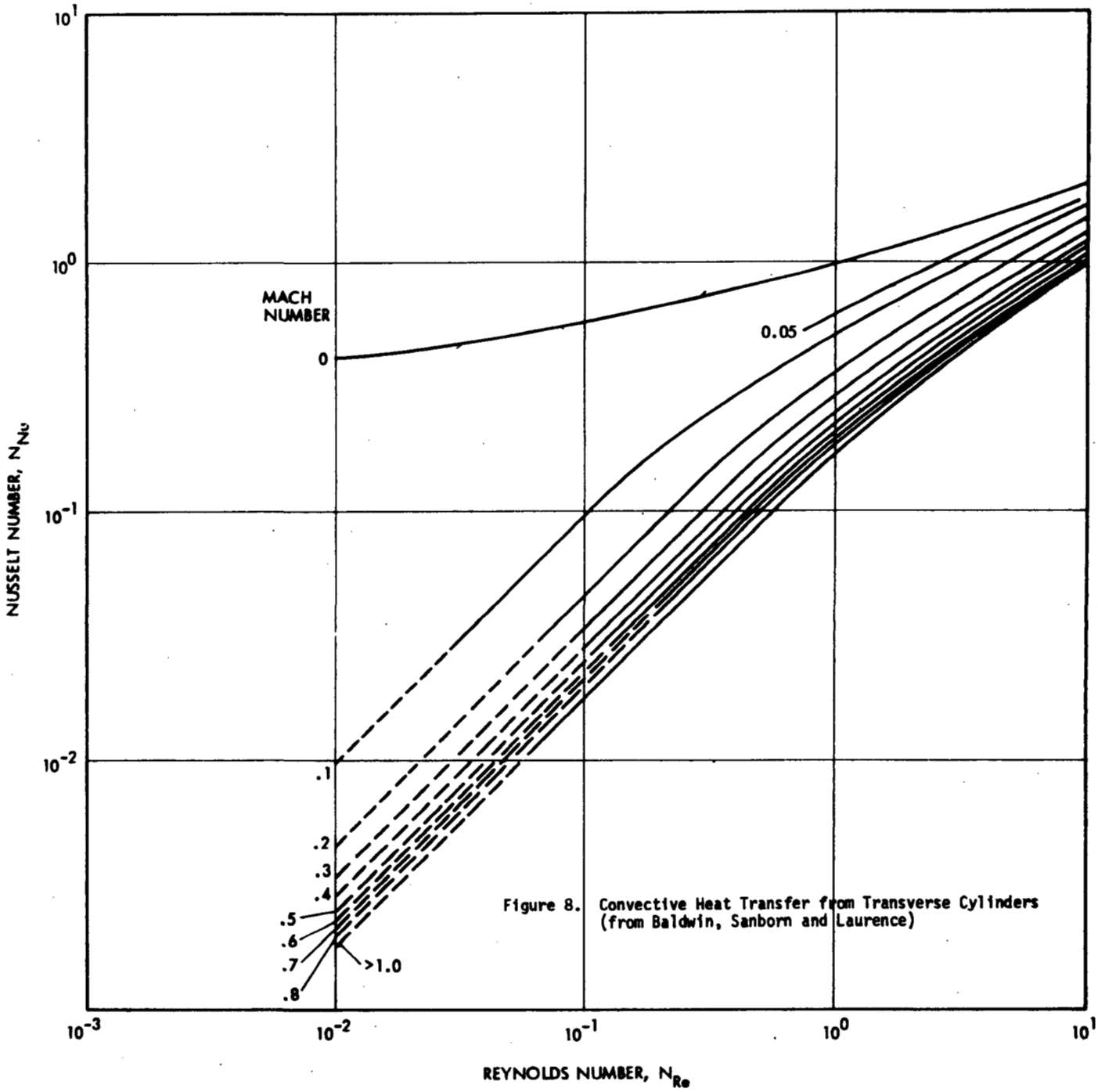

Figure 8. Convective Heat Transfer from Transverse Cylinders (from Baldwin, Sanborn and Laurence)

SECTION II

WIND SENSORS

TABLE OF CONTENTS

Page

1. WIND SENSOR ARRAY DESCRIPTION 1

1.1 Configuration 1

1.2 Principle of Operation 1

2. PERFORMANCE TESTING OF WIND SENSOR 4

2.1 Test Description 4

2.1.1 Facility 4

2.1.2 Wind Sensor Array Model 5

2.2 Test Procedure and Conditions 6

2.3 Test Results 8

2.3.1 Data Reduction 8

2.3.2 Data Presentation 9a

3. PERFORMANCE ANALYSIS OF WIND SENSOR 15

3.1 Performance Requirements 15

3.2 Performance Analysis 15

3.2.1 Measurement Range 15

3.2.2 Wind Speed Accuracy 18

3.2.3 Hysterisis 22

3.2.4 Stability 22

3.2.5 Resolution 22

3.2.6 Calibration Requirements 23

3.2.7 Response Time 23

3.2.8 Warm-up Time 27

3.2.9 Attitude 29

3.2.10 Self-Heating 29

3.2.11 Wind Direction Accuracy 29

3.2.12 Wind Direction Resolution 32

APPENDIX A - WIND SENSOR PERFORMANCE DATA 69

1. WIND SENSOR ARRAY DESCRIPTION

1.1 CONFIGURATION

Figure 1 shows a drawing of the Meteorology Sensor Assembly with the temperature sensor, quadrant sensor and wind sensor array indicated. Figure 2 displays drawings of the wind sensor array elements. The principal components of the wind sensor are the hot film sensing element, the glass-epoxy sting supporting the sensing element and the platinum wire leads extending through the sting to the base of the sensing element. The sensing element consists of a 0.020 inch diameter pyrex rod, a split platinum film on the surface of the rod and an alumina covering for protection of the platinum film from dust abrasion. The platinum paste cap at the tip of the element serves as part of the sensor electrical circuit as does the platinum paste at the element base. Conductive gold epoxy is used to reinforce the lead attachments.

Figure 3 displays the MSA electrical circuitry. An important feature of the circuitry is the existence of Kelvin junctions for each of the wind sensor leads. The Kelvin junctions permit measurement of the element resistances and the resistances of the leads running to the junctions exclusive of the additional circuitry running to the wind module and the MEA. This feature increases the precision of sensor resistance measurements.

1.2 PRINCIPLE OF OPERATION

Each of the wind sensor array elements is a hot film anemometer, i.e., it is an instrument which permits the calculation of wind speed from the power required to maintain a specified overheat temperature. The sensor convective heat transfer may be represented by the Nusselt number

$$Nu = Q/(\pi\ L\ k_F\ \Delta T) \tag{1}$$

where Q is the power convected to the fluid, L is the element length, k_F is the gas thermal conductivity (at the gas film temperature) and ΔT is the element overheat temperature. For an infinite cylinder, the Nusselt number is related to the film Reynolds number, Re_F, by the empirical relation

$$Nu = (T_F/T_A)^{.17}\ (A + B\ Re_F^{\ n}) \tag{2}$$

where T_F and T_A are the film temperature and the cylinder adiabatic recovery temperature, respectively, and A, B and n are constants (Reference 1).

Equation (2) is valid for gas velocities which are perpendicular to the cylinder axis. For gas velocities which are not perpendicular to the cylinder axis, the Nusselt number is reduced to a value which can be adequately represented, for the purpose of the present discussion, by the relation

$$Nu = (T_F/T_A)^{.17}\ [A + B\ (Re_F\ \cos\theta)^n] \tag{3}$$

where θ is defined in Figure 4. This equation holds that the convective heat transfer is simply determined by the cross-flow Reynolds number. It is the variability of convective heat transfer with flow angle (in addition to wind speed) that is the essence of the wind array principle of operation. Each wind sensor element may have its convective heat transfer represented by an equation like Equation (3); for example,

$$Nu_1 = (T_F/T_A)^{.17}\ [A + B\ (Re_F\ \cos\theta)^{1/2}] \tag{4}$$

$$Nu_2 = (T_F/T_A)^{.17}\ [A + B\ (Re_F\ \cos[\theta - 90°])^{1/2}] \tag{5}$$

It is assumed here that the attitude angle ψ is zero where ψ is defined in Figure 5. The Nusselt numbers are calculated from the flight data using Equation (1). Equations (4) and (5) are then determinate permitting a solution for Re_F and θ; the wind speed is calculated using the definition of the Reynolds number and the known sensor and gas properties. Note that the quadrant sensor is needed to determine the true solution from the four possible solutions.

It should be noted that the power supplied to the wind sensor elements is lost through the parasitic heat transfer modes, heat conduction and radiation, in addition to heat convection. Since only heat convection is related to the wind velocity, the parasitic heat losses should be subtracted from the total power before a solution for the wind velocity can be obtained.

2. PERFORMANCE TESTING OF WIND SENSOR

2.1 TEST DESCRIPTION

2.1.1 Facility

Figure 6 shows a drawing of the Viking Wind Tunnel. The test gas flow is produced by the pressure difference between the atmospheric pressure at the intake and the partial vacuum in the manifold pipe leading to the pumps. Air or CO_2 at ambient temperature and pressure flows into the intake manifold and through one of the three volumetric flow meters. These meters are used as guides in producing the desired flow and are not used in calculating the test section flow properties. The gas then flows into the stagnation chamber, into the tunnel test section and through a sonic orifice plug valve before entering the manifold. The test section Reynolds number is determined (approximately) by the mass flow rate into the tunnel and the Mach number by the ratio of the test section cross-sectional area to the sonic orifice area. A precise calculation of the test section flow properties is permitted by measurements of the total temperature and pressure in the stagnation chamber and the pressure differentials between the total pressure and the wall pressure at three locations along the test section (Figure 7).

Figure 8 shows the electrical circuitry between the wind array, the heat flux systems and the digital voltmeters. The heat flux system bridge voltage was monitored on the voltmeter in order to increase the precision of the measurements. A simplified schematic of the heat flux system bridge is shown in Figure 9. The bridge voltage (E) is automatically adjusted such that the wind sensor leg resistance ($R_S + R_L$) equals the heat flux system operating resistance (R_H).

2.1.2 Wind Sensor Array Model

The sensor array test model consisted of two wind sensors, a reference temperature sensor and an MSA pedestal combined in the flight configuration. The two wind sensors (Nos. 120/V1 and 117/V2) and the reference temperature sensor (No. 111/V3) were selected from the Phase II batch of breadboard units. A reference temperature capability was not required in the performance tests and sensor 111 was included only to provide a sensor array which was aerodynamically equivalent to the flight unit. The wind sensor array was supported on a calibration fixture which permitted 360° rotation of the model about the reference temperature sensor (in the sensor array plane) and ±25° tilt or attitude change in the plane including the test section axis (Figure 5). Note that the included angle between each wind sensor and the reference temperature sensor is 45°.

An accurate knowledge of the wind sensor dimensions and electrical properties is necessary to properly reduce the wind tunnel data. Sensor electrical resistance versus temperature was measured in a temperature bath at temperatures of 23, 115, and 130°C. The resistance of the platinum wire leads and platinum paste segment between the lead attachments and platinum film was subtracted from the measured resistance to obtain the platinum film resistance versus temperature. The resistance data are presented in Appendix A. Sensing element diameter, platinum film length and the lengths and diameters of the platinum paste segments were measured in Metrology's Dimensional Center and are given in Figure 10. The diameter of the pyrex rod and the thicknesses of the platinum film, platinum paste and alumina layers were determined through measurements obtained from sensing element microsections (sensor 122 of the alumina and platinum film deposition batch containing sensors

117 and 120 was used). These data are required in the calculation of the sensing element heat conduction and radiation losses. Table 1 presents the dimensional data obtained from the microsections.

Table 1. Sensing Element Microsection Data

Alumina Thickness	0.00020 inches
Platinum Film Thickness	0.000025 inches
Platinum Paste Thickness	0.003 inches
Pyrex Rod Diameter	0.02025 inches

Knowledge of the sensing element orientation with respect to the wind array is necessary to properly interpret the wind tunnel performance data. Table 2 presents the sensing element skew data of sensor 117 (only the performance data of sensor 117 is presented in this report). The sensing element orientation is given in terms of the cross-section centroid polar coordinates ($\bar{r}$, λ) at locations 5 and 7 of Figure 10. Figure 11 defines $\bar{r}$ and λ.

Table 2. Sensor 117 Sensing Element Coordinates

Position	$\bar{r}$ (inches)	λ (degrees)
5	.006	347
7	.0085	6

2.2 TEST PROCEDURE AND CONDITIONS

The test procedure first involved the calculation of the sensor overheat resistances. Equation (6) was used in this calculation

$$R_H = R_c + R_o \alpha \Delta T \qquad (6)$$

where

R_H = sensor circuit resistance with the platinum film at the overheat temperature ; equivalently, the heat flux system operating resistance

R_c = sensor circuit resistance with the platinum film at room temperature

R_o = platinum film ice point resistance

α = platinum film resistance-temperature coefficient, $\alpha = 1/R_o \frac{\Delta R}{\Delta T}$

ΔT = platinum film overheat temperature

R_c was measured after the sensor array was placed in the wind tunnel test section. The ambient temperature was measured at the same time using the total temperature thermocouple in the tunnel stagnation chamber. Adding the overheat temperature to the ambient temperature gives the approximate sensor platinum film temperature, i.e., $T_S = T_{amb} + \Delta T$.[1] Note that it is the original ambient temperature that is used in the foregoing equation and not the ambient temperature at the time of any given sensor performance data point; T_S or R_H, once determined, remained unchanged throughout the test.

The following steps comprised the operating procedure for taking a wind sensor performance data point:

(1) Turn on the power to the wind sensor producing the required overheat temperature. Note that this step is generally not required since the sensor power is continued between data points.

(2) Adjust the sensor array rotation and tilt angles to the specified values.

(3) Set the volumetric flow meters and the sonic orifice plug valve to the specified settings.

(4) Wait one minute, when necessary, to permit the wind tunnel and sensor performance to achieve steady state and record the performance parameters.

(5) Close the volumetric flow meter valve. Intermittent wind tunnel operation was followed because of the limited test gas (CO_2) generator capacity.

---

[1] The true platinum film temperature is the solution of the equation for the platinum film resistance, R_S,

$$\alpha T_S^2 + \beta T_S + \gamma = R_S$$

where $R_S = R_S(T_c) + (R_H - R_c)$ and α, β and γ were obtained from temperature bath measurements of the wind sensor resistance (Appendix A).

Test conditions for the wind sensor array were

$$T_\infty \cong 297°K$$

$$4.0 \lesssim P_o \lesssim 57 \text{ Torr}$$

$$2 \lesssim V_\infty \lesssim 141 \text{ m/s}$$

with carbon dioxide as the test gas. These conditions correspond to the Mach number-Reynolds number map shown in Figure 12; also shown in Figure 12 is the required "high accuracy" region calculated from Figures 6 and 7 of Reference 2. (reproduced as Figures 13a and 13b herein). The Knudsen number (based on the film temperature) varied from .0014 to .02 and was found to produce a maximum 10 percent reduction of the Nusselt number from the continuum limit.

The effect of sensing element temperature on Nusselt number was assessed over a wide range of Reynolds number and Mach number. Data were obtained at element overheat temperatures of approximately 58°C, 77°C, 98°C, 118°C and 139°C. Sensor array rotation and attitude covered the ranges $0° \leq \phi_o < 360°$ and $-24° \leq \psi \leq 25°$, respectively.

2.3 TEST RESULTS

2.3.1 Data Reduction

The basic procedure used in reducing the performance test data was to subtract the parasitic radiation and heat condition losses from the total power supplied to the sensing element and so obtain the convective power loss and the element Nusselt number. A finite difference program was used to solve the heat transfer equations. An extensive list of parameters including gas properties, element dimensions, sensor performance data and wind tunnel data comprised the input list of the program. The output included Mach number, Reynolds number,

Nusselt number, platinum film temperature and gas total temperature. A discussion and listing of the program is given in the VMIS Supplier Design Manual[2] (Reference 3). Note that the sensing element skew was considered negligible and was ignored in the reduction of the performance data.

A variable sensing element emissivity was used in calculating the radiation heat transfer in the performance test data reduction. Emittance data were obtained in measurements performed on an alumina deposition "band meter" obtained from Thermo-Systems, Inc.[3] The thickness dependent spectral emissivity of the alumina was determined and the results used to calculate the hemispherical emittance over a range of temperatures and alumina thicknesses. The alumina on platinum emissivity for the performance test sensor (S/N 117) was found to be

$$\varepsilon = 0.63 - 0.00062\ (T - 200.)$$

Note that the bandmeter substrate was stainless steel and the emissivities were accordingly adjusted to represent the expected emittance for a platinum substrate.

---

[2]Several modifications of the program have been made. Updated listings are available.

[3]Thermo-Systems, Inc. was the wind sensor supplier.

Performance test data were simultaneously taken for sensors 117 and 120; however, there was evidence that sensor 120 had previously been broken during handling and it was decided not to analyze the data of this sensor. The loss of sensor 120 data does reduce the detail of the performance test results but the 240 data points produced by sensor 117 are adequate for assessing the sensor performance and acceptably augmenting the flight unit calibration data. Note that sensor 117 is in position V2 (Figures 1 and 5)

2.3.2 Data Presentation

A tabulation of the breadboard wind sensor performance data is given in Appendix A. Both the raw data and the nondimensionalized (reduced) data, e.g., Reynolds number and Nusselt number, are presented. Note that all test section blockage effect corrections are incorporated in the reduced data.

Figure 14 gives the sensor Nusselt number distribution versus film Reynolds number for the case where the wind velocity is perpendicular to the sensing element axis. Also shown for comparison is the Collis and Williams empirical correlation curve for the heat transfer from high aspect ratio circular cylinders (Reference 1). It is seen that the wind sensor performance data are 20% to 30% above the Collis and Williams curve. The overvalues are apparently primarily due to the departure of the wind sensor configuration from the ideal case of the infinite circular cylinder. Aerodynamic interference

of the sting and the low L/D of the sensing element (L/D = 20) are the geometric contributors to the Nusselt number overvalues. Approximately 2% of the overvalue may be attributed to the test gas being CO_2 rather than air, the test gas in the Collis and Williams report.

It is more direct to consider the Nusselt number distribution disagreement in terms of the sensing element power distribution versus Reynolds number. Figure 15 displays this comparison for the sensing element overheat temperature of 97.5°C . The performance test power dissipation was obtained using the formula

$$P = \left(\frac{E}{R_B + R_H}\right)^2 \times R_S(T_S)$$

where R_B and R_H are heat flux system parameters (Figure 9) and R_S and T_S were defined above (page 7).[1] Note that P is the total power dissipation and consequently includes heat conduction and radiation energy transfer in addition to the heat convection energy transfer. In order to permit a direct comparison with Collis and Williams it is necessary to subtract the parasitic heat transfer from P leaving the convective heat transfer The sensor heat conduction and radiation loss in a vacuum at 100°C overheat was .0208 watts (Figure 16). Reference 4 describes the vacuum test equipment and procedure. It was found in the wind tunnel data analysis that the parasitic losses at 100°C overheat were not more than 10% higher than the heat conduction and radiation losses in a vacuum.[4] Neglecting this difference and subtracting the .0208 watts from the total power dissipation obtained in the wind tunnel test gives the wind sensor convective heat transfer curve indicated in Figure 15.

[4]It is generally true that the heat conduction loss will increase with increasing convective heat transfer losses. However, in the case of sensor 117, this effect is substantially cancelled by convective heat transfer losses from the platinum paste segment at the base of the sensing element.

The Collis and Williams curve was obtained using the formula

$$P = \pi L k_F Nu \Delta T$$

where, as previously noted,

L = element length

k_F = gas film thermal conductivity

ΔT = sensing element overheat temperature

and Nu is the Nusselt number given by (Reference 1)

$$Nu = (T_F/T_A)^{.17} (A + B Re^n)$$

with

	$.02 \leq Re_F < 44$	$44 \leq Re_F \leq 140$
A	0.24	0.0
B	0.56	0.48
n	0.45	0.51

T_A is the adiabatic recovery temperature. L was set equal to the total element length (conservatively chosen to be 1.1 centimeters) and ΔT set equal to 100^oC. Note that the 100^oC value is also conservative in that it represents the platinum film temperature which is several degrees higher than the mean sensing element temperature.

It is seen in Figure 15 that the wind sensor data are once again 20 to 30 percent above the Collis and Williams prediction. The indicated conclusion is that the wind sensor power dissipation overvalues are due to the aerothermodynamic characteristics of the sensor and not the manner of interpreting (or reducing) the wind tunnel data.

Returning to the Nusselt number data (Figure 14), a significant effect of flow rarefaction (up to 10 percent) and element overheat temperature can be seen. Concerning the flow rarefaction data, the upright triangles represent the wind tunnel measurements and the inverted triangles represent the same data

when adjusted to the equivalent continuum values. In performing the adjustment, the formula (Reference 1)

$$1/Nu_c = 1/Nu - 2\ Kn$$

was used where Nu is the experimental Nusselt number, Kn is the sensing element film Knudsen number and Nu_c is the equivalent continuum Nusselt number. Three sets of overheat data with sensing element overheat temperatures of 58°C, 97°C and 136°C are shown in the figure. An important overheat dependence is seen to exist; this effect as well as the rarefaction effect should be represented in the flight data reduction logic.

Figure 17 presents the variation of normalized Nusselt number versus sensor angle of attack where Nu_o is the value of the Nusselt number at $\theta = 0°$. Five sets of data covering a film Reynolds number range from 3 to 105 are shown. Note that for $\theta < 0°$ the pedestal is upstream of the sensor and an influence of the pedestal wake on the sensor performance can occur.

Analysis of the data has shown that the decrease in Nu/Nu_o closely follows the $\cos^{1/2}\theta$ variation (obtained from the assumption that only the cross flow Reynolds number is important) to about $\theta = 45°$. The data exhibit a diminishing dependence of Nu/Nu_o on θ with decreasing Reynolds number, a result which is apparently due to the increasing relative importance of the axial flow component at the lower Reynolds numbers. The lack of symmetry in the distribution of Nu/Nu_o is caused by the asymmetric aerodynamic configuration. Note in particular that at $\theta = -90°$ the sensor was located directly downstream of the pedestal and in or near its wake.

Figure 18 shows the variation of Nusselt number with tilt angle for several rotational angles and film Reynolds numbers. The definition of tilt angle and rotational angle is given in the schematic on the figure and in Figure 5. Five sets

of data are displayed. Two sets are for $\theta_0 = 90$ with $Re_F \cong 8$ and 92. The sensor of interest (No. 117) is at an angle of 135° from the upstream direction (i.e., $\beta = 135°$). These data show a weak dependence on tilt angle. The $Re_F = 8.0$ data show an asymmetric and slightly irregular variation with ψ; it's not clear what causes this effect which is approximately ±3% about the mean value but the proximity of the sensor 120 and 111 wakes coupled with the presence of the pedestal is the probable cause.

The data taken at $\beta = 180°$ and 200° show markedly different distributions considering the small difference in rotation angle. The $\beta = 200°$ data are symmetric and nearly uniform while the $\beta = 180°$ data exhibit a considerably distorted distribution. This irregular variation has to be attributed to the presence of the wake. It is hypothesized that the reduction of Nu/Nu_0 as ψ increases from 0° to 10° is due to the emergence of the sensing element from the wake of the pedestal. The subsequent increase at $\psi = 25°$ may be due to the further tilting of the sensor into the flow. It is difficult to say what is causing the variation of Nu/Nu_0 for $\psi < 0°$.

The data set for $\beta = 10°$ is interesting in two ways. First, the data are symmetric about $\psi = 3°$, suggesting that the local velocity vector is vertically rotated 3°, an effect introduced by the presence of the pedestal. Second, the data, when presented in terms of the angle between the freestream velocity vector and the plane perpendicular to the sensor axis, are in close agreement with the same Reynolds number data in Figure 17 for $\theta > 0$. Figure 19 shows this comparison ($\phi_0 = 325°$). The agreement is substantially complete when the induced 3° rotation of the velocity vector is taken into account.

Similar data comparisons are given in Figure 19 for ϕ_0 = 25°, 135°, 190°, 215°, and 350°. Close agreement is seen to exist for $\theta > 0$; for $\theta < 0$, however, less agreement is observed, particularly for the ϕ_0 = 135° case where the sensor is directly downstream of the pedestal.

3. PERFORMANCE ANALYSIS OF WIND SENSOR

3.1 PERFORMANCE REQUIREMENTS

Table 1 presents the wind sensor array performance requirements (Reference 2 , pages 10 to 12), the actual sensor performance and the manner of establishing this performance.

3.2 PERFORMANCE ANALYSIS

3.2.1 Measurement Range

The wind sensor array will operate over the required performance ranges. In order to properly operate in the specified environments the sensor array must (1) survive repeated exposure to the ambient temperature extremes and (2) function as an anemometer over the specified environments. Regarding the first item, a thermal cycling test covering the temperature range from 130°K to 360°K was performed to establish that the wind sensors will survive the temperature extremes. The temperature cycle, shown in Figure 20, had a 2 hour period and was continuously performed for 48 hours giving 24 sensor exposures to each temperature extreme. Two sensors were tested and the sensor resistances and chamber temperature were frequently measured in order to detect a degradation if it occurred. The chamber temperatures were measured with a thermocouple located in the vicinity of the sensors. Figure 21 shows a plot of the measured sensor resistances versus chamber temperature. Also shown are the ice point and boiling point sensor resistances obtained in an independent calibration (sensor 101 resistance at 212°F unavailable). While there is significant scatter in the data due to the unsteady and non-uniform chamber temperature, the measurements suggest that the sensor electrical properties and, hence, platinum film, lead attachments, etc., were not degraded by the thermal

Table 1. Wind Sensor Functional Requirements

Specification PD7400090 Paragraph	Requirement	Performance	Verification	Remarks
3.1.1.2.2.1	RANGE - 2 to 150 M/sec at pressure 2 to 20 millibars and temp 130°K to 350°K over an azimuth of 360°	Meets requirements	Performance Test and Analysis	Performance tests cover most of the high accuracy range. Additional tests and analysis show sensor survives and transmits data over remainder of range
2.2	ACCURACY - ±4 M/sec or 20% (whichever is greater) absolute accuracy and ±2 meters/sec or ±10% (whichever is greater) relative accuracy over high range operating conditions; no requirement over low range	Meets absolute accuracy requirements Meets relatively accuracy requirements for $V \lesssim 13$ m/s	Error Analysis based on Performance Test Data	
2.3	HYSTERESIS - Increasing and decreasing wind speed shall not differ by more than ±0.5 or 5%, whichever is greater	Meets requirements	Design	
2.4	STABILITY - Calibration shall be better than ± 0.5 M/sec or 5% (whichever is greater) over operating and non-operating life of system		Design	Demonstration to be performed in the Flight Unit Acceptance Reports
2.5	RESOLUTION - ±0.5 M/sec or 5%, whichever is greater	Meets requirements for $V \lesssim 8$ m/s and $V \gtrsim 16$ m/s	Error Analysis based on Performance Test Data	

Table 1. Wind Sensor Functional Requirements
(continued)

Specification PD 7400090 Paragraph	Requirement	Performance	Verification	Remarks
3.1.1.2.2.6	CALIBRATION - The sensor shall be calibrated and retain this calibration to within the specified stability		Performance Test, Development Tests and Design	Demonstration to be performed in the Flight Unit Acceptance Reports
2.7	RESPONSE TIME - The response time to a step change in wind speed shall not exceed 2 sec	Meets requirement	Analysis	Characteristic response time is 0.09 seconds
2.8	WARM-UP TIME - Meet performance requirement 4 sec after input power applied to electronics	Meets requirement	Analysis	Worst case warm-up is 0.8 sec
2.9	ATTITUDE - Shall operate in any attitude within ±25 degrees of nominal position	Meets requirement	Performance Test and Design	
2.10	SELF-HEATING - Shall operate with sensor 20 to 140°C above ambient	Meets requirement	Performance Test and Design	
2.11	DIRECTION ACCURACY - Absolute accuracy ±20 degrees at speeds 5 to 25 M/sec and ±10 degrees over high accuracy regions (Reference P.D., Figures 6 and 7). No direction accuracy requirements in reduced accuracy range	In substantial compliance with requirements	Error Analysis based on Performance Test Data	
2.12	DIRECTION RESOLUTION - ±10 degrees at speeds 5 to 25 M/sec and ±5 degrees at speeds of 25 to 150 M/sec	In substantial compliance with requirements	Error Analysis based on Performance Test Data	

environment. The sensor resistance data display a greater precision when the resistances are cross-plotted as shown in Figure 22. The self-consistency of the thermal cycling data and their agreement with the independent calibration data indicate that the sensors survived the thermal environment.

Turning now to the satisfactory performance of the sensor as an anemometer, Figure 12 shows the freestream Mach number-Reynolds number map corresponding to the required high accuracy region. Also shown are the performance test ranges. It is seen that the substantial part of the required operating region is covered by the performance test. The Reynolds number extremes are beyond the wind tunnel capability. On the basis of the many cylinder heat convection experiments reported in the literature, the sensor performance data may be extrapolated to cover the remaining regions. It is concluded then that the sensor does perform as an anemometer over the required atmospheric conditions and hence, since it survives over these conditions, meets the measurement range performance requirement.

3.2.2 Wind Speed Accuracy

The sources and magnitudes of error in the wind sensor array data transmitted from Mars are as follows where the errors are the 3σ values:

Wind Tunnel	±3%
Sensing Element Resistance Versus Temperature	±1°K
Sensing Element Dimensions	Negligible
Heat Conduction Loss	±10%
Radiation Loss	±10%
Solar Heating	±0.5 mw
Freestream Temperature (Temperature Sensor)	±2.3°C
Sensing Element Temperature	±2.25°C
Sensing Element Power Dissipation	±1.0%
Sensing Element Power Deadband	±1.5 mw
CO_2 Viscosity	±0.5%
CO_2 Thermal Conductivity	±2.5%

These error source values were used in calculating the absolute wind velocity error for the worst case conditions using a computer program written for this purpose. Analyses of several possible worst case conditions resulted in the selection of T_∞ = 280°K and P_∞ = 4 mb as those which produce maximum errors. The wind speed and wind direction ranges considered were

$$V_\infty = 5 \text{ m/s to } 140 \text{ m/s}$$

$$\phi_0 = 0° \text{ to } 360°$$

$$\psi = 0°$$

where ϕ_0 and ψ are defined in Figure 5. It was felt that the error results at $\psi = 0°$ would be representative of the $\psi \neq 0°$ performance.

In the computer analysis the error source values were first cast in terms of the equivalent sensing element Nusselt number uncertainties for the specified flow conditions; the root-mean-square Nusselt number uncertainties were then obtained followed by an iteration procedure to finally arrive at the wind speed and wind direction errors.

The performance test data were represented in the program by a tabulation of normalized Nusselt number versus rotation angle at Re_F = 60 and two functions representing the variation of Nusselt number with Reynolds number at $\beta = 0°$ and 90° where β is the angle between the velocity vector and the sensor axis. The Nu vs. β distribution for Re_F = 60 could be adjusted to adequately reproduce the Nu vs. β variation at any Reynolds number. The small variations in these distributions among the four wind direction quadrants were ignored as were the effects of Mach number.

The steps followed in calculating the wind speed and wind direction errors were the following:

1. Specify V_∞, ϕ_0, P_∞, T_∞, overheat temperature and the error magnitudes;

2. Calculate the film Reynolds number and the Nusselt numbers of each of the two wind sensors (at 90° included angle);

3. Calculate the uncertainty in Nusselt number for each wind sensor;

4. Increment the wind sensor Nusselt numbers by the corresponding uncertainties producing four cases (i.e., $Nu_1' = Nu_2 \pm \delta Nu_1$ and $Nu_2' = Nu_2 \pm \delta Nu_2$);

5. Use a Newton-Raphson iteration to determine the values of Re_F and ϕ_0 which satisfy each combination of Nu_1' and Nu_2' and the represented performance data;

6. Determine the maximum departures of the values of Re_F and ϕ_0 from the given original values;

7. Calculate the normalized uncertainty in wind speed from δRe_F, Re_F and the uncertainties in element temperature, freestream temperature and gas viscosity.

Step 6 provides the error in wind direction in degrees and step 7 gives $\delta v/v$. The temperature dependent gas viscosity and thermal conductivity were used in the calculations.

Figure 23 shows the calculated absolute wind speed error versus wind speed for the considered worst case. The wind speed error is seen to exhibit a weak dependence on wind direction. Also shown on the figure as the solid curve is the specified maximum error. The wind speed errors are seen to be well within the specified maximum levels.

Certain of the error sources indicated in the table on page 18 do not apply in the relative wind velocity error calculations. These are the heat conduction energy loss, the radiation energy loss and the solar heating. These error sources do not apply because their effect on the wind speed (and wind direction) errors is not a function of wind speed.[5] The remaining error sources, while of constant value, do introduce a wind speed dependent effect on the wind speed error and must be considered. Actually, the element power deadband

[5] The parasitic losses (radiation and heat conduction) do have a slight dependence on wind speed but this dependence is considered negligible.

is not velocity related but it is the nature of this error source that it must be retained in the relative error calculation.

It is probably worthwhile to briefly reflect on why most of the error sources are important in the relative error calculation. Note first that the wind speed error, relative or absolute, is obtained primarily from the Nusselt number uncertainty. This uncertainty is calculated from the formula

$$Nu = \dot{Q}/(\pi\ L\ k_F\ \Delta T)$$

giving

$$\delta Nu = \delta\dot{Q}/(\pi\ L\ k_F\ \Delta T) - \frac{\dot{Q}\ \delta L}{\pi\ k_F\ \Delta T\ L^2} - \frac{\dot{Q}\ \delta k_F}{\pi\ L\ \Delta T\ k_F^{\ 2}} - \frac{\dot{Q}\ \delta(\Delta T)}{\pi\ L\ k_F\ (\Delta T)^2}$$

$$= Nu[\delta\dot{Q}/\dot{Q} - \delta L/L - \delta k_F/k_F - \delta(\Delta T)/\Delta T]$$

where

Nu = Nusselt number

$\dot{Q}$ = convective heat transfer

L = sensing element length

k_F = gas film thermal conductivity

ΔT = sensing element overheat

The important point contained in the above relation is that even though, for example, the normalized uncertainty in element overheat temperature, $\delta(\Delta T)/\Delta T$, is independent of wind speed, its effect on the Nusselt number is wind speed dependent since it is in product with Nu which is the wind speed dependent. The error source must therefore be included in the relative error calculation.

The same program used in the absolute error calculation was used in the relative error calculation. In the case of the relative error calculation,

however, the list of error source values input to the program was reduced by the parasitic losses and the solar radiation uncertainties. Again, the worst case condition was P_∞ = 4 mb and T_∞ = 280°K. Figure 24 presents the calculated wind speed relative error versus wind speed. Also shown is the specified relative accuracy which is half the absolute accuracy requirement. It is seen that the calculated relative accuracy exceeds the specified accuracy over most of the wind speed range. Note that the relative accuracy is not significantly reduced from the absolute accuracy.

3.2.3 Hysterisis

No mechanism for hysterisis exists in the sensor or electronics design; hence the hysterisis requirement is satisfied.

3.2.4 Stability

No studies in the development phase of the wind sensor array stability were performed by TRW. The sensor component which is principally susceptible to a change in electrical properties is the platinum film. Note that there is no indication in the experience of Thermo-Systems Inc. (the wind sensor supplier) that a correctly deposited platinum film could become unstable.

Tests are performed in the wind sensor production phase to confirm the platinum film stability. The deposition batch run-in test sensor (selected at random from the batch) is operated at 300°C for at least thirty minutes. In addition, each sensor assembly is subjected to a 24 hour test at 200°C overheat. In these tests the sensor resistance is measured before and after the test and compared to establish that the film properties are stable.

3.2.5 Resolution

The limits to sensor resolution are the wind electronics sensing element power deadband of 1.5 mw and the temperature sensor temperature

measurement deadband of 0.5°C. The computer program described above was executed for these error sources only and the resulting wind speed resolution versus wind speed is shown in Figure 25. As before, the worst case of P_∞ = 4 mb and T_∞ = 280°K was considered. Also shown in the figure is the specified resolution. It is seen that the required resolution is satisfied except for the wind speed range $8 \leq V \leq 16$ meters per second.

3.2.6 Calibration Requirements

The breadboard wind sensor was calibrated and the results presented in Section 2.2. Since the platinum film stability could not be affirmed (see Paragraph 3.2.4), the stability of the calibration cannot be established. Note that the sensor configuration is stable so that the only source of instability is the electrical properties of the platinum film. As noted in Paragraph 3.2.4, each sensor will be subjected to a 24 hour run-in test at 200°C overheat to confirm the stability of the platinum film properties.

3.2.7 Response Time

The governing equation for the response of the sensing element temperature to a change in convective heat transfer (or wind speed) is

$$\rho c v \frac{dT_S}{dt} = \left[\frac{E_p^{\,2} - E_S^{\,2}}{R_S\,(T_a - T_b)} - \pi L\, k_F\, Nu - \bar{Q}_p\right] T_S + \left[\frac{T_a\, E_S^{\,2} - T_b\, E_p^{\,2}}{(T_a - T_b)\, R_S} + \pi L\, k_F\, Nu\, T_c + \bar{Q}_p\, T_c\right] \tag{7}$$

where

ρ = sensing element mass density

c = sensing element specific heat

v = sensing element volume = $\pi D^2 L/4$

T_S = sensing element temperature (assumed uniform throughout sensing element)

t = time

E_p = pulse amplitude (volts)

E_S = sensing power voltage amplitude

R_S = sensor platinum film resistance

T_a, T_b = sensor temperatures defining MEA duty cycle ramp length (Figure 26b)

L = sensing element length

k_F = CO_2 film thermal conductivity

Nu = Nusselt number

T_c = ambient temperature

$\overline{Q}_L$ = parasitic losses, per degree centigrade, heat conduction and radiation

Figures 26a and 26b show the MEA duty cycle and the components of the sensing element power dissipation versus platinum film temperature. $T_b - T_a$ is the MEA "ramp length" over which the wind sensor sensing element temperatures are stabilized. The dashed line in Figure 26b represents the sensing phase of the duty cycle during a portion of which the platinum film resistance (and, hence, temperature) is sampled. The sensing phase is on or operational when the primary or driving pulse is off. The applied voltage is designated E_S. We then have

$$Q_S = \frac{E_S^{\,2}}{R_S} \frac{T_a - T_S}{T_a - T_b} .$$

For the sensing power dissipation rate in the platinum film. Similarly for the driving pulse power we have

$$Q_p = \frac{E_p^{\,2}}{R_S} \times \frac{T_S - T_b}{T_a - T_b} .$$

The rate at which energy is transferred from the sensing element is

$$Q_T = \pi L k_F Nu (T_S - T_c) + Q_L$$

$$= \pi L k_F Nu (T_S - T_c) + \overline{Q}_p (T_S - T_c)$$

where Q_L is the total parasitic heat loss. Then the net energy transfer is

$$Q_{net} = Q_p + Q_S - Q_T$$

$$= \frac{E_p^2}{R_S} \frac{T_S - T_b}{T_a - T_b} + \frac{E_S^2}{R_S} \frac{T_a - T_S}{T_a - T_b} - \pi L k_F Nu (T_S - T_c) - \overline{Q}_L (T_S - T_c)$$

and Equation (7) follows directly.

Equation (7) may be written

$$A(T_S)\, dT_S/dt + B(T_S)\, T_S = C(T_S). \tag{8}$$

Meaningful results can be obtained with the assumption that the parameters contained in A, B and C are temperature independent. Then Equation (8) has the solution

$$T_S = A\, e^{-\frac{B}{A}t} + C/B .$$

Applying the initial condition $T_S = T_i$ at $t = 0$ gives the complete solution

$$T_S = [T_i - C/B]\, e^{-\frac{B}{A}t} + C/B .$$

The system time constant is

$$\tau = A/B$$

$$= \rho c v / \left\{ \frac{E_p^{\,2} - E_S^{\,2}}{R_S\,(T_a - T_b)} - \pi\, L\, k_F\, Nu - \overline{Q}_p \right\} .$$

In evaluating the system time constant for varying MEA sensitivity or $T_b - T_a$ we choose the following parameter values:

$$\rho = 3.85 \text{ gm/cm}^3$$

$$c = 0.84 \text{ watt-sec/gm } ^\circ\text{K}$$

$$v = 2.156 \times 10^{-3} \text{ cm}^3$$

$$E_p = 5.0 \text{ volts}$$

$$E_S = .64 \text{ volts}$$

$$R_S = 20 \text{ ohms}$$

$$L = 1.1 \text{ cm}$$

$$k_F = 0.243 \times 10^{-3} \text{ watt/cm-}^\circ\text{K}$$

$$Nu = 6.0$$

$$\overline{Q}_p \cong 2.0 \times 10^{-4} \text{ watts/}^\circ\text{C}$$

Figure 27 shows the variation of the system time response versus ramp width, $T_b - T_a$. For a ramp width of 15°C the system time response is 0.09 seconds. Note that the MEA has an inherent time constant which permits a minimum system response time of 46 ms.

0.046 sec min
0.09 sec +-15°C ramp

3.2.8 Warm-up Time

The wind sensor warm-up time may be calculated from the following equation

$$\rho c \frac{\pi D^2}{4} \times L \times \frac{d}{dt} (\Delta T) = P - \overline{Q}\, \Delta T \qquad (9)$$

where

ρ = sensing element mass density

c = sensing element specific heat

D = sensing element diameter

L = sensing element length

t = time

ΔT = sensing element overheat temperature

P = maximum electric power dissipated in the sensing element

$\overline{Q}$ = total heat transfer rate from the sensing element per degree centigrade overheat (heat convection, heat conduction and radiation).

The left hand side of Equation (9) is the rate at which energy is absorbed in the sensing element and the right hand side represents the availability of energy for raising the sensing element temperature. This equation is considerably simplified by choosing P and $\overline{Q}$ to have representative constant values.

Solving equation (9) for ΔT gives

$$\Delta T = (P/\bar{Q})\ (1 - \exp[-\ \bar{Q}t/(\rho c\ \frac{\pi D^2}{4}\ L)])$$

Solving this equation for t gives the warm-up time relation for the wind sensor

$$t = -\ \frac{\rho c\ \pi\ D^2\ L}{4\bar{Q}}\ \ln[1 - \frac{\bar{Q}}{P}\ \Delta T] \qquad (10)$$

Listed below are the flow conditions which maximize the warm-up time

$$T_\infty = 350°K$$

$$P_\infty = 20\ mb$$

$$V_\infty = 150\ m/s$$

where the wind velocity is perpendicular to the sensing element axis. For these conditions, the sum of the heat convection, heat conduction and radiation energy transfer rates is $\lesssim 0.50$ watts. Taking the operating overheat to be 100°C gives $\bar{Q} = 0.006$. P may be approximated by $P = E^2/R_S$ where E is the amplitude of the modulated voltage applied to the sensor circuit and R_S is the sensor resistance. The maximum duty cycle of 87% is assumed. E is 5.0 volts and R_S is assumed to be 20 ohms. Hence P = 1.09 watts. The remaining parameters were given the following values

$$\rho = 3.85\ gm/cm^3$$

$$c = 0.84\ watts\text{-}sec/gm\text{-}°K$$

$$D = 0.05\ cm$$

$$L = 1.1\ cm$$

$$\Delta T = 100°C$$

Substituting these values into Equation (10) and evaluating gives a warm-up time of 0.8 second.

The wind electronics have a warm-up time which is considerably less than one second. It is seen therefore that the total warm-up time of the wind sensor and wind electronics is well within the 4 second limit.

3.2.9 Attitude

The effect of attitude on the wind sensor array performance was studied in the performance tests and reported in Paragraph 2.3.2. These data may be incorporated in the flight data reduction logic to permit the wind velocity to be determined at arbitrary attitude.

3.2.10 Self-Heating

The wind sensor was designed to operate within the required overheat temperature range. MEA tests and analyses show that the sensor overheat will be maintained near a 100°C overheat.

3.2.11 Wind Direction Accuracy

The wind direction error worst case conditions are P_∞ = 4 mb and T_∞ = 280°K which are the same as those for the wind speed error. The computer program described in Paragraph 3.2.2 was used to generate the wind direction error data presented below. In fact, the wind speed and wind direction errors were calculated during the same program executions.

Figure 28 shows the calculated wind direction absolute error and the specified maximum absolute error. For wind directions interpreted (i.e., measured) to be outside of ±15° bands about each sensor axis, the calculated errors are seen to be within the specified maximum values. For the case where the interpreted wind direction is parallel to either of the wind sensor axes, however, the calculated wind direction error exceeds the maximum allowable when the wind speeds are greater than 25 meters/sec.

It is possible to increase the wind direction accuracy through use of the quadrant sensor data. Note first that, when operating in the quadrant sensor mode the sensor will determine which of eight wind direction sectors contains the velocity vector. Figure 29 illustrates this capability. The quadrant sensor performance is such that either one or two of the four heated wake detecting thermocouples will be in the sensor thermal wake. The shaded wind direction sectors of the figure are those where the thermal wake contains two thermocouples and the unshaded sectors represent those where the wake contains one thermocouple. By observing the magnitude and sense of the thermocouple pair output voltages, the sector containing the wind velocit vector can be deduced (see Section III for the quadrant sensor discussion).

Also indicated on Figure 29 are the wind sensor axes which are seen to coincide with sector boundaries (but only approximately, in general). The four possible wind velocity solutions as determined by the wind sensor array will be symmetrically placed about the wind sensor axes. It is apparent then that by knowing which quadrant sensor sector contains the wind velocity vector, the true wind velocity solutions can be selected from among the four possible solutions. In addition, the quadrant sensor data can be used to increase the wind sensor wind direction accuracy for the case where the interpreted wind direction is near a sensor axis. Note that for the worst case conditions with an indicated wind speed of 25 m/s and an indicated wind direction of $\beta = 90°$, the actual "3σ" wind direction could be anywhere within $\pm 15°$ about the sensor axis. The quadrant sensor can identify the quadrant which contains the wind velocity vector. It is seen then that by specifying the wind direction to be $\beta = 83.5°$ or $\beta = 96.5°$, depending on the wind quadrant, the wind direction uncertainty may be reduced to 1/2 its original value.

Unfortunately, the full 50% error reduction is not possible due to the quadrant sensor deadband existing about the boundaries between the shaded and unshaded sectors shown in Figure 29 (see Section III-4.2.7 for the quadrant sensor deadband discussion). Figure 30 shows the quadrant sensor deadband versus wind speed for the wind sensor error worst case (see also Figure 46 of Section III). As can be seen in Figure 31, the appropriate formula for calculating the improved wind direction error is

$$e_W' = (e_W + d_Q)/2 \qquad (11)$$

Suppose, for example, the quadrant sensor indicates the wind velocity vector is in the sector containing the radii a and b. Then we know the wind vector must be in the angle e-0-c. It is also known that the wind velocity vector must be in the angle a-0-d. It therefore follows that the width of the wind direction region is $e_W + d_Q$. Specifying that the wind vector bisect the angle known to contain the wind vector then gives Equation (11).

Figure 32 presents the maximum wind direction errors obtained when the quadrant sensor is used to advantage. It is seen that the errors are now within the specified limits except for wind speeds between 35 and 50 meters per second. Note that for sufficiently low wind speeds, the quadrant sensor is capable of determining the wind direction, requiring only the freestream Reynolds number from the wind array; accordingly, since the quadrant sensor is more accurate than the wind sensor and should be used to determine wind direction where possible, the quadrant sensor error curve is given in Figure 30 for wind speeds less than 32 meters/second. For wind speeds between 32 and 35 meters/second the shaded region of Figure 28 provides the maximum error. And for wind speeds greater than 35 meters/second Equation (11) is used.

3.2.12 Wind Direction Resolution

The limits to sensor resolution, as discussed in Section 3.2.5 are the wind electronics deadband of 1.5 mw and the temperature measurement deadband of 0.5°C. Sensor wind direction resolution as a function of wind speed is given in Figure 33 for the worst case conditions of P_∞ = 4 mb and T_∞ = 280°K. As is to be expected, the poorest resolution occurs for the case where the wind direction is along the axis of either sensor. It is seen that the resolution requirement is satisfied over the substantial part of the required conditions.

REFERENCES

1. Collis, D. C. and Williams, M. J., "Two Dimensional Convection from Heated Wires at Low Reynolds Numbers," J. Fluid Mech. 6, pp. 357-389, 1959.

2. "Meteorology Instrument System," Document No. PD 7400090, Revision S, March 5, 1973.

3. "Viking Meteorology Instrument System: Supplier Design Manual", Report No. METC-011, December 12, 1972.

4. "VMIS Wind Sensor Assembly Test Procedure," Report No. LM-16T-02B, April 5, 1973.

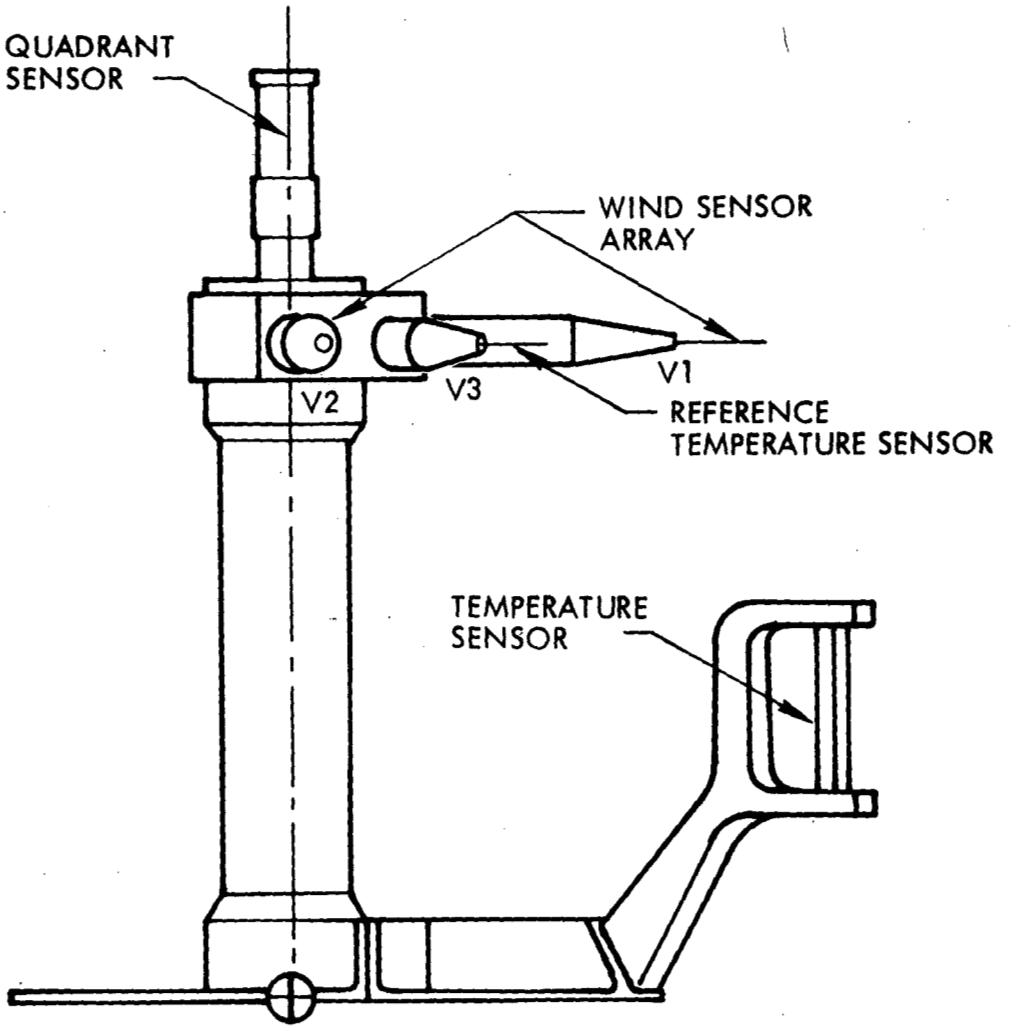

Figure 1. Wind Velocity Sensor Elements

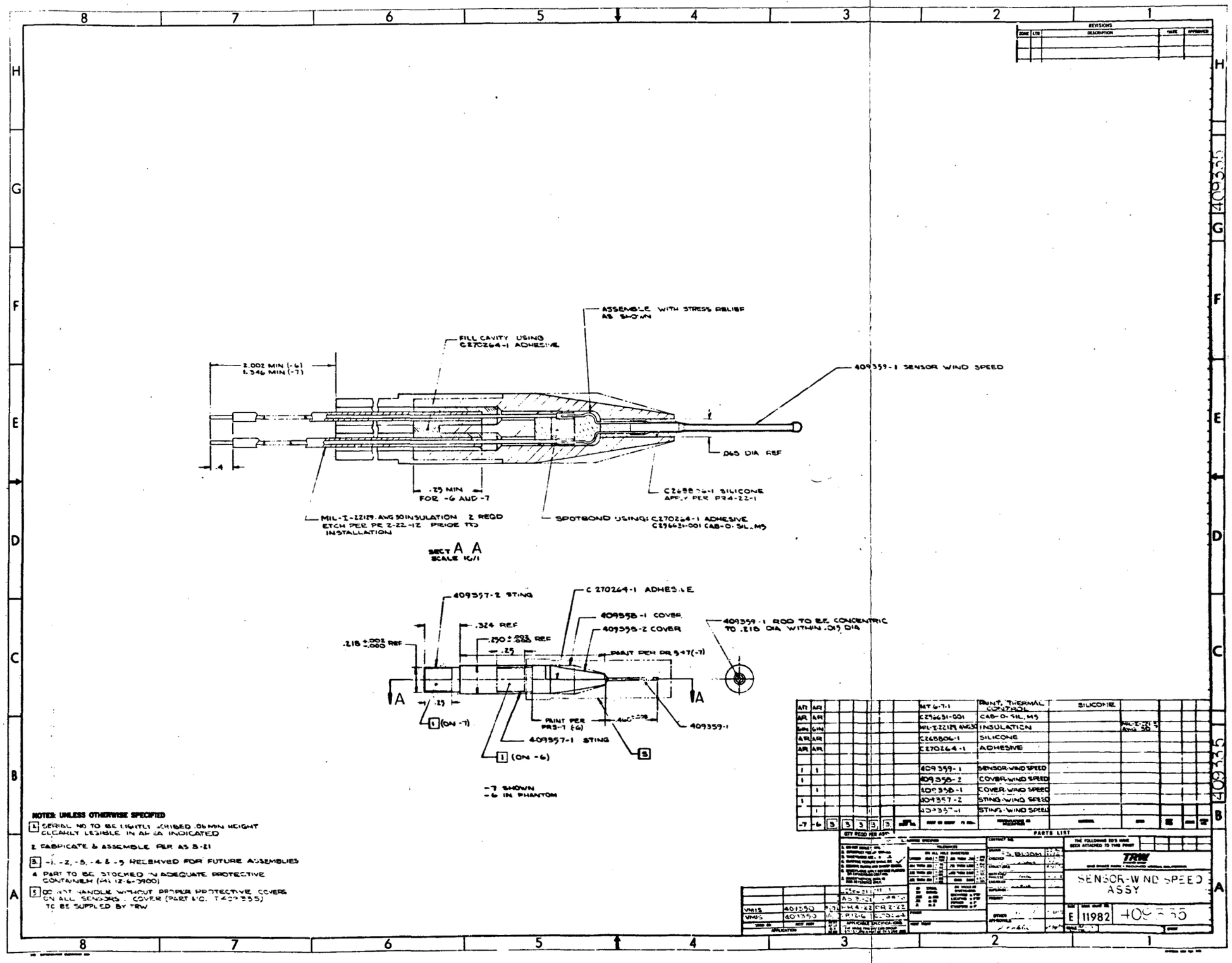

Figure 2a. Wind Velocity Sensor Elements

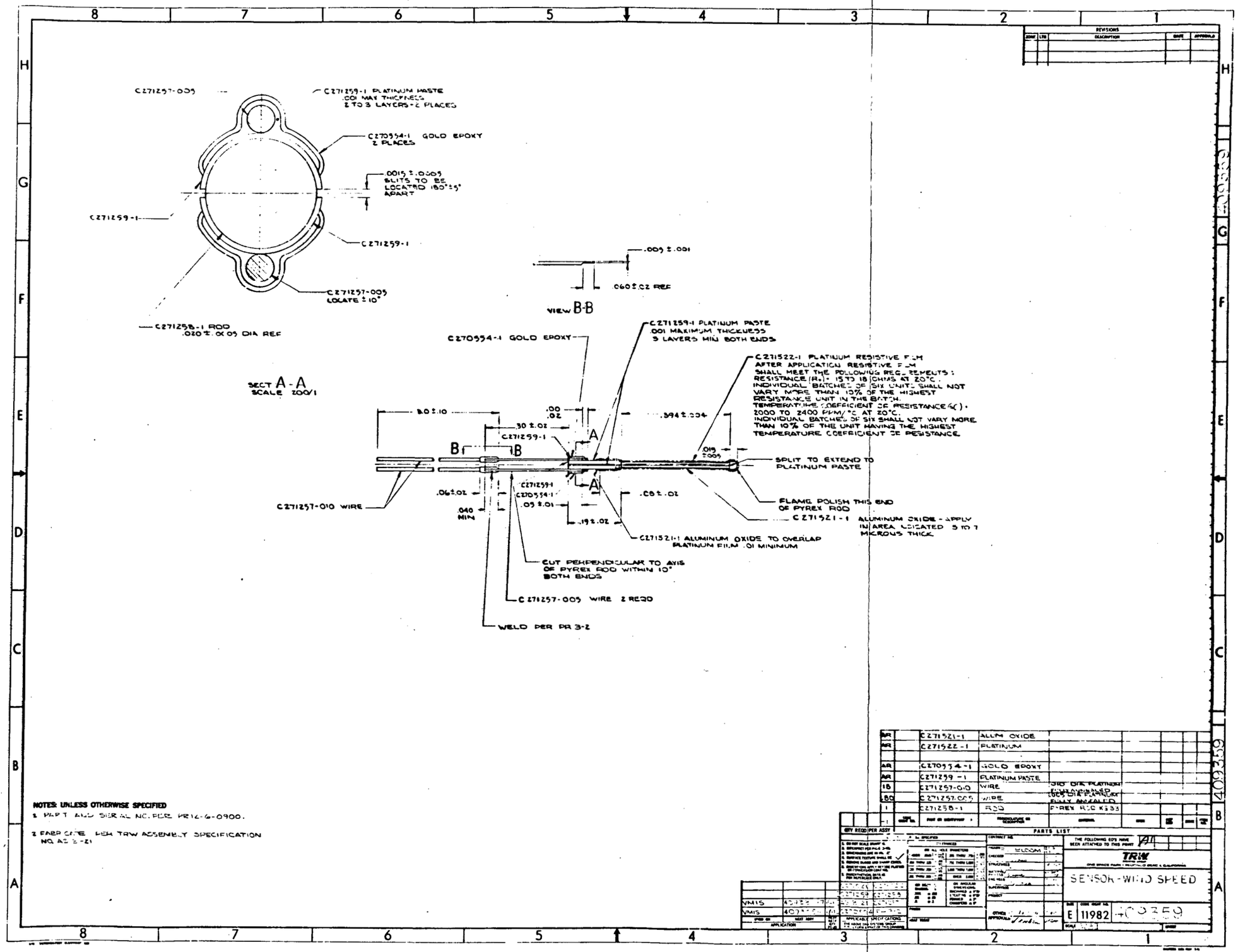

Figure 2b. Wind Velocity Sensor Elements

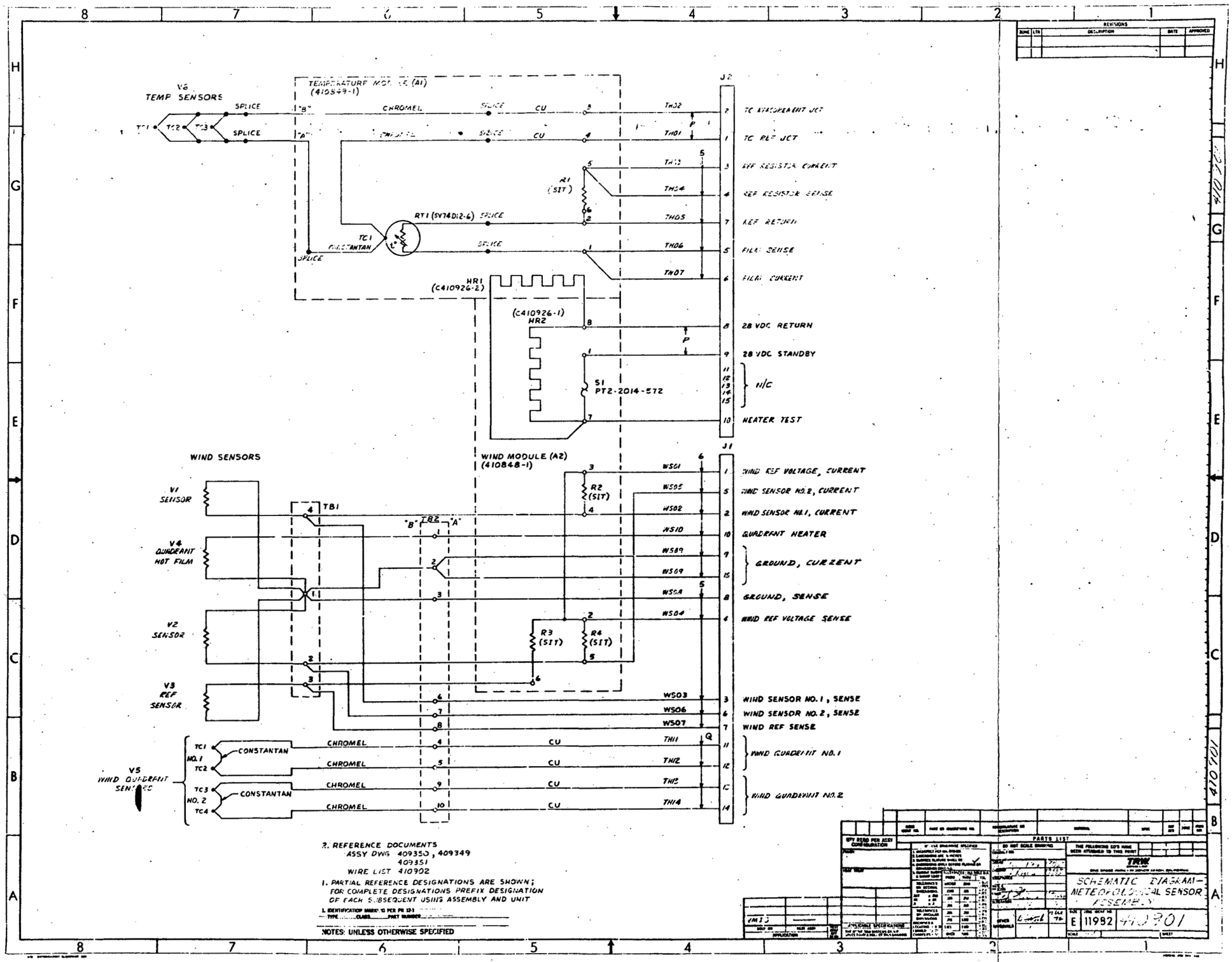

Figure 3. MSA Circuitry Schematic

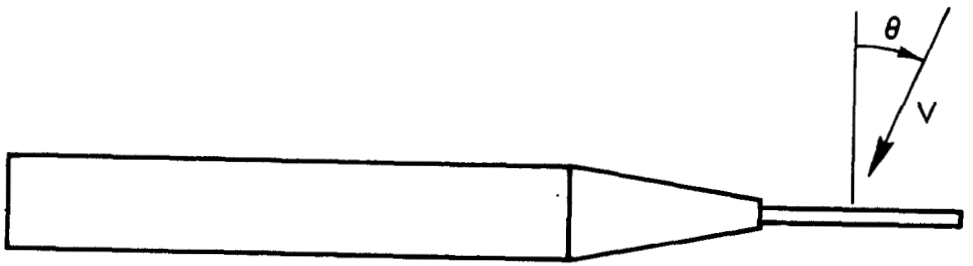

Figure 4. Definition of the Sensing Element Angle of Attack

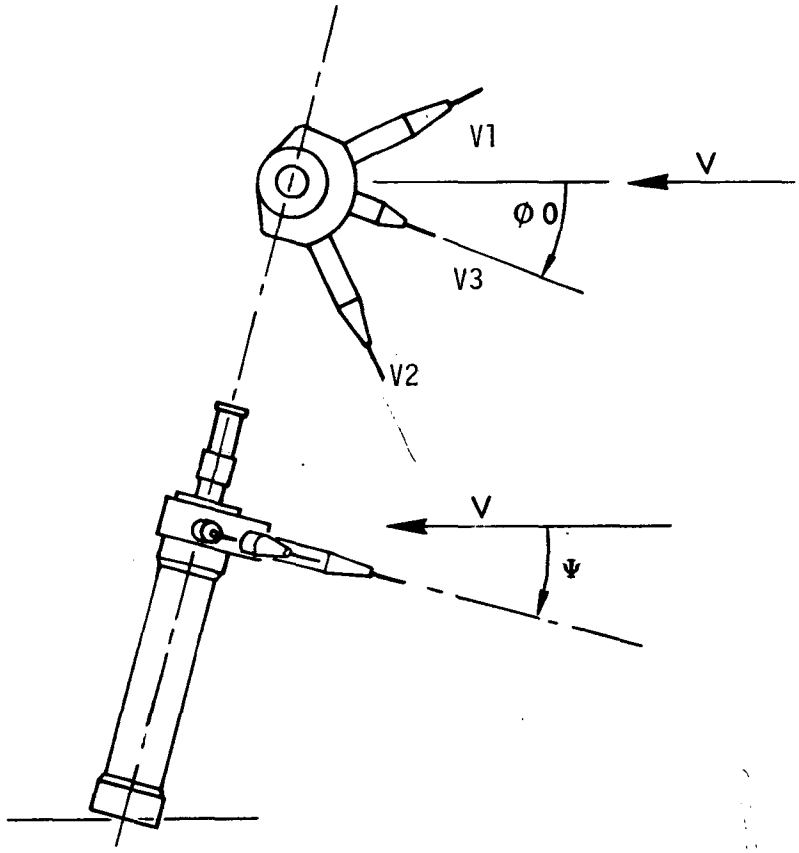

Figure 5. Definition of Wind Sensor Array Rotation and Attitude Angles

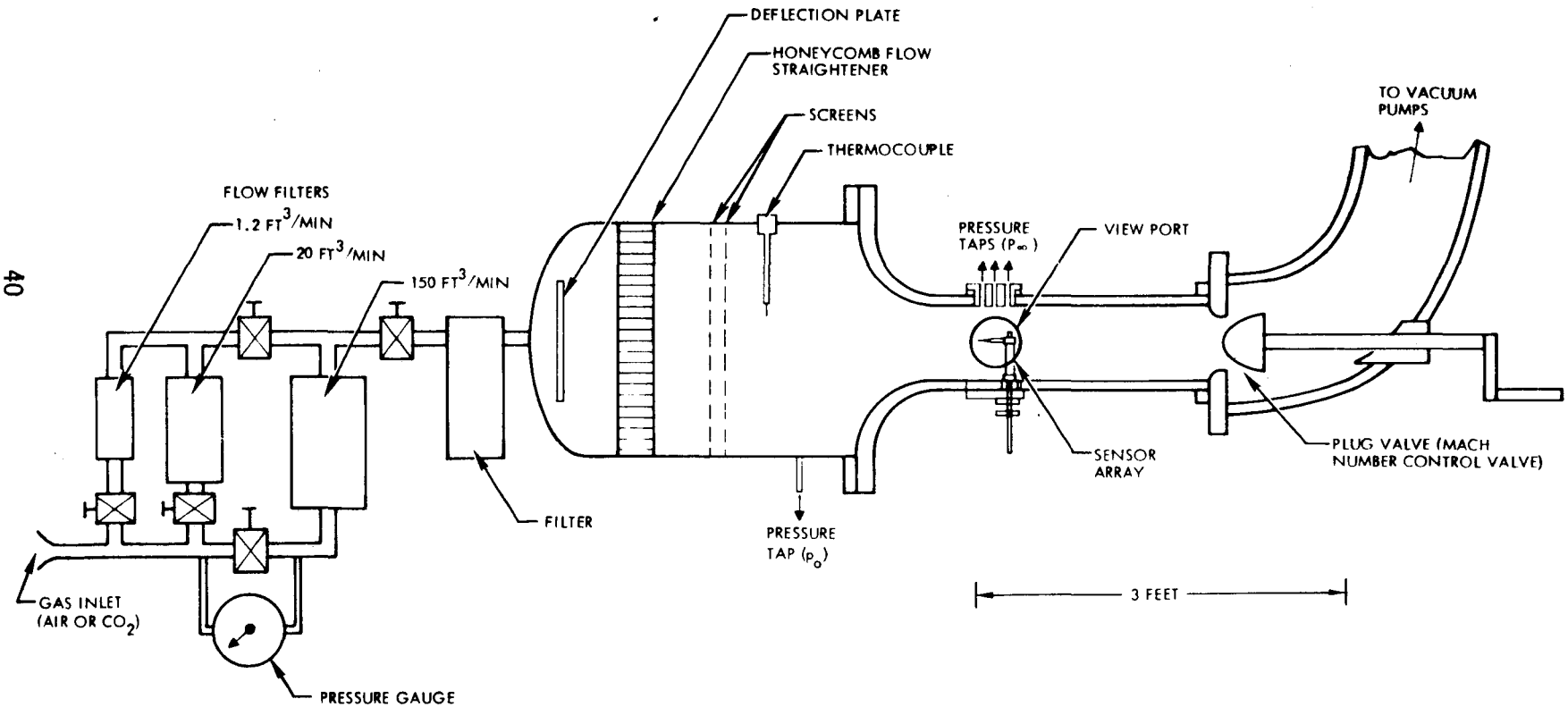

Figure 6. Schematic of Low Pressure Wind Tunnel

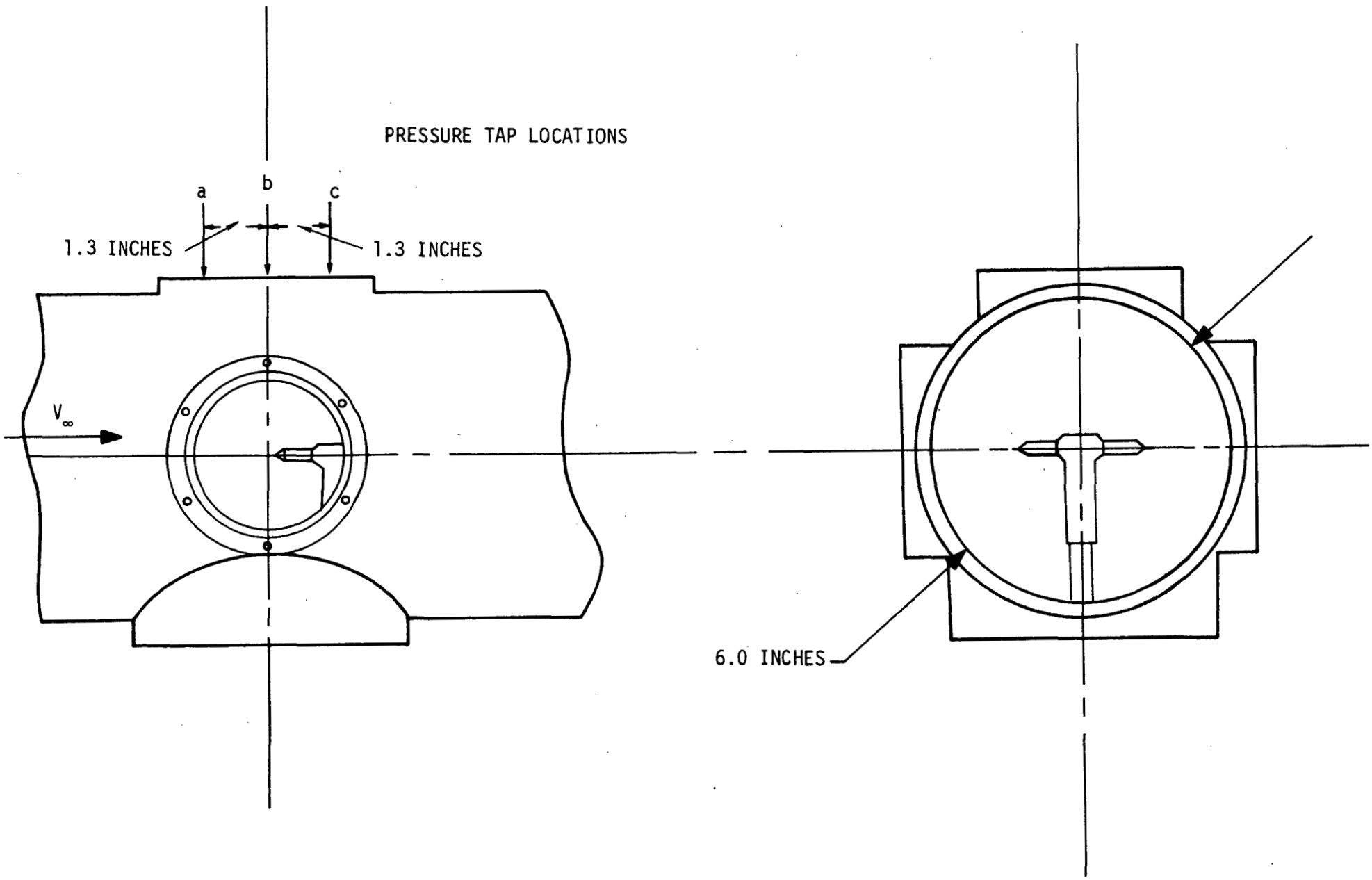

Figure 7. Test Section Pressure Tap Locations

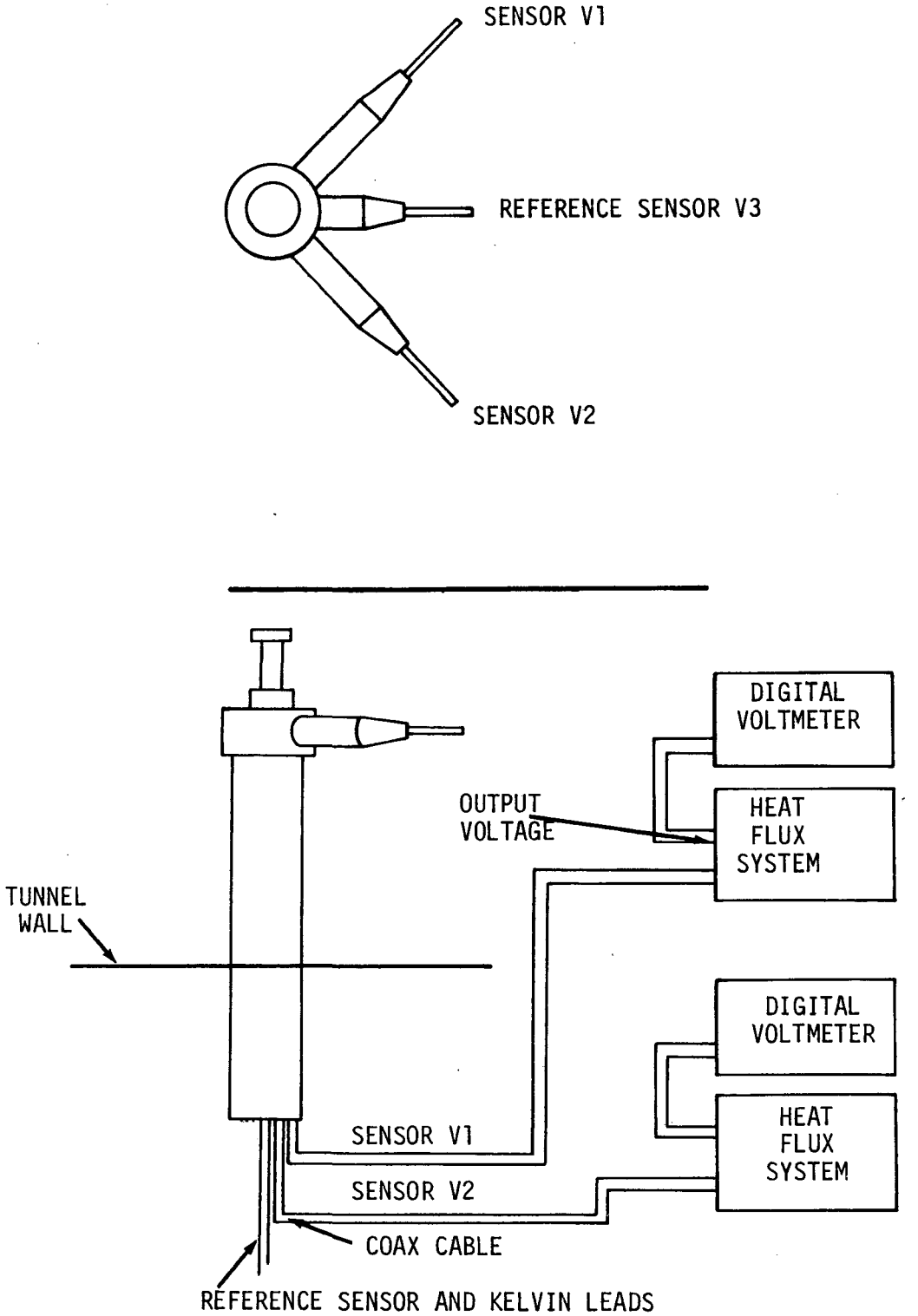

Figure 8. Wind Sensor Circuitry

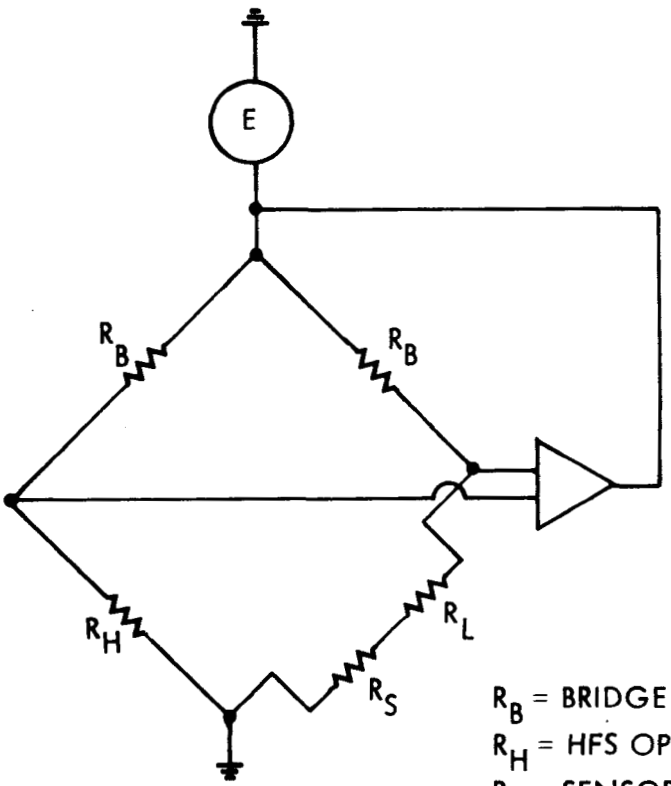

R_B = BRIDGE COMPLETION RESISTANCE
R_H = HFS OPERATING RESISTANCE
R_S = SENSOR PLATINUM FILM RESISTANCE
R_L = TOTAL LEAD RESISTANCE
E = BRIDGE VOLTAGE

Figure 9. Schematic of Heat Flux System Bridge

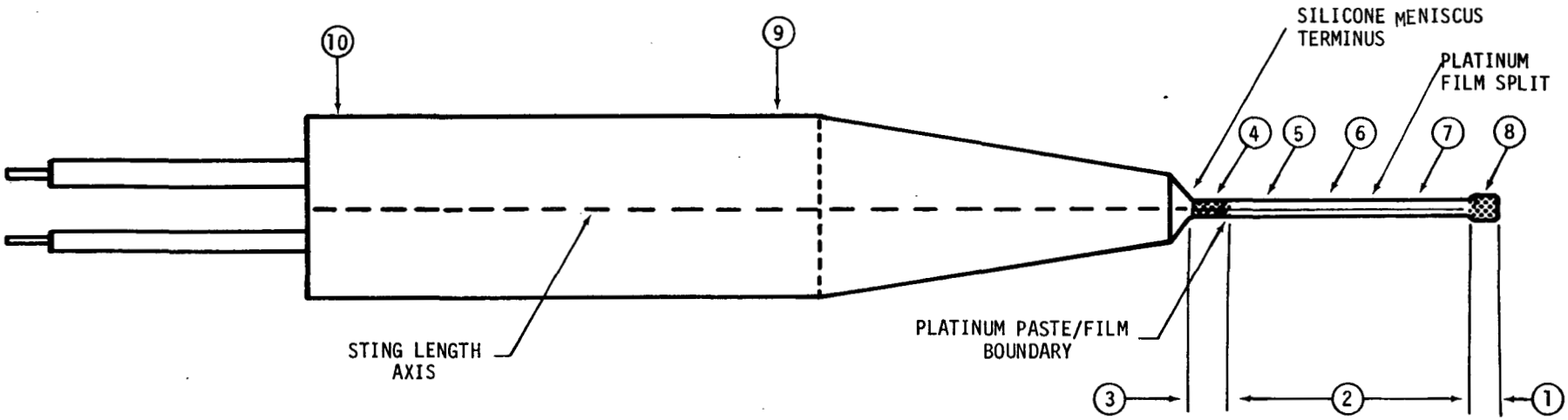

POSITION	DIMENSION (INCHES)
1	.0135
2	.4041
3	.0140
4	.02308
5	.02095
6	.02087
7	.02090
8	.02060
9	.250
10	.250

NOTE: MEASUREMENTS 5 AND 7 MADE ONE ROD DIAMETER FROM THE FILM/PASTE INTERFACE

Figure 10. Sensor 117 Dimensional Data

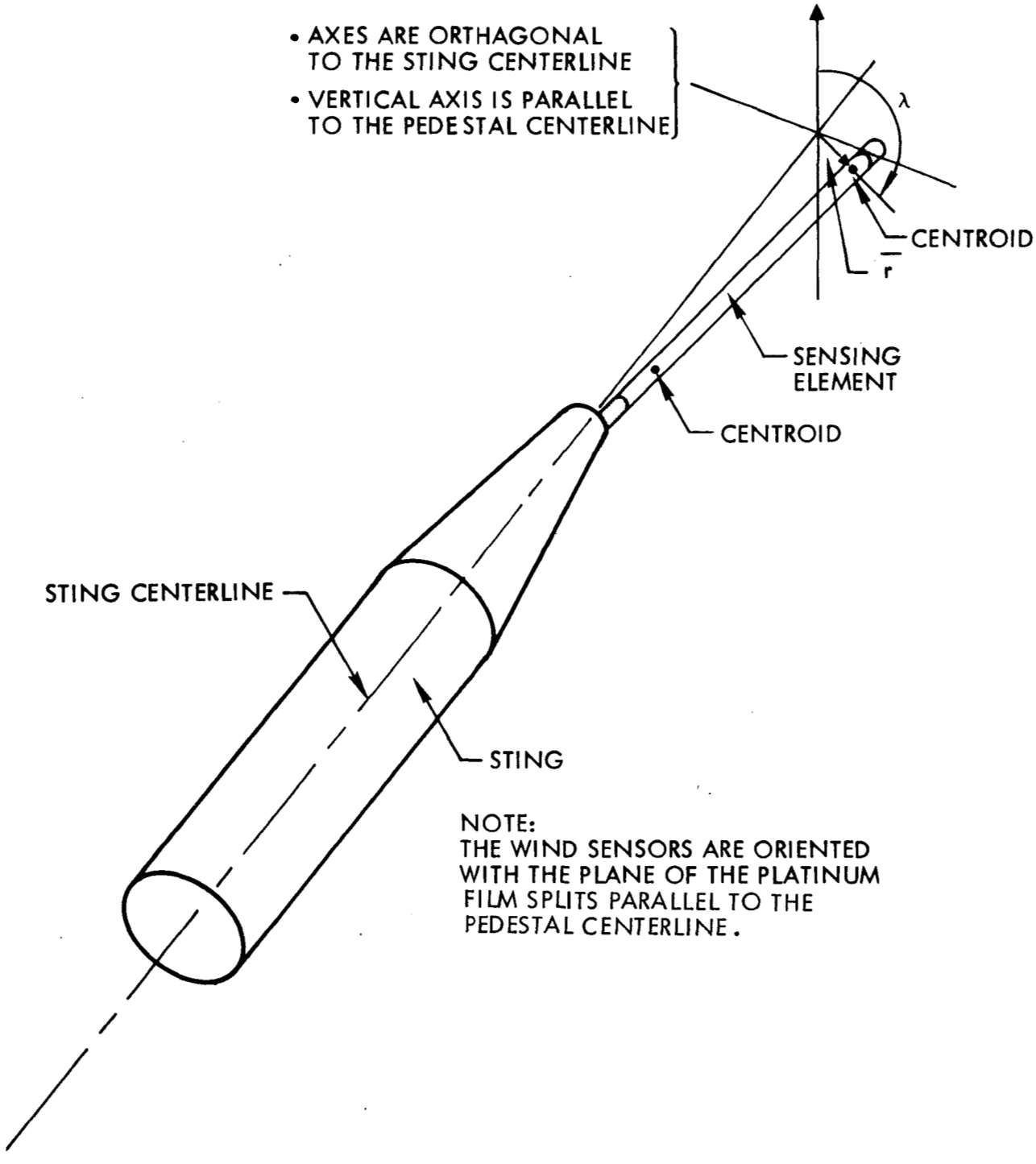

Figure 11. Coordinates of Sensing Element Centroid

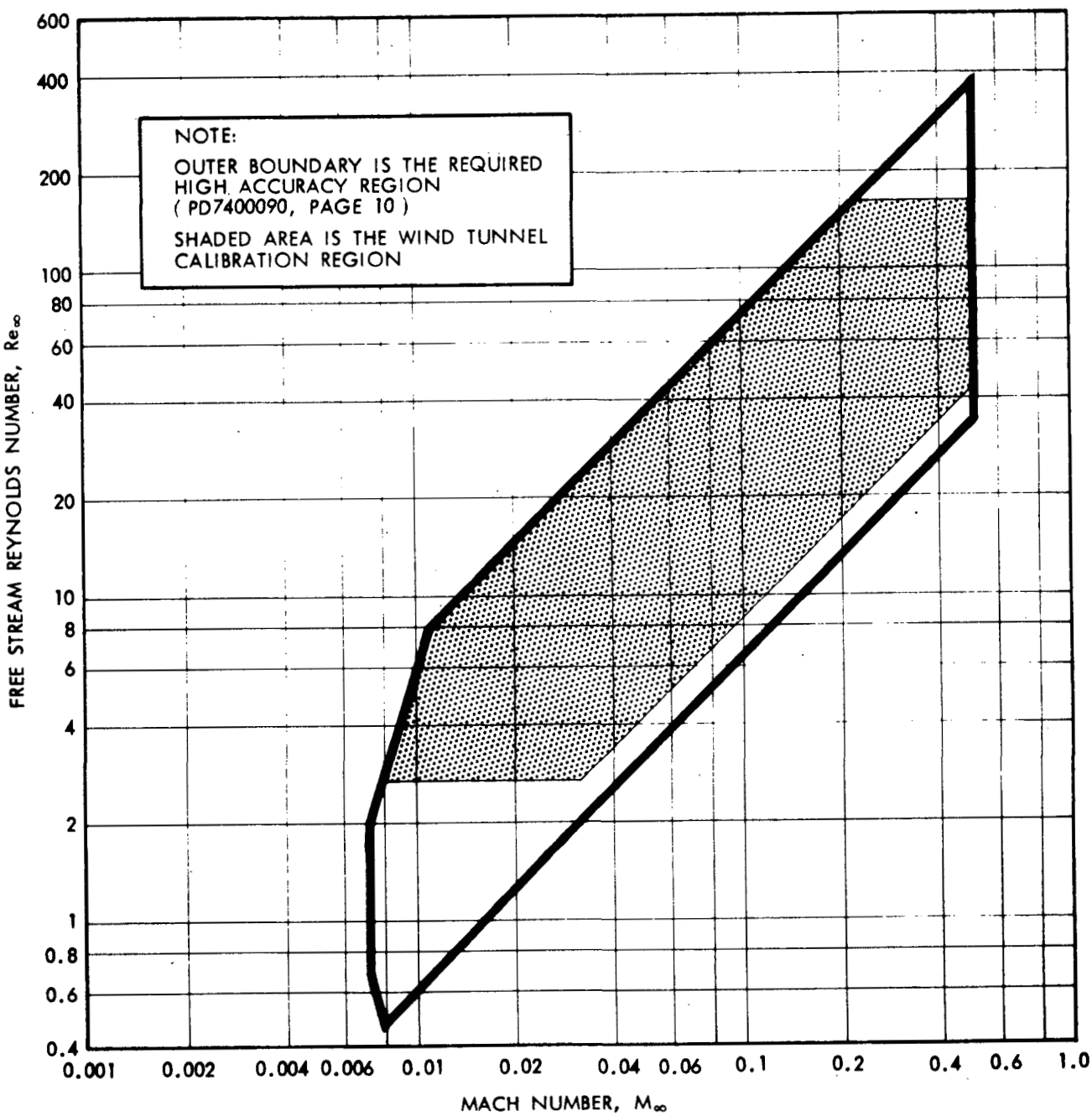

Figure 12. Wind Sensor Performance Ranges: Reynolds Number Versus Mach Number

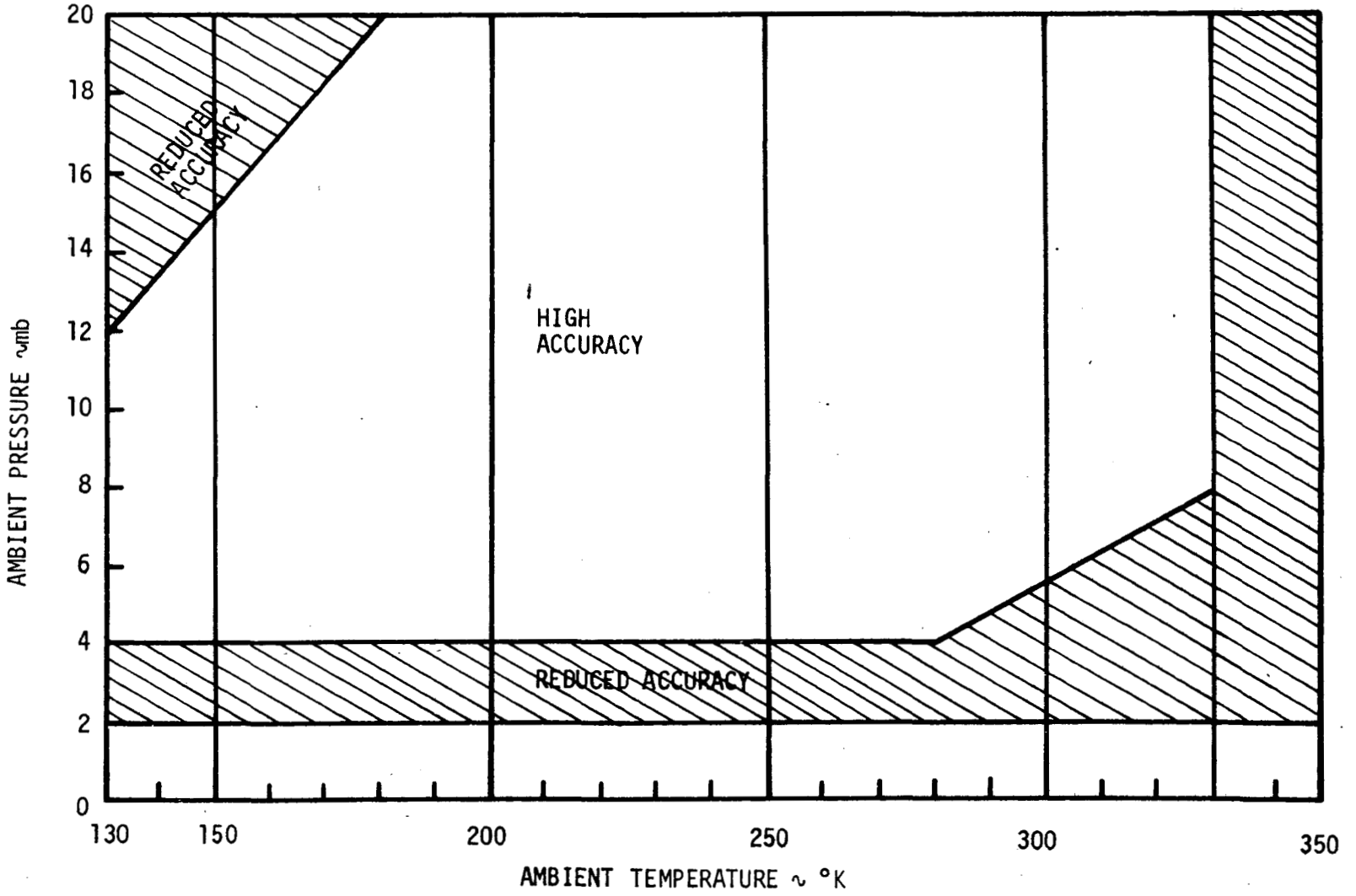

Figure 13a. Operation Conditions: Pressure-Temperature Map

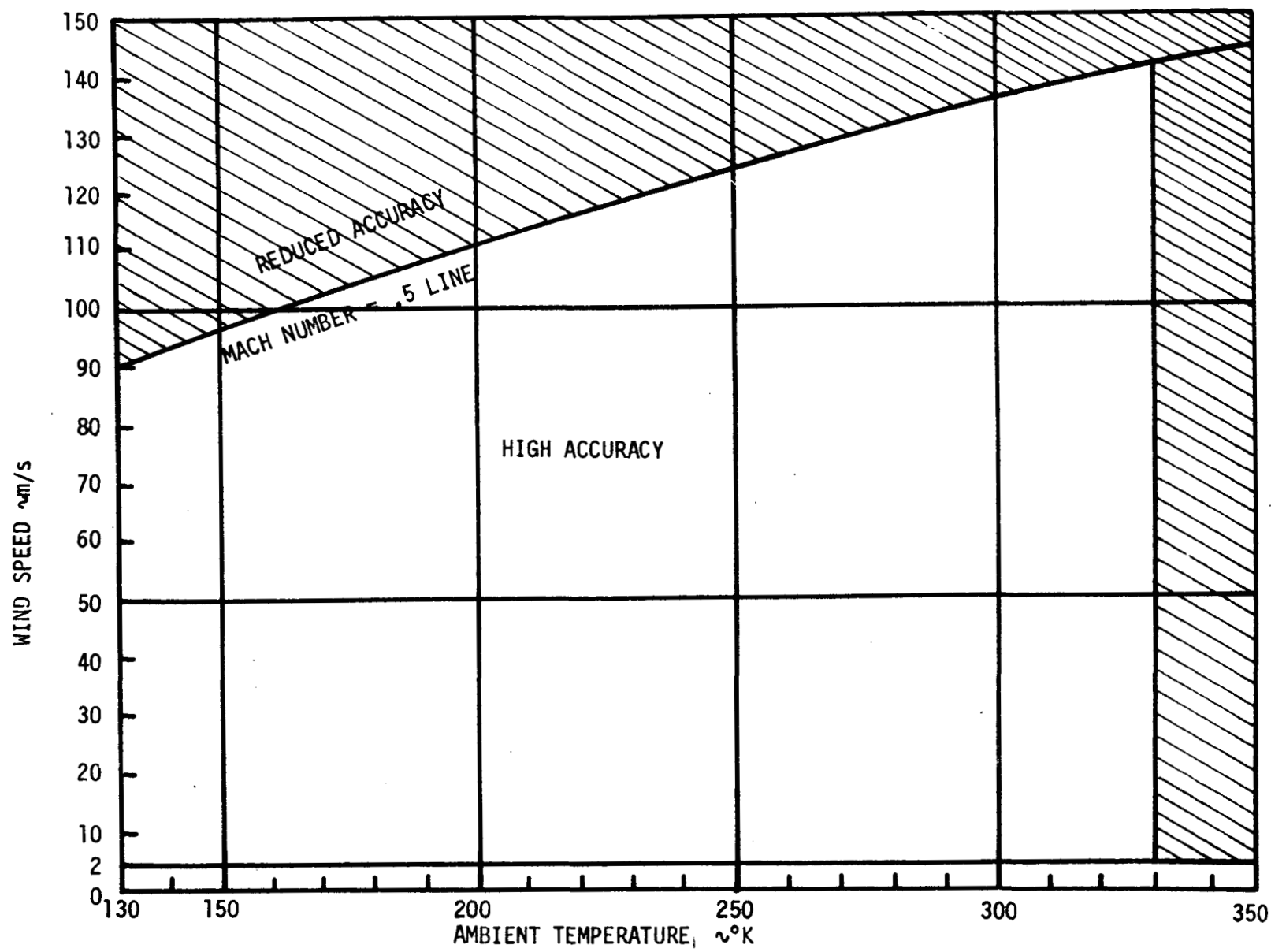

Figure 13b. Operation Conditions: Velocity-Temperature Map

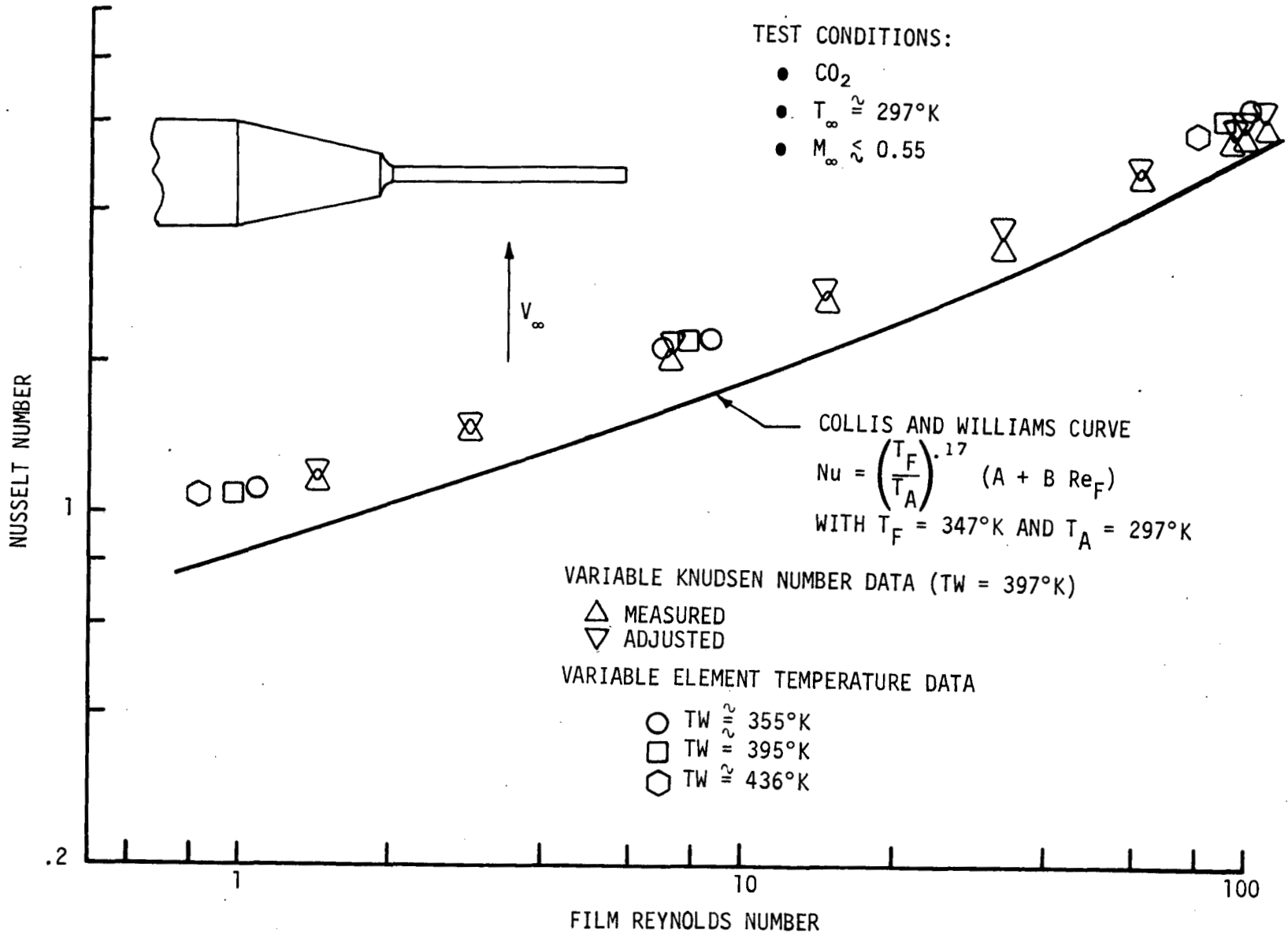

Figure 14. Nusselt Number Variation with Reynolds Number, Knudsen Number and Element Temperature

Nusselt

2-3

Fig. 6 page 191

- Sore Nusselt

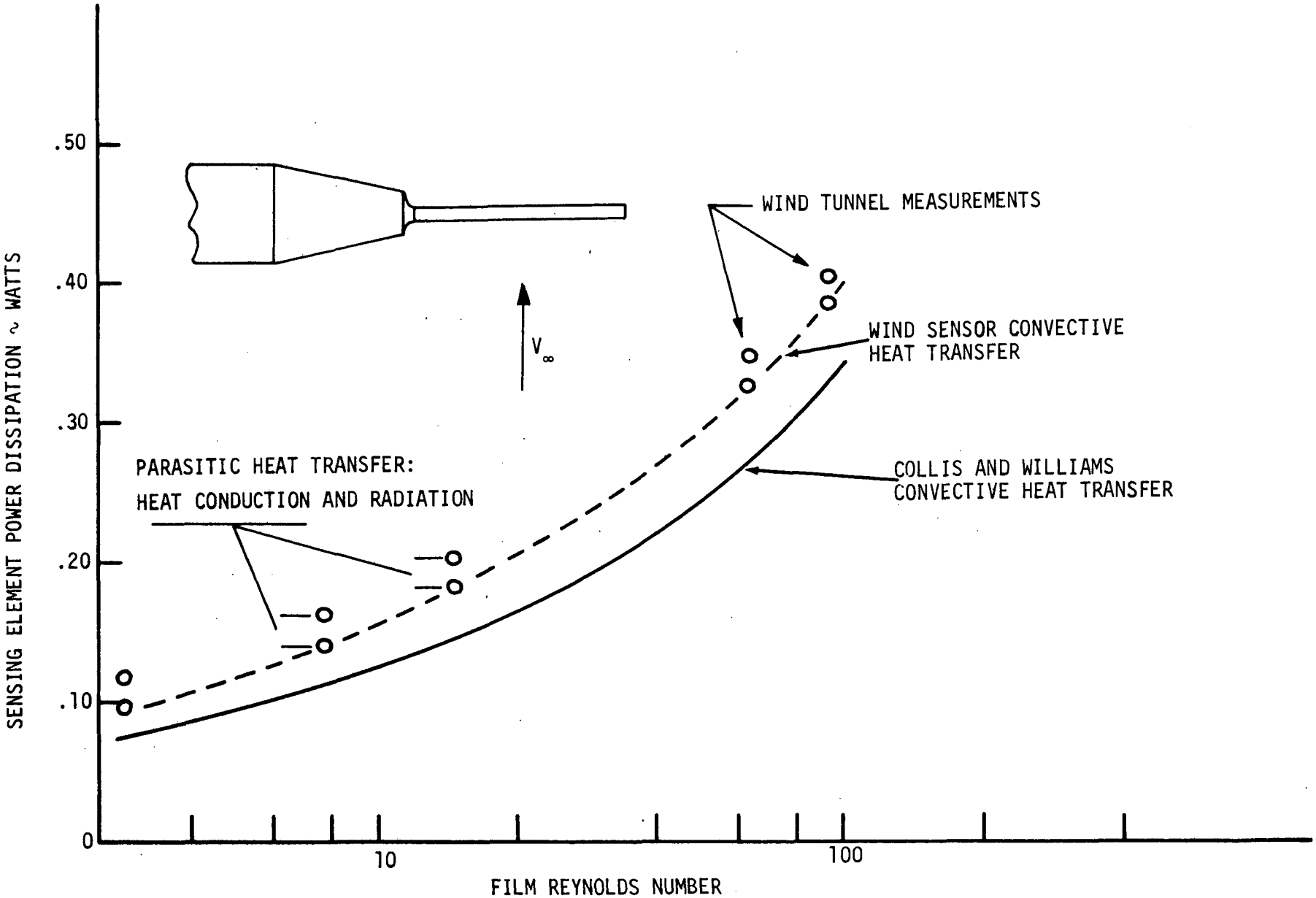

Figure 15. Sensing Element Power Dissipation: Comparison with Collis and Williams Data

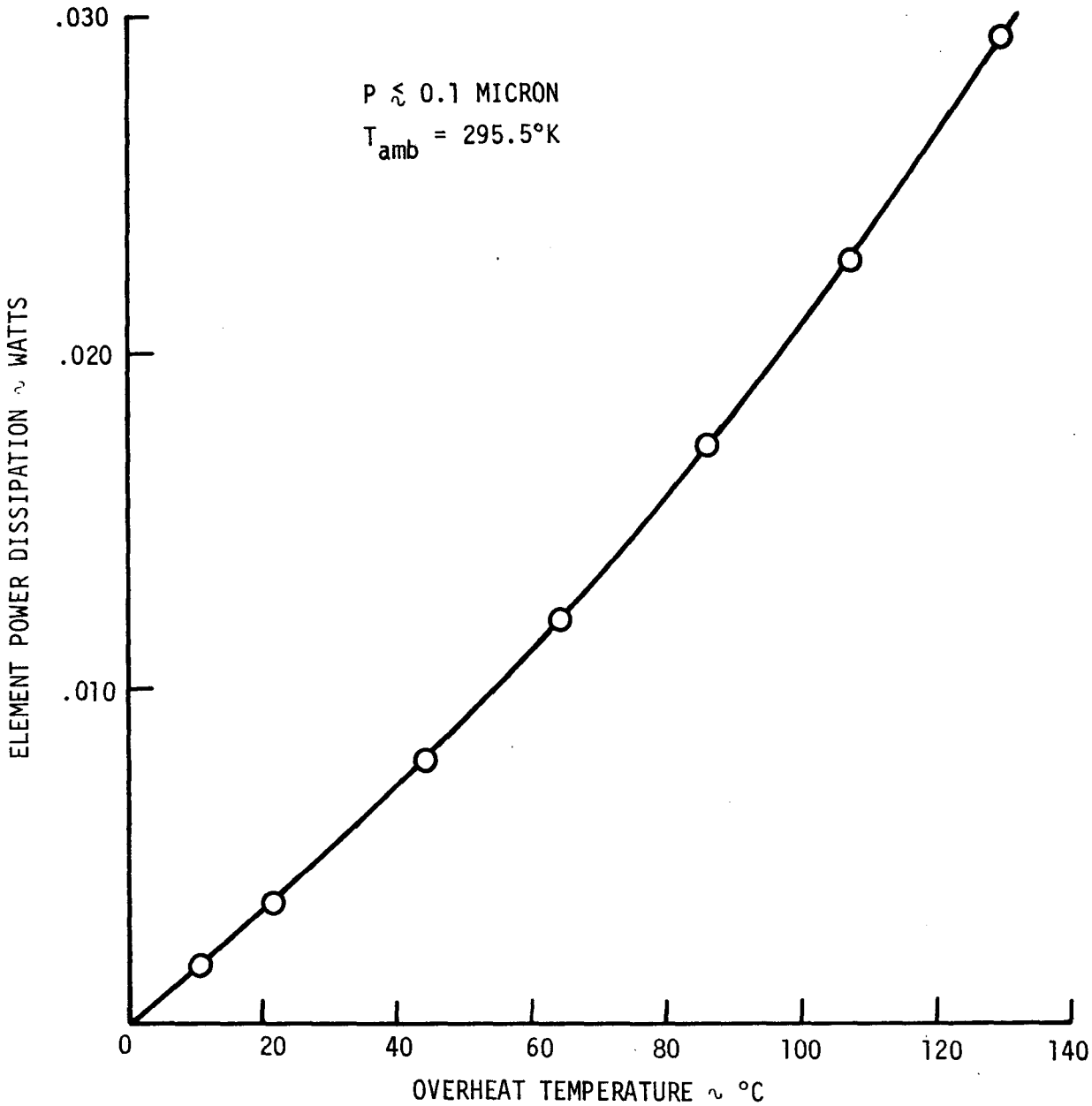

Figure 16. Element Power Dissipation Versus Overheat in a Vacuum

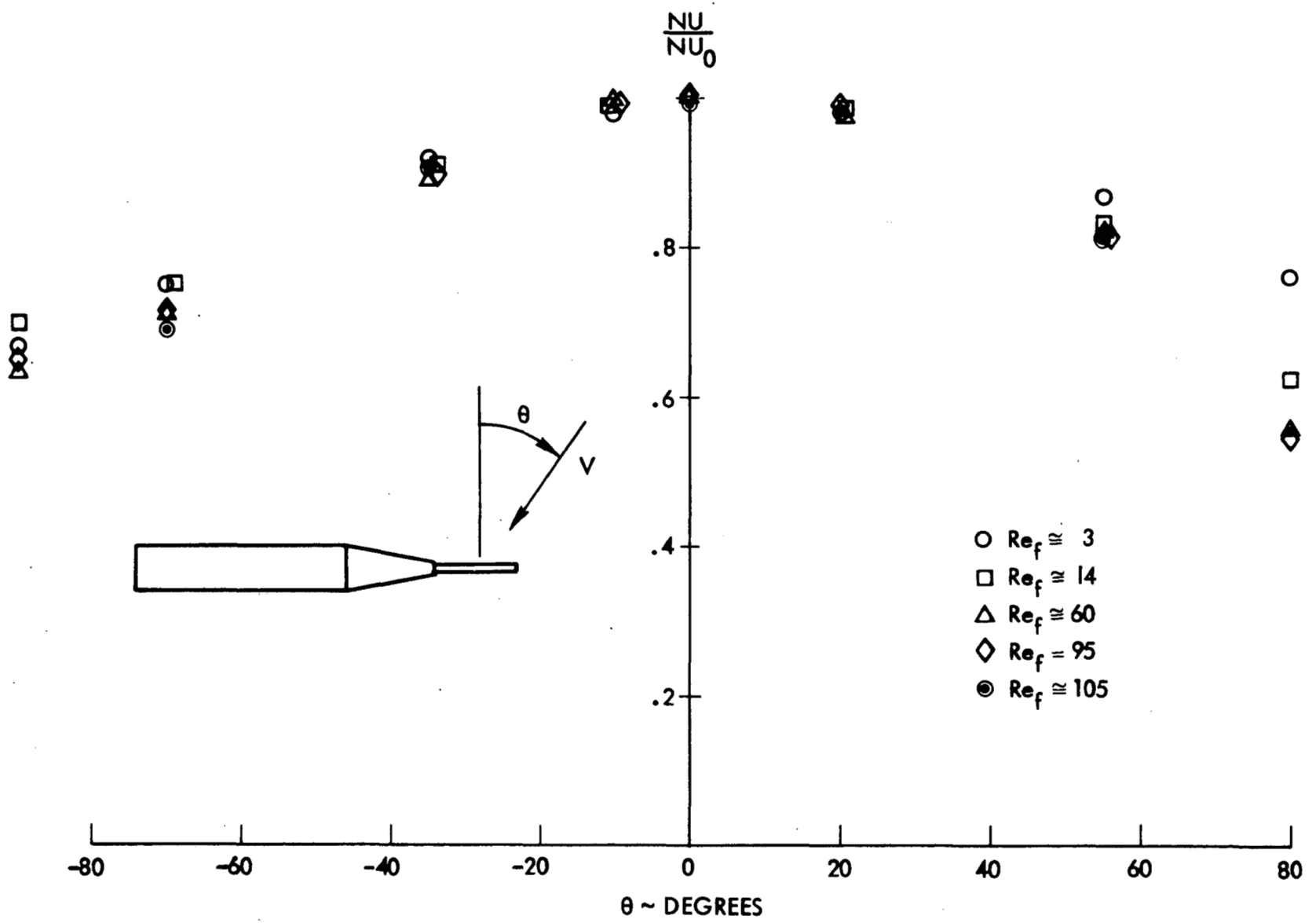

Figure 17. Variation of Nusselt Number with Rotation Angle: $\psi = 0$

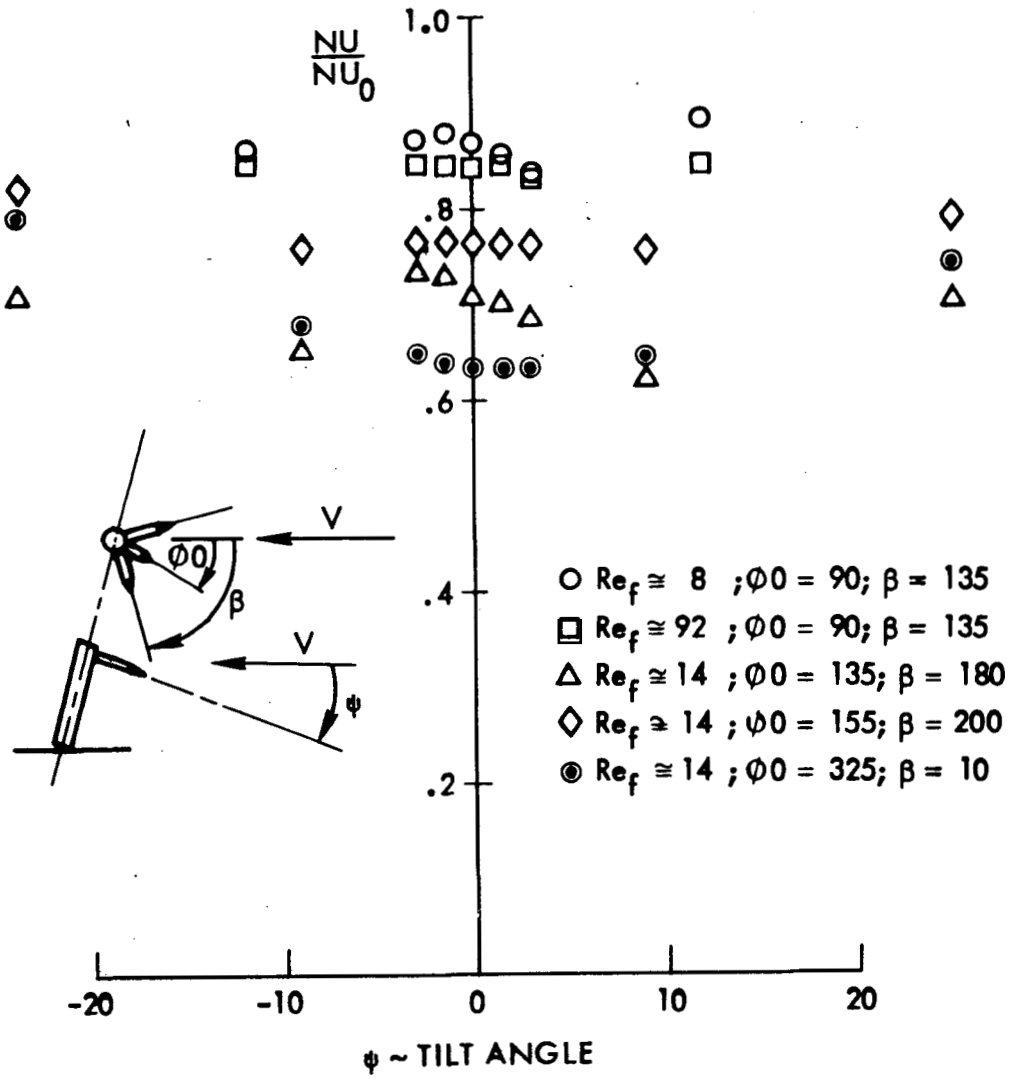

Figure 18. Variation of Nusselt Number with Tilt Angle

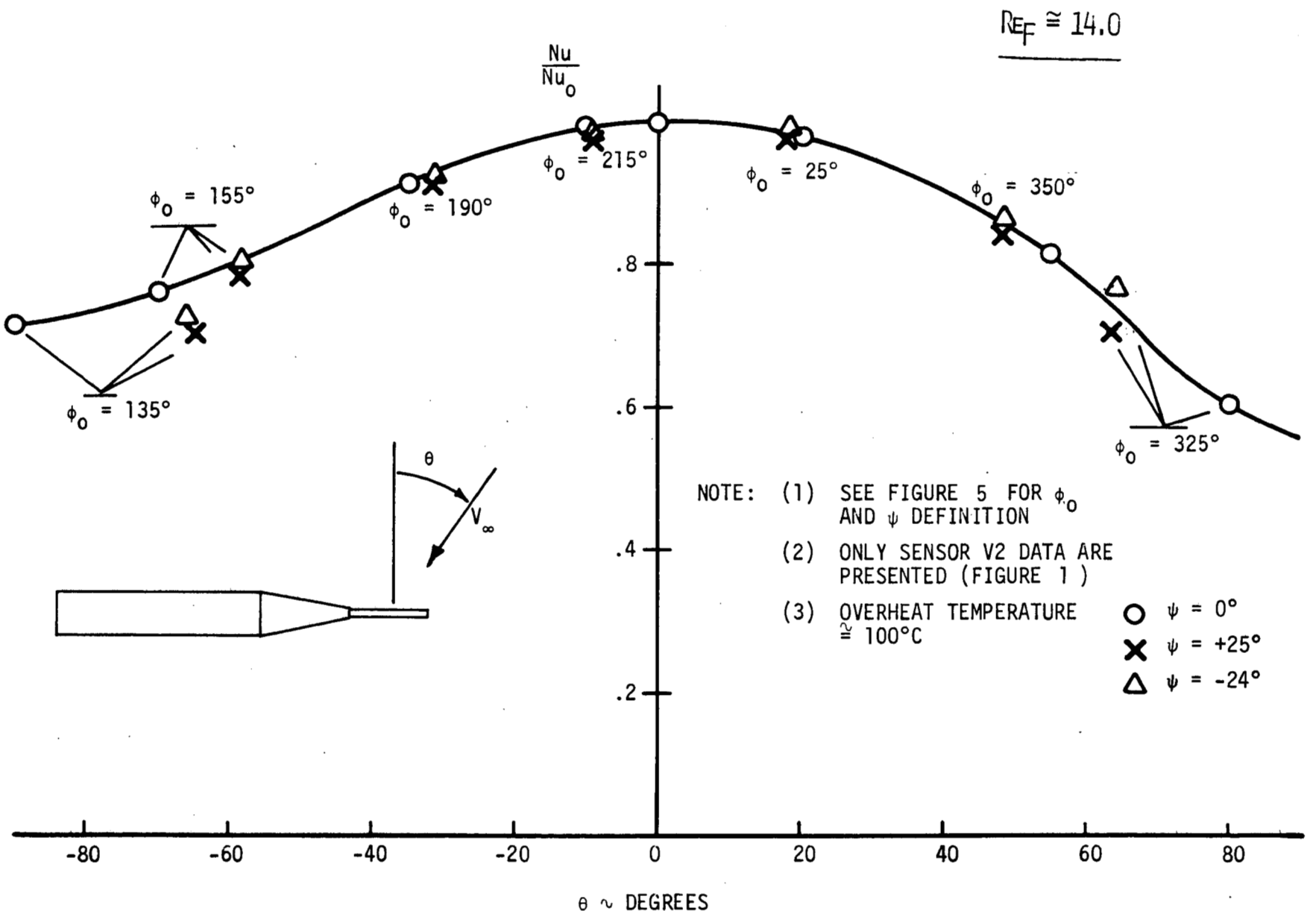

Figure 19. Variation of Nusselt Number with Angle of Attack

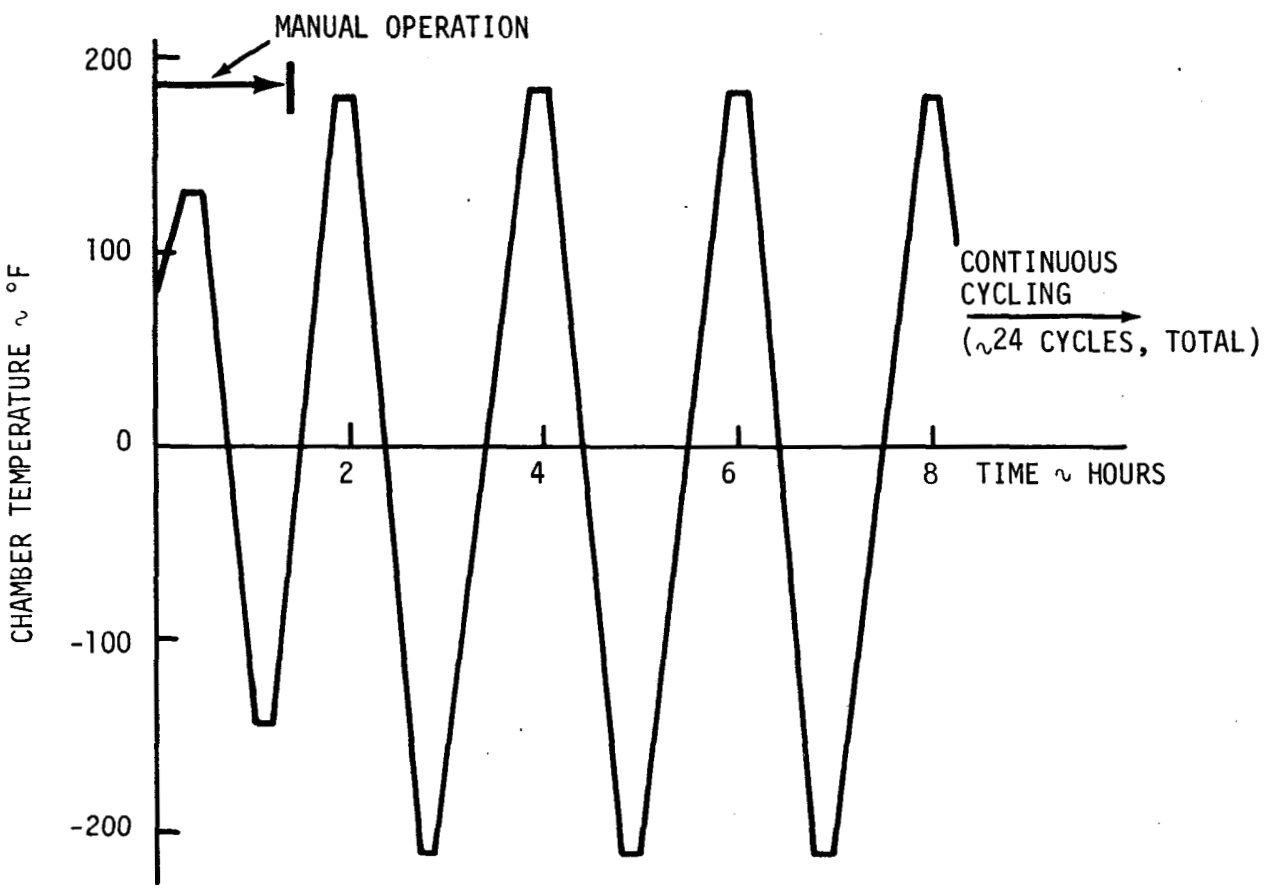

Figure 20. Temperature Cycling Test: Temperature Cycle

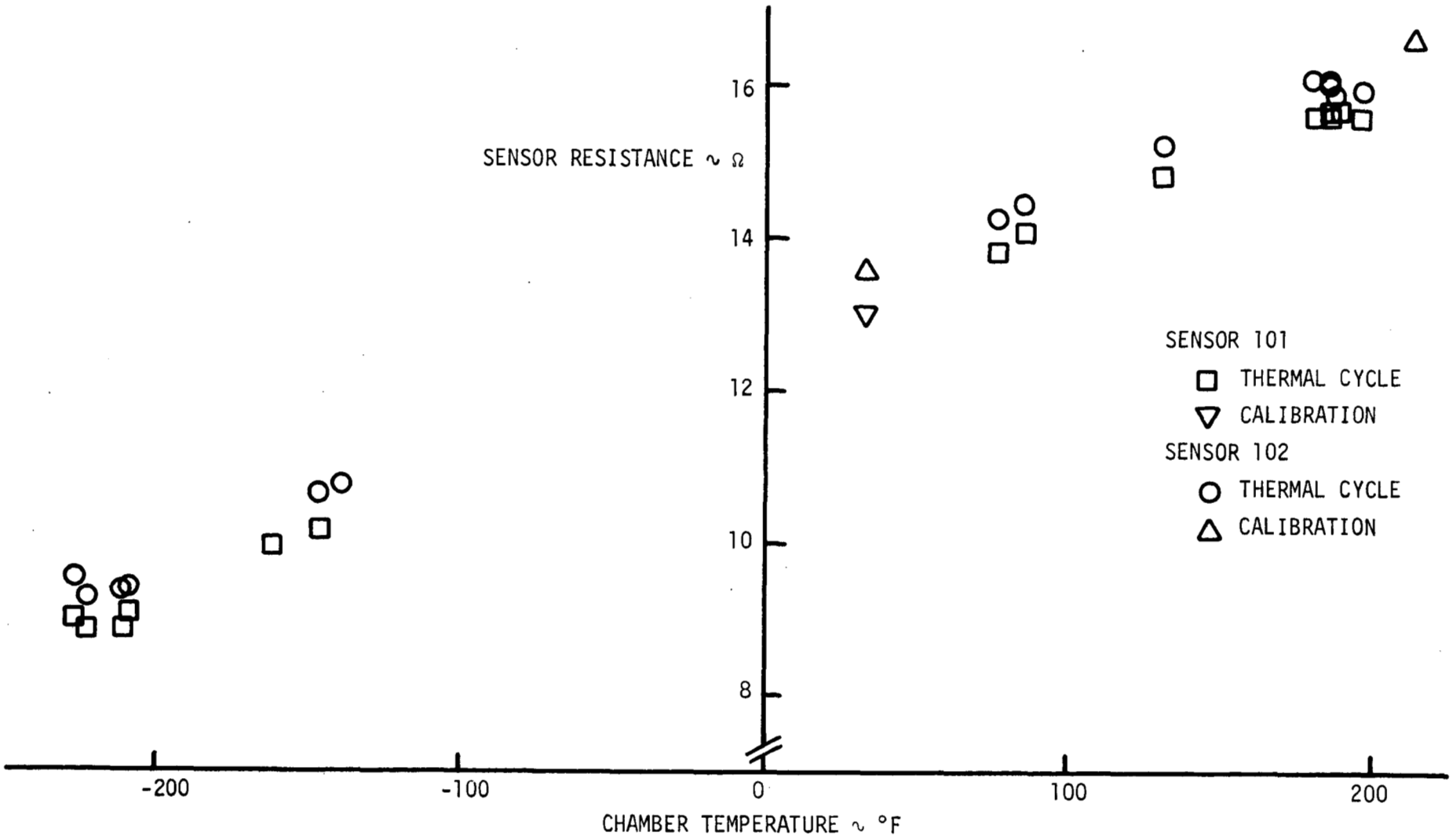

Figure 21. Temperature Cycling Test: Sensor Resistance Versus Temperature

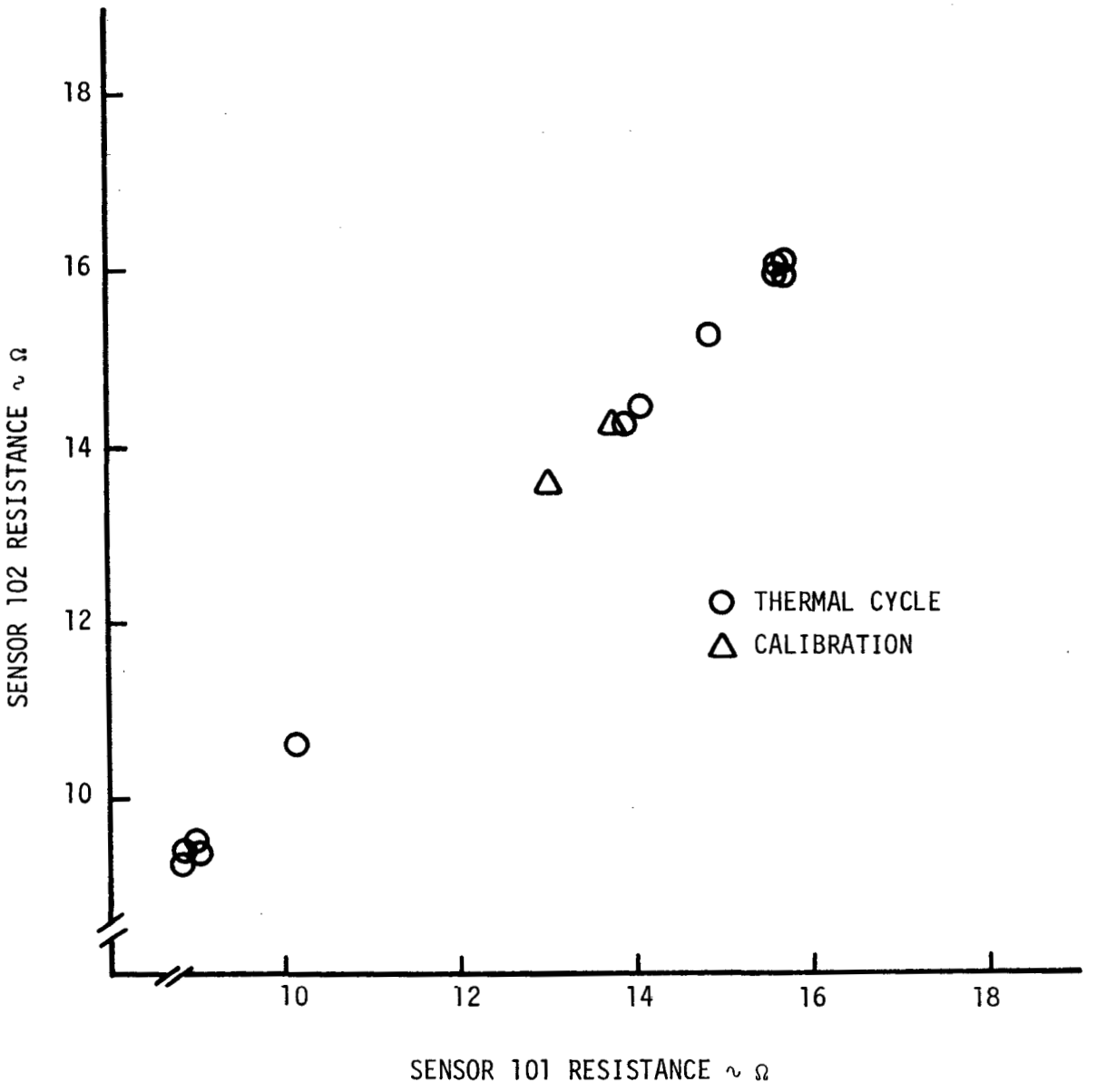

Figure 22. Temperature Cycling Test: Wind Sensor Resistances Cross-Plot

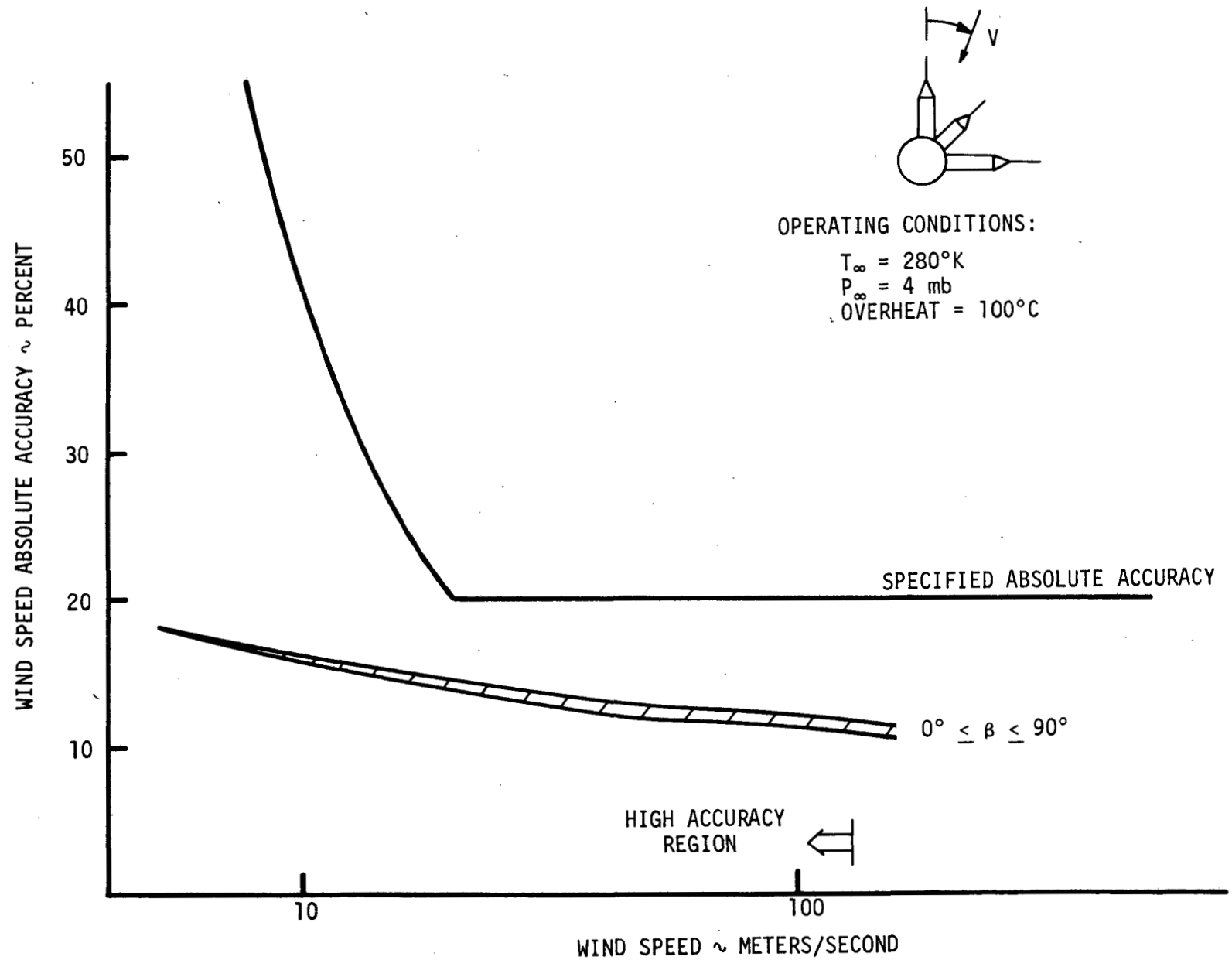

Figure 23. Wind Speed Absolute Accuracy Versus Wind Speed

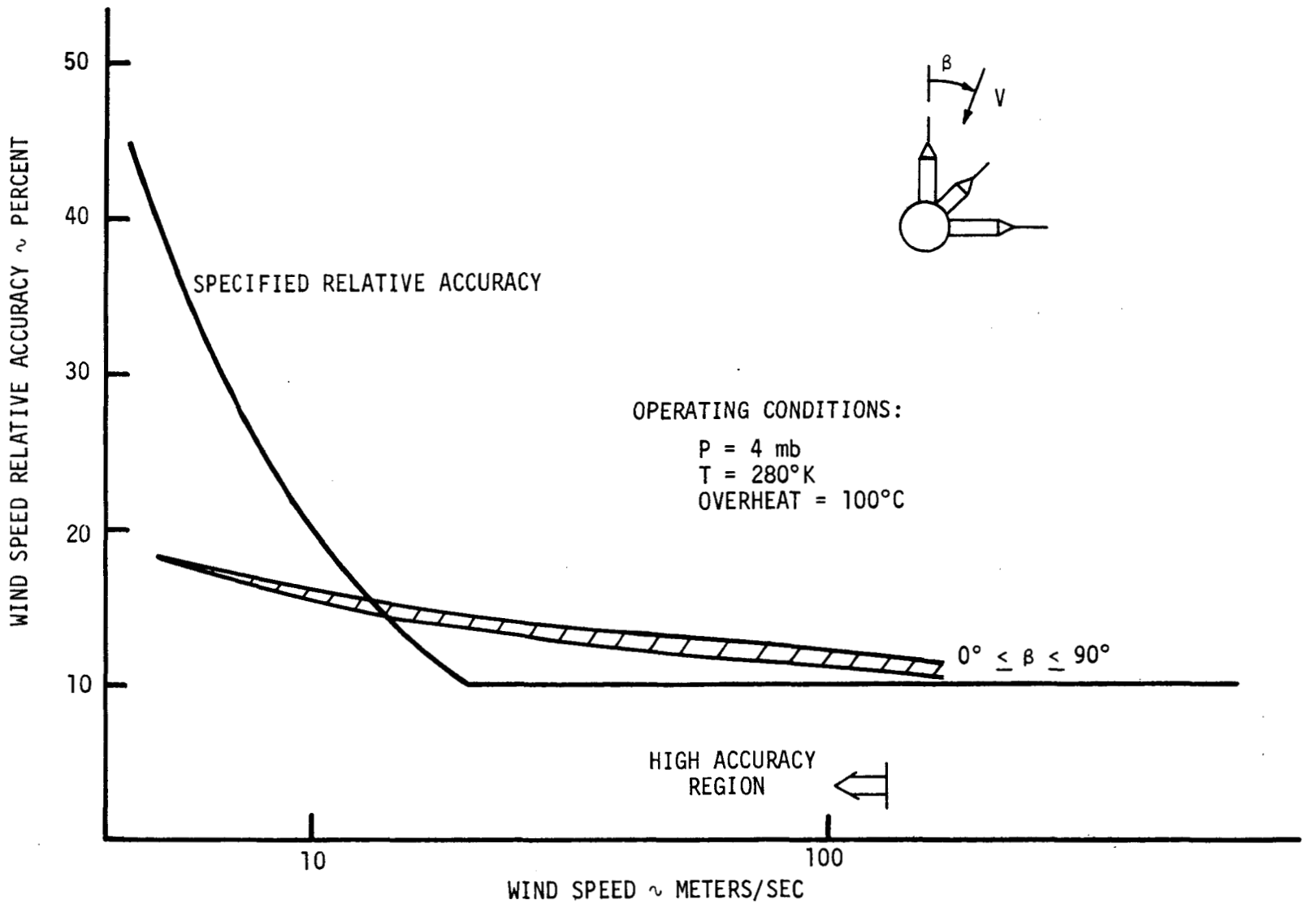

Figure 24. Wind Speed Relative Accuracy Versus Wind Speed

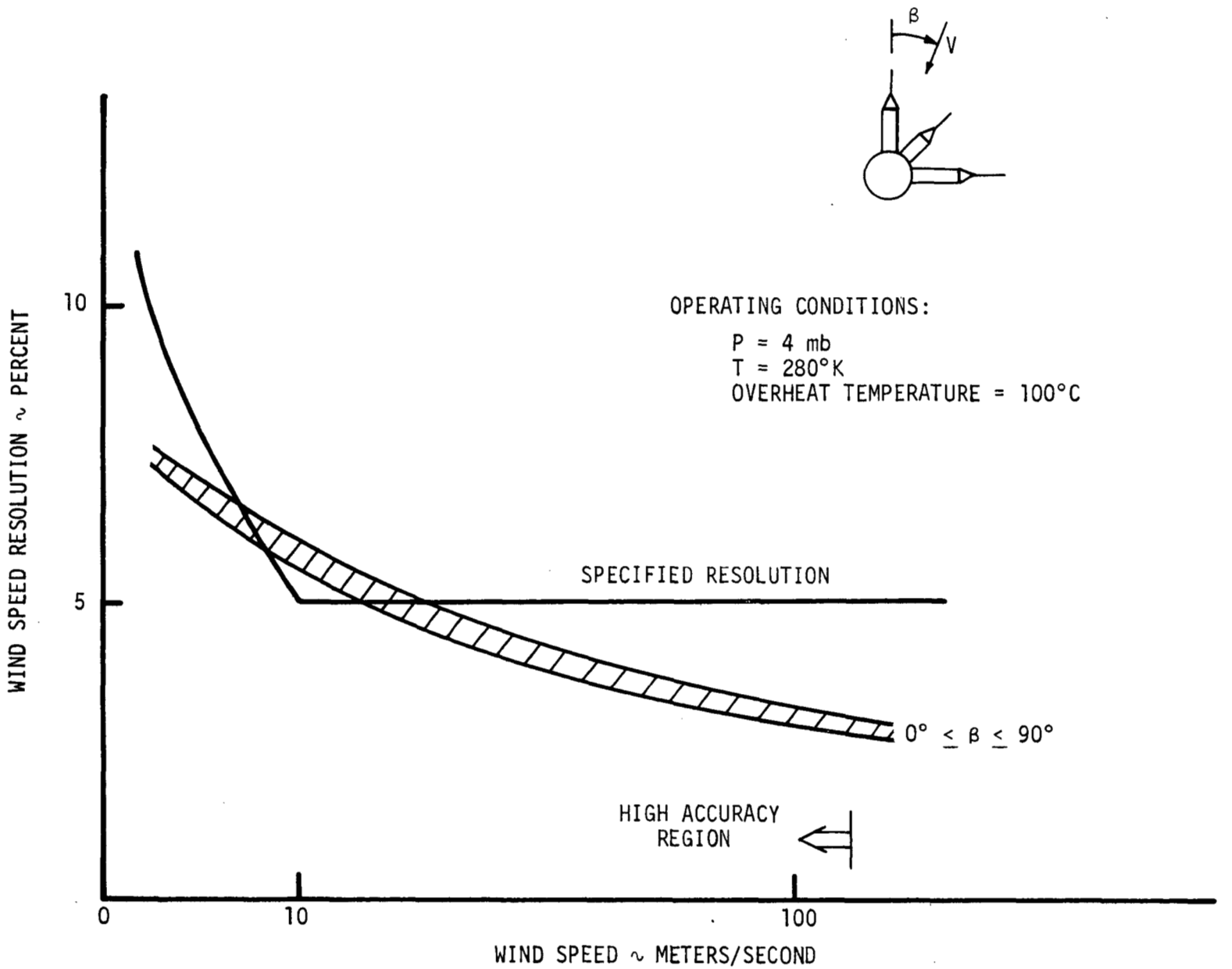

Figure 25. Wind Speed Resolution Versus Wind Speed

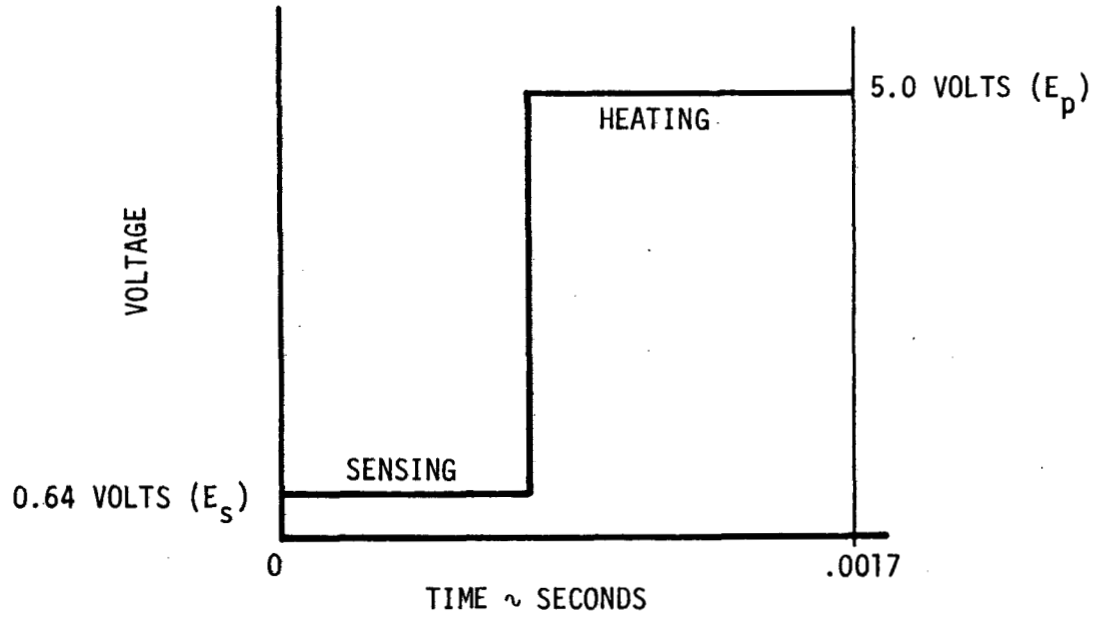

Figure 26a. MEA Duty Cycle

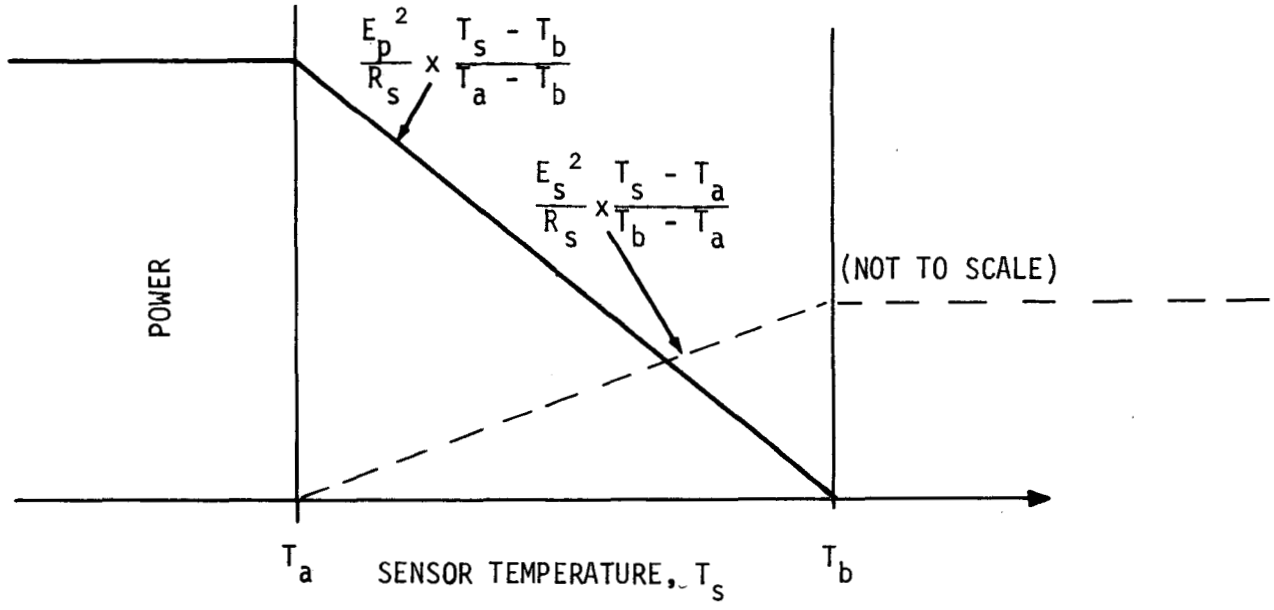

Figure 26b. Sensing Element Power Dissipation

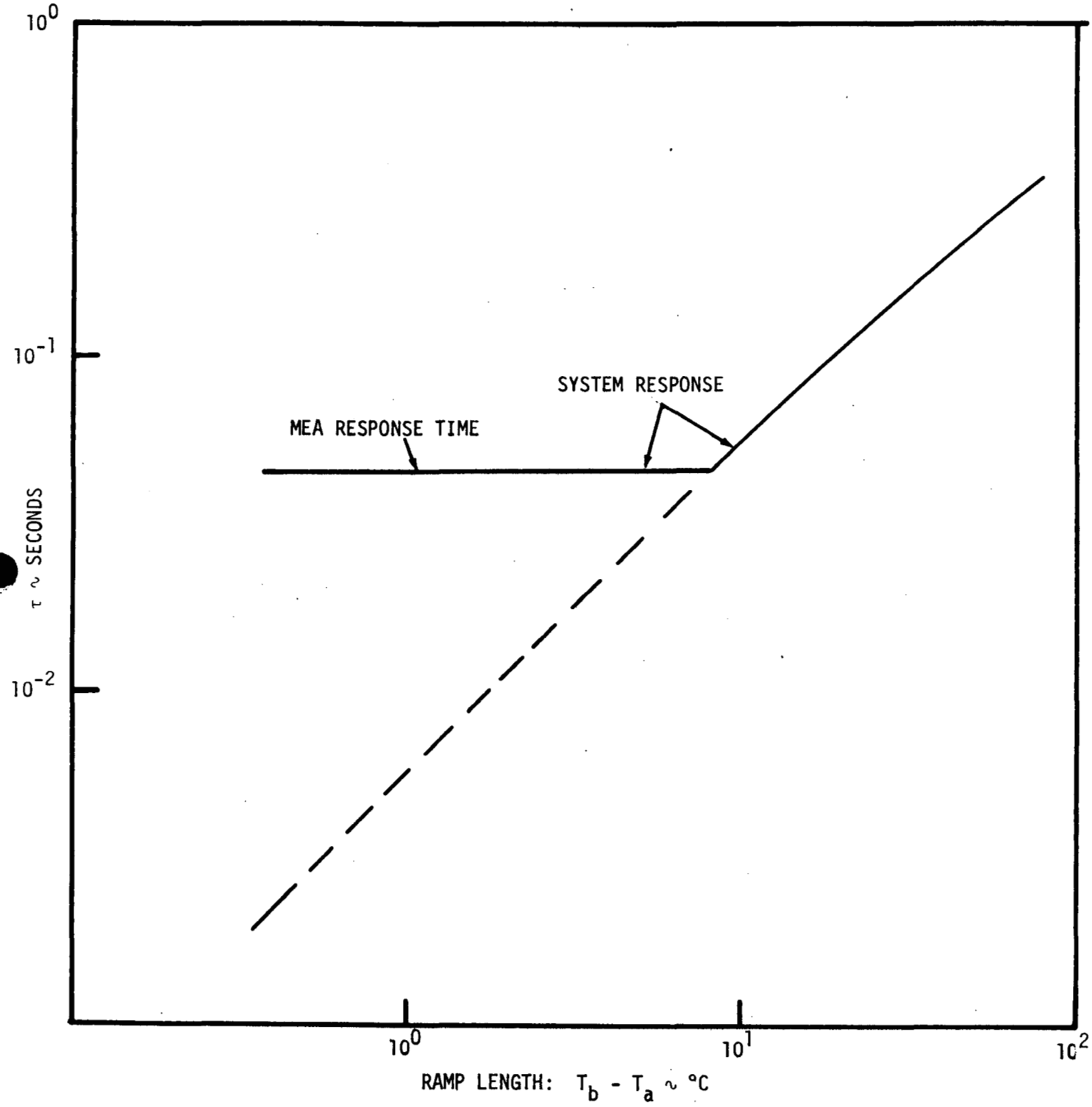

Figure 27. Response Time of the MEA -- Wind Sensor System

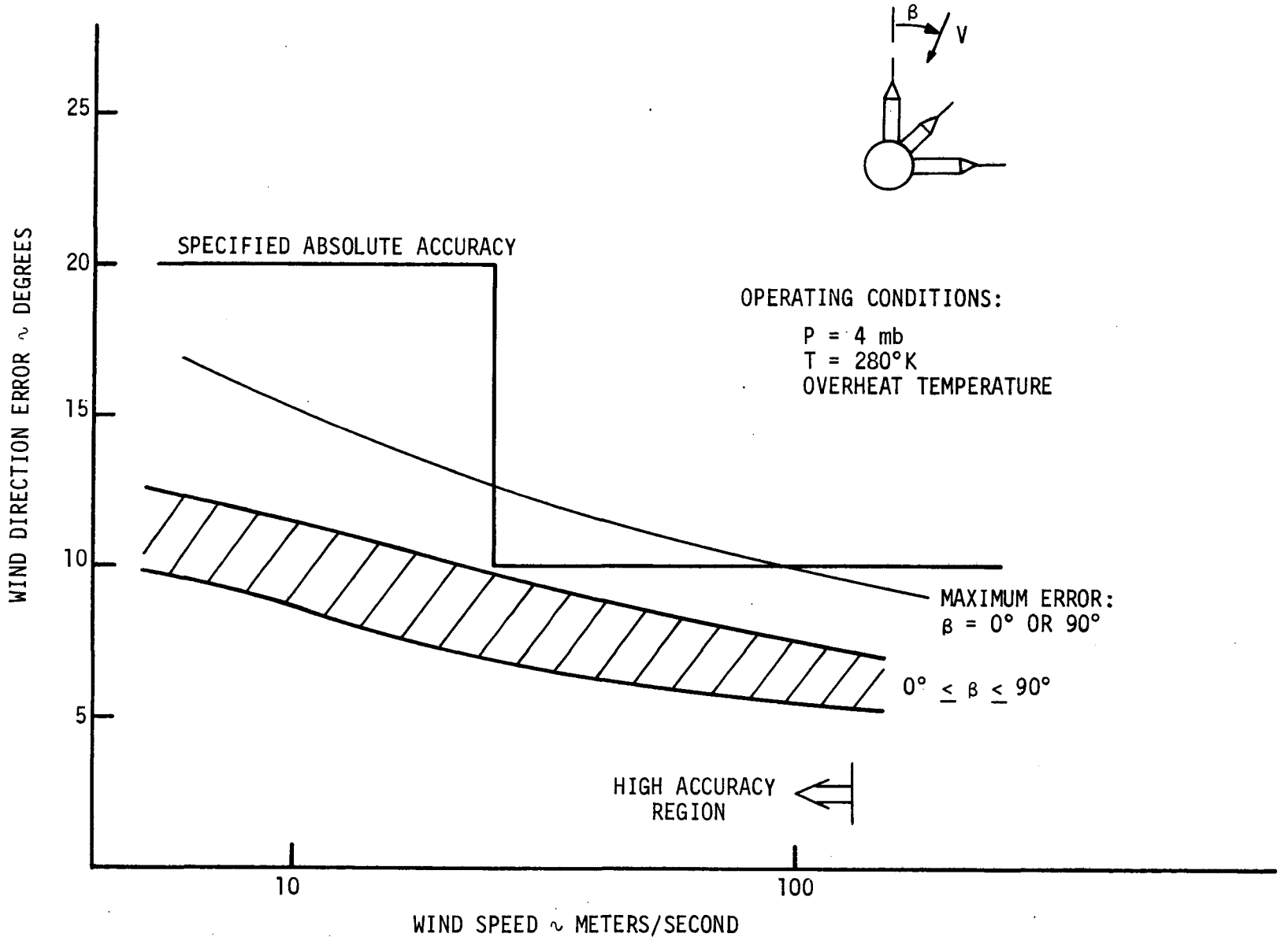

Figure 28. Wind Direction Error Versus Wind Speed

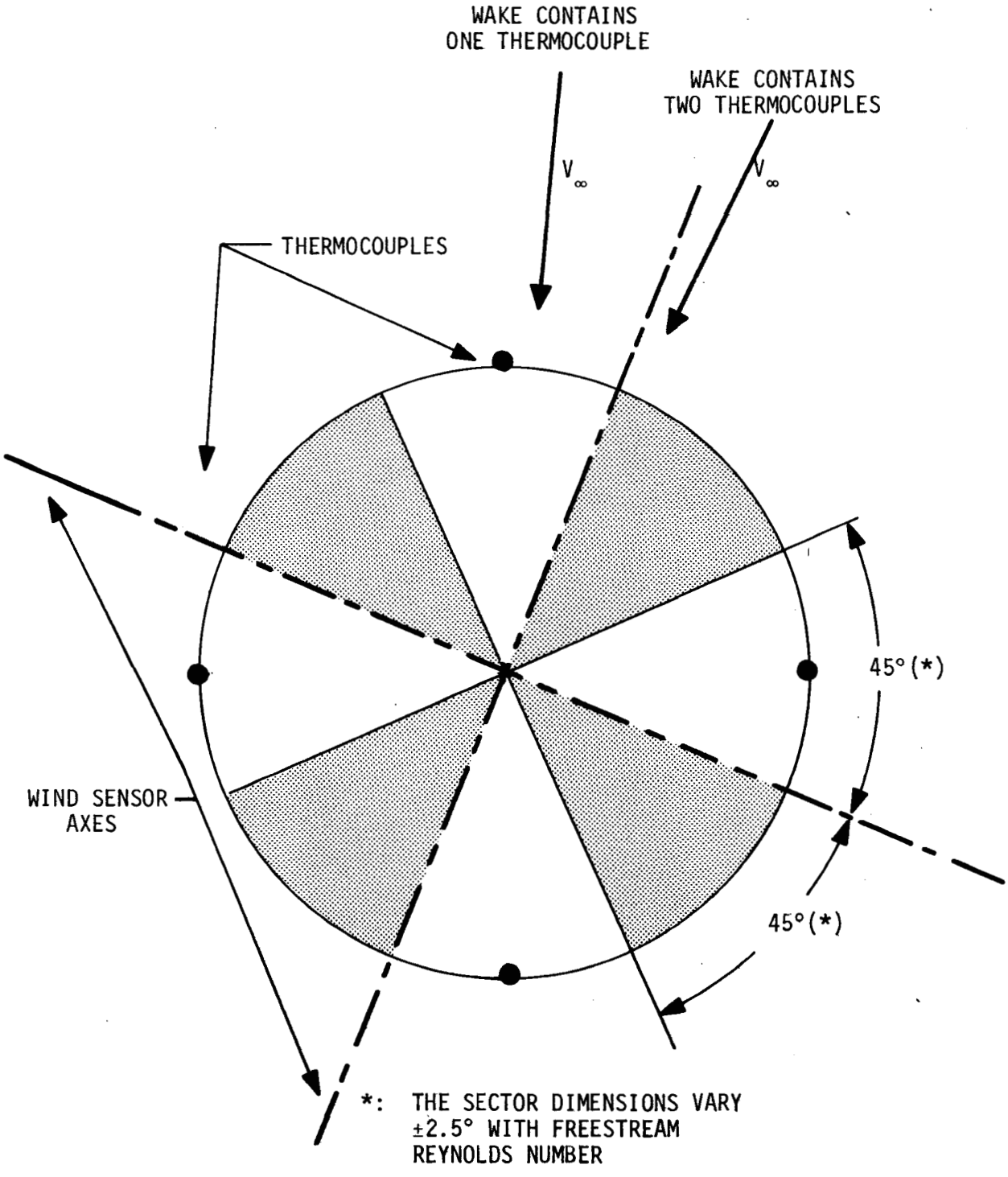

Figure 29. Illustration of Wind Direction Sectors Containing One and Two Quadrant Sensor Thermocouples

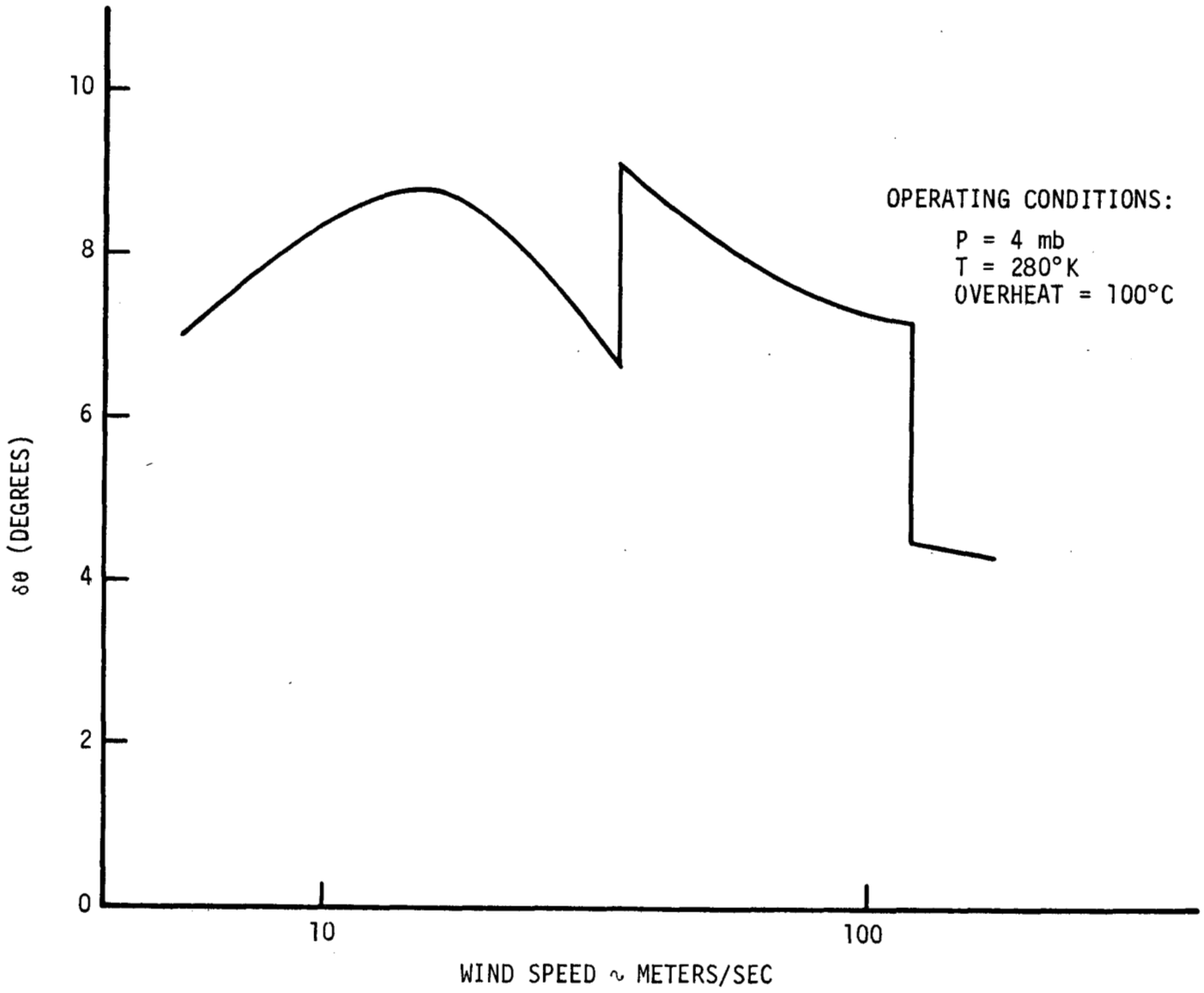

Figure 30. Quadrant Sensor Deadband Versus Wind Speed

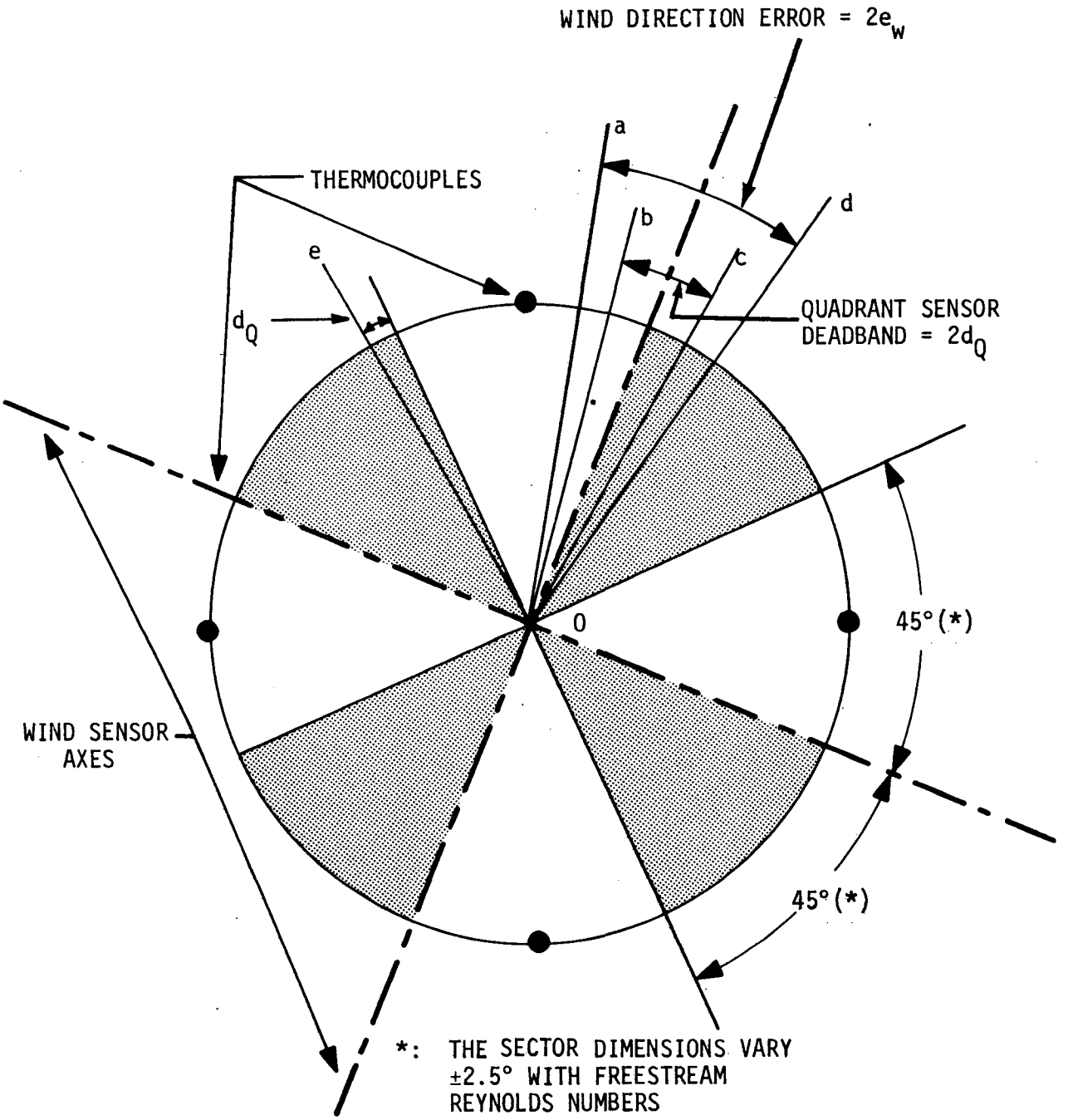

Figure 31. Quadrant Sensor and Wind Sensor Error Sectors about Wind Sensor Axis

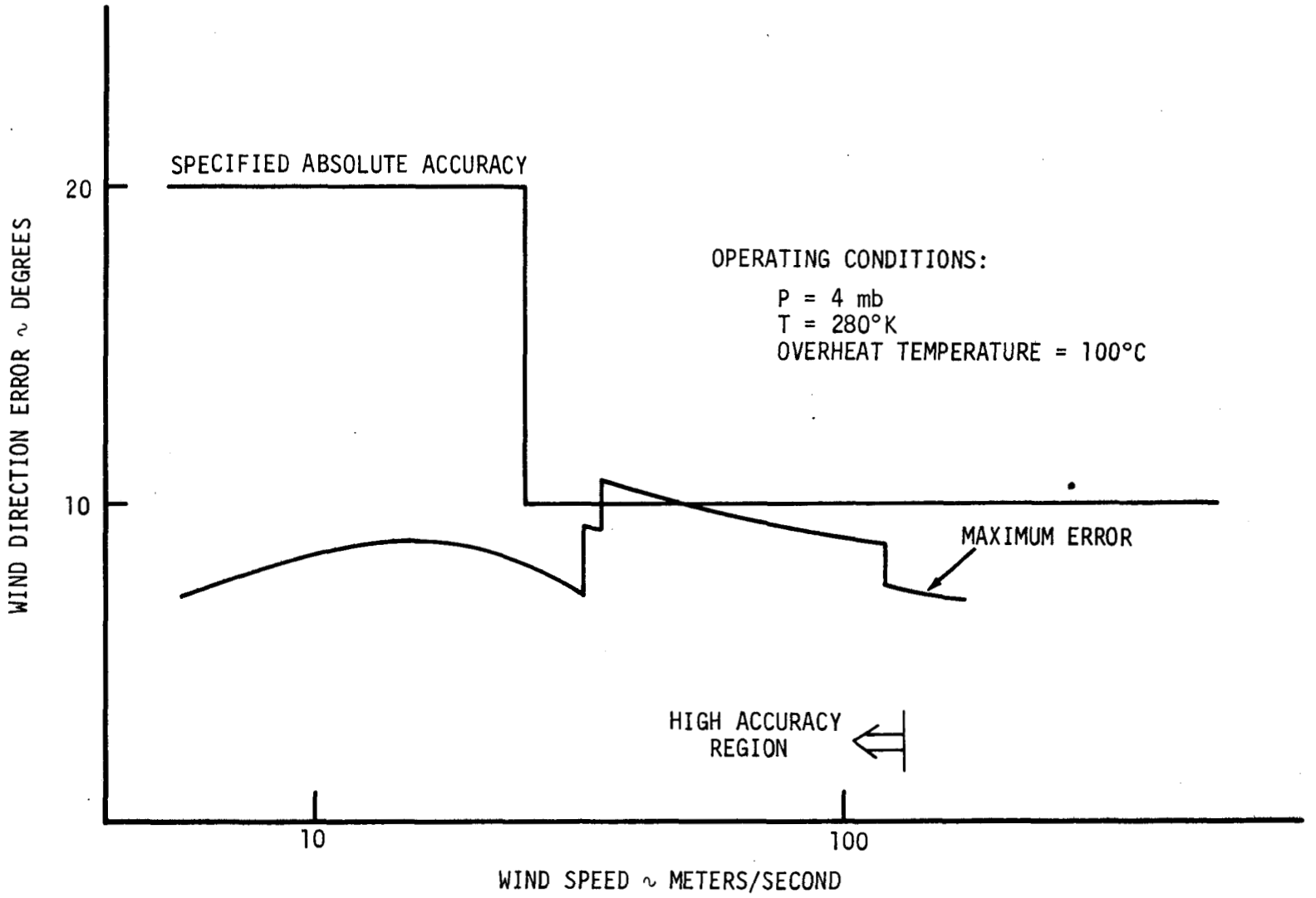

Figure 32. Wind Direction Error Versus Wind Speed: Quadrant Sensor Assistance.

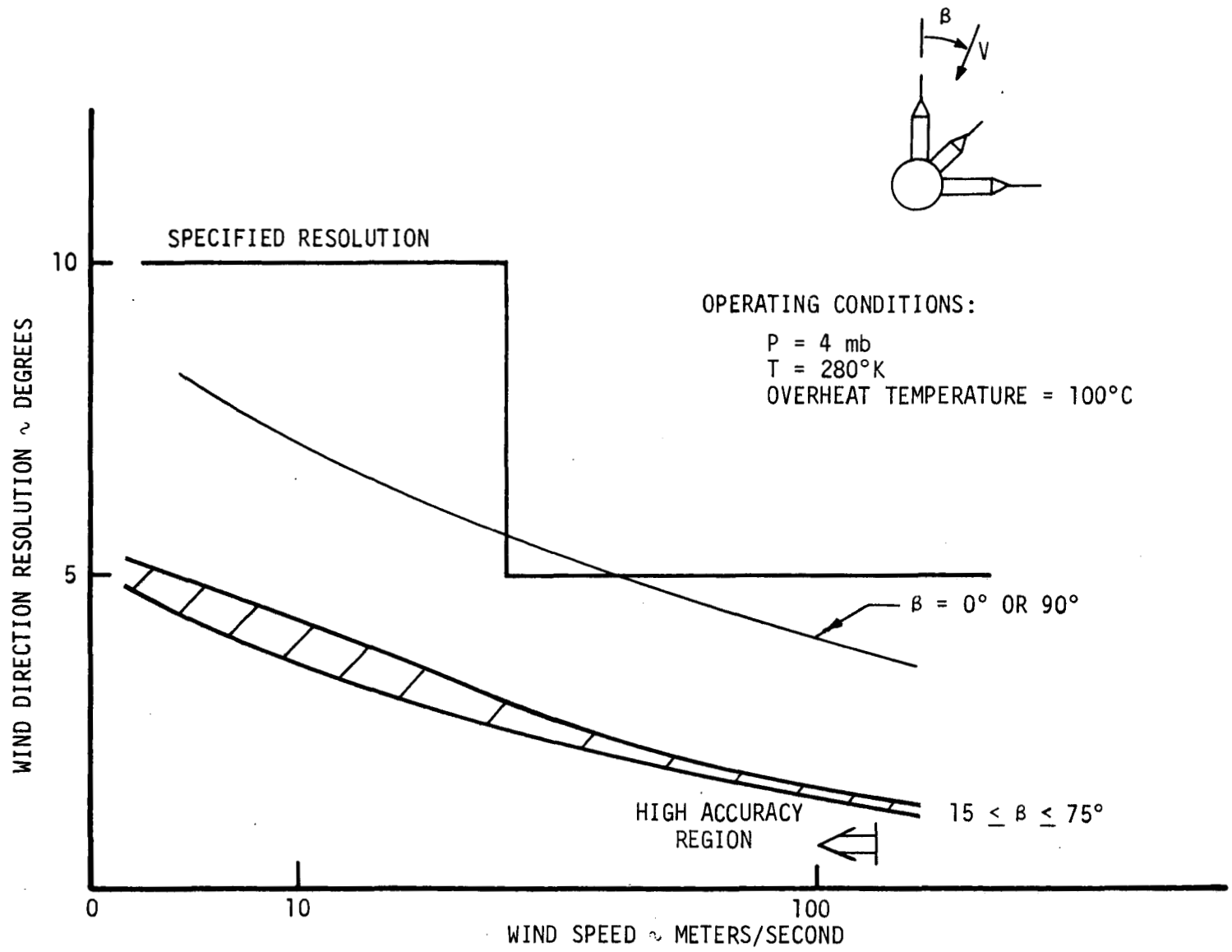

Figure 33. Wind Direction Resolution Versus Wind Speed

APPENDIX A

WIND SENSOR PERFORMANCE DATA

A.1 INTRODUCTION

Only wind sensor V2 (Figure 1) was calibrated in the breadboard model performance tests since there was evidence that V1 had been broken during handling. The performance data are presented in four categories:

a) Variation of Reynolds number and Mach number

b) Variation of rotation angle

c) Variation of array attitude

d) Variation of element overheat temperature

Both raw and reduced (nondimensionalized) data are tabulated. Note that the test section flow blockage effect corrections have been applied to the wind tunnel data (M_∞ and Re_∞).

A.2 PLATINUM FILM RESISTANCE VERSUS TEMPERATURE DATA

Sensor 117 was calibrated in a Rosemount temperature bath and the data analyzed to determine the platinum film resistances at the three temperature settings. Table A1 presents the sensor resistance data where R_T is the total resistance measured including the sensor leads and R_S is the platinum film resistance (see Reference 4 , page 12 for the procedure used in calculating R_S).

Table A1. Sensor 117 Resistance Versus Temperature

T_S (°C)	R_T (ohms)	R_S (ohms)
23	12.408	11.375
115	14.965	13.596
130	15.394	13.970

The R_S values at T_S = 23°C and 130°C were used to calculate the values of β and γ in the relation

$$\alpha T_S^2 + \beta T_S + \gamma = R_S \qquad \text{(A1)}$$

where α was specified on the basis of resistance versus temperature data obtained from the production phase wind sensors. The resulting coefficient values were

$$\alpha = -1.05 \times 10^{-5}$$

$$\beta = 0.02586$$

$$\gamma = 10.7858$$

A.3 SYMBOL DEFINITION

T_o = gas total temperature

P_o = gas total pressure

ΔP_a, ΔP_b, ΔP_c = differences between the total pressure and the test section pressure at the test section axial locations a, b or c (Figure 7)

R_H = operating resistance of the TSI heat flux system. This resistance is the indicated resistance deck reading when the heat flux system is in the "run" mode (Figure 9). Corrected resistances are given.

T_S = sensing element platinum film temperature. T_S is the solution of

$$\alpha T_S^2 + \beta T_S + \gamma = R_S\ (T_S)$$

where $R_S = R_S(T_c) + (R_H - R_c)$ and α, β and γ were obtained from the temperature bath measurements of the wind sensor resistance (discussed above). R_S is the platinum film resistance.

E = heat flux system bridge voltage (Figure 9).

ϕ_o = rotation angle of the wind sensor array. The measurement was made from the plane of symmetry of the pedestal cap supporting the wind array (Figure 5).

M_∞ = freestream Mach number. The measured local Mach number was adjusted to its equivalent freestream value taking into account test section flow blockage effects.

Kn = Knudsen number, ℓ/D, where ℓ is the molecular mean free path and D is the sensing element diameter. ℓ was evaluated at the film temperature = $(T_S + T_A)/2$ where T_A was the adiabatic recovery temperature.

Re_F = film Reynolds number. The pressure and wind speed are the calculated freestream values taking into account the flow blockage effects.

Nu = sensing element Nusselt number corrected to the equivalent continuum value.

D = sensing element diameter.

R_c = room temperature sensor circuit resistance as measured by the TSI heat flux system.

R_B = heat flux system bridge resistance (Figure 9).

R_o = sensing element platinum film ice point resistance.

α = platinum film resistance-temperature coefficient, $\alpha = \frac{1}{R_o}\frac{\Delta R}{\Delta T}$.

A.4 PERFORMANCE DATA TABULATION

Certain of the performance data do not vary during the course of the test and these are listed below:

$$D = 0.05314 \text{ cm}$$
$$R_B = 39.96\ \Omega$$
$$R_c = 13.30\ \Omega$$

VARIATION OF REYNOLDS NUMBER AND MACH NUMBER

T_o (°C)	P_o (torr)	Δp_a (torr)	Δp_b (torr)	Δp_c (torr)	R_H (ohms)	T_S (°C)	E (volts)	ϕ_o (degrees)	ψ (degrees)	M_∞	Kn	Re_f	Nu
23.7	3.94	.00104	.00114	.00123	15.68	121.56	4.637	45	0	2.07×10^{-2}	2.00×10^{-2}	1.42	1.205
24.5	10.94	.00157	.00168	.00182			5.144			1.51×10^{-2}	7.22×10^{-3}	2.87	1.513
24.3	5.54	.00316	.00340	.00368			5.112			3.02×10^{-2}	1.42×10^{-2}	2.91	1.527
24.2	4.19	.00416	.00447	.00484			5.090			3.98×10^{-2}	1.88×10^{-2}	2.90	1.537
24.2	22.30	.00549	.00582	.00629			6.000			1.97×10^{-2}	3.54×10^{-3}	7.63	2.148
24.2	11.53	.01076	.01148	.01234			5.964			3.84×10^{-2}	6.85×10^{-3}	7.68	2.151
24.2	5.93	.02116	.02251	.02420			5.900			7.51×10^{-2}	1.34×10^{-2}	7.70	2.242
24.5	4.03	.03136	.03343	.03544			5.841			1.11×10^{-1}	1.98×10^{-2}	7.71	2.176
24.6	56.60	.00792	.00841	.00892			6.733			1.48×10^{-2}	1.40×10^{-3}	14.51	2.818
23.8	29.10	.01552	.01641	.01750			6.734			2.89×10^{-2}	2.71×10^{-3}	14.58	2.813
23.8	15.00	.03019	.03191	.03408			6.697			5.62×10^{-2}	5.27×10^{-3}	14.56	2.796
24.0	7.75	.05901	.06252	.06677			6.620			1.10×10^{-1}	1.03×10^{-2}	14.59	2.798
24.2	17.80	.12853	.13530	.14350			7.648			1.06×10^{-1}	4.47×10^{-3}	32.42	3.781
25.9	5.57	.4663	.4974	.5369			7.418			3.76×10^{-1}	1.55×10^{-2}	32.76	3.778
24.5	50.60	.16744	.17568	.18576			8.830			7.18×10^{-2}	1.57×10^{-3}	62.40	5.069
24.5	21.74	.4015	.4224	.4474			8.807			1.71×10^{-1}	3.70×10^{-3}	76.12	5.046
25.5	10.54	.883	.940	1.012			8.545			3.76×10^{-1}	8.20×10^{-3}	61.87	4.977
24.9	21.54	.926	.981	1.043			9.493			2.64×10^{-1}	3.83×10^{-3}	93.32	6.069
25.2	12.37	1.895	2.050	2.202			9.260			5.30×10^{-1}	7.60×10^{-3}	93.01	5.892
24.7	36.35	.668	.703	.744			9.840			1.70×10^{-1}	2.21×10^{-3}	104.60	6.431
25.0	13.10	1.999	2.156	2.369			9.389			5.27×10^{-1}	7.16×10^{-3}	98.44	6.036
25.2	14.75	2.234	2.410	2.647			9.634			5.25×10^{-1}	6.36×10^{-3}	110.52	6.367

VARIATION OF ROTATION ANGLE

T_o (°C)	P_o (torr)	Δp_a (torr)	Δp_b (torr)	Δp_c (torr)	R_H (ohms)	T_S (°C)	E (volts)	ϕ_o (degrees)	ψ (degrees)	M_∞	Kn	Re_f	Nu
24.5	21.08	.00084	.00091	.00098	15.68	121.56	5.159	45	0	7.80×10^{-3}	3.75×10^{-3}	2.93	1.523
24.7	21.04	.00084	.00088	.00096			5.120	25		7.87×10^{-3}	3.75×10^{-3}	2.85	1.493
24.7	21.04	.00084	.00088	.00095			4.851	350		7.85×10^{-3}	3.75×10^{-3}	2.78	1.296
24.7	21.03	.00085	.00090	.00097			4.598	325		7.91×10^{-3}	3.76×10^{-3}	2.76	1.131
24.9	21.03	.00090	.00097	.00107			4.428	135		8.36×10^{-3}	3.76×10^{-3}	3.09	1.032
24.7	21.03	.00089	.00100	.00105			4.622	155		8.50×10^{-3}	3.76×10^{-3}	3.07	1.150
24.7	21.02	.00089	.00094	.00104			4.989	190		8.23×10^{-3}	3.76×10^{-3}	2.91	1.393
24.7	21.02	.00089	.00100	.00106			5.110	215		8.41×10^{-3}	3.76×10^{-3}	2.90	1.477
24.7	50.44	.16644	.17450	.1840			8.795	45		7.17×10^{-2}	1.57×10^{-3}	62.05	5.013
24.0	49.30	.1615	.1696	.1800			8.685	25		7.14×10^{-2}	1.61×10^{-3}	60.05	4.839
24.6	48.92	.1596	.1659	.1743			7.895	350		7.08×10^{-2}	1.62×10^{-3}	58.00	3.951
24.1	48.92	.1615	.1693	.1788			6.655	325		7.12×10^{-2}	1.62×10^{-3}	57.90	2.723
24.2	49.18	.1744	.1814	.1838			7.180	135		7.57×10^{-2}	1.64×10^{-3}	61.71	3.210
24.1	49.16	.1730	.1783	.1791			7.514	155		7.43×10^{-2}	1.61×10^{-3}	61.77	3.544
24.0	49.20	.1726	.1768	.1772			8.396	190		7.38×10^{-2}	1.61×10^{-3}	61.10	4.499
24.3	48.80	.1727	.1788	.1803			8.718	215		7.39×10^{-2}	1.62×10^{-3}	60.17	4.904
24.1	34.34	.6373	.6699	.7099			9.731	45		1.71×10^{-1}	2.34×10^{-3}	99.28	6.289
24.0	34.16	.6287	.6561	.6930			9.634	25		1.70×10^{-1}	2.35×10^{-3}	97.05	6.156
24.1	34.00	.6228	.6472	.6813			8.710	350		1.69×10^{-1}	2.37×10^{-3}	94.56	4.966
23.8	34.00	.6300	.6608	.7008			7.262	325		1.70×10^{-1}	2.37×10^{-3}	94.08	3.302
24.1	34.15	.6821	.7090	.7159			7.998	135		1.79×10^{-1}	2.36×10^{-3}	101.34	4.132
24.0	34.15	.6772	.6972	.6988			8.267	155		1.77×10^{-1}	2.36×10^{-3}	100.48	4.424
24.1	34.08	.6756	.6924	.6925			9.248	190		1.77×10^{-1}	2.36×10^{-3}	99.39	5.647
24.0	34.07	.6789	.7044	.7080			9.682	215		1.77×10^{-1}	2.36×10^{-3}	98.54	6.211
24.2	6.77	.00027	.00030	.00032			4.472	45		8.10×10^{-3}	1.17×10^{-2}	.95	1.071
24.5	6.80	.00027	.00030	.00034			4.318	350		8.06×10^{-3}	1.16×10^{-2}	.92	.976
24.5	6.80	.00028	.00032	.00034			4.194	155		8.46×10^{-3}	1.16×10^{-2}	.99	.906
24.5	6.80	.00030	.00034	.00035			4.375	190		8.70×10^{-3}	1.16×10^{-2}	.99	1.020
24.6	42.38	.00284	.00307	.00330			6.004	45		1.03×10^{-2}	1.86×10^{-3}	7.62	2.148
24.5	42.22	.00279	.00295	.00318			5.546	350		1.02×10^{-2}	1.87×10^{-3}	7.20	1.781

VARIATION OF ROTATION ANGLE (Continued)

T_o (°C)	P_o (torr)	Δp_a (torr)	Δp_b (torr)	Δp_c (torr)	R_H (ohms)	T_S (°C)	E (volts)	ϕ_o (degrees)	ψ (degrees)	M_∞	Kn	Re_f	Nu
24.3	42.47	.00306	.00324	.00334	15.68	121.56	5.210	155	0	1.08×10^{-2}	1.86×10^{-3}	7.80	1.533
24.3	42.47	.00307	.00324	.00334			5.773	190		1.07×10^{-2}	1.86×10^{-3}	7.68	1.947
24.1	30.77	.5757	.6060	.6424			9.494	45		1.72×10^{-1}	2.62×10^{-3}	89.38	5.984
24.0	30.80	.5646	.5873	.6196			8.540	350		1.69×10^{-1}	2.61×10^{-3}	85.74	4.744
23.8	30.87	.6154	.6343	.6355			8.099	155		1.78×10^{-1}	2.61×10^{-3}	91.17	4.251
23.8	30.87	.6124	.6281	.6282			9.092	190		1.77×10^{-1}	2.61×10^{-3}	90.25	5.460
25.1	25.86	1.1135	1.1700	1.255			9.885	45		2.63×10^{-1}	3.19×10^{-3}	112.00	6.577
24.7	25.55	1.083	1.130	1.195			8.897	350		2.60×10^{-1}	3.23×10^{-3}	106.14	5.224
25.0	25.33	1.1825	1.220	1.225			8.418	155		2.75×10^{-1}	3.27×10^{-3}	111.81	4.630
24.9	25.30	1.1790	1.2090	1.2095			9.421	190	1.5	2.73×10^{-1}	3.27×10^{-3}	110.75	5.917

VARIATION OF ARRAY ATTITUDE

T_o (°C)	P_o (torr)	Δp_a (torr)	Δp_b (torr)	Δp_c (torr)	R_H (ohms)	T_S (°C)	E (volts)	ϕ_o (degrees)	ψ (degrees)	M_∞	Kn	Re_f	Nu
24.6	56.35	.00795	.00843	.00895	15.68	121.56	6.725	45	0	1.49×10^{-2}	1.40×10^{-3}	14.50	2.813
24.1	56.35	.00799	.00845	.00898			6.741		1.5	1.49×10^{-2}	1.40×10^{-3}	14.51	2.807
24.0	56.35	.00802	.00849	.00907			6.743		3	1.49×10^{-2}	1.40×10^{-3}	14.54	2.807
24.0	56.33	.00805	.00855	.00911			6.741		9	1.50×10^{-2}	1.40×10^{-3}	14.46	2.804
24.0	56.30	.00826	.00879	.00923			6.730		25	1.52×10^{-2}	1.40×10^{-3}	14.36	2.783
24.0	56.30	.00791	.00840	.00892			6.748		358.5	1.49×10^{-2}	1.40×10^{-3}	14.51	2.809
24.0	56.30	.00790	.00838	.00890			6.749		357	1.48×10^{-2}	1.40×10^{-3}	14.52	2.810
23.8	56.30	.00785	.00830	.00884			6.743		351	1.48×10^{-2}	1.40×10^{-3}	14.59	2.803
24.0	56.30	.00779	.00817	.00862			6.723		336	1.47×10^{-2}	1.40×10^{-3}	14.65	2.791
23.7	56.00	.00785	.00827	.00876			6.687	25	0	1.48×10^{-2}	1.41×10^{-3}	14.17	2.729
23.7	56.00	.00783	.00827	.00877			6.685		1.5	1.48×10^{-2}	1.41×10^{-3}	14.15	2.727
23.7	56.00	.00783	.00829	.00879			6.684		3	1.48×10^{-2}	1.41×10^{-3}	14.15	2.726
23.7	56.00	.00787	.00835	.00884			6.676		9	1.48×10^{-2}	1.41×10^{-3}	14.10	2.719
23.7	56.00	.00809	.00861	.00909			6.672		25	1.51×10^{-2}	1.41×10^{-3}	14.04	2.715
23.7	56.00	.00783	.00826	.00876			6.688		358.5	1.48×10^{-2}	1.41×10^{-3}	14.19	2.729
23.7	56.00	.00782	.00823	.00870			6.694		357	1.47×10^{-2}	1.41×10^{-3}	14.18	2.735
23.7	56.00	.00777	.00815	.00864			6.700		351	1.47×10^{-2}	1.41×10^{-3}	14.25	2.767
23.8	56.01	.00773	.00806	.00847			6.714		336	1.46×10^{-2}	1.41×10^{-3}	14.35	2.777
24.6	56.70	.00775	.00818	.00861			6.147	350	0	1.45×10^{-2}	1.39×10^{-3}	13.88	2.272
24.5	56.66	.00772	.00812	.00860			6.158		1.5	1.45×10^{-2}	1.40×10^{-3}	13.83	2.278
24.5	56.62	.00774	.00815	.00863			6.166		3	1.46×10^{-2}	1.40×10^{-3}	13.83	2.285
24.5	56.57	.00776	.00822	.00871			6.176		9	1.46×10^{-2}	1.39×10^{-3}	13.79	2.292
24.3	56.38	.00788	.00842	.00882			6.234		25	1.48×10^{-2}	1.40×10^{-3}	13.59	2.348
24.3	56.18	.00764	.00802	.00848			6.158		358.5	1.45×10^{-2}	1.41×10^{-3}	13.74	2.275
24.2	56.10	.00761	.00793	.00844			6.166		357	1.44×10^{-2}	1.41×10^{-3}	13.67	2.278
24.2	56.06	.00757	.00786	.00836			6.203		351	1.44×10^{-2}	1.41×10^{-3}	13.71	2.329
24.2	56.04	.00758	.00783	.00825			6.332		336	1.44×10^{-2}	1.41×10^{-3}	13.86	2.414
24.5	56.67	.00785	.00831	.00883			5.420	325	0	1.46×10^{-2}	1.39×10^{-3}	13.79	1.693
24.3	56.66	.00786	.00834	.00886			5.412		1.5	1.47×10^{-2}	1.39×10^{-3}	13.78	1.685
24.2	56.65	.00785	.00833	.00884			5.410		3	1.46×10^{-2}	1.39×10^{-3}	13.75	1.681

VARIATION OF ARRAY ATTITUDE (Continued)

T_o (°C)	P_o (torr)	Δp_a (torr)	Δp_b (torr)	Δp_c (torr)	R_H (ohms)	T_S (°C)	E (volts)	ϕ_o (degrees)	ψ (degrees)	M_∞	Kn	Re_f	Nu
24.2	56.64	.00792	.00844	.00894	15.68	121.56	5.436	325	9	1.48×10^{-2}	1.39×10^{-3}	13.72	1.707
24.2	56.62	.00817	.00871	.00920			5.778		25	1.50×10^{-2}	1.40×10^{-3}	13.64	1.964
24.2	56.65	.00787	.00834	.00885			5.436		358.5	1.47×10^{-2}	1.39×10^{-3}	13.84	1.704
24.2	56.65	.00785	.00831	.00882			5.467		357	1.46×10^{-2}	1.39×10^{-3}	13.84	1.724
24.2	56.62	.00778	.00820	.00872			5.595		351	1.45×10^{-2}	1.39×10^{-3}	13.84	1.821
24.2	56.61	.00774	.00810	.00854			5.982		336	1.44×10^{-2}	1.39×10^{-3}	13.99	2.139
23.7	56.41	.00845	.00888	.00915			5.820	135	0	1.54×10^{-2}	1.40×10^{-3}	14.93	1.989
23.7	56.39	.00847	.00888	.00914			5.765		1.5	1.54×10^{-2}	1.40×10^{-3}	14.91	1.945
23.6	56.38	.00848	.00888	.00912			5.735		3	1.54×10^{-2}	1.40×10^{-3}	14.89	1.920
23.7	56.36	.00854	.00888	.00910			5.480		9	1.55×10^{-2}	1.40×10^{-3}	14.83	1.723
23.7	56.36	.00856	.00882	.00904			5.780		25	1.54×10^{-2}	1.40×10^{-3}	14.65	1.957
23.7	56.34	.00845	.00890	.00918			5.875		358.5	1.55×10^{-2}	1.40×10^{-3}	14.95	2.033
23.7	56.32	.00843	.00892	.00922			5.900		357	1.55×10^{-2}	1.40×10^{-3}	14.98	2.053
23.7	56.31	.00837	.00900	.00934			5.610		351	1.56×10^{-2}	1.40×10^{-3}	15.08	1.824
23.7	56.30	.00811	.00870	.00942			5.810		336	1.53×10^{-2}	1.40×10^{-3}	15.64	2.029
23.7	56.29	.00838	.00872	.00887			5.985	155	0	1.53×10^{-2}	1.40×10^{-3}	14.70	2.121
23.6	56.28	.00838	.00872	.00885			5.980		1.5	1.53×10^{-2}	1.40×10^{-3}	14.62	2.115
23.6	56.26	.00840	.00871	.00885			5.965		3	1.53×10^{-2}	1.40×10^{-3}	14.62	2.104
23.6	56.26	.00843	.00870	.00882			5.942		9	1.53×10^{-2}	1.40×10^{-3}	14.63	2.085
23.7	56.25	.00844	.00864	.00876			6.040		25	1.54×10^{-2}	1.40×10^{-3}	14.52	2.172
23.6	56.25	.00838	.00874	.00888			5.995		358.5	1.54×10^{-2}	1.40×10^{-3}	14.72	2.127
23.6	56.24	.00836	.00875	.00890			5.990		357	1.54×10^{-2}	1.40×10^{-3}	14.70	2.123
23.7	56.22	.00831	.00882	.00910			5.960		351	1.55×10^{-2}	1.40×10^{-3}	14.89	2.101
23.7	56.21	.00804	.00863	.00930			6.113		336	1.50×10^{-2}	1.40×10^{-3}	14.11	2.228
23.6	56.19	.00837	.00868	.00880			6.480	190	0	1.53×10^{-2}	1.40×10^{-3}	14.55	2.543
23.6	56.17	.00834	.00864	.00877			6.477		1.5	1.54×10^{-2}	1.40×10^{-3}	14.72	2.537
23.6	56.16	.00835	.00864	.00875			6.477		3	1.53×10^{-2}	1.40×10^{-3}	14.46	2.539
23.6	56.14	.00839	.00861	.00872			6.476		9	1.52×10^{-2}	1.40×10^{-3}	14.40	2.536
23.6	56.13	.00839	.00857	.00868			6.520		25	1.52×10^{-2}	1.40×10^{-3}	14.26	2.576
23.6	56.11	.00834	.00867	.00881			6.481		358.5	1.53×10^{-2}	1.41×10^{-3}	14.51	2.543

VARIATION OF ARRAY ATTITUDE (Continued)

T_o (°C)	P_o (torr)	Δp_a (torr)	Δp_b (torr)	Δp_c (torr)	R_H (ohms)	T_S (°C)	E (volts)	ϕ_o (degrees)	ψ (degrees)	M_∞	Kn	Re_f	Nu
23.6	56.10	.00833	.00868	.00882	15.68	121.56	6.485	190	357	1.53×10^{-2}	1.41×10^{-3}	14.53	2.546
23.6	56.08	.00822	.00873	.00905			6.490		351	1.54×10^{-2}	1.41×10^{-3}	14.64	2.550
23.6	56.07	.00791	.00851	.00909			6.515		336	1.52×10^{-2}	1.41×10^{-3}	14.78	2.573
25.2	56.44	.00843	.00882	.00904			6.664	215	0	1.50×10^{-2}	1.40×10^{-3}	14.24	2.763
25.0	.5639	.00842	.00880	.00902			6.663		1.5	1.52×10^{-2}	1.40×10^{-3}	14.32	2.734
24.7	56.28	.00842	.00880	.00903			6.662		3	1.52×10^{-2}	1.40×10^{-3}	14.29	2.727
24.5	56.37	.00850	.00883	.00905			6.665		9	1.53×10^{-2}	1.40×10^{-3}	14.28	2.724
24.5	56.35	.00851	.00876	.00892			6.649		25	1.52×10^{-2}	1.40×10^{-3}	14.12	2.709
24.5	56.33	.00842	.00884	.00909			6.678		358.5	1.53×10^{-2}	1.40×10^{-3}	14.38	2.736
24.5	56.33	.00841	.00885	.00911			6.679		357	1.53×10^{-2}	1.40×10^{-3}	14.40	2.736
24.4	56.32	.00831	.00887	.00925			6.683		351	1.53×10^{-2}	1.40×10^{-3}	14.48	2.739
24.4	56.32	.00803	.00862	.00934			6.676		336	1.51×10^{-2}	1.40×10^{-3}	14.59	2.734
24.5	10.06	.00040	.00044	.00048			4.703	45	0	8.05×10^{-3}	7.86×10^{-3}	1.41	1.221
24.5	10.06	.00041	.00045	.00049			4.698		1.5	8.14×10^{-3}	7.86×10^{-3}	1.43	1.215
24.3	10.07	.00042	.00046	.00051			4.703		3	8.22×10^{-3}	7.85×10^{-3}	1.45	1.216
24.3	10.18	.00040	.00045	.00049			4.698		12	8.09×10^{-3}	7.76×10^{-3}	1.41	1.213
24.3	10.12	.00039	.00043	.00047			4.709		358.5	7.93×10^{-3}	7.81×10^{-3}	1.41	1.220
24.3	10.05	.00040	.00043	.00047			4.709		357				
24.3	10.04	.00041	.00044	.00048			4.713		348	8.40×10^{-3}	7.84×10^{-3}	1.37	1.222
24.2	10.03	.00038	.00041	.00045			4.494	350	0	7.76×10^{-3}	7.88×10^{-3}	1.31	1.086
24.3	10.03	.00037	.00040	.00045			4.490		1.5	7.68×10^{-3}	7.88×10^{-3}	1.36	1.086
24.3	10.06	.00038	.00042	.00046			4.486		3	7.86×10^{-3}	7.85×10^{-3}	1.38	1.086
24.3	10.04	.00039	.00044	.00048			4.480		12	8.06×10^{-3}	7.87×10^{-3}	1.38	1.072
24.3	10.07	.00038	.00040	.00044			4.487		358.5	7.65×10^{-3}	7.85×10^{-3}	1.30	1.083
24.3	10.08	.00036	.00039	.00043			4.485		357	7.55×10^{-3}	7.84×10^{-3}	1.28	1.081
24.4	10.09	.00037	.00040	.00043			4.508		348	7.64×10^{-3}	7.83×10^{-3}	1.32	1.094
24.5	10.06	.00034	.00044	.00047			4.326	155	0	8.15×10^{-3}	7.86×10^{-3}	1.42	.981
24.5	10.05	.00039	.00043	.00046			4.336		1.5	8.06×10^{-3}	7.86×10^{-3}	1.39	.986
24.5	10.04	.00041	.00045	.00047			4.341		3	8.26×10^{-3}	7.87×10^{-3}	1.41	.989
24.5	10.04	.00042	.00045	.00047			4.377		12	8.26×10^{-3}	7.87×10^{-3}	1.40	1.008

VARIATION OF ARRAY ATTITUDE (Continued)

T_o (°C)	P_o (torr)	Δp_a (torr)	Δp_b (torr)	Δp_c (torr)	R_H (ohms)	T_S (°C)	E (volts)	ϕ_o (degrees)	ψ (degrees)	M_∞	Kn	Re_f	Nu
24.5	10.04	.00040	.00044	.00047	15.68	121.56	4.324	155	358.5	8.16×10^{-3}	7.87×10^{-3}	1.41	.978
24.5	10.04	.00039	.00042	.00045			4.318		357	7.98×10^{-3}	7.87×10^{-3}	1.38	.975
24.6	10.04	.00038	.00042	.00045			4.313		348	7.98×10^{-3}	7.87×10^{-3}	1.40	.972
24.2	10.00	.00042	.00046	.00048			4.581	190	0	8.34×10^{-3}	7.90×10^{-3}	1.40	1.132
24.2	10.00	.00042	.00046	.00048			4.581		1.5	8.34×10^{-3}	7.90×10^{-3}	1.40	1.131
24.3	10.00	.00042	.00046	.00049			4.581		3	8.34×10^{-3}	7.90×10^{-3}	1.40	1.132
24.3	10.00	.00045	.00047	.00049			4.582		12	8.43×10^{-3}	7.90×10^{-3}	1.41	1.133
24.3	9.99	.00043	.00046	.00049			4.583		358.5	8.35×10^{-3}	7.91×10^{-3}	1.41	1.134
24.3	9.95	.00041	.00044	.00048			4.584		357	8.18×10^{-3}	7.94×10^{-3}	1.37	1.134
24.2	10.00	.00040	.00044	.00047			4.591		348	8.16×10^{-3}	7.90×10^{-3}	1.40	1.139
24.2	50.34	.04523	.04753	.05035			7.766	45	0	3.74×10^{-2}	1.57×10^{-3}	32.52	3.861
24.0	50.31	.04526	.04759	.05039			7.768		1.5	3.74×10^{-2}	1.57×10^{-3}	32.48	3.849
23.8	50.31	.04530	.04767	.05044			7.769		3	3.75×10^{-2}	1.57×10^{-3}	32.45	3.845
23.7	50.31	.04581	.04843	.05078			7.773		12	3.78×10^{-2}	1.57×10^{-3}	32.35	3.846
23.7	50.29	.04516	.04741	.05023			7.783		358.5	3.74×10^{-2}	1.57×10^{-3}	32.57	3.855
23.7	50.31	.04509	.04731	.05014			7.786		357	3.73×10^{-2}	1.57×10^{-3}	32.59	3.860
23.7	50.29	.04477	.04671	.04953			7.798		348	3.71×10^{-2}	1.57×10^{-3}	32.80	3.872
23.7	50.27	.04444	.04627	.04872			7.088	350	0	3.68×10^{-2}	1.57×10^{-3}	31.18	3.113
23.7	50.27	.04449	.04636	.04885			7.087		1.5	3.69×10^{-2}	1.57×10^{-3}	31.17	3.111
23.6	50.27	.04452	.04647	.04897			7.087		3	3.69×10^{-2}	1.57×10^{-3}	31.16	3.111
23.6	50.88	.04482	.04711	.04962			7.105		12	3.70×10^{-2}	1.55×10^{-3}	31.28	3.126
23.6	50.25	.04434	.04610	.04856			7.102		358.5	3.68×10^{-2}	1.57×10^{-3}	31.16	3.124
23.6	50.25	.04431	.04604	.04849			7.110		357	3.68×10^{-2}	1.57×10^{-3}	31.18	3.131
23.5	50.21	.04409	.04553	.04783			7.173		348	3.66×10^{-2}	1.57×10^{-3}	31.24	3.188
24.3	49.79	.04743	.04902	.04939			6.738	155	0	3.87×10^{-2}	1.59×10^{-3}	32.68	2.798
24.1	49.77	.04740	.04885	.04926			6.742		1.5	3.86×10^{-2}	1.59×10^{-3}	32.62	2.796
24.0	49.75	.04740	.04874	.04914			6.745		3	3.86×10^{-2}	1.59×10^{-3}	32.57	2.796
23.8	49.73	.04744	.04844	.04883			6.778		12	3.85×10^{-2}	1.59×10^{-3}	32.38	2.824
23.8	49.71	.04729	.04900	.04938			6.770		358.5	3.87×10^{-2}	1.59×10^{-3}	32.67	2.816
23.7	49.69	.04718	.04894	.04946			6.778		357	3.87×10^{-2}	1.59×10^{-3}	32.68	2.821

VARIATION OF ARRAY ATTITUDE (Continued)

T_o (°C)	P_o (torr)	Δp_a (torr)	Δp_b (torr)	Δp_c (torr)	R_H (ohms)	T_S (°C)	E (volts)	ϕ_o (degrees)	ψ (degrees)	M_∞	Kn	Re_f	Nu
23.7	49.66	.04662	.04930	.05028	15.68	121.56	6.780	155	348	3.89×10^{-2}	1.59×10^{-3}	32.88	2.823
23.7	49.74	.04707	.04841	.04868			7.458	190	0	3.84×10^{-2}	1.59×10^{-3}	39.79	3.484
23.7	49.71	.04713	.04838	.04859			7.457		1.5	3.84×10^{-2}	1.59×10^{-3}	32.21	3.484
23.7	49.70	.04713	.04829	.04855			7.452		3	3.84×10^{-2}	1.59×10^{-3}	32.16	3.480
23.7	49.68	.04713	.04790	.04815			7.448		12	3.89×10^{-2}	1.59×10^{-3}	32.20	3.477
24.3	42.65	.00308	.00332	.00353			5.692	90	0	1.08×10^{-2}	1.85×10^{-3}	8.04	1.911
24.2	42.65	.00306	.00330	.00351			5.651		1.5	1.08×10^{-2}	1.85×10^{-3}	8.00	1.866
24.1	42.66	.00307	.00331	.00352			5.592		3	1.08×10^{-2}	1.85×10^{-3}	8.00	1.821
24.1	42.60	.00313	.00336	.00354			5.752		12	1.09×10^{-2}	1.85×10^{-3}	7.95	1.942
24.1	42.59	.00304	.00329	.00350			5.721		358.5	1.08×10^{-2}	1.85×10^{-3}	8.01	1.925
24.1	42.50	.00303	.00328	.00351			5.716		357	1.08×10^{-2}	1.86×10^{-3}	8.04	1.923
24.1	42.44	.00293	.00323	.00350			5.678		348	1.07×10^{-2}	1.86×10^{-3}	8.10	1.883
24.2	31.12	.6142	.6544	.6817			8.931		0	1.79×10^{-1}	2.59×10^{-3}	92.75	5.233
23.8	31.10	.6147	.6542	.6804			8.937		1.5	1.79×10^{-1}	2.59×10^{-3}	93.46	5.213
24.3	30.57	.6043	.6420	.6656			8.802		3	1.79×10^{-1}	2.64×10^{-3}	91.62	5.057
24.3	30.55	.6113	.6454	.6655			8.888		12	1.79×10^{-1}	2.64×10^{-3}	91.31	5.192
24.3	30.79	.6046	.6443	.6733			8.912		358.5	1.78×10^{-1}	2.62×10^{-3}	92.72	5.222
24.1	30.80	.6028	.6432	.6736			8.928		357	1.78×10^{-1}	2.62×10^{-3}	92.88	5.233
24.2	30.61	.5923	.6334	.6740			8.960		348	1.77×10^{-1}	2.63×10^{-3}	93.83	5.278

VARIATION OF ELEMENT OVERHEAT TEMPERATURE

T_o (°C)	P_o (torr)	Δp_a (torr)	Δp_b (torr)	Δp_c (torr)	R_H (ohms)	T_S (°C)	E (volts)	ϕ_o (degrees)	ψ (degrees)	M_∞	Kn	Re_f	Nu
24.2	21.24	.00077	.00082	.00089	14.73	82.52	3.915	20	0	7.56×10^{-3}	3.42×10^{-3}	3.09	1.535
24.1	21.24	.00077	.00082	.00089	15.20	101.15	4.569			7.56×10^{-3}	3.56×10^{-3}	2.91	1.525
24.1	21.24	.00079	.00084	.00090	15.68	121.56	5.151			7.65×10^{-3}	3.72×10^{-3}	2.78	1.504
24.0	21.24	.00079	.00084	.00090	16.16	142.35	5.718			7.65×10^{-3}	3.87×10^{-3}	2.62	1.496
24.0	21.23	.00077	.00082	.00089	16.63	163.10	6.205			7.55×10^{-3}	4.02×10^{-3}	2.46	1.478
24.0	21.22	.00077	.00083	.00090	14.73	82.52	3.955	45		7.61×10^{-3}	3.42×10^{-3}	3.16	1.569
24.0	21.22	.00078	.00084	.00092	15.20	101.15	4.628			7.66×10^{-3}	3.57×10^{-3}	3.01	1.570
24.0	21.22	.00078	.00084	.00092	15.68	121.56	5.217			7.66×10^{-3}	3.72×10^{-3}	2.84	1.549
24.0	21.22	.00076	.00083	.00091	16.16	142.35	5.776			7.61×10^{-3}	3.89×10^{-3}	2.67	1.545
24.1	21.22	.00076	.00083	.00091	16.63	163.10	6.281			7.61×10^{-3}	4.03×10^{-3}	2.52	1.519
23.5	48.60	.15932	.16587	.17485	14.73	82.52	6.641	20		7.11×10^{-2}	1.50×10^{-3}	66.10	5.000
23.5	48.59	.15936	.16586	.17484	15.20	101.15	7.708			7.12×10^{-2}	1.56×10^{-3}	62.22	4.921
23.5	48.59	.15932	.16582	.17480	15.68	121.56	8.646			7.11×10^{-2}	1.63×10^{-3}	58.77	4.806
23.8	48.99	.16092	.16740	.17638	16.16	142.35	9.524			7.12×10^{-2}	1.68×10^{-3}	55.87	4.721
23.8	48.99	.16092	.16740	.17638	16.63	163.10	10.33			7.12×10^{-2}	1.75×10^{-3}	52.79	4.619
23.5	48.95	.16260	.17062	.18059	14.73	82.52	6.788	45		7.19×10^{-2}	1.48×10^{-3}	68.11	5.239
23.8	48.91	.16305	.17115	.18095	15.20	101.15	7.853			7.21×10^{-2}	1.55×10^{-3}	64.14	5.141
23.6	48.94	.16294	.17106	.18095	15.68	121.56	8.817			7.20×10^{-2}	1.62×10^{-3}	60.62	5.016
23.5	48.94	.16300	.17104	.18090	16.16	142.35	9.717			7.20×10^{-2}	1.68×10^{-3}	57.27	4.955
23.5	48.94	.16296	.17100	.18096	16.63	163.10	10.53			7.20×10^{-2}	1.75×10^{-3}	54.09	4.832
24.0	6.72	.00028	.00031	.00034	14.73	82.52	3.404			8.26×10^{-3}	1.08×10^{-2}	1.09	1.103
24.0	6.72	.00028	.00031	.00034	15.68	121.56	4.506			8.26×10^{-3}	1.17×10^{-2}	.97	1.096
24.0	6.72	.00024	.00027	.00031	16.63	163.10	5.443			7.71×10^{-3}	1.27×10^{-2}	.82	1.078
24.3	42.60	.00286	.00308	.00331	14.73	82.52	4.594			1.03×10^{-2}	1.70×10^{-3}	8.61	2.246
24.1	42.60	.00286	.00308	.00331	15.68	121.56	6.049			1.03×10^{-2}	1.85×10^{-3}	7.66	2.201
24.0	42.60	.00287	.00309	.00332	16.63	163.10	7.264			1.04×10^{-2}	2.01×10^{-3}	6.84	2.122
24.0	30.80	.5709	.6003	.6366	14.73	82.52	7.333			1.71×10^{-1}	2.40×10^{-3}	100.12	6.279
23.8	30.80	.5709	.6003	.6366	15.68	121.56	9.552			1.71×10^{-1}	2.61×10^{-3}	89.05	6.038
23.8	30.78	.5703	.5997	.6360	16.63	163.10	11.36			1.71×10^{-1}	2.83×10^{-3}	79.25	5.741
23.8	56.37	.00795	.00844	.00895	15.20	101.15	6.012			1.49×10^{-2}	1.34×10^{-3}	15.35	2.863

VARIATION OF ELEMENT OVERHEAT TEMPERATURE (Continued)

T_o (°C)	P_o (torr)	Δp_a (torr)	Δp_b (torr)	Δp_c (torr)	R_H (ohms)	T_S (°C)	E (volts)	ϕ_o (degrees)	ψ (degrees)	M_∞	Kn	Re_f	Nu
23.7	56.36	.00791	.00842	.00895	15.68	121.56	6.769	45	0	1.49×10^{-2}	1.40×10^{-3}	14.52	2.821
23.6	56.36	.00790	.00838	.00890	16.16	142.35	7.490	↓	↓	1.48×10^{-2}	1.46×10^{-3}	13.64	2.780
23.5	15.04	.03019	.03192	.03410	15.20	101.15	5.969	↓	↓	5.61×10^{-2}	5.04×10^{-3}	15.46	2.871
23.6	15.04	.03020	.03192	.03410	15.68	121.56	6.712	↓	↓	5.61×10^{-2}	5.26×10^{-3}	14.59	2.805
23.6	15.03	.03020	.03193	.03411	16.16	142.35	7.404	↓	↓	5.61×0^{-2}	5.48×10^{-3}	13.78	2.780
23.3	7.82	.05916	.06269	.06706	15.20	101.15	5.920	↓	↓	1.09×10^{-1}	9.74×10^{-3}	15.54	2.865
23.6	7.82	.05924	.06271	.06706	15.68	121.56	6.648	↓	↓	1.09×10^{-1}	1.02×10^{-2}	14.69	2.818
23.7	7.82	.05923	.06269	.06702	16.16	142.35	7.332	↓	↓	1.09×10^{-1}	1.06×10^{-2}	13.84	2.774

SECTION III

QUADRANT SENSOR

TABLE OF CONTENTS

	Page
1. SYSTEM DESCRIPTION	1
1.1 Sensor Output	1
2. OPERATION OF SENSOR	4
2.1 Operation as a Quadrant Sensor	4
2.2 Operation as a Wind Direction Sensor	5
3. PERFORMANCE TESTING OF QUADRANT SENSOR	7
3.1 Test Description	7
3.2 Test Procedure	7
3.2.1 Range of Test Conditions	7
3.3 Test Results	8
3.3.1 Primary Data Base	8
3.3.2 CO_2 Results	8
3.3.3 High Mach Number Results	8
3.3.4 Variable Overheat Results	9
3.3.5 Angle of Attack Data	9
4. PERFORMANCE VERIFICATION	11
4.1 Performance Requirements	11
4.2 Performance Analysis	11
4.2.1 Range	11
4.2.2 Calibration	11
4.2.3 Response Time	12
4.2.4 Warm Up Time	12
4.2.5 Attitude	15
4.2.6 Self-Heating	15
4.2.7 Direction Accuracy	16
4.2.8 Direction Resolution	32

1. SYSTEM DESCRIPTION

The wind direction as determined by the wind sensors has an inherent four-fold ambiguity. In order to overcome this difficulty, an approximate but unambiguous secondary wind direction measurement is necessary. The quadrant sensor obtains this secondary measurement by locating the thermal wake of a heated vertical cylinder. This is accomplished by determining the temperature distribution about the cylinder with four chromel-constantan thermocouples. The geometry and critical dimensions of the quadrant sensor are presented in Figure 1.

A block diagram of the quadrant sensor is shown in Figure 2. The thermocouple electronics are essentially identical to those for the temperature sensor, and the heater controller and temperature readout are similar to those used for the wind sensor. Note that opposing thermocouple junctions are connected in series so that each pair measures the temperature difference across the sensor. This eliminates the need for a reference junction temperature measurement.

1.1 SENSOR OUTPUT

Typical results of performance testing on a breadboard model of the quadrant sensor are shown in Figures 3 and 4. The plots show the output of each thermocouple pair at 100°C overheat, as a function of wind direction (in quadrant sensor coordinates), with a zero azimuth line defined by one thermocouple pair, designated arbitrarily as pair 1. Alternately, in Figure 3 consider that the wind vector is fixed along the 0° ray and the quadrant sensor free to rotate. For 0° orientation of the quadrant sensor, the thermocouple junctions forming pair number 1 are located along the 0°-180° ray, one on either side of the center. The junctions forming pair number 2 are located along the 90°-270° ray. The outputs of the two thermocouple pairs are both indicated by points along the 0° ray (marked 1 and 2 in Figure 3). If the quadrant sensor is rotated to 30° (for example) with respect to the wind, the thermocouple junctions forming pair 1 will lie along the 30°-210° line, while pair 2 will lie along the 120°-300° line. The output from both pairs, however, is indicated by points located along the 30° ray (marked 1' and 2' in Figure 3).

As the quadrant sensor is rotated past 180° with respect to the wind vector, the patterns for thermocouple pairs 1 and 2 repeat, except that the signs of the outputs reverse as the junctions forming each pair reverse their positions in the flowfield. The Reynolds numbers written on each figure are defined at the film temperature, i.e.,

$$Re_f = \frac{\rho_f u_\infty D}{\mu_f}$$

where the density ρ_f and viscosity μ_f are defined at the film temperature

$$T_f = \frac{T_\infty + T_{heater}}{2}$$

where T_∞ is the freestream adiabatic recovery temperature. It has been shown that, for fixed geometry and fixed overheat, the film Reynolds number effectively determines the temperature distribution about the cylinder.

For variable overheat, performance test results show that the sensor output E can be corrected by:

$$E_{100°} = E \cdot \frac{100}{T_{heater} - T_\infty}$$

where $E_{100°}$ is the corrected output for one thermocouple pair.

The thermal power of each thermocouple junction (dE/dT) is a function of the junction temperature. Hence the output of the sensor will be a function of ambient temperature as well as the temperature difference across the sensor. Thus the sensor output must be corrected before the output can be compared to calibration data. The correction procedure will use thermocouple calibration data and the ambient temperature as measured by the temperature sensor.

For sufficiently high Mach numbers, a slight dependence of the patterns on Mach number also occurs. The maximum deviation in the output of each thermocouple pair from the incompressible case is of the order of 7 percent. The performance tests show that the correction factor can be estimated from:

$$E_i = E_c \frac{Nu_i}{Nu_c}$$

where E refers to the emf output of one thermocouple pair, Nu refers to the average Nusselt number for the cylinder, subscript i refers to the incompressible (low Mach number) result, and subscript c to the compressible (high Mach number) result. The ratio Nu_i/Nu_c as a function of Mach number and Reynolds number is known to the precision required from experimental data on flow across infinite cylinders which is available in the open literature.

At low temperatures, the thermal conductivity of the CO_2 is much lower than the thermal conductivity of the calibration fluid (room temperature air). Thus, while heat conduction down the thermocouple wires is negligible with respect to convective heat transfer for calibration conditions, this is not necessarily true for the coldest Martian ambient conditions and a correction may be required.

2. OPERATION OF SENSOR

2.1 OPERATION AS A QUADRANT SENSOR

The operation of the quadrant sensor in its intended mode is accomplished by sensing whether or not the downstream member of each thermocouple pair is inside the thermal wake. As an illustration of how this information can indicate the wind quadrant, consider the geometry shown in Figure 5. Let the wake have a well defined edge (written in terms of the apparent half angle α at the radius of the thermocouple junctions). Further assume that each thermocouple pair gives one result (marked +,- in Figure 5) if one member is inside the wake, a second result (-,+) if the opposite member is inside the wake, and a third result (designated 0,0) if neither member is within the wake. If the true wind vector is slightly to the left of one wind sensor as in case 1, with $\theta < 2\alpha - 90°$, the output of the thermocouple pairs 1 and 2 will be, respectively, +,-; +,-. If the true wind vector is slightly to the right of the wind sensor, as in case 2 (again with $\theta < 2\alpha - 90°$), the output will be +,-; 0,0. The sign of the outputs in either case quickly eliminates two of the false solutions. Furthermore, the two cases can be distinguished from one another so that the correct solution of the remaining pair is determined. If we have $2\alpha - 90° < \theta < 45°$ with the true wind vector on the left as in case 3, the output will be 0,0; +,-; and, for case 4 with the true wind vector on the right, the output will be +,-; 0,0. Thus again, we can distinguish between these two cases. For $\theta > 45°$, rotate the pattern in Figure 5 by 90° and the pattern repeats. Because the angle θ is uniquely determined by the wind sensors, we always know which of the above cases to consider.

In Figure 6, we define the wake width in terms of the output of each sensor at the arbitrarily defined wake half widths α of 65°, 67.5° and 70°, using data like that shown in Figures 3 and 4. Ideally, we would like to assume that for thermocouple pairs oriented at angles less than the wake half width from the direction of the wind vector, the absolute magnitude of the output will always be greater than the threshold value shown in Figure 6. This condition would be associated with a +,- or -,+ output in the above discussion. Similarly, when the angle of each thermocouple pair with respect

to the wind vector is greater than the wake half width, the output would be less than the threshold value and would be labeled 0,0. If this were truly the case, any of the wake width definitions shown in Figure 6 would be acceptable, provided that the quadrant sensor were oriented at an angle α with respect to one wind sensor.

Unfortunately, the situation is not so simple. For a 65° half-angle wake definition, for example, the wake edge at $Re_f \approx 150$ is about 2 mv. The output from each thermocouple pair is less than this value for the case when one of the thermocouples is in the exact center of the wake. This is because of a central minimum in the temperature field of the wake. To overcome this difficulty, we can choose to increase the half angle α or equivalently reduce the wake edge thermocouple output below the central minimum. Unfortunately, in order to accomplish this, the wake half width must be increased so much (to approximately 70°) that, for high Reynolds numbers, no measurable thermocouple output is obtained at the wake edge. For example, for $Re_f \cong 400$ the orientation at which the output from each thermocouple pair vanishes is less than 70° with respect to the wind vector.

For these reasons a compromise of wake width definition and quadrant sensor orientation is required. Such a compromise is indicated by heavy lines in Figure 6. The wake half width defined by these curves varies from 70° to about 65°. The thermocouple orientation would be 67.5° with respect to one wind sensor. The implication is, for $Re_f \approx 100$ for example, that the quadrant sensor would not be able to resolve the true wind vector from the closest false wind vector when the wind vector lies closer than 2.5° to one wind sensor axis. This uncertainty of 2.5° is small compared with the wind sensor directional error, however, and is acceptable.*

2.2 OPERATION AS A WIND DIRECTION SENSOR

For low Reynolds numbers ($Re_f < 63$) the quadrant sensor can be used as an accurate wind direction sensor. Figure 7 illustrates this.

---

*Although the threshold EMF is reduced, for $62.7 < Re_f < 210$, so that the wake edge thermocouple output will be less than the wake center thermocouple output for nominal conditions, errors arising in non-ideal operation may reduce the thermocouple output at the wake center below the threshold. We therefore strongly recommend, when a thermocouple output below threshold is obtained, that the wind sensor wind angle be checked against the quadrant sensor output to be absolutely certain that the thermocouple in question is not near the wake centerline. This procedure will eliminate ambiguous results.

The axes of Figure 7 represent the outputs of each of the thermocouple pairs in millivolts. The curves show contours of constant wind angle with respect to the axis defined by thermocouple pair 1. The Reynolds number varies from point to point along each contour.

In order to use the plot to obtain the wind angle, the outputs from each thermocouple pair are corrected for systematic errors and the corrected values are plotted on Figure 7. The wind angle can be read directly.

Note that, for Reynolds numbers greater than about 63, the contours at the corners of the figure merge. Where the curves cross, one pair of thermocouple outputs corresponds to two different angles and the technique can no longer be used.

3. PERFORMANCE TESTING OF QUADRANT SENSOR

3.1 TEST DESCRIPTION

The primary function of performance testing of the breadboard model quadrant sensor is to establish the performance characteristics of the sensor for operation in the "normal" mode (100° overheat, zero angle of attack, in air, at low Mach number). The secondary function is to determine the effects of operation at extreme conditions (i.e., extreme angle of attack, extremely high Mach number, variable overheat, calibration in CO_2 rather than air).

The performance tests were carried out in two different wind tunnels: the Viking wind tunnel for the lower part of the Reynolds number range and the TRW Low Speed Wind Tunnel for the highest Reynolds numbers. The Viking wind tunnel permits variable Mach number, variable angle of attack, and variable gas composition, while the low speed wind tunnel is limited to a single Mach number at each Reynolds number, permits zero angle of attack measurements only, and uses air as the working fluid.

3.2 TEST PROCEDURE

3.2.1 Range of Test Conditions

Figure 8 shows the range of operating conditions on Mars for which an accuracy requirement has been placed on the instrument. The two axes represent freestream Reynolds number (not film Reynolds number, as above) and freestream Mach number. The conditions for which data points were obtained are indicated on the map. Circles represent points taken in the Viking wind tunnel and squares represent points taken in the low speed wind tunnel.

The test procedure involved first setting up one of the flow conditions indicated by points in Figure 8, then recording the sensor output while the sensor was rotated in regular increments (10° or 20°) through a complete circle with respect to the flow direction. The outputs of the two thermocouple pairs were measured by digital voltmeters and a permanent record was obtained by recording the voltmeter readings manually, or on a digital printer.

3.3 TEST RESULTS

3.3.1 Primary Data Base

The primary data base (for "normal" operation) is depicted in polar format in Figures 3 and 4, discussed above, and Figures 9 through 15. Figures 5, 6 and 7 illustrate the use of this data to determine the wind quadrant and directly measure the wind direction at low Reynolds numbers.

3.3.2 CO_2 Results

The CO_2 data points are correlated with results taken in air in Figure 16 (showing wake edge definition) and Figure 17 (showing wind direction determination at low Reynolds number). The wake edge threshold thermocouple output is very slightly changed by the use of air rather than CO_2 to calibrate the sensor. The effect is to narrow the wake half width angle for constant threshold emf by about 3° at $Re_f \cong 6$, 2° to 3° at $Re_f \cong 25$, and about 1° at $Re_f \cong 200$. All calibrations of deliverable hardware will be carried out in air, and a threshold emf correction factor, determined from Figure 16, will be applied to correct for operation in CO_2. From Figure 17, the effect of calibration in air rather than CO_2 on the direct measurement of wind direction is negligible.

3.3.3 High Mach Number Results

For three film Reynolds numbers (approximately 18, 63 and 25) the sensor output was determined at the minimum Mach number and maximum Mach number permitted by the operating map (see Figure 8). In only one case ($Re_f \sim 63$) is a significant difference between high and low Mach number results obtained. The ratio of thermocouple outputs for the high and low Mach number results at $Re_f \sim 63$ is shown in Figure 18. The ratio is seen to be nearly constant with respect to angle. A comparison with the Nusselt number ratio for the two cases, determined by direct measurement of the power required to operate the heater, is also given and, as expected, the agreement is very close.

In conclusion, the maximum change in thermocouple output due to Mach number variations at constant Reynolds number is approximately 6%. Corrections of this order can be made with the required accuracy using available data on Nusselt number variation with Mach number and Reynolds number. Therefore,

no further tests or calibrations at high Mach number are planned. All calibrations will be performed at the minimum Mach number that is associated with each Reynolds number by the operating map (Figure 8).

3.3.4 Variable Overheat Results

Results were obtained at three different overheats (50°C, 100°C, 123°C) for film Reynolds numbers of approximately 6 and 245. The thermocouple outputs were converted to a measured temperature difference, corrected for the slight variation in film Reynolds number with overheat, and the results are plotted, for constant film Reynolds number, as a function of overheat temperature in Figures 19, 20, 21 and 22. In all cases and at all wind direction angles, the thermocouple outputs are linear, to an excellent approximation, with overheat temperature. This information will be used to correct the mission data to a nominal 100°C overheat before comparison with the calibration data.

3.3.5 Angle of Attack Data

Results were obtained with the quadrant sensor inclined at 24° with respect to the wind tunnel flow axis. The sensor axis was inclined downstream so that the large support flange and the top of the pedestal supporting the quadrant sensor were in the worst position (i.e., providing maximum blockage of the flow over the sensor).

Comparison of wake edge threshold definitions for sensors at 24° angle of attack and 0° angle of attack are shown in Figure 23. The effect of angle of attack is to reduce the apparent wake half width by about 1° at $Re_f \sim 17$, less than 1° at $Re_f \sim 60$, and 2 to 3° at $Re_f \sim 240$. Our conclusion is that the effects of angle of attack less than ±25° on this mode of operation are small and it seems unnecessary to further characterize or calibrate the sensor over the full range of angles of attack. Instead, an average correction for angle of attack will be applied to all data, regardless of the true angle of attack. The maximum quadrant error accruing from this procedure will evidently be of order ±1.5° to 2°.

The effect of 24° angle of attack on the operation of the quadrant sensor as a wind direction sensor is shown in Figure 24. Clearly, the effect is negligible for $Re_f = 17.6$ and the maximum error for $Re_f = 61.6$ is about 3°

to 4°. Again, no attempt will be made to obtain and apply a correction factor as a function of angle of attack. Instead, an average correction factor will be estimated from the data in Figure 24 and applied to all data, regardless of angle of attack.

4. PERFORMANCE VERIFICATION

4.1 PERFORMANCE REQUIREMENTS

The requirements levied on the quadrant sensor by Martin Marietta Specification PD 7400090 are presented in Table 1. Also indicated is the way in which the performance requirements have been demonstrated.

4.2 PERFORMANCE ANALYSIS

4.2.1 Range

The fluid mechanical operation of the quadrant sensor over the high accuracy range (see Direction Accuracy, Table 1) has been demonstrated by the wind tunnel performance tests described above. The pressure, temperature, and velocity ranges corresponding to the high accuracy range were reduced to equivalent Mach and Reynolds number ranges and the sensor was tested over the resulting Mach number-Reynolds number map.

The effect of the ambient temperature range on the survival of the quadrant sensor has been determined by temperature cycling over the entire required range (130°K to 350°K). Operational tests have been carried out only at the lower extreme, but the survival temperature of the polyimide resin ($\sim$530°K) which is the most likely component to fail, is above the maximum temperature that will be attained by the heater, even at 100° overheat and 350° ambient temperature.

The ambient pressure (always much less than one atmosphere) can degrade the sensor only by inducing outgassing. Breadboard model sensors have been subjected to vacuum at pressures well below the minimum specified Martian pressure without noticeable effect.

The combined effect of temperature, pressure, and wind speed can destroy the sensor if the dynamic pressure due to wind loading becomes large enough to fracture the polyimide supporting structure of the thermocouple wires. For the specified conditions, the maximum dynamic pressure ($\sim$.13 lb/in^2) is not large enough to cause damage under any circumstances.

4.2.2 Calibration

The calibration requirement levied by PD 7400090 states that the sensor shall be calibrated by the supplier. By our performance tests of the

Quad worst case = 1.24 sec

breadboard model quadrant sensor, we have demonstrated our ability to perform the required calibrations.

4.2.3 Response Time

The quadrant sensor is required to respond to a change in wind within 2 seconds. The main factor limiting the response time of the quadrant sensor, once the heater has attained a steady state temperature, is the ability of the thermal mass of the thermocouple junctions to track the ambient temperature.* Tests have been performed in the Viking wind tunnel to measure the response time of the ambient temperature sensor, which also uses 3 mil thermocouple wire. These tests show that the worst case sensor time constant will be 1.24 seconds.

4.2.4 Warm Up Time

The basic warm up time of the instrument is limited by the rate at which the maximum available heater power can increase the temperature of the heater, when opposed by heat losses due to convection and conduction. The electrical power delivered to the sensor is determined by the sensor resistance, which depends upon the ambient temperature. Similarly, the rate of convection of heat away from the heater depends upon ambient conditions. The parameters controlling the heat conduction through the polyimide support structure are not as dependent upon ambient conditions.

A warm-up test, corresponding to one set of ambient conditions (stagnant room temperature air), has been conducted using the breadboard MEA to power quadrant sensor S/N Q-3. In the following section, a mathematical model of the transient heat transfer occurring during this test is formulated. The combination of parameters controlling the heat conduction through the sensor structure (which, as mentioned above, is insensitive to ambient conditions) is evaluated by comparison with the test data. The mathematical model is then applied to the range ambient conditions obtained during operation of the instrument on Mars using this empirical constant. Finally, the worst case (or minimum)

*There is a slower time constant associated with the rate of conduction of heat down the thermocouple wire from the supports. The corresponding change in junction temperature with time can be calculated and corrected for, however; and so this effect is not considered to be a true limit on the sensor response time.

overheat to be expected after a four second warm-up is computed and presented as a function of Reynolds number. The implication of this worst case overheat (which is smaller than the steady state value) is a slight reduction in the directional accuracy although the sensor still meets the specified accuracy requirement. This will be discussed further in Sections 4.2.7.1.2.2 and 4.2.7.1.2.5.

The assumptions employed in the mathematical model are four fold. The convective heat transfer to the gas surrounding the sensor is assumed to be quasi-steady. The heat conduction through the heater wire is assumed to be sufficiently rapid that the heater surface temperature is independent of location. The thermal mass of the heater is assumed negligible, and the unsteady heat conduction inside the polyimide heater support is assumed to be axisymmetric, with negligible end effects. The temperature within the heater support is given by:

$$\frac{\rho c}{k_p} \frac{\partial T}{\partial t} = \frac{1}{r} \frac{\partial}{\partial r} \left(r \frac{\partial T}{\partial r}\right) \tag{1}$$

where ρ is the density of the polyimide

c is the heat capacity of the polyimide

k_p is the thermal conductivity of the polyimide (1.44×10^4 erg/cm^2 sec °K)

and r is the radial coordinate of the polar coordinate system centered on the heater axis

The initial condition for Eq. (1) is given by

$$T = T_0 \quad \text{when} \quad t = 0 \tag{2}$$

and the boundary condition is

$$k_p \frac{\partial T}{\partial r} = \frac{V^2}{R} (.87) - \frac{Nu\, k_g\, (T - T_\infty)}{L} \tag{3}$$

$$\text{at } r = r_a$$

where V is the maximum voltage available from the MEA heater power supply (5 V)

.87 is the maximum possible duty cycle for the heater control electronics

R is the heater resistance

Nu is the Nusselt number of the flow over the sensor

k_g is the thermal conductivity of the gas surrounding the sensor

and L is the characteristic dimension of the sensor

(L = heater length = .797 cm for free convection heat transfer
L = heater diameter = .35 cm for forced convection heat transfer)

The heater resistance, R, is also a function of its temperature. To simplify the solution of the problem, the complicated fourth order polynomial describing R is replaced by a linear expansion about the initial temperature, T_o. For the test case (i.e., sensor Q-3 starting from room temperature), the resistance is given by:

$$R = 11.86 + .0418\ (T - 23°C)\ \Omega \qquad (4)$$

The set of equations [(1), (2), (3) and (4)] was solved, using finite difference techniques, for initial conditions corresponding to the warm-up test and a Nusselt number corresponding to free convection heat transfer over the vertical cylinder. The parameter ρc appearing in Eq. (1) was left unspecified, which effectively leaves the relationship between the time interval, Δt, and the radius interval, Δr, unspecified:

$$\Delta t = \frac{\rho c}{2k_p} (\Delta r)^2$$

The time interval was then fixed by requiring the predicted temperature rise after 4 seconds to equal the measured temperature rise. Figure 25 shows the temperature variation of the test data, which has a nearly exponential rise with a characteristic time of 4.4 seconds. The test therefore indicates an overheat of 59.75°C after 4 seconds. The radius increment used in the calculation was .0175 cm and the number of time steps required to attain a

surface temperature of 59.75°C was 12.1. The resulting value of the quantity ρc is:*

$$\rho c = 3.113 \times 10^7 \text{ ergs/cm}^3 \text{ °K}$$

This empirical value of ρc was then used with Eq. (1) to determine the rate of temperature rise for Martian operating conditions. The slowest rate of temperature rise at each Reynolds number is expected for the maximum initial sensor temperature and maximum gas thermal conductivity, both of which reduce the power input to the heater. These conditions correspond to the maximum temperature associated with each film Reynolds number by the requirements of PD 7400090. The minimum overheat, after a 4 second warm-up, is plotted as a function of Reynolds number in Figure 26. The effect on instrument accuracy is discussed in Section 4.2.7.

4.2.5 Attitude

As indicated by the results discussed above (Section 3), the performance tests at angle of attack prove that the sensor will operate and meet performance requirements when oriented within 25° of vertical. Because we do not propose to properly correct for the small systematic error that results from a non-vertical sensor, a contribution to the overall sensor error results. This is discussed below (Section 4.2.7).

4.2.6 Self-Heating

The range of overheats which the quadrant sensor will attain in steady state operation is shown in Figure 27. This range of overheats is calculated from the properties of a heater meeting the acceptance test criteria

$$R = 12\Omega \pm .35\Omega \text{ at } 23°$$

$$\alpha = \left.\frac{1dR}{RdT}\right)_{0°C} = .00385/°C \pm .0001/°C$$

---

*Note that the value of ρc can be independently determined. The empirical value, however, takes some account of the errors introduced by the mathematical approximations. The end effects are probably not totally negligible in relation to radial heat transfer within the polyimide cylinder, for example. Our model also does not account for the heat loss or gain due to the heater lead wire running down the center of the cylinder. It can be demonstrated, however, that the empirically derived value of ρc is approximately correct. If the properties of water are assumed, for example, the product ρc would have the value $\rho c = 4.18 \times 10^7$ ergs/cm^3 °K.

All overheats are greater than 20°C and less than 140°C, as required by the specification.

The sensor will meet all performance requirements for the overheats shown in Figure 27. The maximum possible sensor temperature is 435°K, well below the polyimide failure temperature. As is shown above, and in Section 4.2.7.1, the sensor will meet all specified requirements within the required 4 seconds under worst case conditions. The compliance of the sensor to the accuracies specified in PD 7400090 with the overheats shown in Figure 25 is also discussed in Section 2.4.7.

4.2.7 Direction Accuracy

Two separate error analyses have been performed for the quadrant sensor: one for operation as a quadrant sensor and the second for operation, at low Reynolds numbers, as a wind direction sensor.

4.2.7.1 Quadrant Sensor

For operation of the quadrant sensor as a wind quadrant detector, the data reduction process discussed above (Section 2.1) is used. The film Reynolds number is obtained from the wind sensor data, the corresponding wake edge criterion (thermocouple emf) is obtained from the calibration data, and each of the measured thermocouple outputs is compared with the wake edge criterion to determine whether or not the downstream member of the pair is within the thermal wake.

In real life the situation is complicated by the fact that the film Reynolds number is not known exactly so that the correct wake edge criterion is not known exactly. Also errors in measurement of the thermocouple emfs cause the value we compare to the calibration data to differ from the ideal thermocouple output under identical conditions. This situation is shown in Figure 28 for a half width angle $\alpha = 67.5°$. ΔE_R is the real or ideal thermocouple output and ΔE_m is the measured value. Because of measurement errors, we would interpret the data as indicating the downstream thermocouple of the pair in question to be inside the thermal wake when in fact it is outside the wake.

Note that this situation can only occur when the true thermocouple output lies very close to the threshold value, or when the wind vector lies very

close to the one wind sensor. The result is that the error analysis defines a range of wind vector orientations (or dead band) around each wind sensor axis for which the wind quadrant cannot be unambiguously determined, since the true wind vector solution and one false solution both must be within the dead band (see Figure 29). For wind sensor solutions outside this range, the quadrant sensor has no trouble discriminating against all of the false solutions. The goal of designing the quadrant sensor is therefore to keep the dead band half width smaller than the wind direction accuracy permitted by the specification. Then, when the true wind vector lies within one of the dead bands (forcing one of the false wind sensor solutions to also lie within the same dead band on the opposite side of the nearest wind sensor axis, see Figure 29), we can achieve the required wind direction accuracy by declaring the wind vector to coincide with the corresponding wind sensor axis.

The errors considered in estimating the total dead band angle are summarized in Table 2. The errors are divided into two groups: those which are random in nature and can be combined in root-sum-square fashion, and those which are systematic (heat conduction, errors, and errors due to compromises in wake edge definition) and must be combined by adding. The errors marked with asterisks contribute significantly to the total error and the techniques used to estimate them are briefly discussed below. Some of the errors not discussed below are discussed in detail in the performance test section (effect of calibration in air rather than CO_2, rarefaction errors, and angle of attack induced errors).

Two cases have been analyzed for each quadrant sensor film Reynolds number: the case corresponding to the minimum possible ambient temperature at each Reynolds number (cold case), and the case corresponding to the maximum possible temperature at each Reynolds number (hot case). Since the temperatures for these two cases vary with Reynolds number, the labels "cold case" and "hot case" do not refer to fixed temperatures.

4.2.7.1.1 Systematic Errors

4.2.7.1.1.1 Heat Conduction Errors

The thermocouple junctions are suspended on 3 mil thermocouple wire from polyimide supports which may be up to 100°C different from the gas temperature

around the junction (see Figure 30). Thus the temperature attained by each junction is the result of a balance between convective heat transfer, radiative heat transfer (rendered negligible by gold plating the junction to reduce the emissivity), and conductive heat transfer. The equation for the temperature attained by each junction in steady state is:

$$k_w A_w \frac{d^2T}{dx^2} - k_g \, Nu \, \pi \, (T - T_a) = 0 \, . \tag{5}$$

where k_w is the thermal conductivity of the thermocouple wire (almost equal for chromel and constantan, average value used)

k_g is the thermal conductivity of the gas

Nu is the Nusselt number of the flow about the wire

and the other units and boundary conditions are defined in Figure 30. Equation (5) has the following solution at $x = -\delta$ (location of the junction):

$$T = T_a + (T_s - T_a) \frac{\cosh \sqrt{\frac{k_g \, \pi \, Nu}{k_w \, A_w}} \, \delta}{\cosh \sqrt{\frac{k_g \, \pi \, Nu}{k_w \, A_w}} \, \frac{L}{2}} \tag{6}$$

Now typically, the quantity $\sqrt{k_g \, \pi \, Nu / k_w \, A_w}$ is large enough that we can reduce this to the following approximation:

$$T = T_a + (T_s - T_a) \, e^{-\sqrt{\frac{k_g \, \pi \, Nu}{k_w \, A_w}} \, \ell} \tag{7}$$

where $\pi = L/2 - \delta$.

What we measure, however, is not the temperature of any single junction but the temperature <u>difference</u> across the sensor. This can be expressed

$$\Delta T = \Delta T_a + (T_s - T_a)_1 \, e^{-\sqrt{\frac{k_{g_1} \pi Nu_1}{k_w A_w}} \ell} - (T_s - T_a)_2 \, e^{-\sqrt{\frac{k_{g_2} Nu_2}{k_w A_w}} \ell} \tag{8}$$

where subscripts 1 and 2 refer to the conditions on either side of the sensor. If the temperature change due to conduction is not sufficiently large that the thermal power is seriously affected, the error in measured thermocouple output, E, due to conduction will be

$$\delta E = K(\Delta T - \Delta T_a) = k \left\{ (T_s - T_a)_1 \, e^{-\sqrt{\frac{k_{g_1} \pi Nu_1}{k_w A_w}} \ell} - (T_s - T_a)_2 \, e^{-\sqrt{\frac{k_{g_2} \pi Nu_2}{k_w A_w}}} \right\} \tag{9}$$

where $K = \partial E / \partial T$.

The square root of the thermal conductivity will not vary seriously between the two sides of the heater. Furthermore, because of the relative insensitivity of the Nusselt number to Reynolds number at low Re (see Figure 31), the Nusselt number of the flow about the wire is also not very different on the two sides of the sensor, even when one thermocouple is directly upstream with the other directly downstream. Thus, another useful approximation can be made:

$$\delta E = K(T_{a_2} - T_{a_1}) \, e^{-\sqrt{\frac{k_g \pi Nu}{k_w A_w}} \ell} \tag{10}$$

Note that the support temperature T_s is now completely gone from our expression.

The expression for error must be further modified since we calibrate the sensor at room temperature with some heat conduction effect already present. The quantity that we really seek is the difference between the heat conduction correction δE at Martian operating temperature and the heat conduction

correction δE for calibration. This correction is the one that should, in theory, be applied to the data before comparison with calibration curves. Let this quantity be ΔE. Then

$$\Delta E = K_{op} (T_{a_2} - T_{a_1}) e^{-\sqrt{\frac{k_{g_{op}} \pi Nu}{k_w A_w}} \ell}$$

$$- K_{cal} (T_{a_2} - T_{a_1}) e^{-\sqrt{\frac{k_{g_{cal}} \pi Nu}{k_w A_w}} \ell} \qquad (11)$$

(we have assumed k_w independent of temperature since k_w changes much more slowly than k_g). Now, since $K = dE/dT$ is a weak function of temperature,

$$\Delta E \cong K (T_{a_2} - T_{a_1}) \left\{ e^{-\sqrt{\frac{k_{g_{op}} \pi Nu}{k_w A_w}} \ell} - e^{-\sqrt{\frac{k_{g_{cal}} \pi Nu}{k_w A_w}} \ell} \right\} . \qquad (12)$$

EMF errors for the hot and cold cases were calculated from Equation (8). The results for percent change in δE [or, equivalently, $\Delta E/k(T_{a_2} - T_{a_1})$] are shown in Figure 32. The corresponding effect on the thermocouple output at points near the wake edge (i.e., the effect on the wake edge definition) is illustrated for the cold case by Figure 33. The largest effect is to introduce a change in thermocouple emf approximately equivalent to a 7° contribution to the quadrant dead band (at $Re_f \sim 30$).

The dead band contribution introduced by heat conduction is a systematic error and can consequently be corrected for. The simplest error correction scheme is similar to that employed for the correction of angle of attack induced errors: an average correction (shown in Figure 32) is introduced into the calibration curve. The result is to introduce a maximum symmetric error of one-half the difference between the hot and cold cases. The maximum symmetric error contribution to the quadrant dead band induced by this approximate heat conduction correction is shown in Figure 34.

4.2.7.1.1.2 Wake Edge Definition Errors

As discussed above (Section 2), a systematic error is built into the data reduction scheme over part of the Reynolds number range. The wake edge threshold EMF is artificially reduced (by an amount equivalent to about 2.5°) from $Re_f = 62.7$ to $Re_f = 210$. This is done to avoid spurious indications that the thermocouple is outside the wake due to the minimum in thermocouple output when one thermocouple is directly downstream of the heater. At film Reynolds numbers above about 300, the wake edge threshold EMF is artificially increased (again by an amount equivalent to 2.5°) to avoid signal to noise ratio problems. The systematic (additive) error contribution to the dead band due to these effects is shown in Figure 35.

4.2.7.1.1.3 Total Systematic Error

The total systematic error is found by combining the results from Figures 34 and 35 using logic discussed below. The total or net systematic error is then added to the total random error (to be discussed in Section 4.2.7.1.2) to obtain the total quadrant sensor dead band.

For the cold case, the systematic error due to heat conduction reduces the signal below the expected signal (i.e., the mean systematic error correction is less than the true correction). The EMF error due to compromises in wake edge definition makes the expected threshold signal lower than the actual signal for $62.7 < Re_f < 210$. Thus the systematic errors due to heat conduction (cold case) and wake edge definition are of opposite signs, and the angular dead band contributions from Figures 34 and 35 partially compensate. The absolute value of the difference between these contributions is used as the net systematic error to be added to the total random error. For $Re > 300$, the EMF error due to compromises in wake edge definition makes the expected threshold signal higher than the actual value so, for the cold case, the net systematic error is the sum of the errors from Figures 34 and 35. For the hot case, the systematic heat conduction error increases the signal above the expected value (because the mean systematic error correction is greater than the actual value). Hence for $62.7 < Re_f < 210$, the net systematic error is the sum of the value from Figures 34 and 35 while for $Re_f > 300$, the net systematic error is the absolute magnitude of their difference.

The total or net systematic error is shown in Figure 36.

4.2.7.1.2 Random Error

4.2.7.1.2.1 Uncertainty in Reynolds Number

The film Reynolds number must be obtained from wind sensor data and the measured quadrant sensor heater temperature before the quadrant sensor wake edge criterion can be selected. If a linear viscosity law is assumed (i.e., $\mu \sim T^{1.0}$), then the relationship between Re_f and Re_∞ is:

$$Re_f = Re_\infty \left(\frac{T_\infty}{T_f}\right)^2 \tag{13}$$

As a result of this equation, one can show

$$\frac{1}{Re_f}\frac{\partial Re_f}{\partial Re_\infty} = \frac{1}{Re} \tag{14}$$

$$\frac{1}{Re_f}\frac{\partial Re_f}{\partial T_W} = -\frac{2}{T_W + T_\infty} = -\frac{1}{T_f} \tag{15}$$

$$\frac{1}{Re_f}\frac{\partial Re_f}{\partial T_\infty} = \frac{2}{T_W + T_\infty}\frac{T_W}{T_\infty} = \frac{1}{T_f}\frac{T_W}{T_\infty} \tag{16}$$

Therefore

$$\frac{\delta Re_f}{\delta Re_f} = \sqrt{\left(\frac{\delta Re_\infty}{Re_\infty}\right)^2 + \left(\frac{\delta T_W}{T_f}\right)^2 + \left(\frac{\delta T_\infty}{T_f}\right)^2 \left(\frac{T_W}{T_\infty}\right)^2} \tag{17}$$

The uncertainty in T_∞ (obtained from the temperature sensor) is assumed to be $\pm 3°K$ (from the required temperature sensor accuracy) and the uncertainty in T_W due to measurement errors is assumed to be $\pm 10°K$ (see below). The estimated uncertainty in Re_∞ as measured by the wind sensors is shown in Figure 37. It is nearly independent of the ambient temperature. The resulting worst case uncertainty in Re_f is shown in Figure 38.

The uncertainty in Re_f can be converted to an error in wake edge criterion using Figure 6. This error in wake edge criterion can also be converted to an equivalent dead band angle using performance test data. The results are shown in Figure 39.

4.2.7.1.2.2 Uncertainty in Overheat

The measured heater temperature is assumed to be in error by as much as ±10°K because of uncertainty introduced by the electronics.* Additionally, the ambient temperature must be assumed to be in error by as much as ±3°K. Thus the total uncertainty in overheat temperature will be ±10.44°K.

For a heater within the specified tolerance [$R = 12\Omega \pm .35\Omega$ at 23°C, $\alpha = (1/R)\ (dR/dT)\}_{0°C} = .00385/°C \pm .0001/°C$] the variation in overheat with ambient temperature is given in Figure 27. For the cold case and hot case conditions under consideration here (minimum and maximum ambient temperature consistent with each film Reynolds number) the variation of the error in sensor overheat (also the error in the thermocouple output after correction for overheat variations, see Section 3.34) with film Reynolds number is shown in Figure 40. Additionally, for the worst case (slowest) warm up conditions (see Figure 26) the overheat error attained after a 4 second warm up is presented. The equivalent contributions to the quadrant sensor dead band are shown in Figure 41.

Note that this overheat error source enters the picture twice: once during calibration and once during measurement. During calibration, however, the overheat variation is negligibly small because the conditions of the test are much more carefully controlled. Thus the error in overheat during calibration has been neglected in comparison with that obtained during the measurement.

4.2.7.1.2.3 Errors Due to Movement of Thermocouple Junctions

If the thermocouple junctions change their nominal positions relative to the quadrant sensor heater due to differential expansion, the thermocouple outputs for a given sensor orientation relative to the wind vector will be changed. The thermocouples are installed on the sensor at room temperature in a taut configuration under about 30 grams tension. During the initial exposure to the extreme low operating condition, they are stretched by differential expansion beyond the yield point so that, upon return to higher temperatures, the wire tends to "sag" more than before exposure to the low

*Based on an informal internal specification placed on the heater electronics. This accuracy requirement is easily met under most conditions and could actually be tightened, if required.

temperature. Nevertheless, for ambient temperatures below room temperature, the differential expansion is not sufficient to relax all of the tensile stress in the wires, and they remain taut. For ambient temperature above room temperature, however, the wires do move from their nominal or "straight" locations. Nevertheless, for the "cold case" conditions we are considering, as well as calibration conditions, errors due to movement of thermocouple junctions are negligible. For some of the "hot case" conditions, this error source must be accounted for.

Differential Expansion Analysis of Quadrant Sensor

The configuration shown in Figure 1 will be analyzed assuming the following properties:

Thermal expansion coefficient of polyimide support, $\alpha_p = 9 \times 10^{-6}/°C$

Thermal expansion coefficient of thermocouples, $\alpha_w = 14 \times 10^{-6}/°C$

Young's modulus of thermocouple wire, $E_w = 24 \times 10^6$ psi

Yield point of thermocouple wire, $Y_w = 20{,}000$ psi (typical for constantan)

The quadrant sensor thermocouples are assembled onto the polyimide support at room temperature and under some tension (about 30 grams or 9,000 psi). At the operating condition corresponding to maximum stretch of the thermocouple wire (130°K ambient with 100°C overheat) the differential contraction from room temperature ($\delta_{wire} - \delta_{polyimide\ support}$) for an unrestrained wire will be

$$\alpha_w (296 - 130)(.388") - \alpha_p (296 - 230)(.388") = 6.7 \times 10^{-4} (") \quad (18)$$

The increase in stress required to force the wire to match the support would be:

$$E_w \left(\frac{6.7 \times 10^{-4}}{.388}\right) = 41{,}500 \text{ psi} \quad (19)$$

if the wire obeyed Hook's law. In fact the total stress would then be 50,500 psi which exceeds the yield point of the wire (although not its tensile strength).*

*Elongation at breaking point should be greater than 10% or .04".

For our further analysis we assume a stress-strain relationship for the wire of the form shown below.*

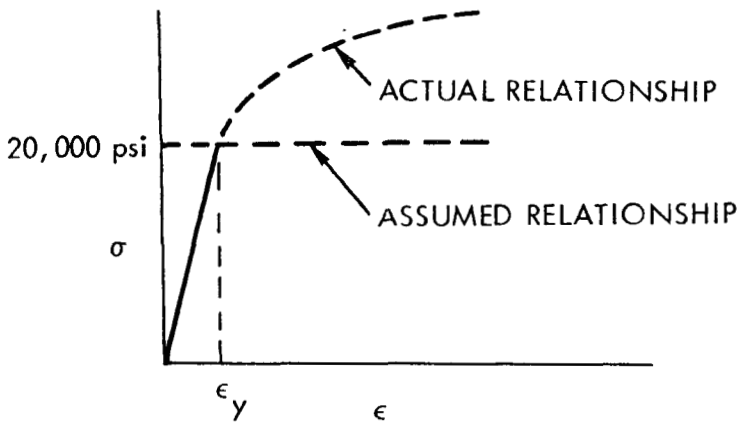

Then once the sensor thermocouples have been subjected to maximum stretch the new stress-strain curve will be displaced as shown below:

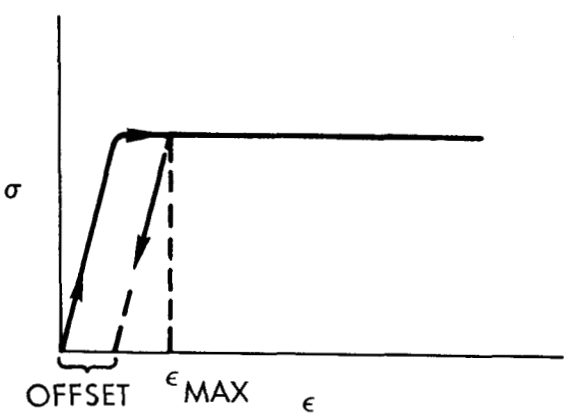

The offset will produce a sag in the thermocouple when the ambient temperature increases. In the remainder of this analysis we assume that, for the first time the sensor is subjected to maximum stretching, the wire follows the path indicated by the arrows on the stress-strain diagram immediately above. Hence for further thermal cycling the thermocouple wire stress-strain relationship follows the dotted line in the figure, and the stress in the wire exactly equals the yield stress each time the operating condition of maximum stretch is subsequently attained.

*This is actually a worst case since the actual wire will deform less for a given ε in excess of ε_y and will show less sag at the higher temperatures.

The change in the wire length due to complete relaxation of the yield stress will be

$$\delta_{wire} = \frac{.388Y}{E_W} = .323 \times 10^{-3} \text{ inches} \tag{20}$$

and the change in wire length required to conform to the differential expansion of the thermocouple wire and polyimide support from operation at 130°K ambient to operation at room temperature (with 100°C sensor overheat in both cases) is:

$$\delta_{wire} = (\alpha_W - \alpha_p)\ (166)\ (.388)$$

$$= .322 \times 10^{-3} \tag{21}$$

which is entirely made up by relaxation of the yield stress. Therefore, for operation at room temperature (i.e., calibration conditions) following operation at the coldest possible ambient temperature, the wires remain tight. There is therefore no change in the positions of the thermocouple junctions relative to the heater between calibration conditions and operation at ambient temperatures below 296°K.

For operation at 330°K after exposure to the cold extreme, the change in wire length required to conform to differential expansion will be

$$\delta_{wire} = (\alpha_W - \alpha_p)\ (200)\ (.388)$$

$$= .389 \times 10^{-3} \text{ inches} \tag{22}$$

Relaxation of the yield stress accounts for only $.323 \times 10^{-3}$ inches, so the net "sag" in the wires is 6.6×10^{-5} inches. This corresponds to a horizontal displacement (perpendicular to the axis of the thermocouple wire) of 3.51×10^{-3} inches.

Resulting Dead Band Error

A schematic depiction of one thermocouple junction, located near the edge of the wake, and its associated temperature field is given in Figure 42. The oblique lines inclined at an angle with respect to the wake centerline represent isotherms at three different temperatures.

If the thermocouple remains in a fixed orientation with respect to the heater, a rotation of $\delta\theta$ over an arc length λ is required to change the temperature at the thermocouple junction from T_1 to T_3. If the junction is free to move about its nominal location, changing its radius as well as its azimuthal position, it need only move a distance δ for the temperature to change from T_1 to T_3. This will result in an apparent angular error $\delta\theta$. Therefore, for a sagging thermocouple, the largest apparent angular error occurs when the displacement of the junction from its nominal location is perpendicular to the isotherms. The magnitude of this maximum error, for $\theta = 67.5°$, will be

$$\delta\theta_{max} = \frac{\delta}{r[\cos(67.5° - \alpha)]} \tag{23}$$

where δ comes from the differential expansion analysis discussed above and r is the nominal radius of the thermocouple junction about the heater centerline.

Figure 43 shows the magnitude of the maximum angular error $\delta\theta_{max}$,† which is a random contribution to the dead band angle for the hot case. Values of the isotherm divergence angle α†† are shown as a function of Reynolds number in Figure 44.

4.2.7.1.2.4 Total Random Error

The total random error is computed by combining the results presented in Figures 39, 41, and 43, together with minor contributions from other error sources, in root-sum-square fashion. The results are shown in Figure 45.

†The upstream junction of the thermocouple pair in question may also move to a region of different temperature, thereby changing the thermocouple output. The upstream thermocouple exists in a region of smaller temperature gradients, however, and this error contribution has therefore been neglected.

††E. R. G. Eckert and E. Soehngen, "Distribution of Heat Transfer Coefficients around Cylinders in Crossflow at Reynolds Numbers from 20 to 500," Transactions of the ASME, April 1952, pp. 343-347.

4.2.7.1.2.5 Total Dead Band

The total angular dead band half angle, obtained by summing the results from Figures 36 and 45, is shown in Figure 46. The quadrant sensor dead band is always less than ±10°.

4.2.7.3 Wind Direction Sensor

When the quadrant sensor is operated as a wind direction sensor (for $Re_f \lesssim 60$), the data reduction process used is the one discussed in Section 2. The outputs of the two thermocouple pairs are obtained and plotted against one another in the format shown in Figure 7. By comparison with calibration data, plotted in the same manner, the wind angle can be immediately read.

Errors in the thermocouple outputs introduce an uncertainty in the wind angle measurement. A list of the possible errors contributing to the wind direction error is given in Table 3. The error sources marked with asterisks contribute significantly to the total error and are discussed in some detail below. Again, the list is broken down into systematic errors (heat conduction) and random errors.

4.2.7.3.1 Systematic Errors

4.2.7.3.1.1 Heat Conduction Errors

The configuration analyzed and the analysis used are exactly as discussed in Section 4.2.7.1.1.1. Equation (12) from that section (which is independent of angle) was used to estimate the relative error in thermocouple output due to conduction. The results are exactly as shown in Figure 32 for the hot and cold cases.

Note that the relative reduction in the output of each thermocouple pair due to heat conduction from the hot side to the cold side is the same for both thermocouple pairs. The net result of heat conduction is therefore to "shrink" the patterns in Figure 7 radially inward, as is indicated in Figure 47. If the constant angle contours shown in Figure 47 were strictly radial, the angular error due to heat conduction would be zero. For the curved contours shown, an angular error occurs due to the displacement of the operating condition off the calibration curve.

The resulting uncertainties in wind direction, as a function of the sensor orientation (i.e., the orientation of one thermocouple pair with respect to the wind) and the film Reynolds number, are presented in Figure 48 for the cold case and 49 for the hot case. From Figure 7, the error function will have an eight fold symmetry, repeating every 45°. Therefore, the angles shown are representative of the entire azimuth. These errors are systematic and cannot be RSS'sd with the random errors. Instead, they must be added to the total random error.

4.2.7.3.2 Random Errors

4.2.7.3.2.1 Uncertainty in Overheat

The relative error in the overheat, by the results presented in Section 3.3.4, is equivalent to the relative error in the thermocouple output after correction for overheat variations. This relative error is presented in Figure 40.

Like the systematic error due to heat conduction, the relative errors for the two thermocouple pairs due to overheat uncertainty will be identical. Therefore, the effect on the sensor output will be a radial change in the calibration pattern when viewed in the format of Figure 47. The difference with the overheat uncertainty, however, is that the emf error can be positive or negative, so that the pattern can either shrink or swell along radial lines and the angular error can have either sign. Nevertheless, the technique employed in the evaluation of the angular error is similar to that used for heat conduction errors.

The random errors in wind direction due to errors in overheat scaling are shown in Figures 50 (cold case) and 51 (hot case).

4.2.7.3.2.2 Errors Due to Movement of Thermocouple Junctions

The differential expansion analysis used in Section 4.2.7.1.2.3 applies here, as does the analysis relating thermocouple displacement to equivalent angular error. The apparent angular error of each downstream thermocouple* was first computed separately. Since the two thermocouple outputs are not used separately, but are combined to determine the wind direction in the manner

*Although the upstream thermocouple from each pair can also move, the temperature gradients in the flowfield around the upstream junction are assumed negligible.

discussed above, the proper logic must be used for combining the angular errors due to movement of each thermocouple to produce the total angle error due to movement of both thermocouples.

Consider the net shown schematically in Figure 52. The figure represents a section of Figure 7, with one set of oblique lines representing contours of constant wind angle and the other set of lines representing contours of constant Reynolds number. The calculated apparent angular displacements of the two downstream thermocouples ($\delta\theta_1$ and $\delta\theta_2$) are equivalent to two emf errors δE_1 and δE_2 where

$$\delta E_1 = \left.\frac{\partial E_1}{\partial \theta}\right)_{Re} \delta\theta_1 \tag{24}$$

and

$$\delta E_2 = \left.\frac{\partial E_2}{\partial \theta}\right)_{Re} \delta\theta_2 \tag{25}$$

Let

$$a = \left.\frac{\partial E_1}{\partial \theta}\right)_{Re} \tag{26}$$

$$b = \left.\frac{\partial E_2}{\partial \theta}\right)_{Re} \tag{27}$$

$$c = \left.\frac{\partial E_1}{\partial Re}\right)_{\theta} \tag{28}$$

$$d = \left.\frac{\partial E_1}{\partial Re}\right)_{\theta} \tag{29}$$

Then, at point P_4 in Figure 52,

$$E_1(\theta + \delta\theta_T, Re + \delta Re) - E_1(\theta, Re) = \delta E_1 = a\ \delta\theta_T + c\ \delta Re = a\ \delta\theta_1, \tag{30}$$

and similarly

$$\delta E_2 = b\ \delta\theta_T + d\ \delta Re = b\ \delta\theta_2 \tag{31}$$

Eliminating δRe, we have

$$\delta\theta_T = \frac{ad}{ad - bc}\ \delta\theta_1 - \frac{bc}{ad - bc}\ \delta\theta_2 \tag{32}$$

Equivalently:

$$\left.\frac{\partial\theta_T}{\partial\theta_1}\right)_{\theta_2} = \frac{1}{1 - \left.\frac{\partial E_2}{\partial E_1}\right)_{Re} \left.\frac{\partial E_1}{\partial E_2}\right)_{\theta}} \tag{33}$$

$$\left.\frac{\partial\theta_T}{\partial\theta_2}\right)_{\theta_1} = \frac{1}{1 - \left.\frac{\partial E_1}{\partial E_2}\right)_{Re} \left.\frac{\partial E_2}{\partial E_1}\right)_{\theta}} \tag{34}$$

So, if we wish to determine the total random error in θ_T due to contributions $\delta\theta_1$ and $\delta\theta_2$,

$$\delta\theta_T = \sqrt{\left(\frac{1}{1 - \left.\frac{\partial E_2}{\partial E_1}\right)_{Re} \left.\frac{\partial E_1}{\partial E_2}\right)_{\theta}}\right)^2 \delta\theta_1^{\,2} + \left(\frac{1}{1 - \left.\frac{\partial E_1}{\partial E_2}\right)_{Re} \left.\frac{\partial E_2}{\partial E_1}\right)_{\theta}}\right)^2 \delta\theta_2^{\,2}} \tag{35}$$

The values of $\partial E_1/\partial E_2)_{Re}$ and $\partial E_1/\partial E_2)_{\theta}$ can be obtained, graphically, from Figure 7. When the individual errors $\delta\theta_1$ and $\delta\theta_2$ are subsequently combined, according to the above equation, the total random errors shown in Figure 53 are obtained. Again, because of the eight-fold symmetry of Figure 7, estimation of errors between 0° and 45° suffices to completely characterize the sensor for all angles. The errors shown in Figure 53 are for the hot case only since, as was discussed in Section 4.2.7.1.2.3, the thermocouple wires remain taut at ambient temperatures below room temperature (296°K).

4.2.7.3.2.3 Total Random Error

The total random errors in wind direction, determined by combining the results shown in Figures 48, 49, 50, 51 and 53 (with minor contributions from other error sources) in root-sum-square fashion, is shown in Figures 54 (cold case) and 55 (hot case).

4.2.7.3.2.4 Total Wind Direction Error

The total error in the quadrant sensor wind direction measurement is obtained by summing the results shown in Figures 48 and 54 (cold case) and Figures 49 and 55 (hot case). The results are presented in Figures 50 and 57. The total wind direction error is always less than about 10° for $Re_f < 60$.

4.2.8 Direction Resolution

The quadrant sensor must respond to a change in wind direction of ±10° at wind speeds below 25 m/sec and ±5° at wind speeds above 25 m/sec. The only element which limits the resolution of the sensor is the A-D converter which translates the analog thermocouple emf into a digital word. The word length (equivalent to 9 bits) encompasses a range of thermocouple emfs from -5.0 mv to +5.0 mv (about -80° to +80°C) giving a resolution of about .020 mv or about 1/3°C. This resolution is more than adequate to meet the requirement, as can be seen by inspection of Figures 3 and 4, and 9 through 15.

Table 1. Functional Requirements Impacted by Quadrant Sensor

PARAGRAPH (PD 7400090)	REQUIREMENT	PERFORMANCE	HOW VERIFIED	REMARKS
3.1.1.2.2.1	RANGE - 2-150 m/sec at pressure 2-20 millibars and temperature 130°K-350°K over an azimuth of 360°	To specification	Design and Test	
3.1.1.2.2.6	CALIBRATION -	To specification	Test and Analysis	
3.1.1.2.2.7	RESPONSE TIME - The response time to a step change in wind shall not exceed 2 seconds	To specification	Test and Analysis	Based on temperature sensor response time test
3.1.1.2.2.8	WARM UP TIME - Meet performance requirement 4 seconds after input power applied to electronics	To specification	Test and Analysis	Based on MEA-MSA warm up test

Table 1. Functional Requirements Impacted by Quadrant Sensor

(Continued)

PARAGRAPH (PD 7400090)	REQUIREMENT	PERFORMANCE	HOW VERIFIED	REMARKS
3.1.1.2.2.9	ATTITUDE - Meet requirements in any attitude within ±25 degrees of nominal position	To specification	Test and Analysis	
3.1.1.2.2.10	SELF-HEATING - Meet requirements with sensor 20 to 140°C above ambient	To specification	Analysis	
3.1.1.2.2.11	DIRECTION ACCURACY - Absolute accuracy ±20 degrees at speeds 5-25 m/sec and ±10 degrees over high accuracy regions. (Reference P.D. Figures 6 and 7). No direction accuracy requirements in reduced accuracy rnage	To specification	Analysis	
3.1.1.2.2.12	DIRECTION RESOLUTION - ±10 degrees at speeds 5-25 m/sec and ±5 degrees at speeds of 25-150 m/sec	To specification	Analysis	

Table 2. Errors Contributing to Dead Band Angle

Systematic Errors

*Heat Conduction in Thermocouple Wires

*Error Induced by Compromises in Wake Edge Definition

Random Errors

Parasitic Thermocouple Junctions

Thermal Radiation Induced Errors

Solar Radiation Induced Errors

Errors Due to Rarefaction (high M/Re)

*Uncertainty in Reynolds Number as Sensed by Wind Sensor

Electronics:

*Uncertainty in Overheat

Readout of Thermocouple EMF

*Movement of Thermocouple Junctions Relative to Nominal Positions Due to Differential Expansion

Angle of Attack Induced Errors

Calibration Errors:

Uncertainty in Overheat

Readout of Thermocouple EMF

Interpolation Errors

Misalignment of Sensor when Installed in Wind Tunnel or on MSA

Error in Setting Wind Angle During Calibration

Error Induced by Calibrating in Air Rather than CO_2

Errors Induced During Correction of Thermocouple Outputs for Variation of Thermal Power (dE/dT) with Ambient Temperature

Table 3. Errors Contributing to Wind Direction Uncertainty

Systematic Errors

*Heat Conduction in Thermocouple Wires

Random Errors

Parasitic Thermocouple Junctions

Thermal Radiation Induced Errors

Errors Due to Rarefaction (High M/Re)

Electronics:

*Uncertainty in Overheat

Readout of Thermocouple EMF

*Movement of Thermocouple Junctions Relative to Nominal Positions Due to Differential Expansion

Angle of Attack Induced Errors

Calibration Errors:

Uncertainty in Overheat

Readout of Thermocouple EMF

Interpolation Errors

Misalignment of Sensor when Installed in Wind Tunnel or on MSA

Error in Setting Wind Angle During Calibration

Errors Induced During Correction of Thermocouple Outputs for Variation of Thermal Power (dE/dT) with Ambient Temperature

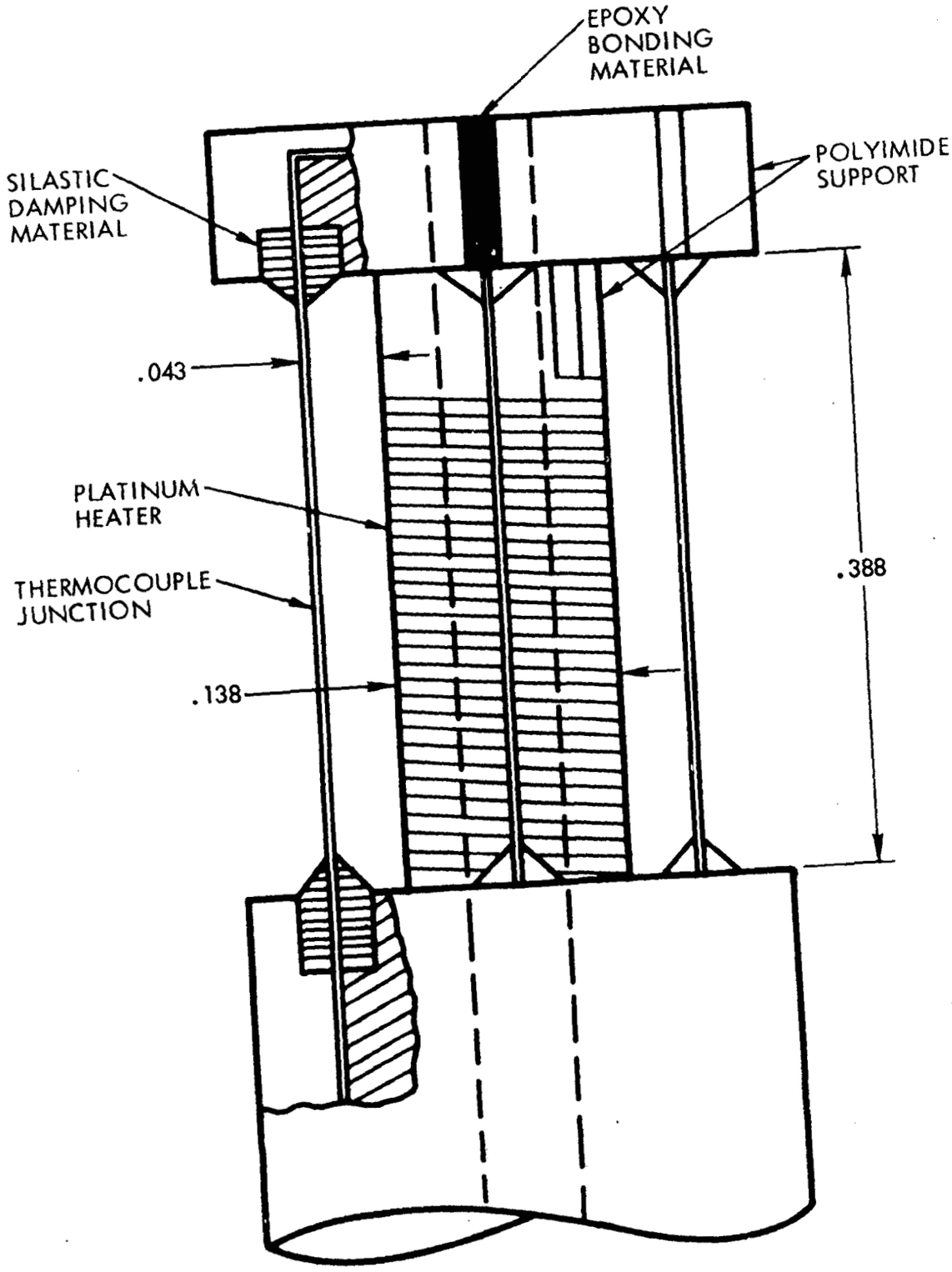

Figure 1. Quadrant Sensor Design

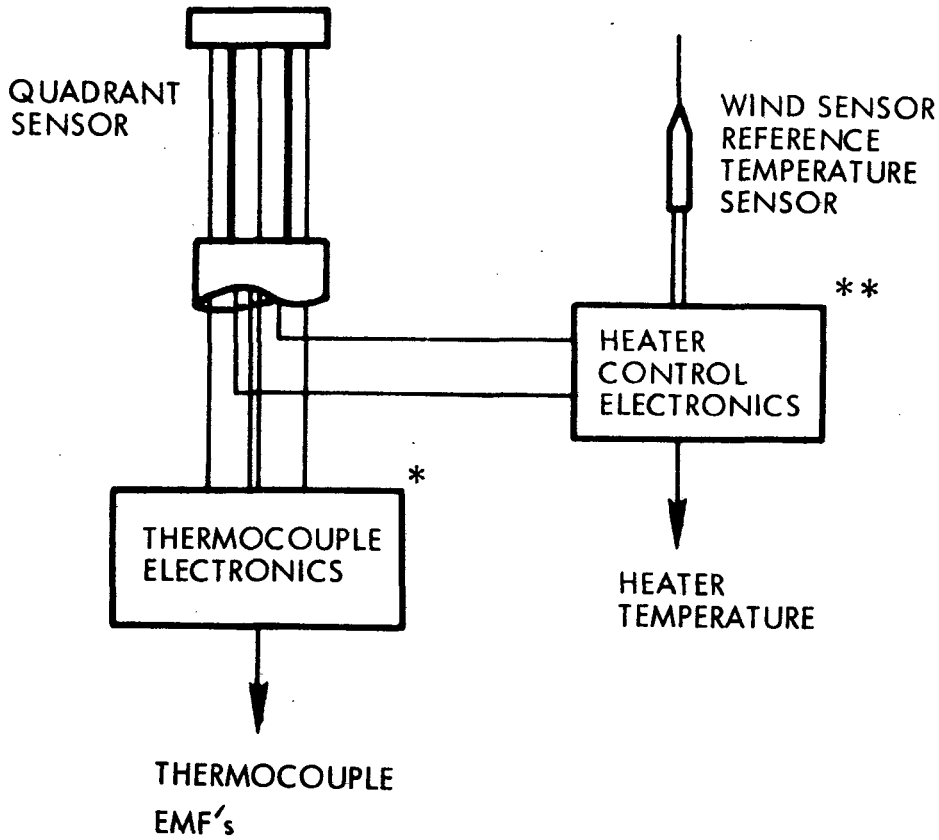

* SIMILAR TO TEMPERATURE SENSOR ELECTRONICS
** SIMILAR TO WIND SENSOR ELECTRONICS

Figure 2. Quadrant Sensor Block Diagram

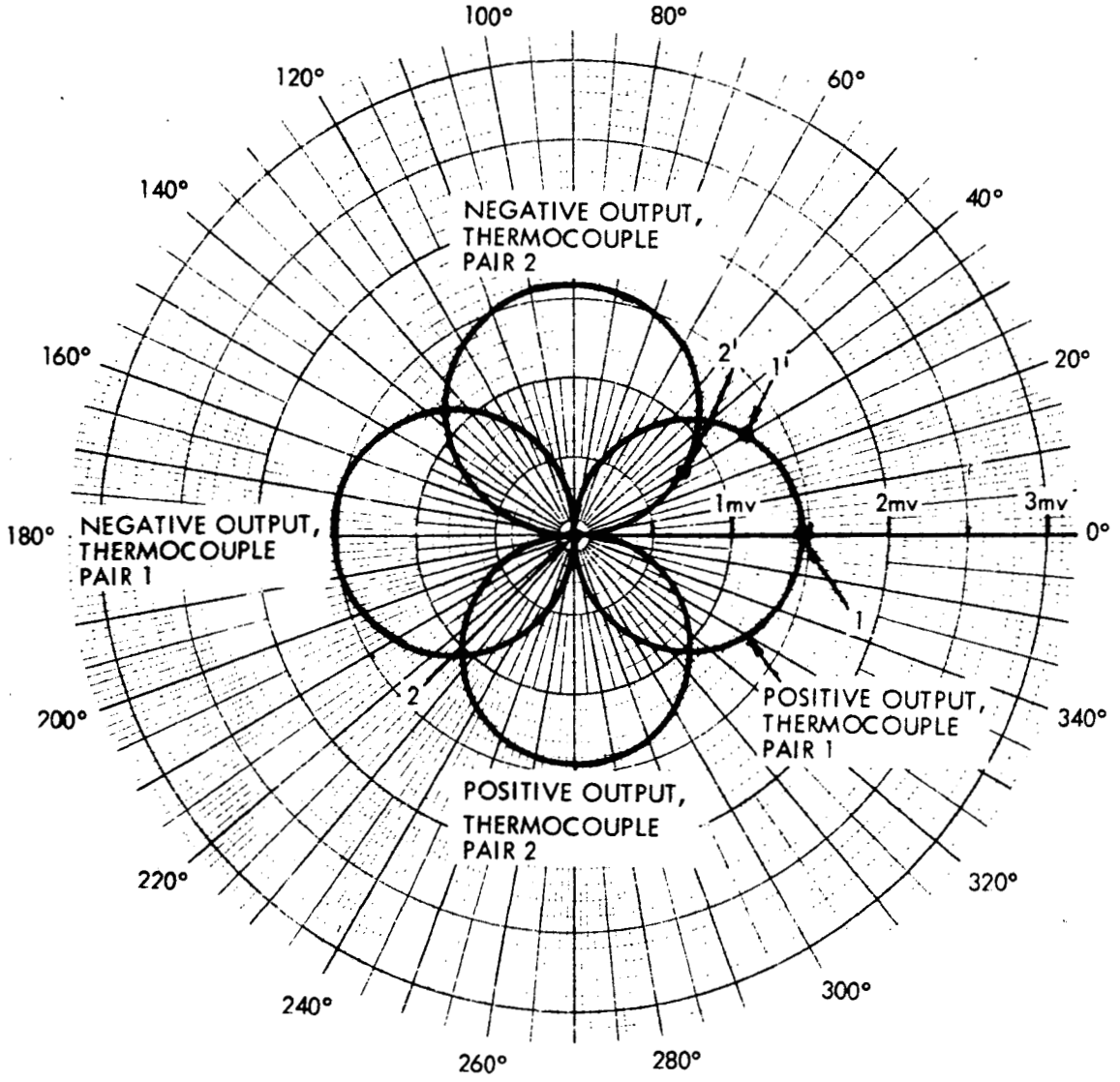

Figure 3. Sensor Output, $Re_f = 6.0$

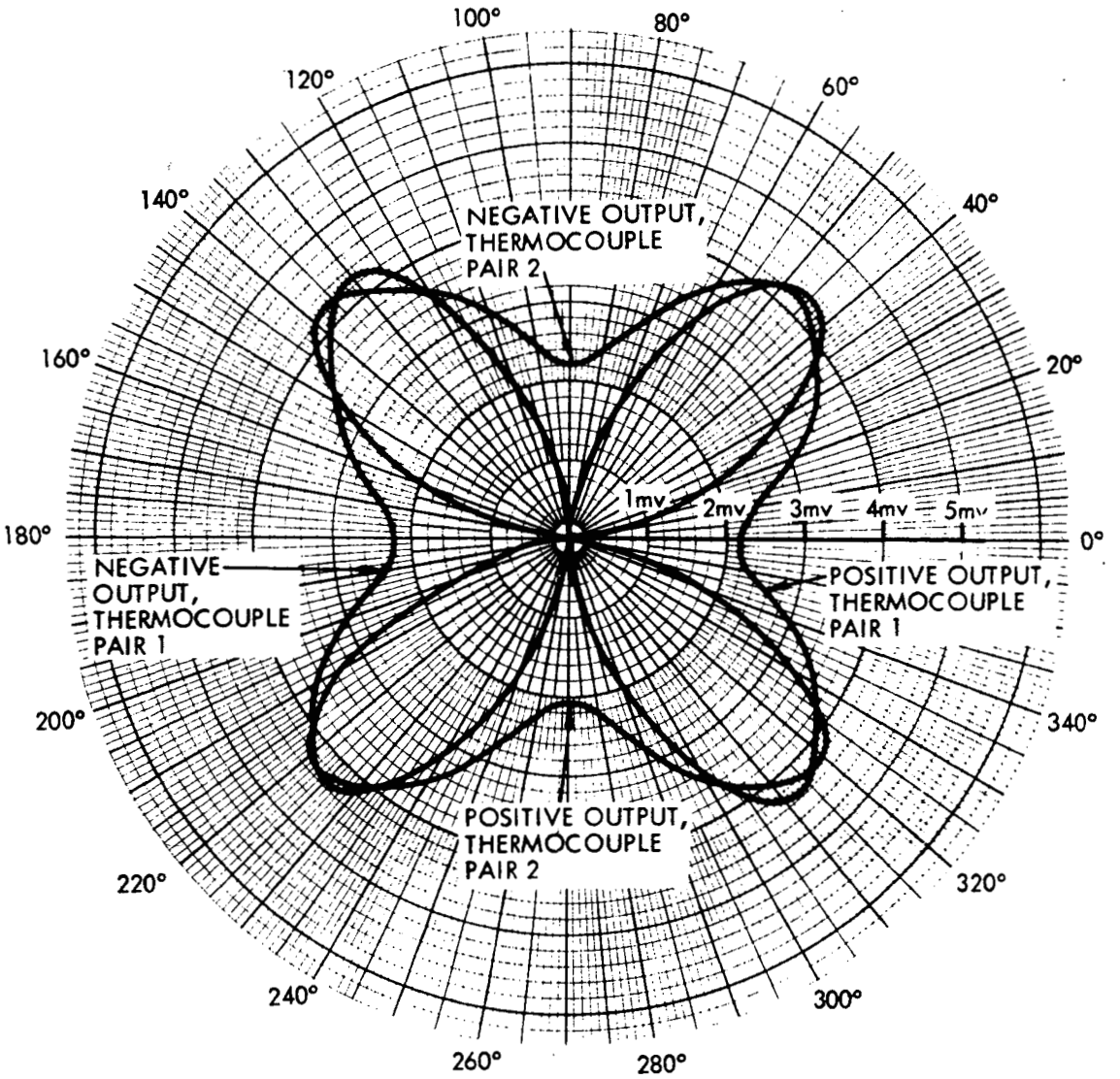

Figure 4. Sensor Output, Re_f = 116

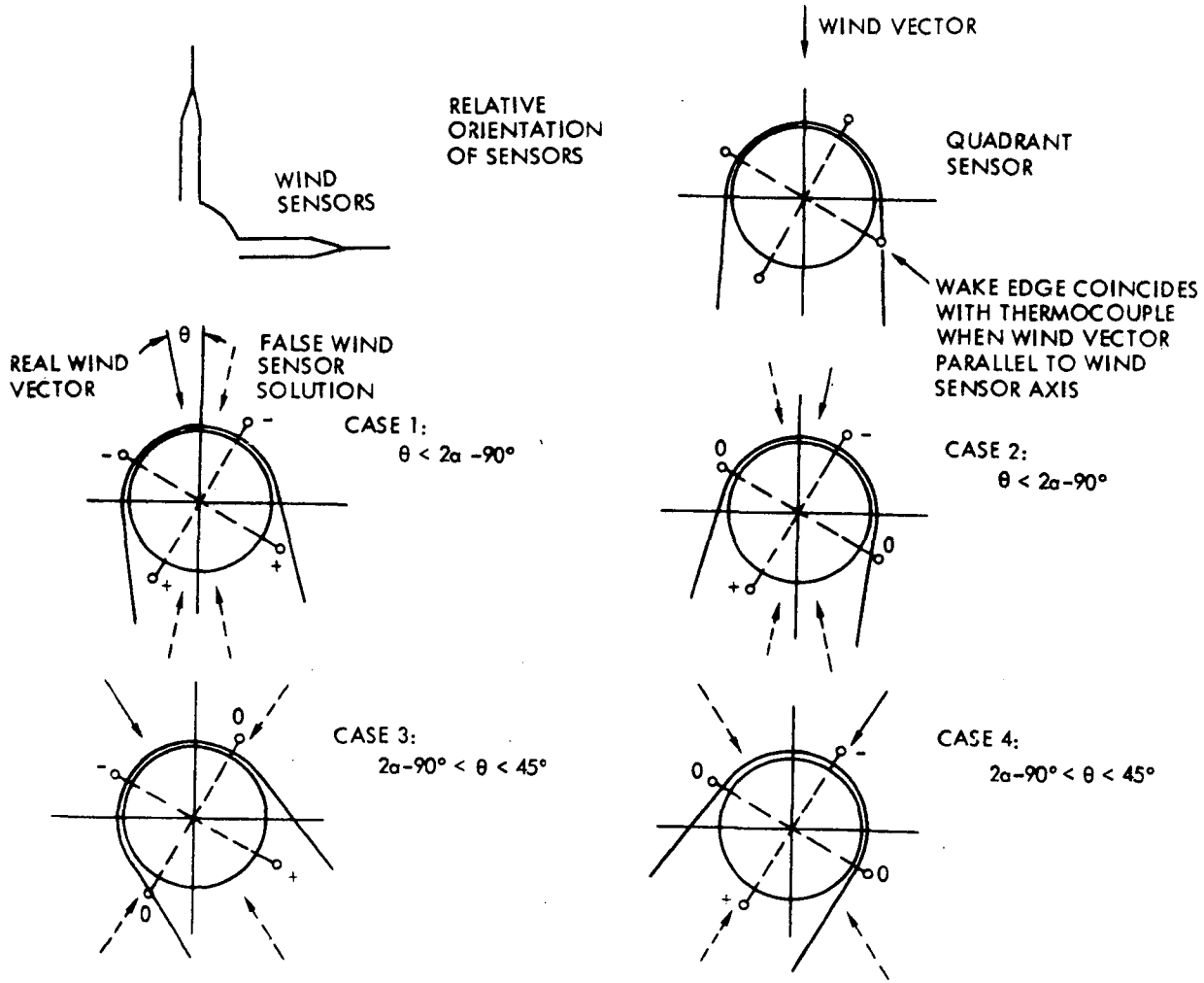

Figure 5. Discrimination against False Wind Sensor Solutions

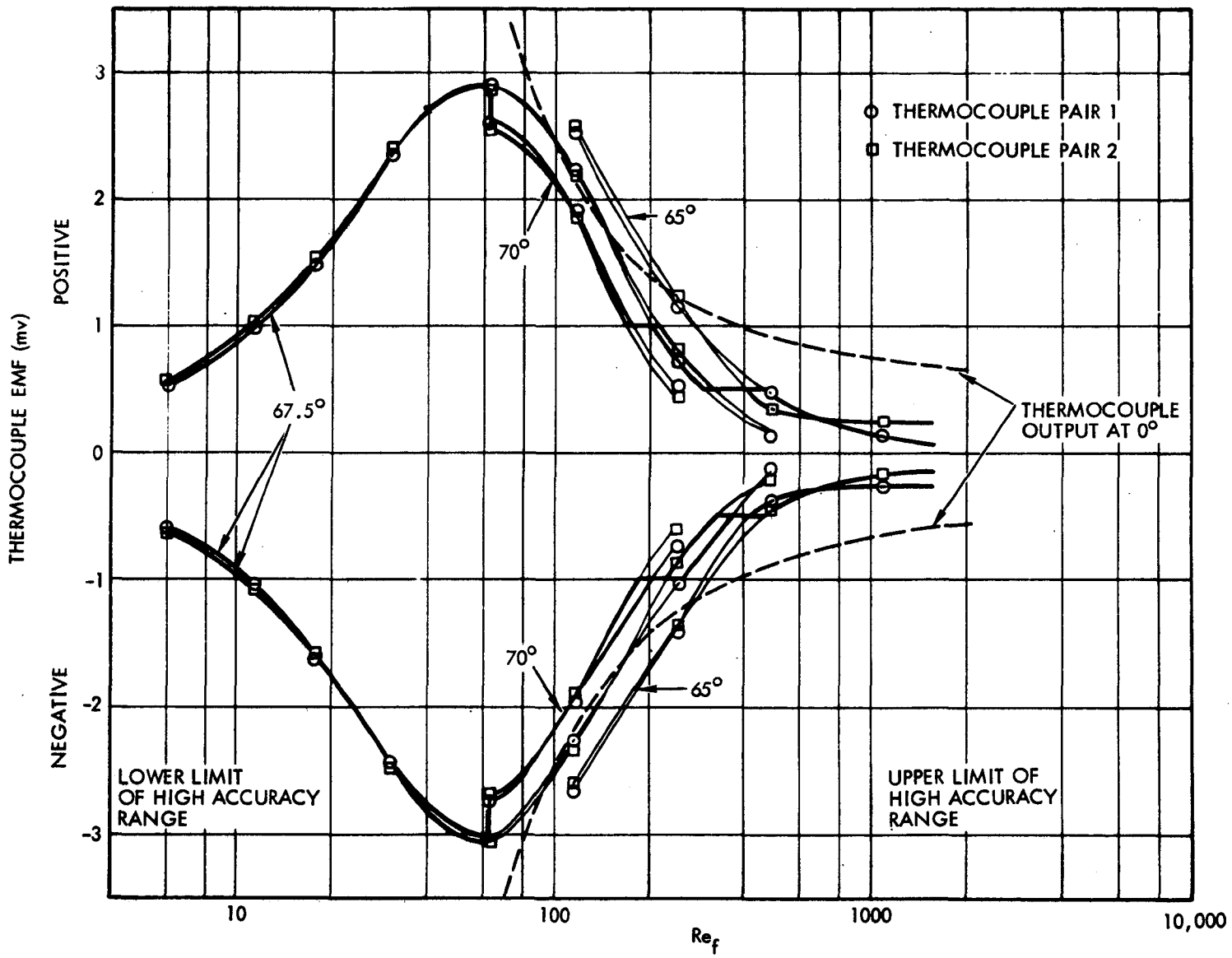

Figure 6. Determination of Wake Edge Criteria.

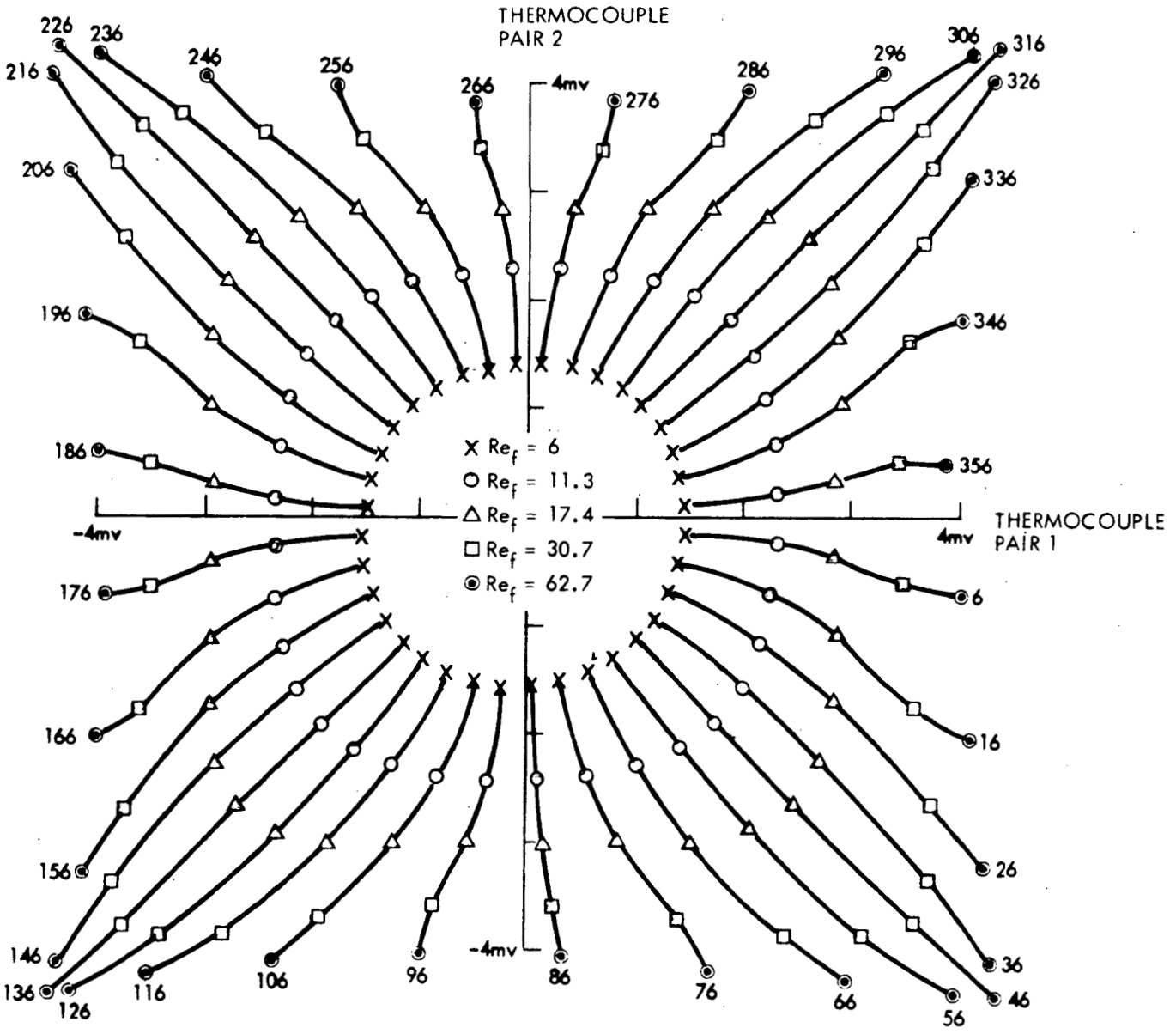

Figure 7. Use of Quadrant Sensor to Determine Wind Direction

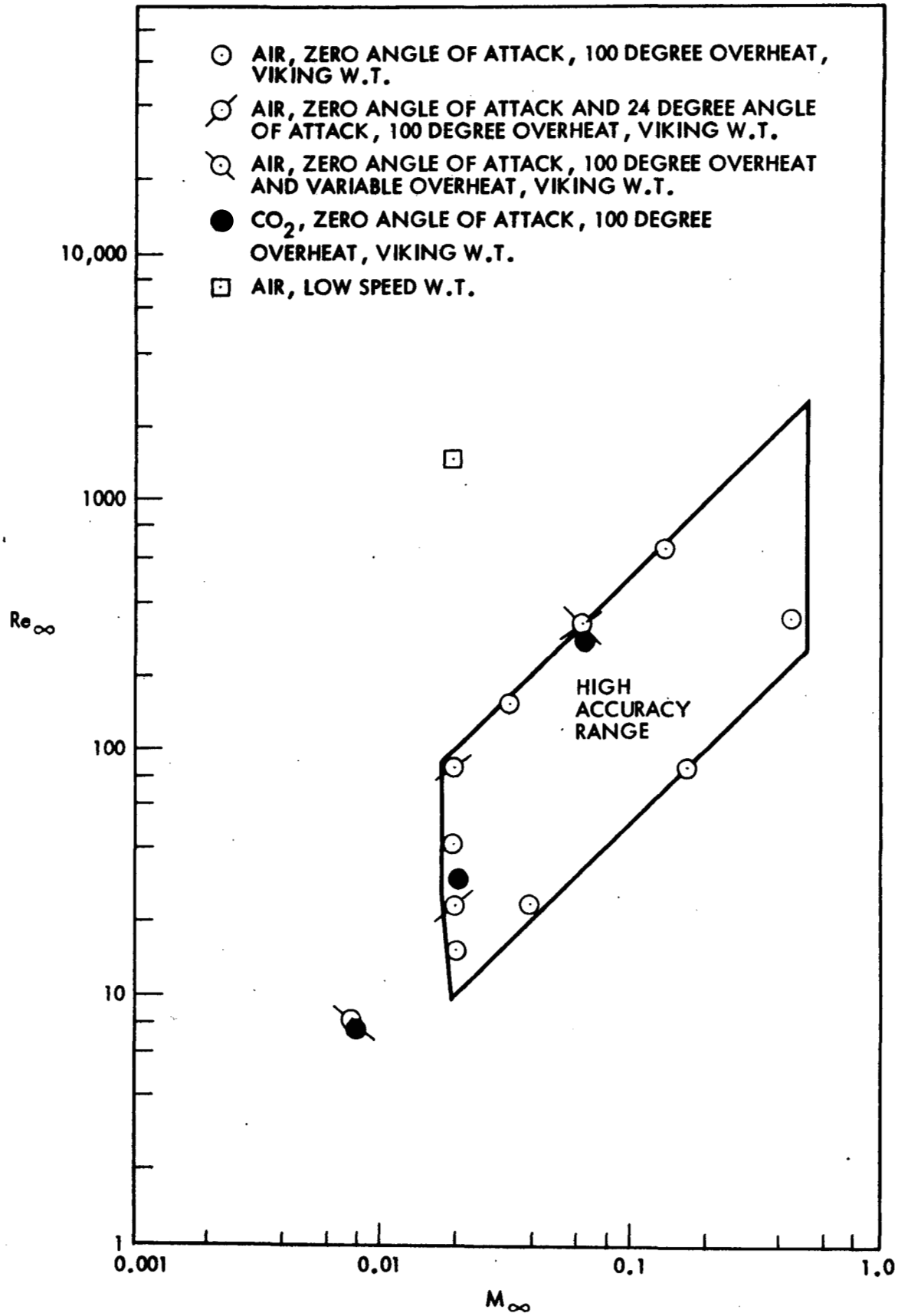

Figure 8. Performance Test Conditions.

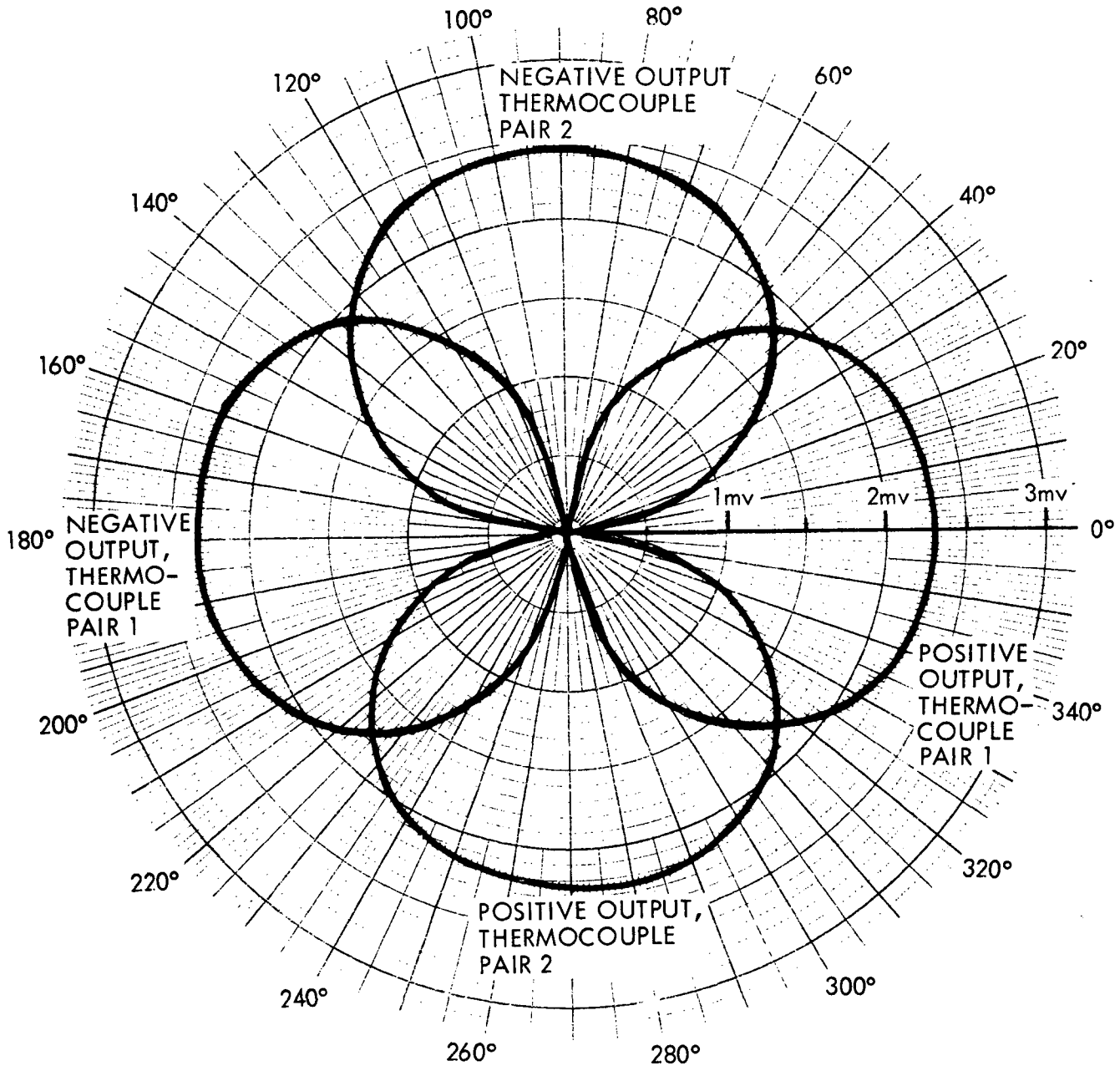

Figure 9. Sensor Output, $Re_f = 11.3$

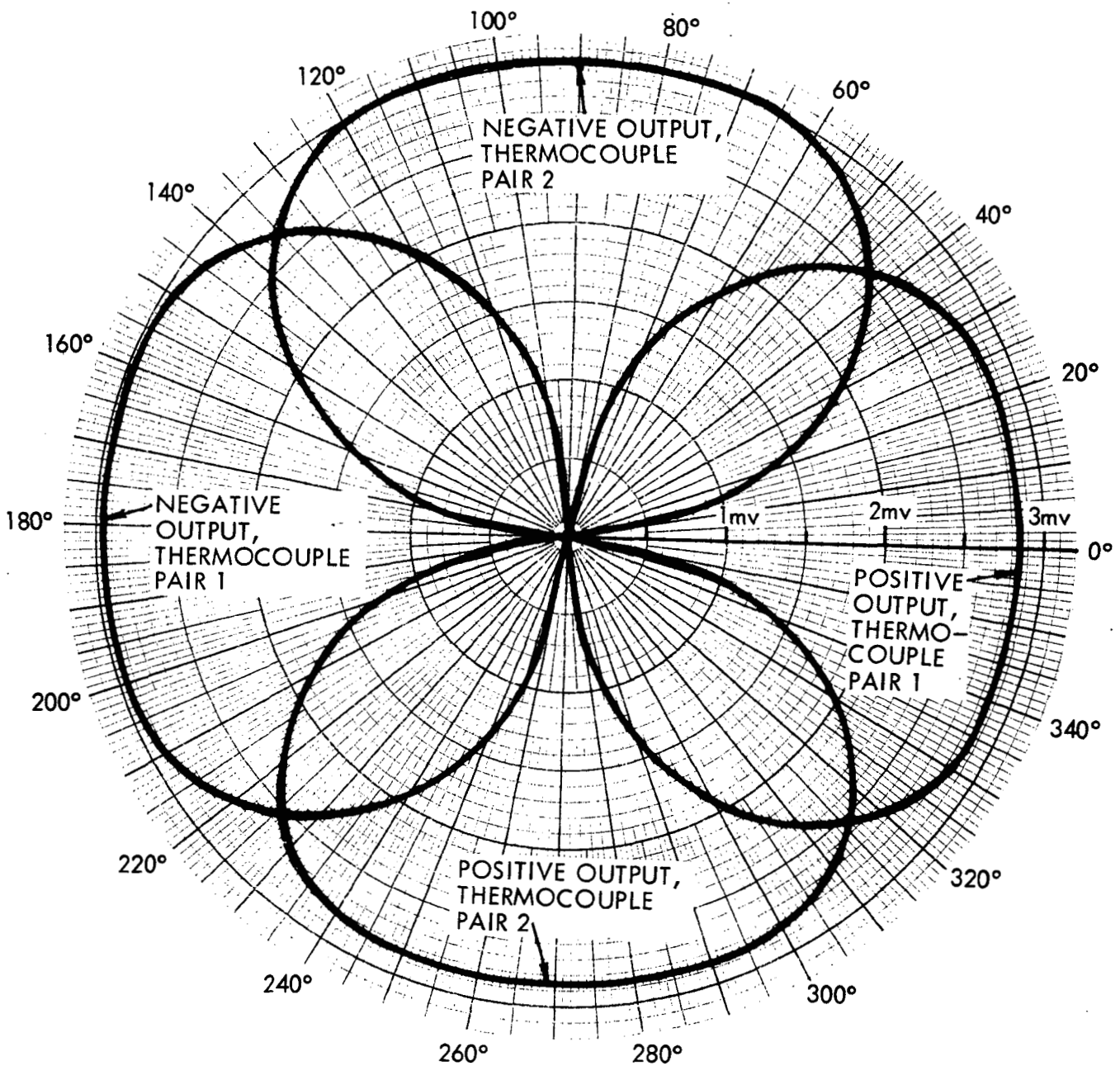

Figure 10. Sensor Output, Re_f = 17.4

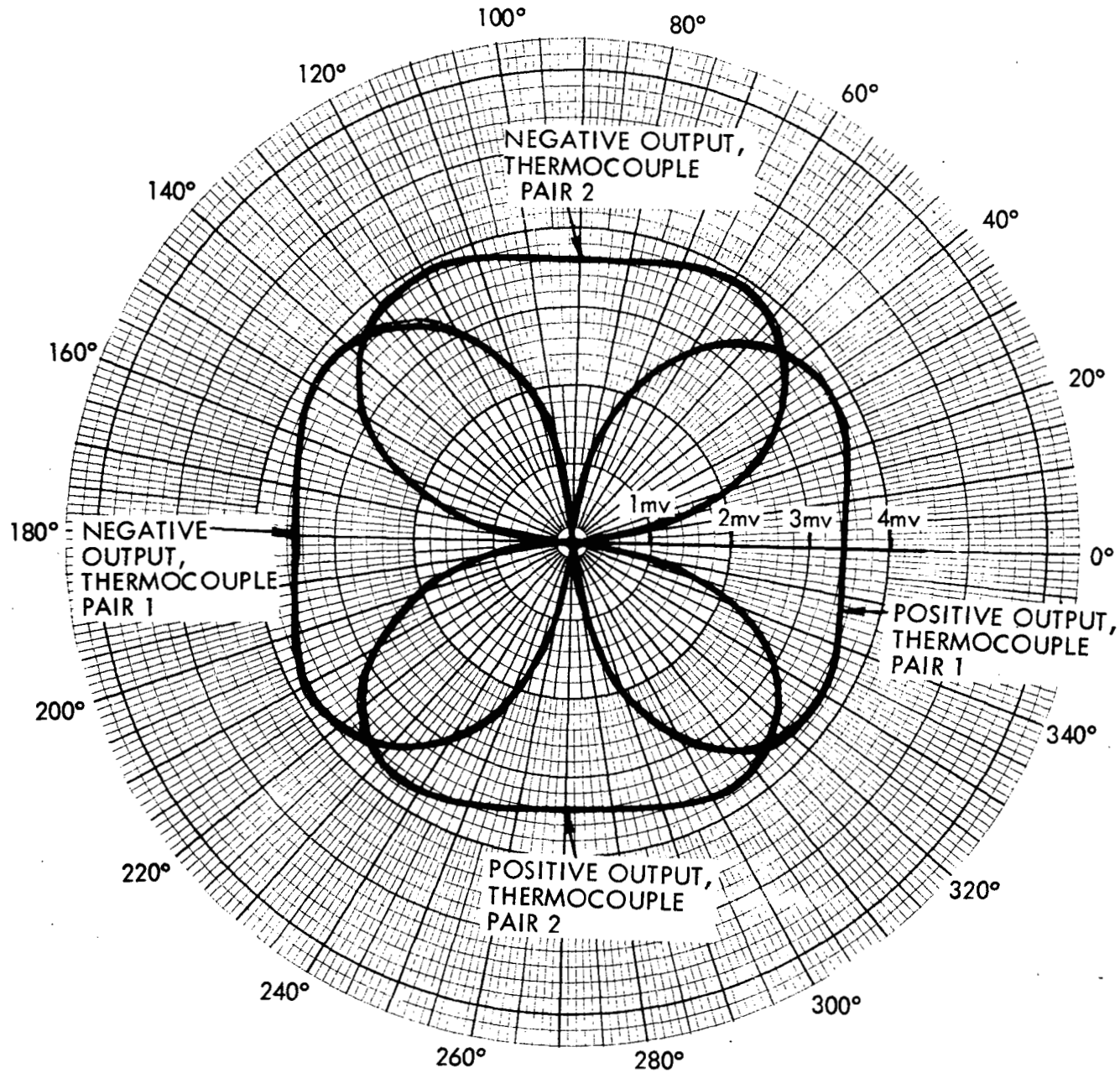

Figure 11. Sensor Output, $Re_f = 30.7$

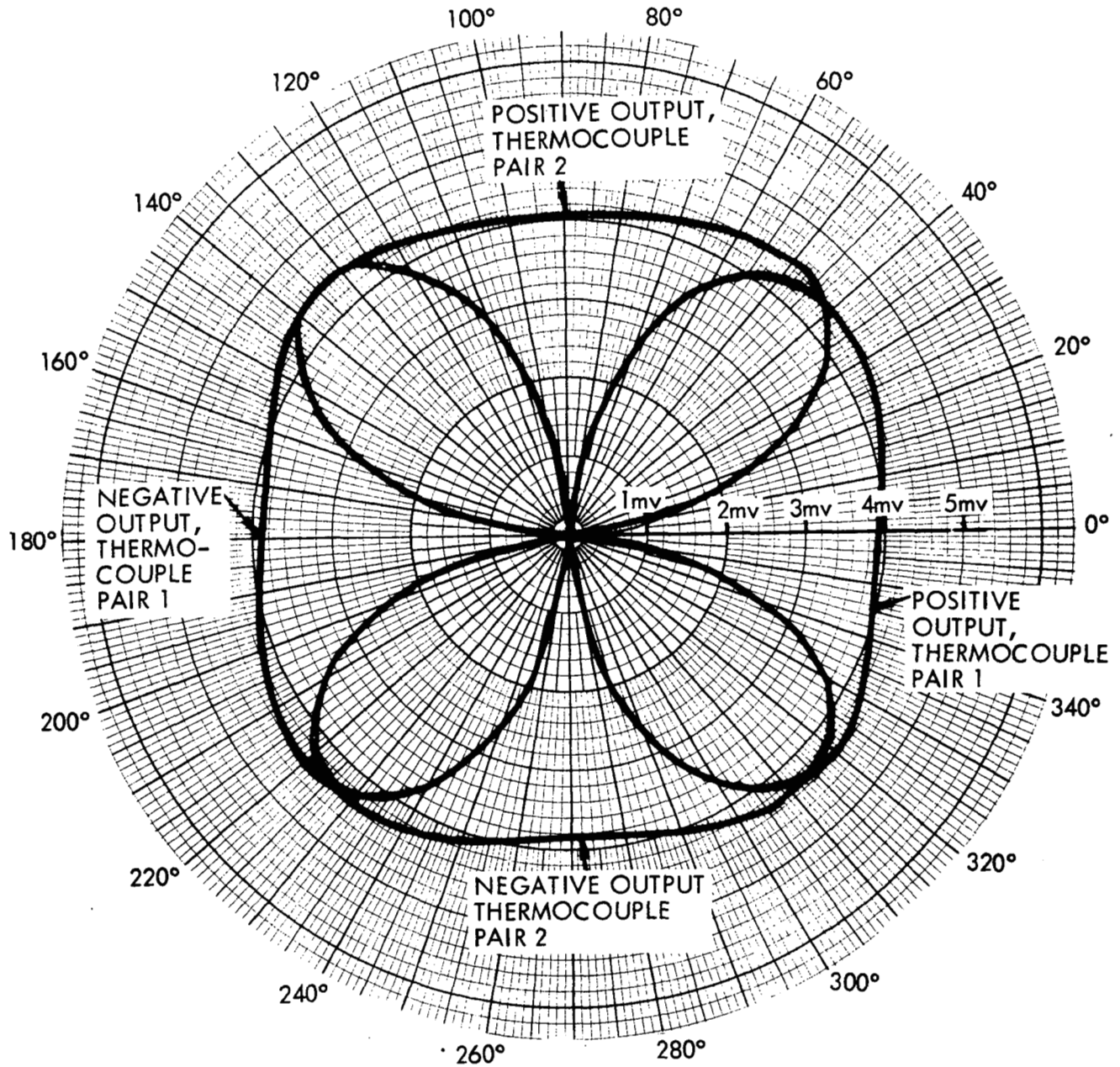

Figure 12. Sensor Output, $Re_f = 62.7$

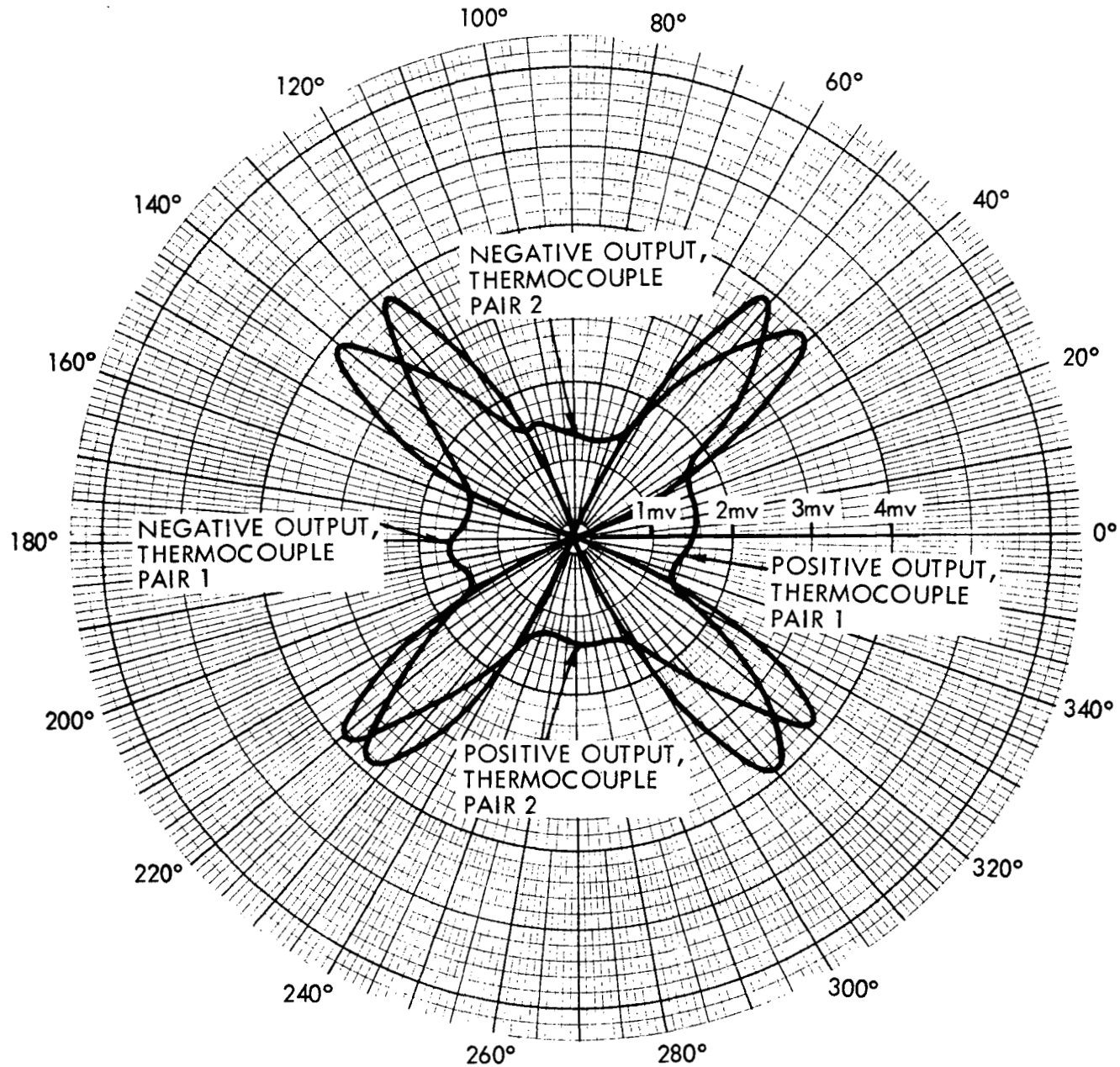

Figure 13. Sensor Output, Re_f = 242

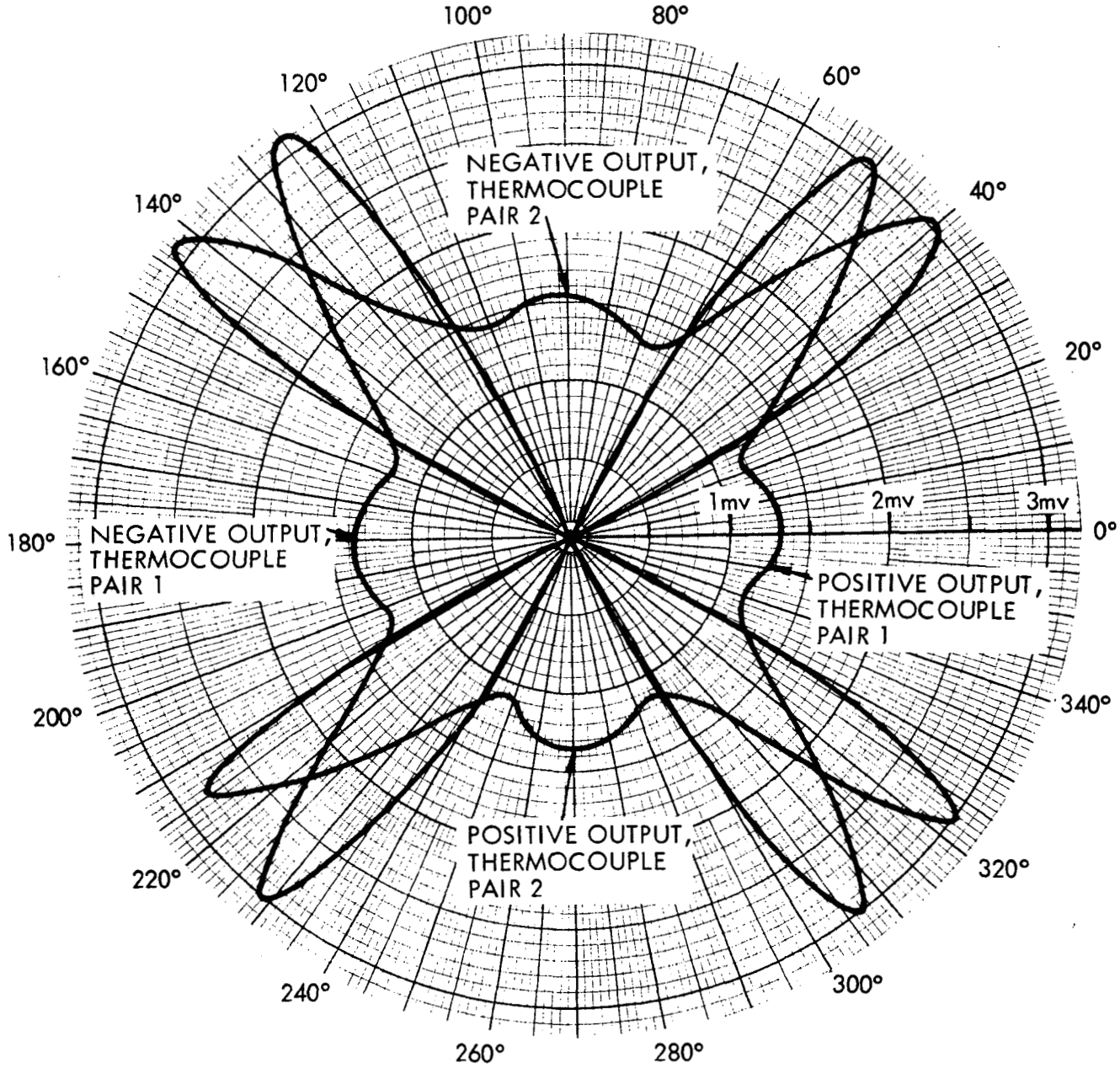

Figure 14. Sensor Output, $Re_f = 491$

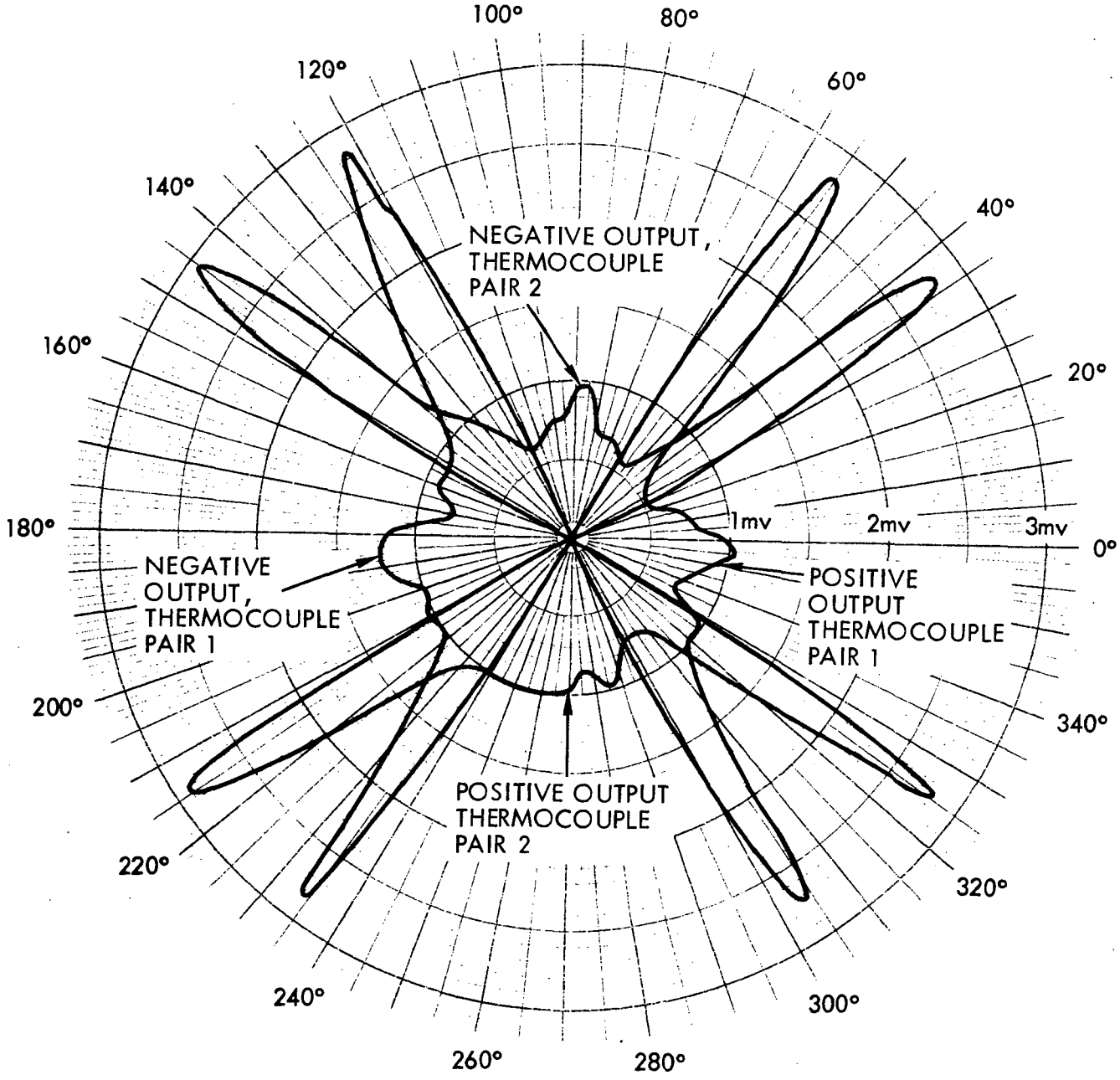

Figure 15. Sensor Output, Re_f = 1090

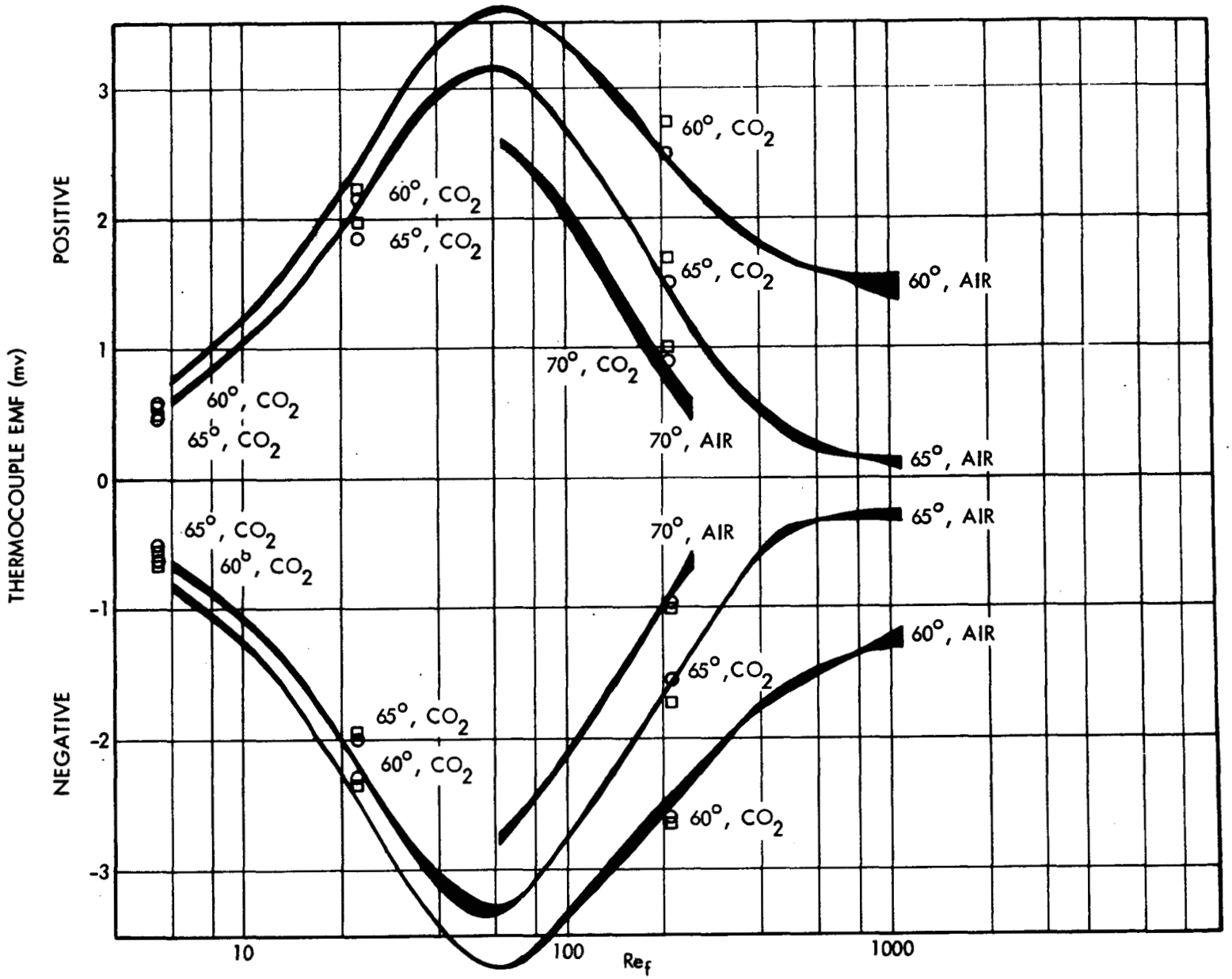

Figure 16. Effect of Gas Composition on Wake Edge Definition

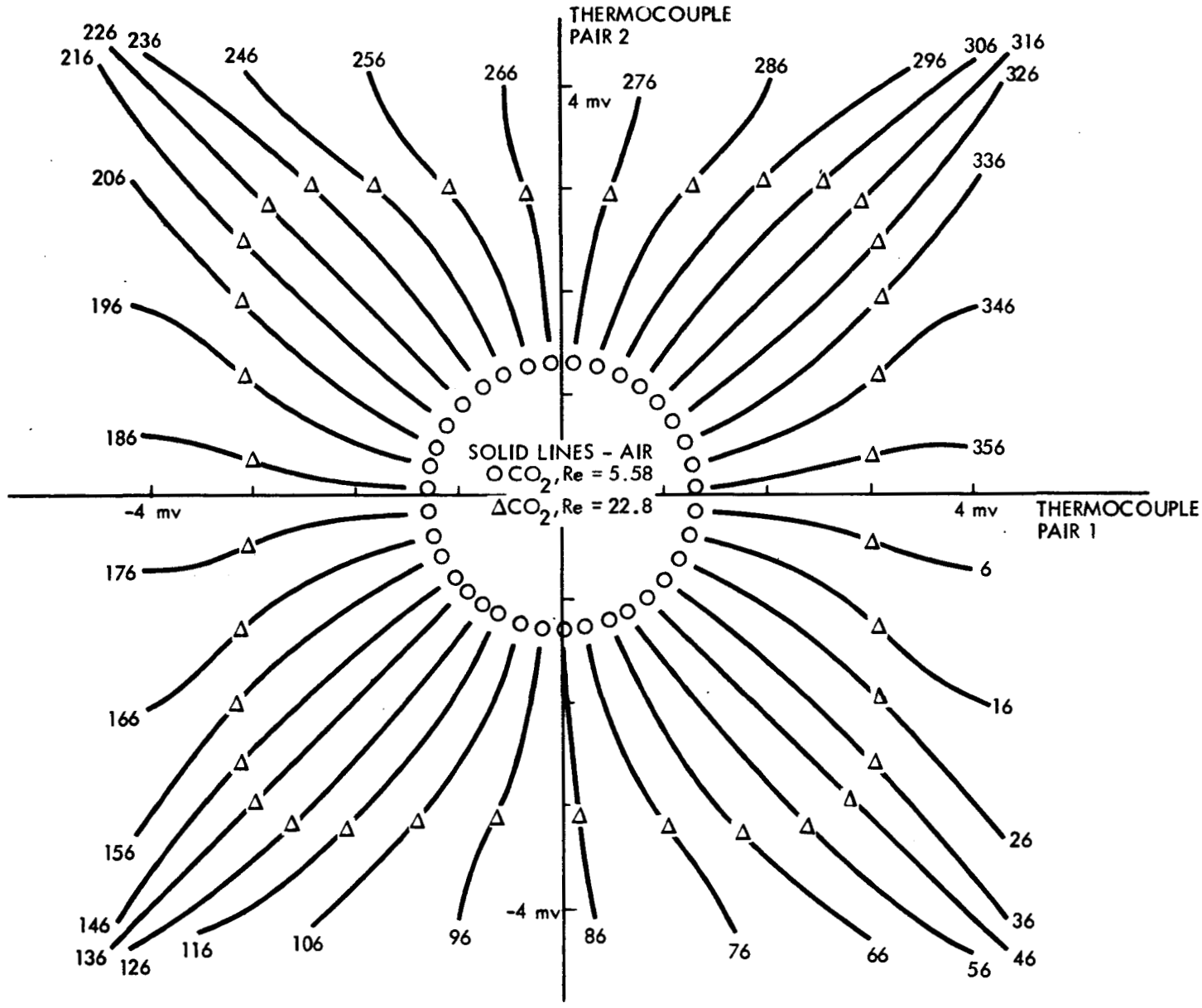

Figure 17. Effect of Gas Composition on Wind Angle Measurement

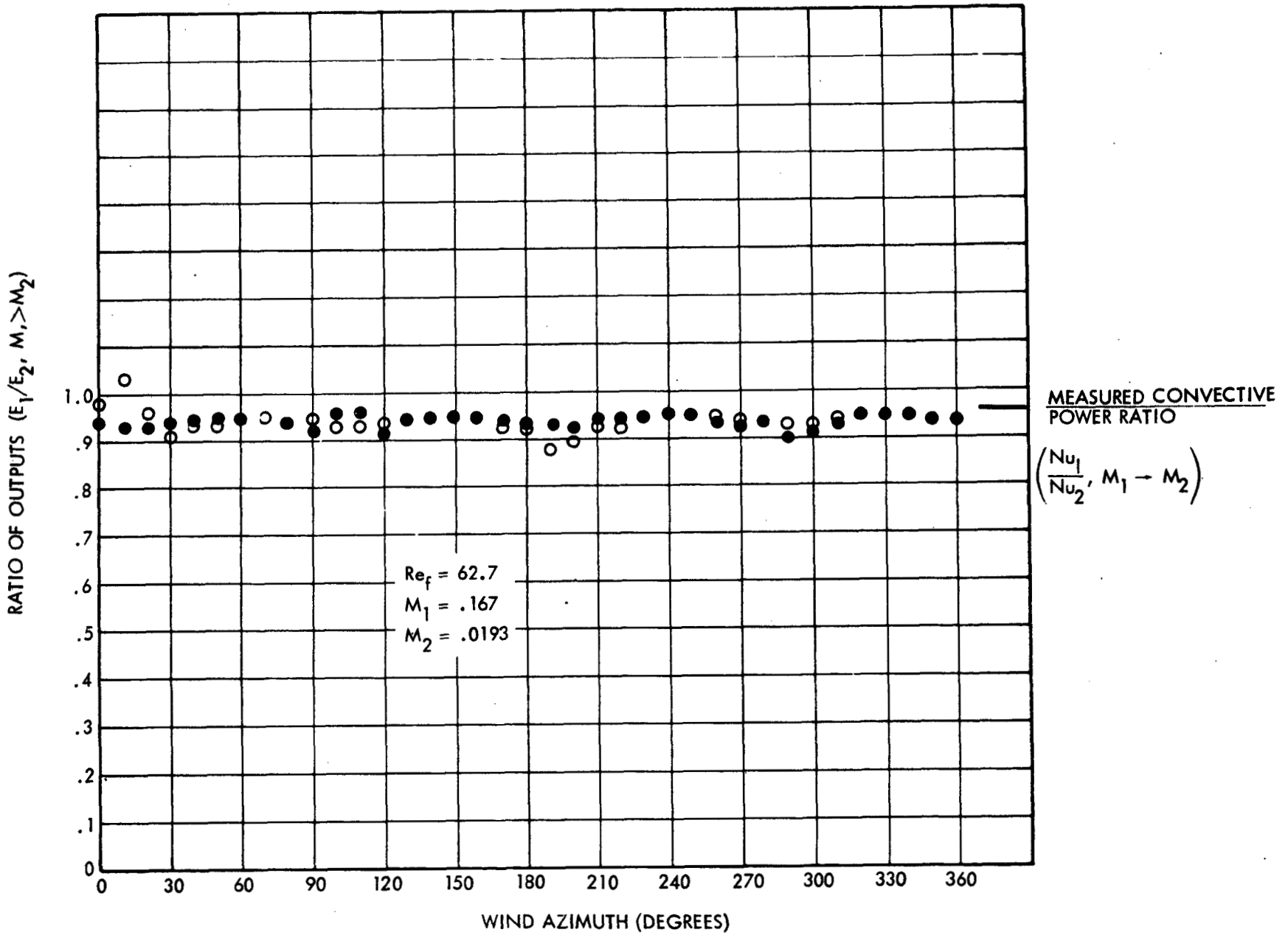

Figure 18. Effect of Rarefaction on Sensor Output.

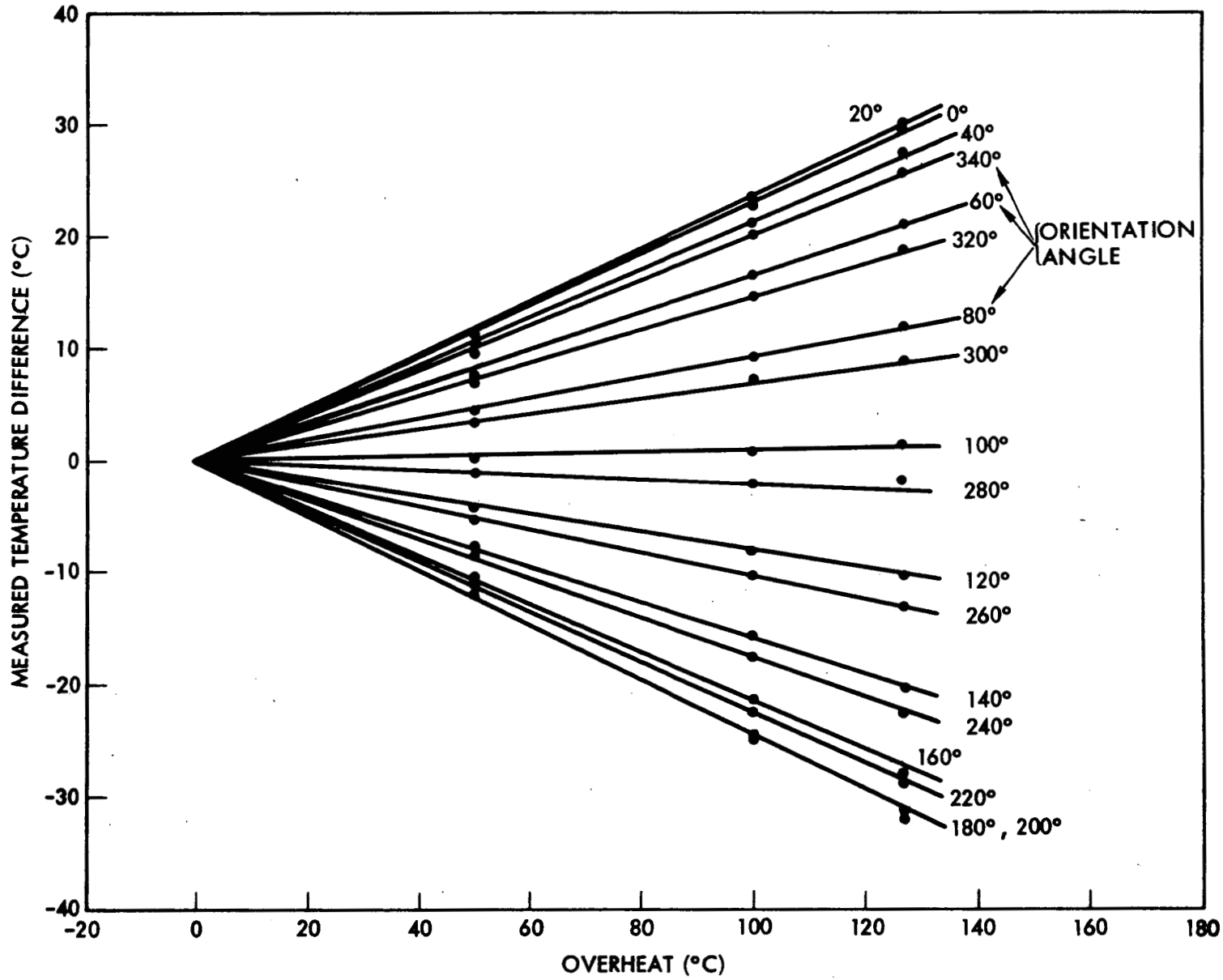

Figure 19. Variation of Thermocouple Output with Overheat, Re_f = 6.0, Thermocouple Pair 1.

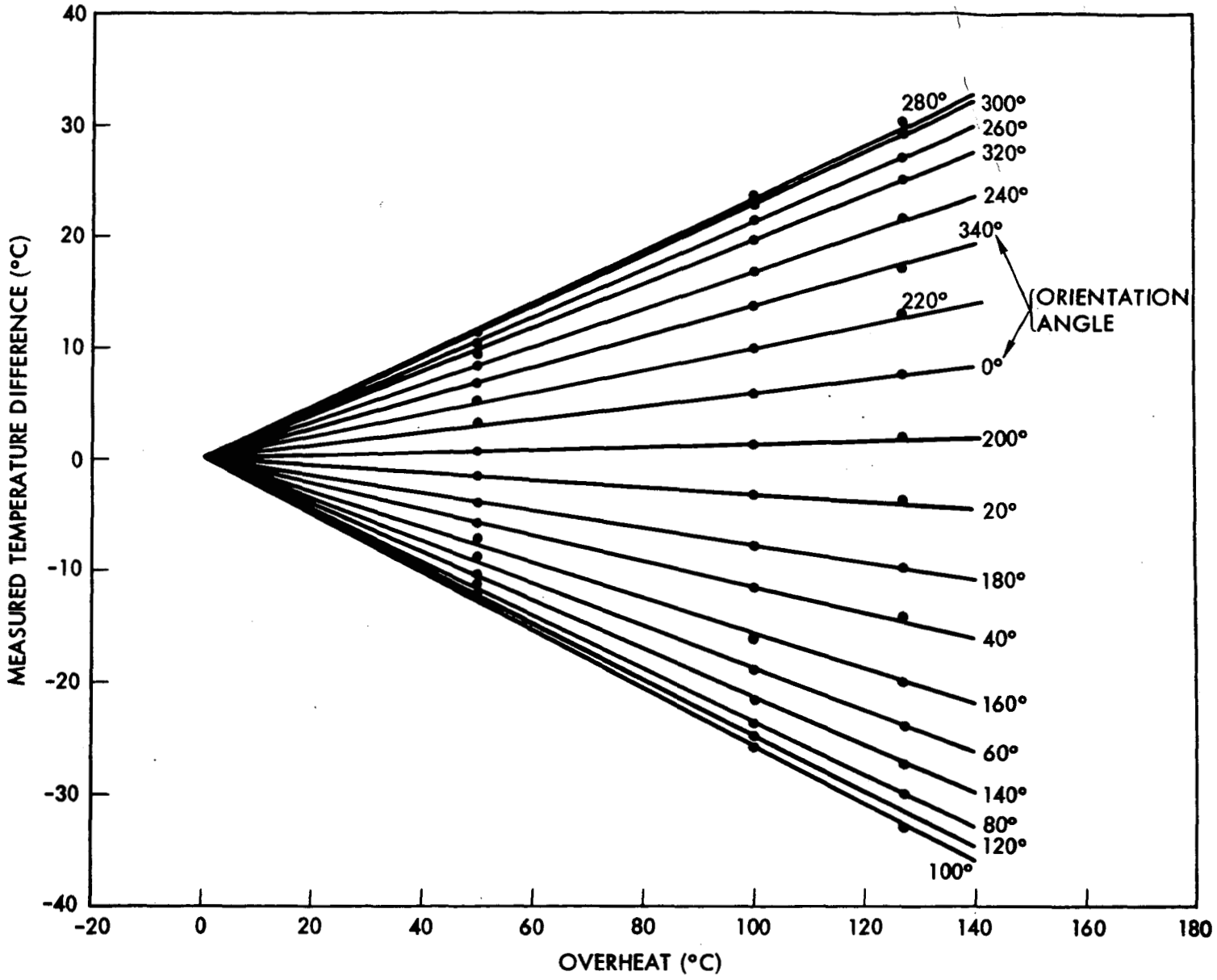

Figure 20. Variation of Thermocouple Output with Overheat, Re_f = 6.0, Thermocouple Pair 2.

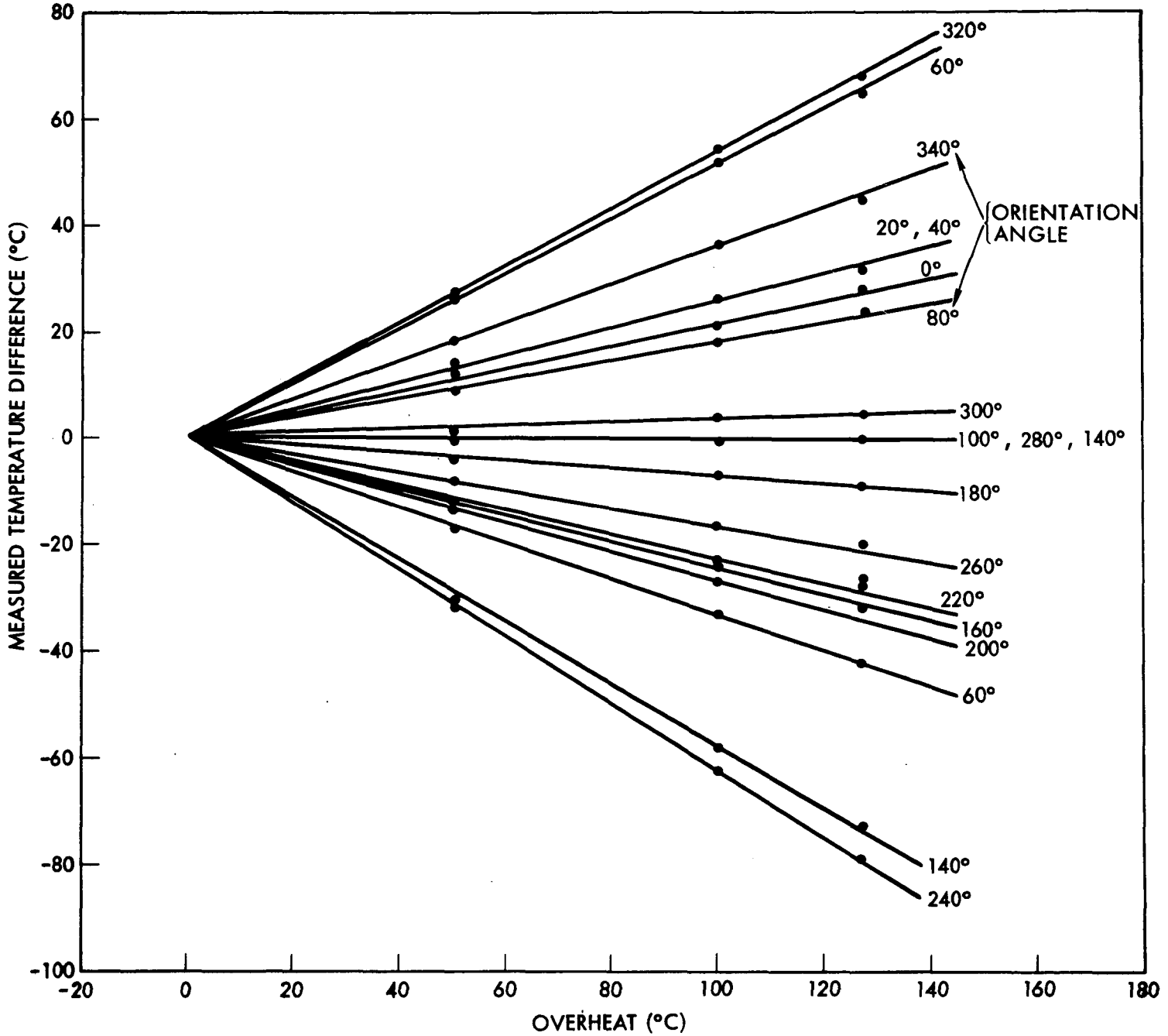

Figure 21. Variation of Thermocouple Output with Overheat, Re_f = 242, Thermocouple Pair 1.

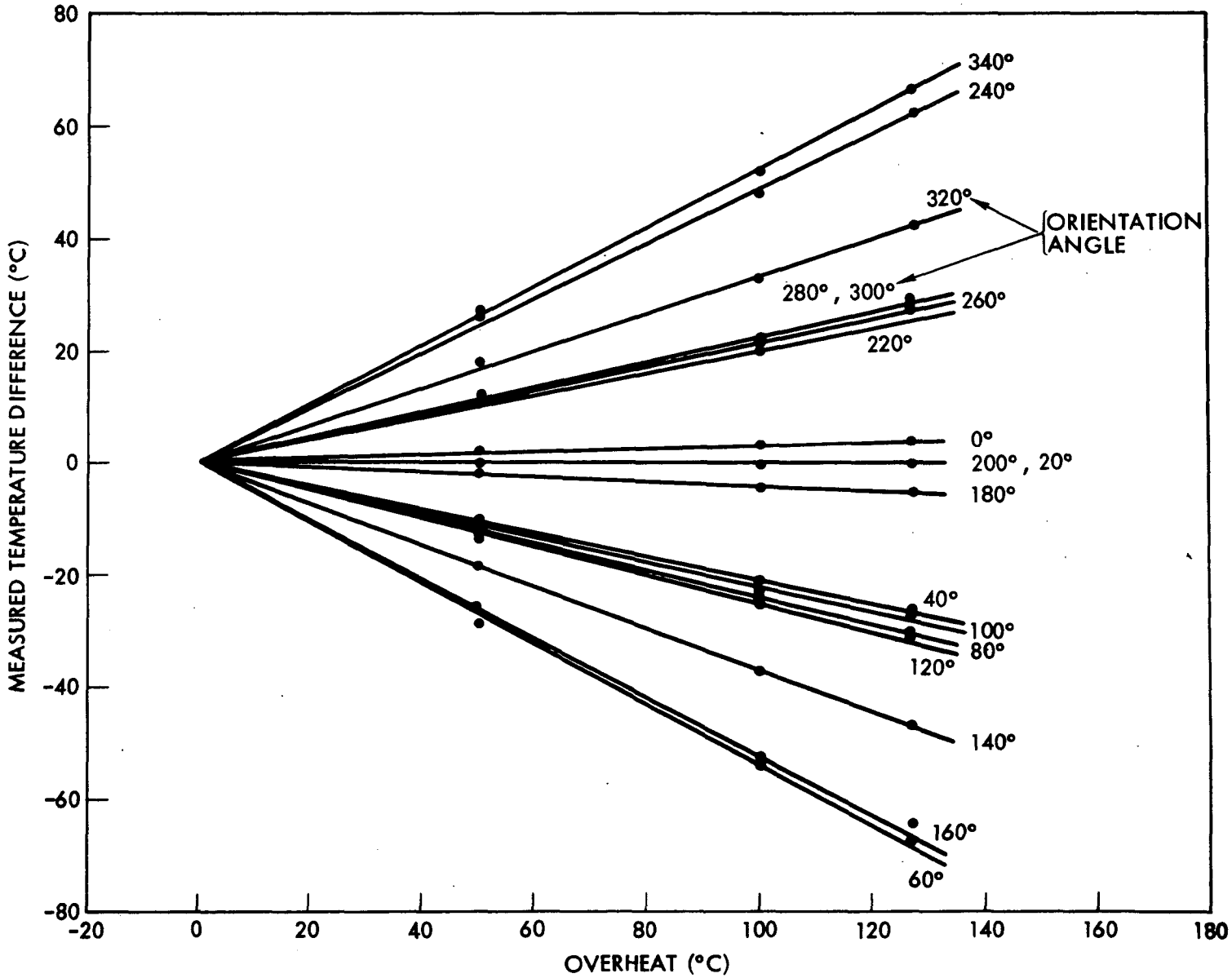

Figure 22. Variation of Thermocouple Output with Overheat, Re_f = 242, Thermocouple Pair 2.

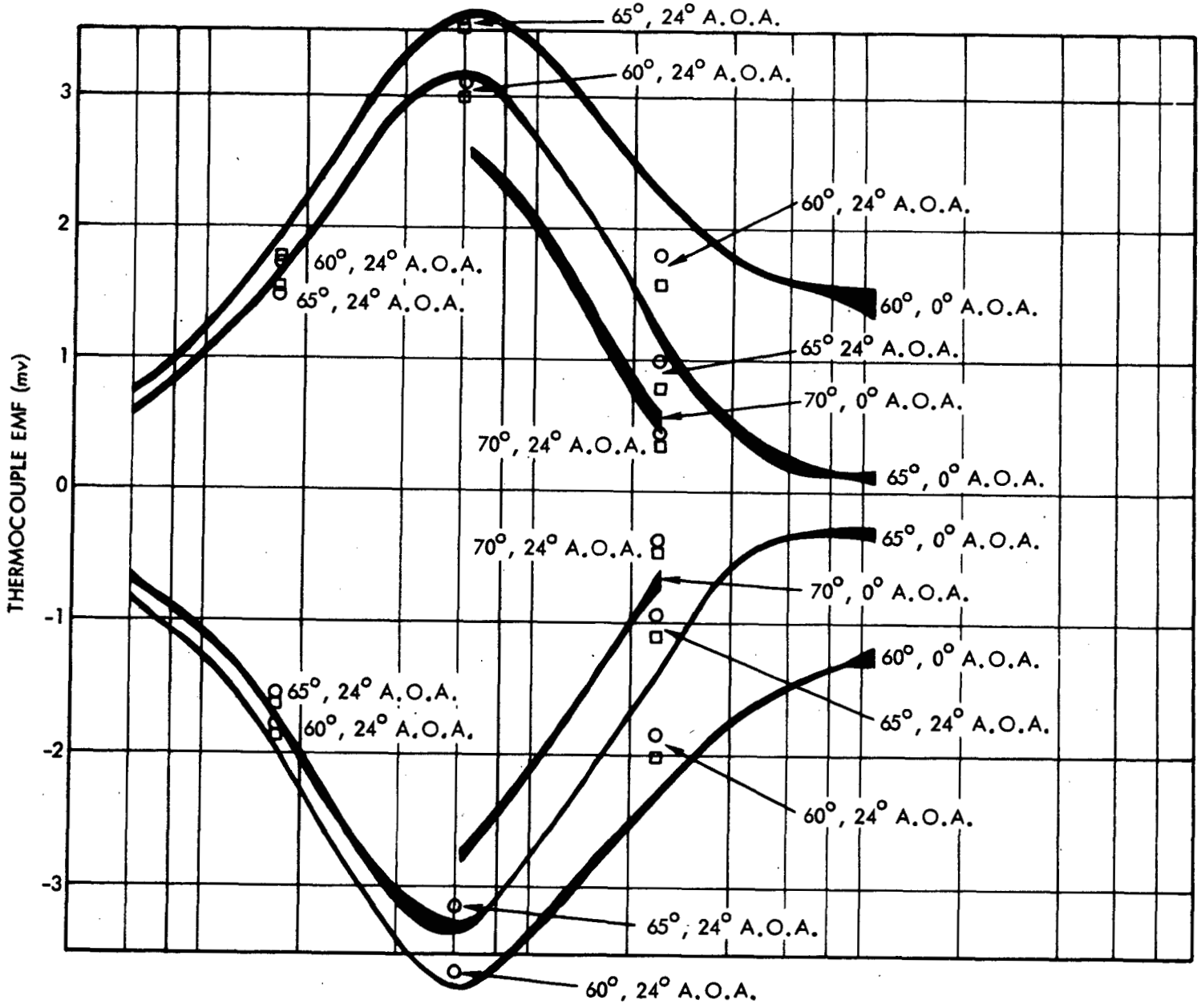

Figure 23. Effect of Angle of Attack on Wake Edge Definition.

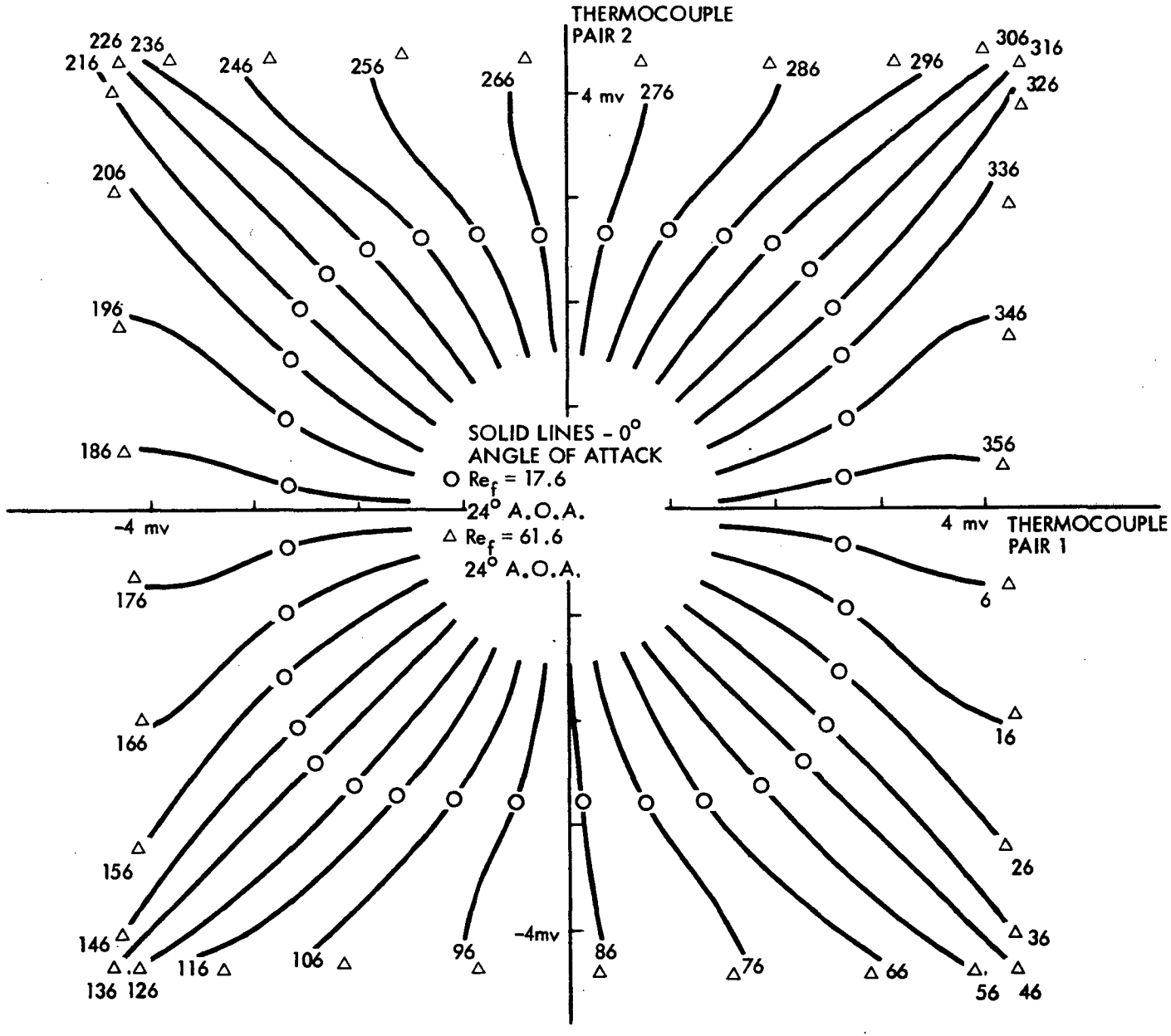

Figure 24. Effect of Angle of Attack on Wind Angle Measurement.

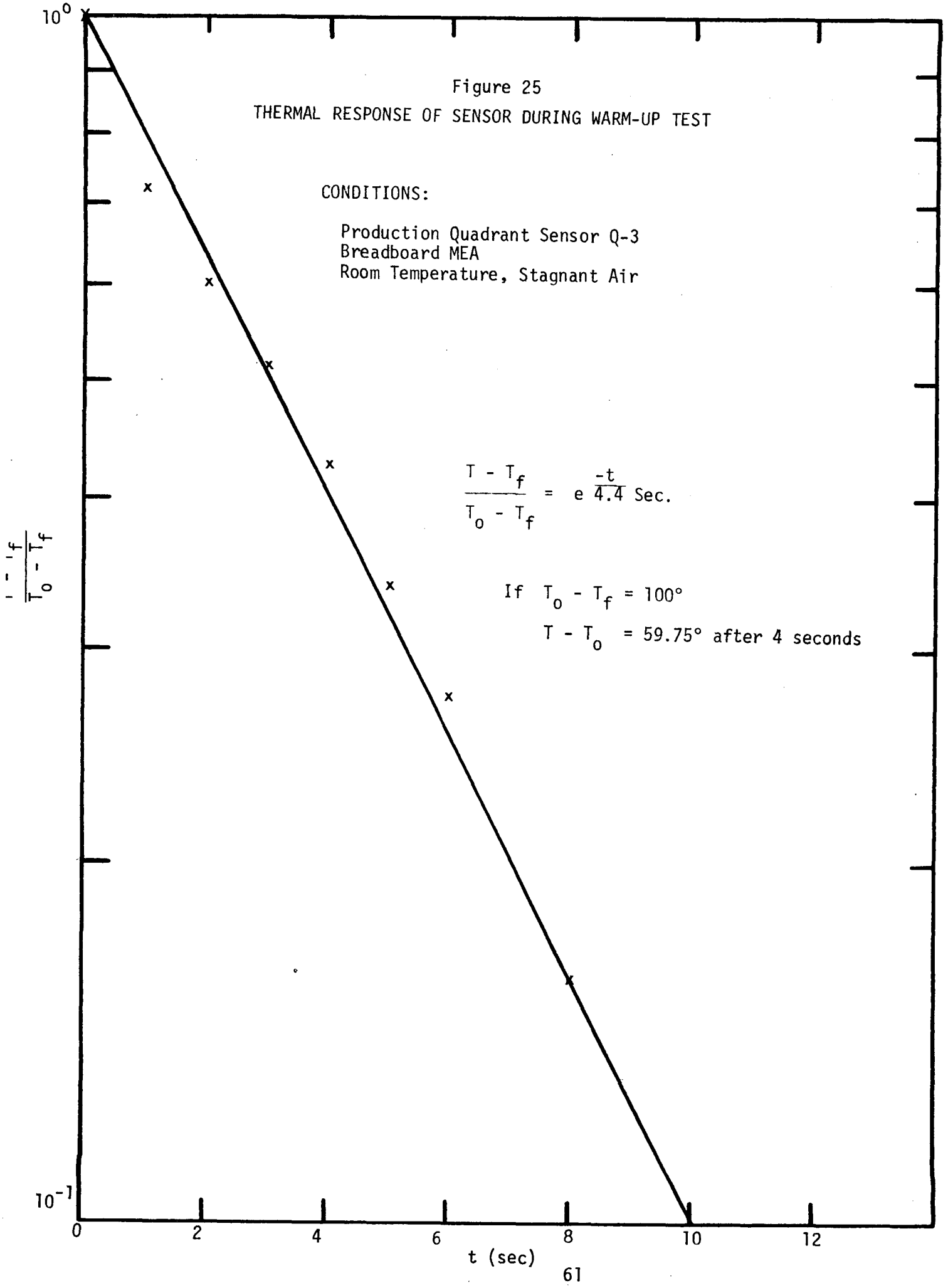
Figure 25
THERMAL RESPONSE OF SENSOR DURING WARM-UP TEST
CONDITIONS:
Production Quadrant Sensor Q-3
Breadboard MEA
Room Temperature, Stagnant Air
$\frac{T - T_f}{T_o - T_f} = e^{\frac{-t}{4.4}}$ Sec.
If $T_o - T_f = 100°$
$T - T_o = 59.75°$ after 4 seconds
10^0
10^{-1}
$\frac{T - T_f}{T_o - T_f}$
0
2
4
6
8
10
12
t (sec)

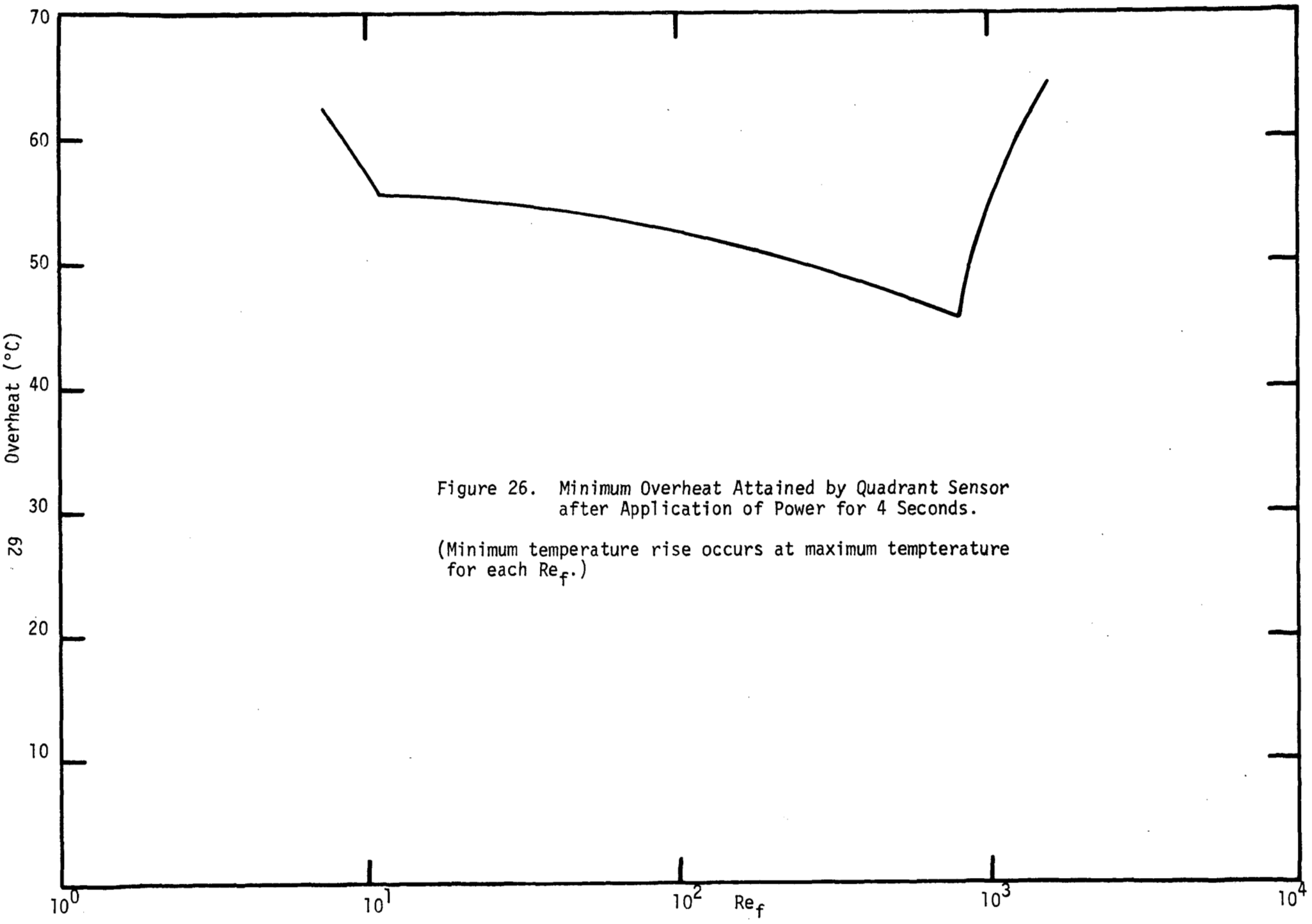

Figure 26. Minimum Overheat Attained by Quadrant Sensor after Application of Power for 4 Seconds.

(Minimum temperature rise occurs at maximum tempterature for each Re_f.)

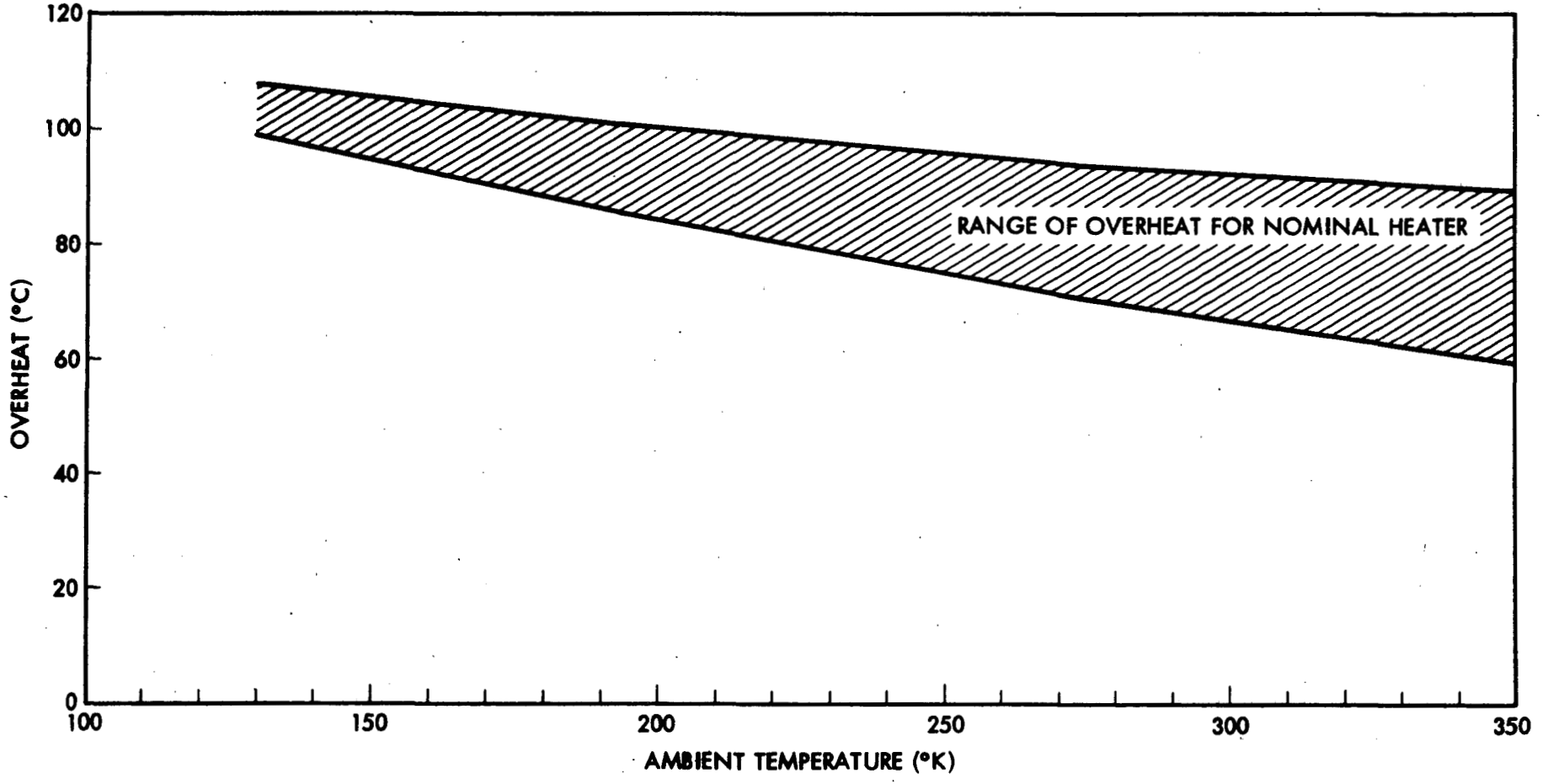

Figure 27. Variation in Overheat with Ambient Temperature.

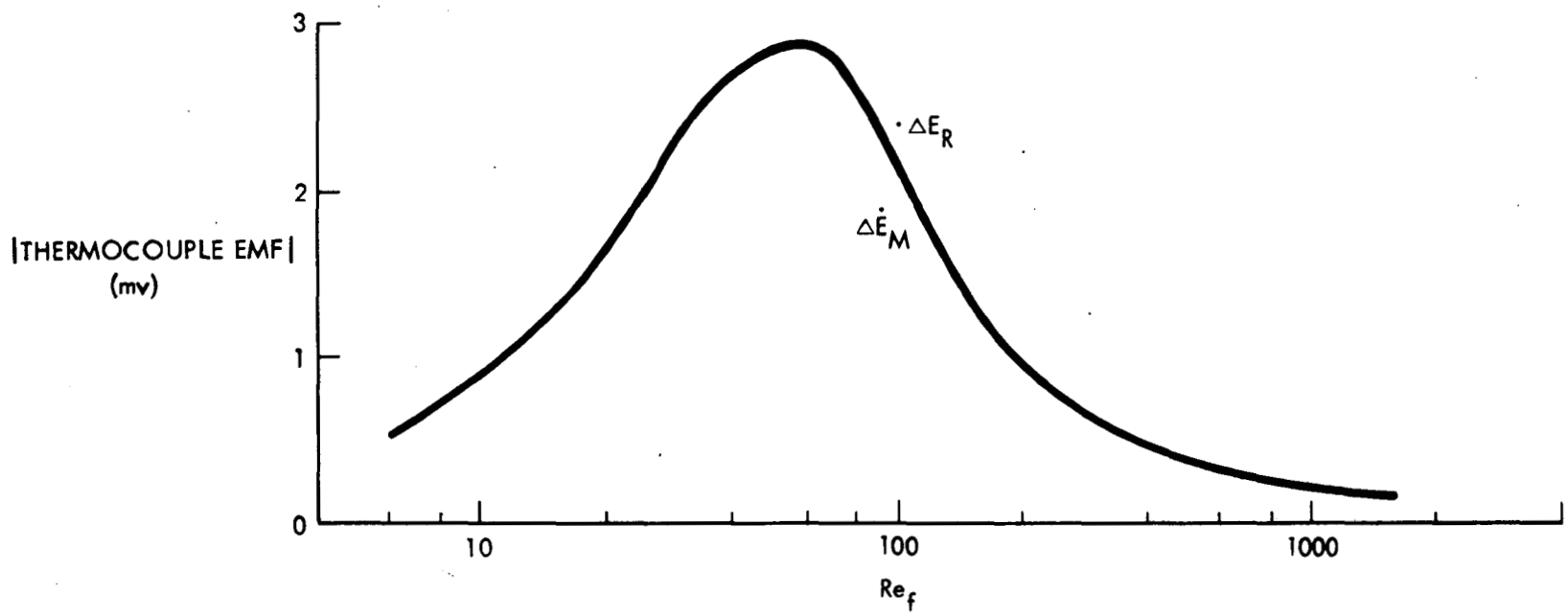

WAKE EDGE CRITERION, $\alpha = 67.5°$

Figure 28. Effect of EMF Error on Wake Edge Detection.

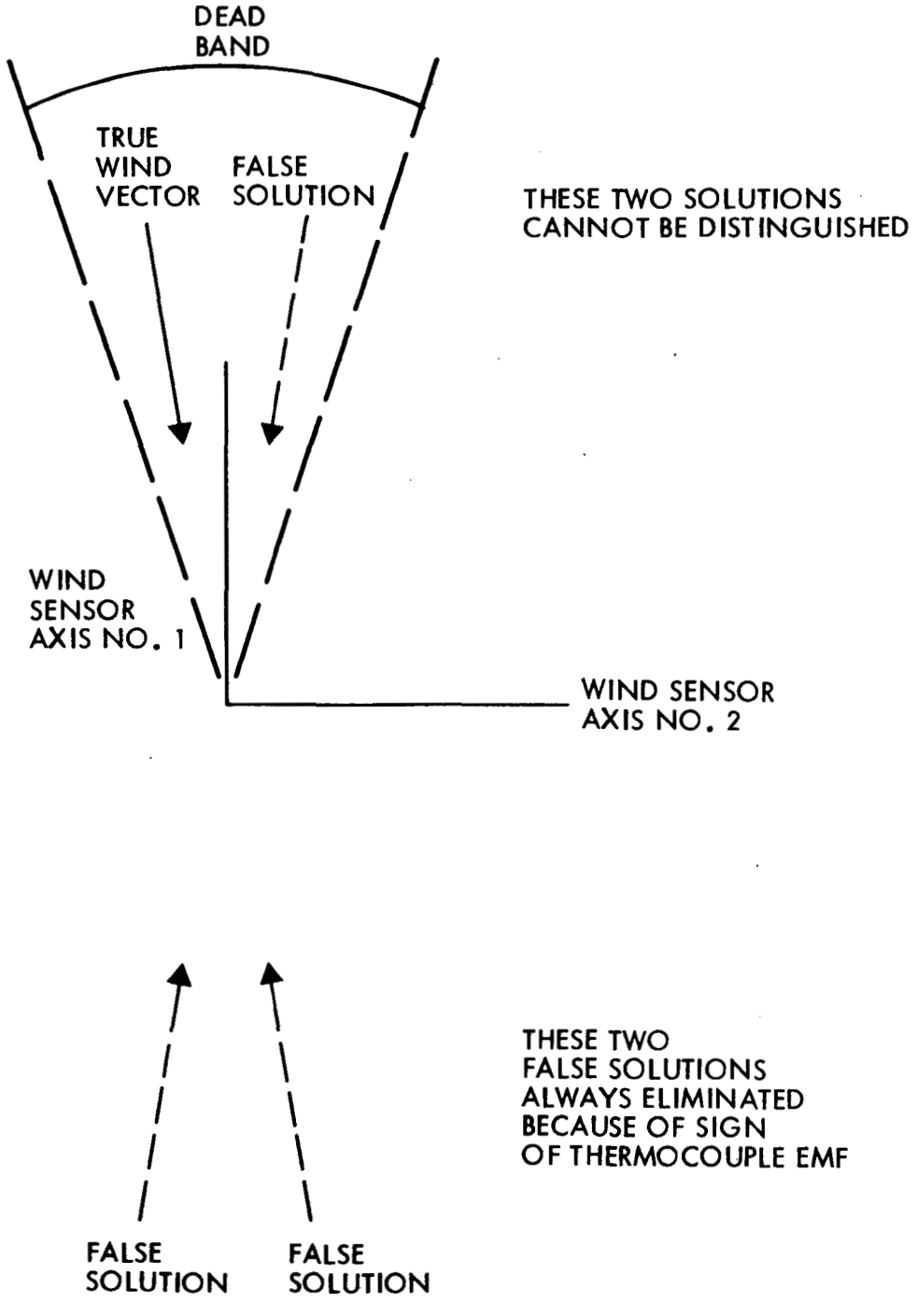

Figure 29. Effect of Dead Band on Wind Quadrant Determination.

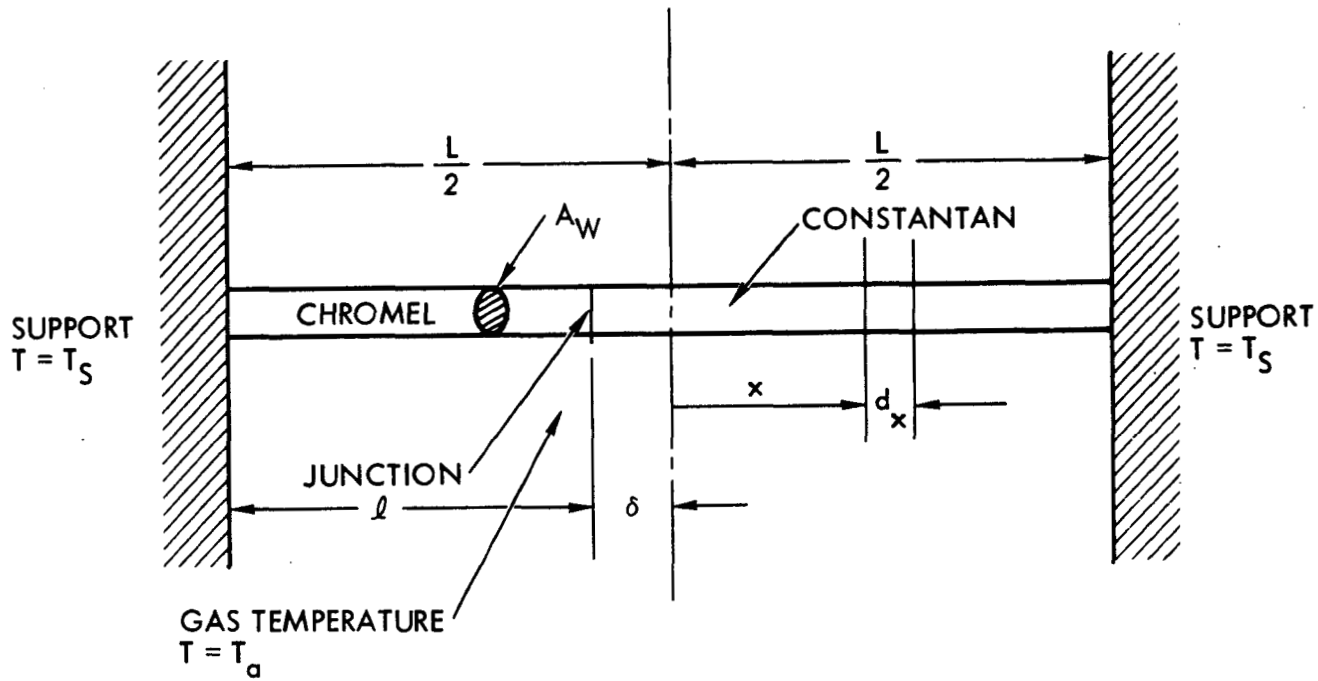

Figure 30. Schematic of Heat Conduction Problem.

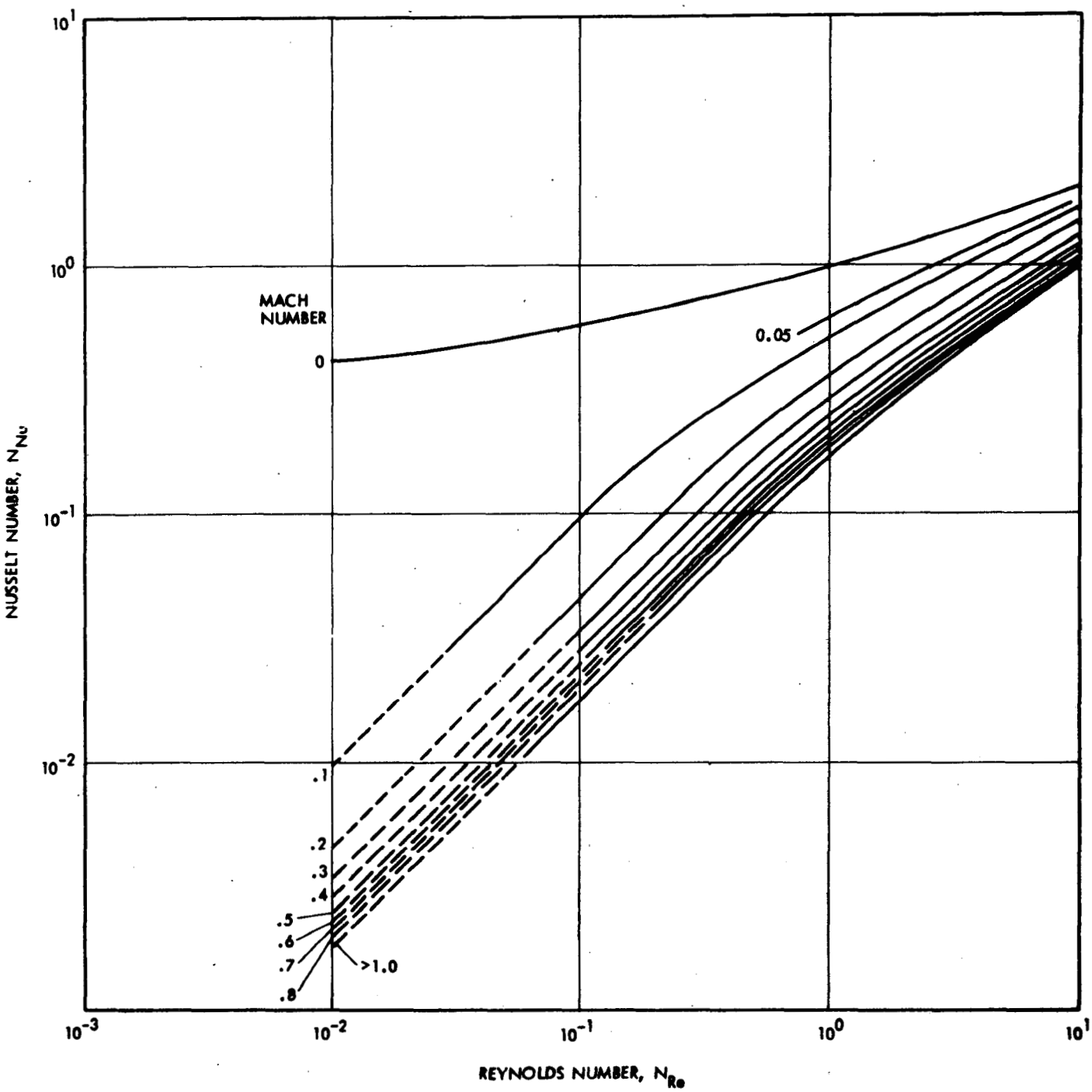

Figure 31. Convective Heat Transfer from Transverse Cylinders (from Baldwin, Sanborn and Lawrence, Journal of Heat Transfer, Transactions of the ASME, Series C, Vol. 82, No. 2, May 1960). Also, Figure 8 from Temperature Sensor Section.

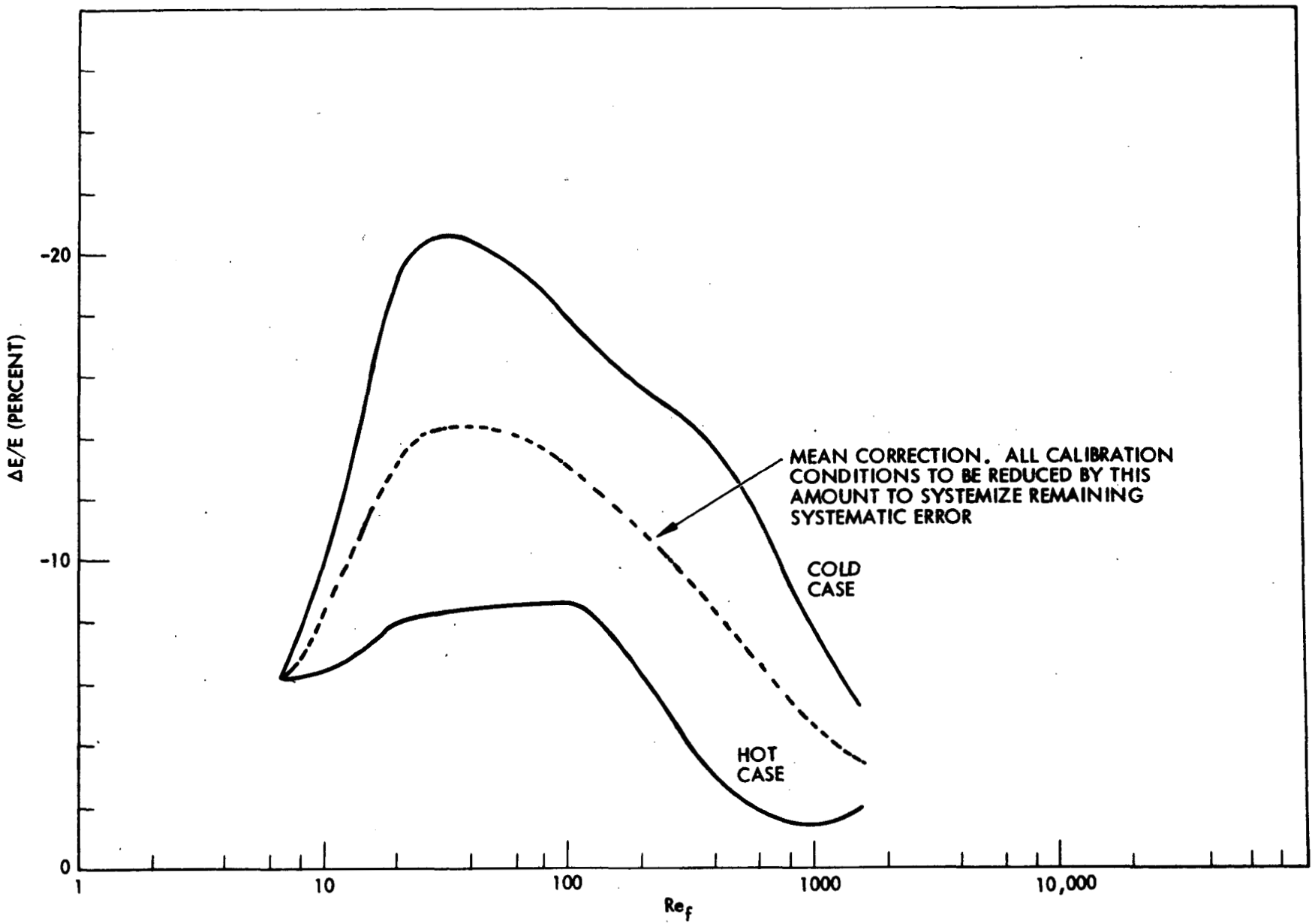

Figure 32. Systematic Error in Thermocouple Output Due to Heat Conduction.

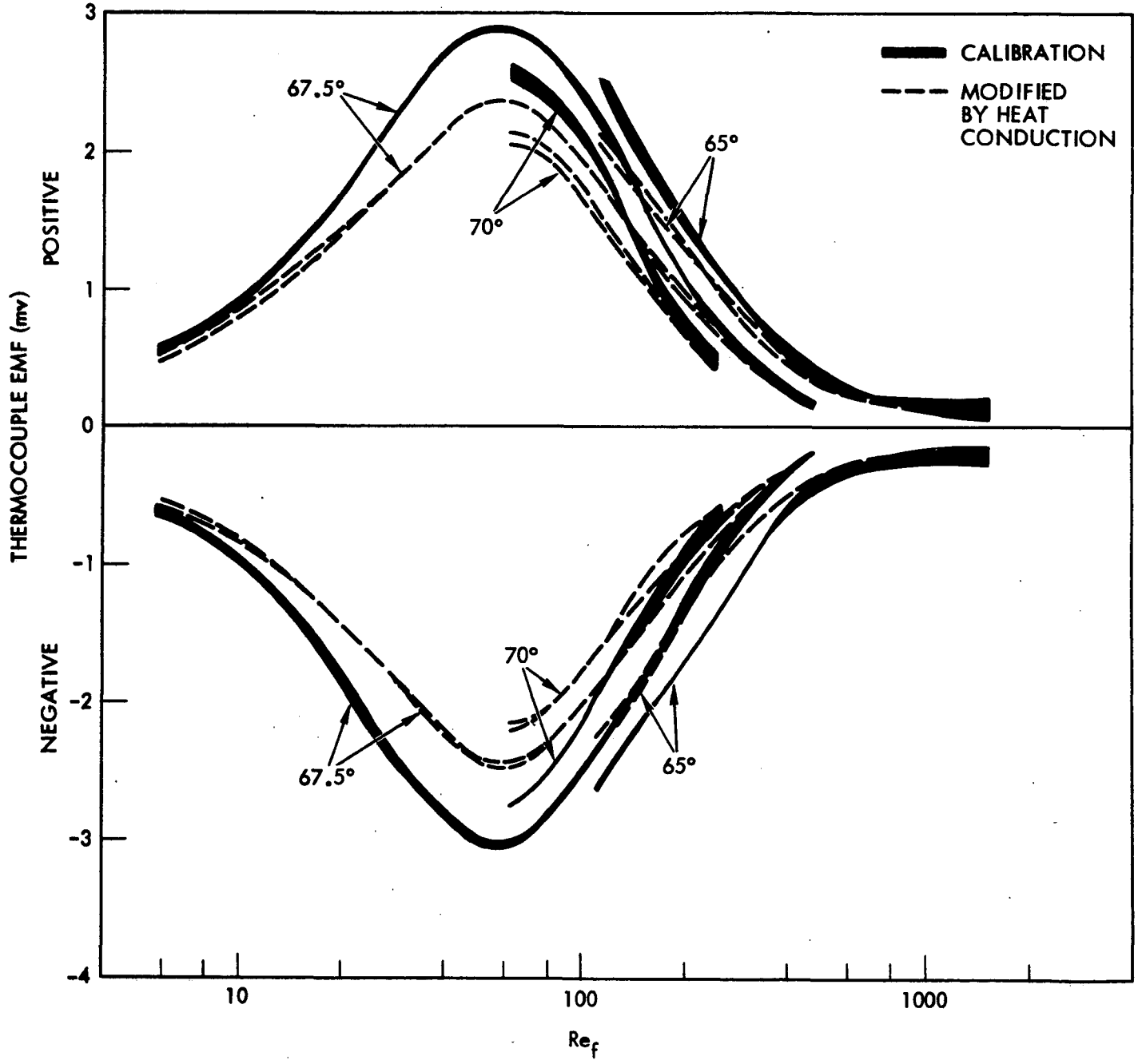

Figure 33. Effect of Heat Conduction on Thermocouple Output at Wake Edge (Cold Case).

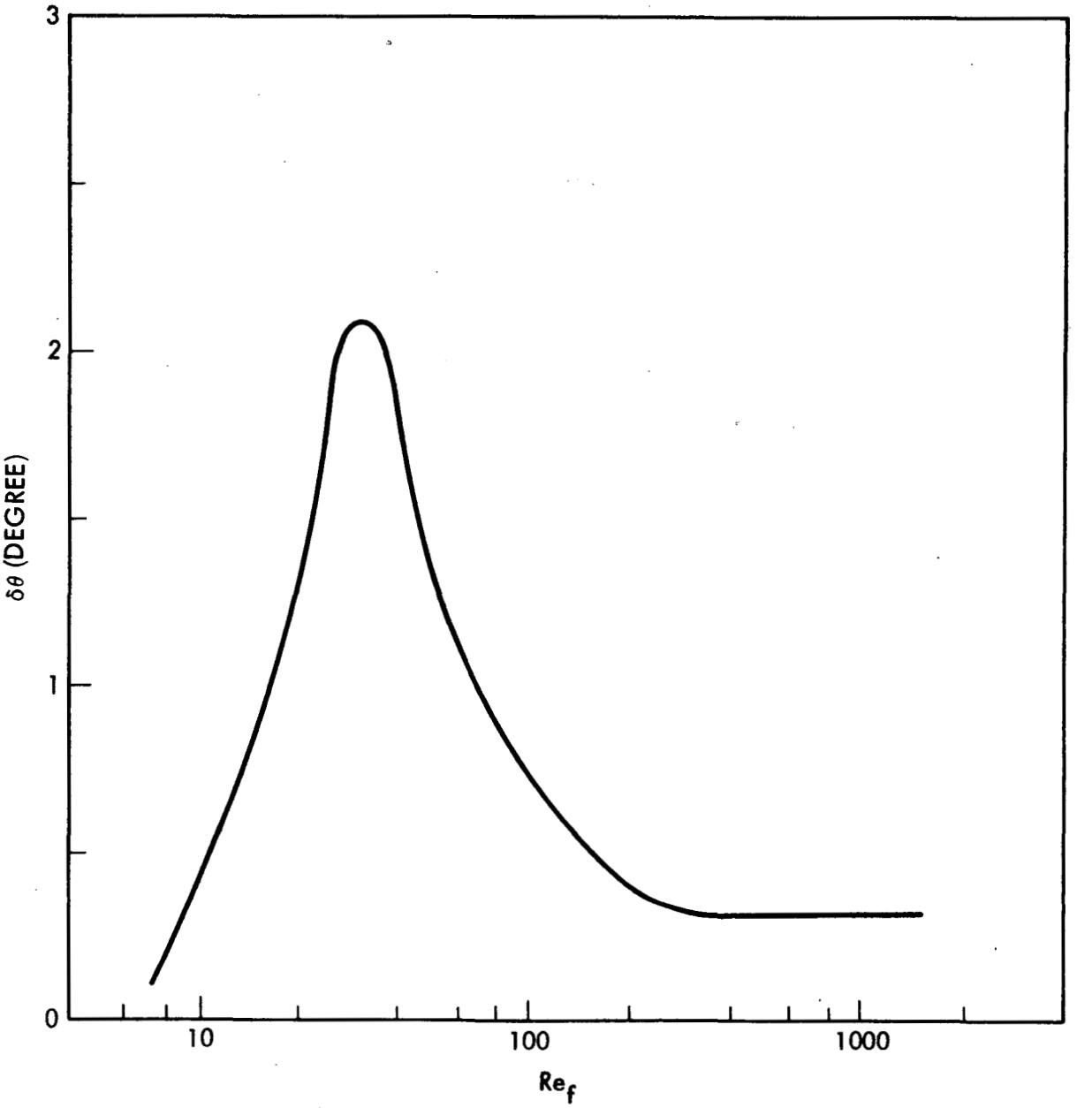

Figure 34. Systematic Error Due to Heat Conduction (Dead Band).

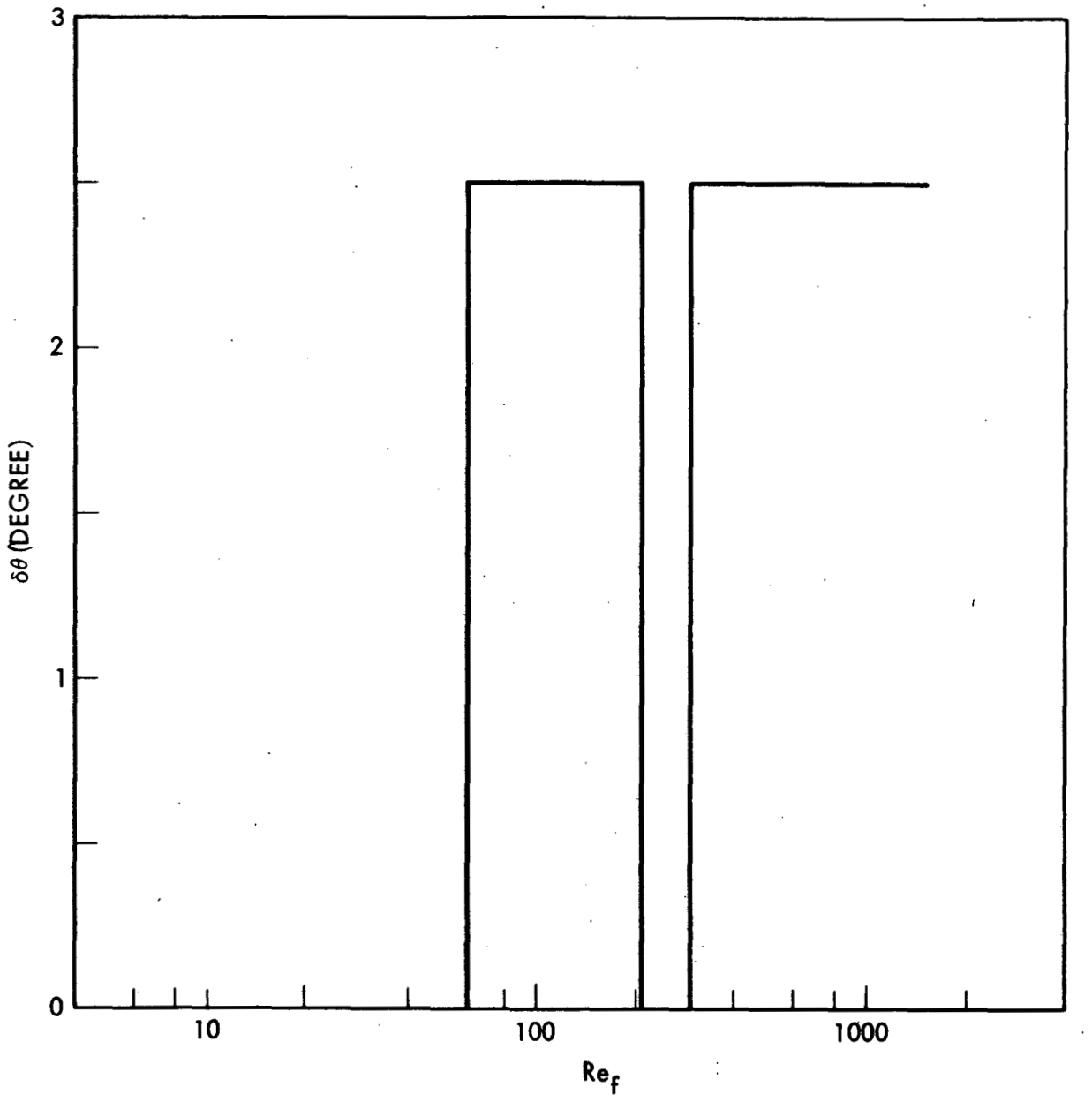

Figure 35. Systematic Error Due to Compromises in Wake Edge Threshold Definition (Dead Band).

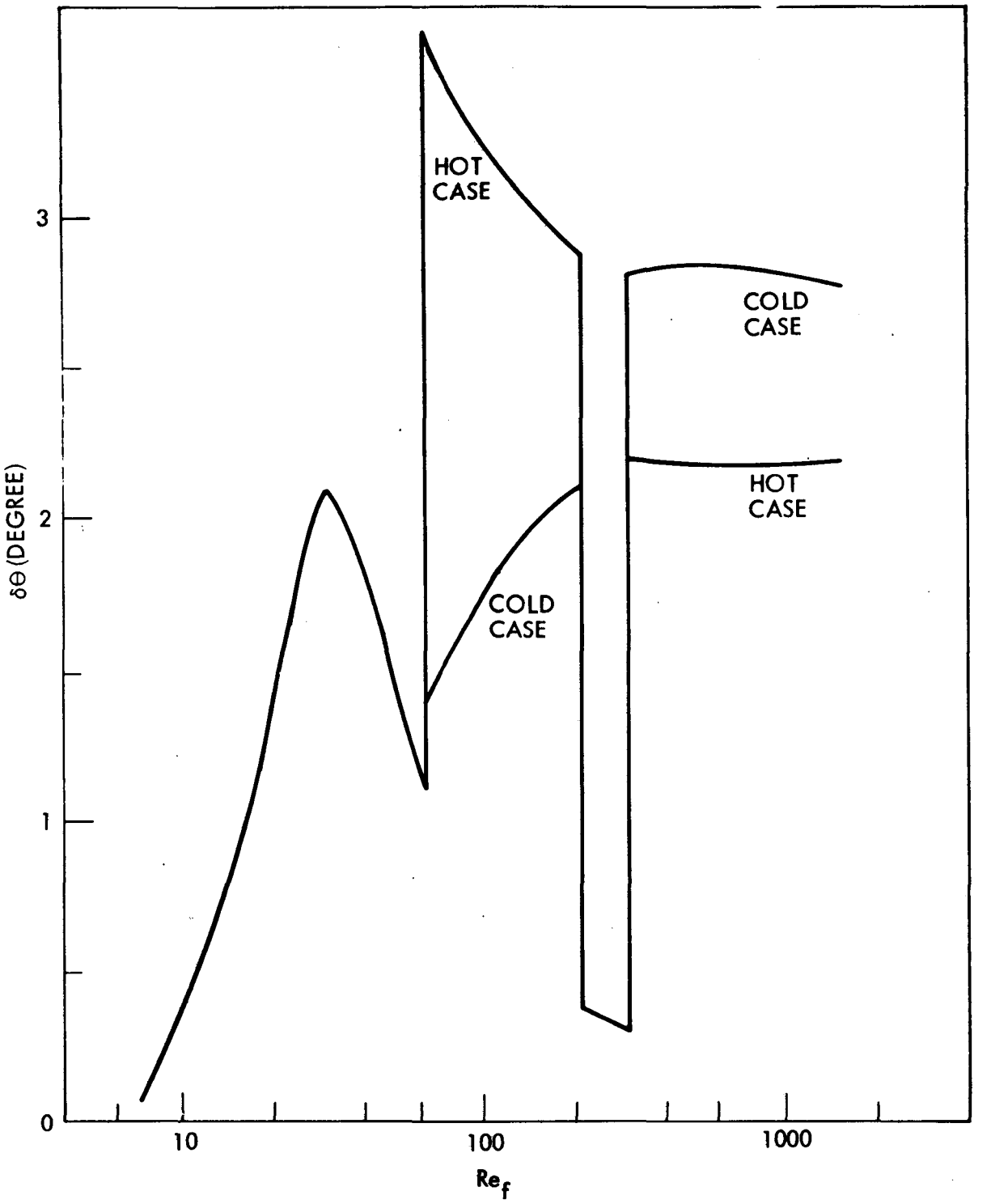

Figure 36. Total Systematic Error (Dead Band).

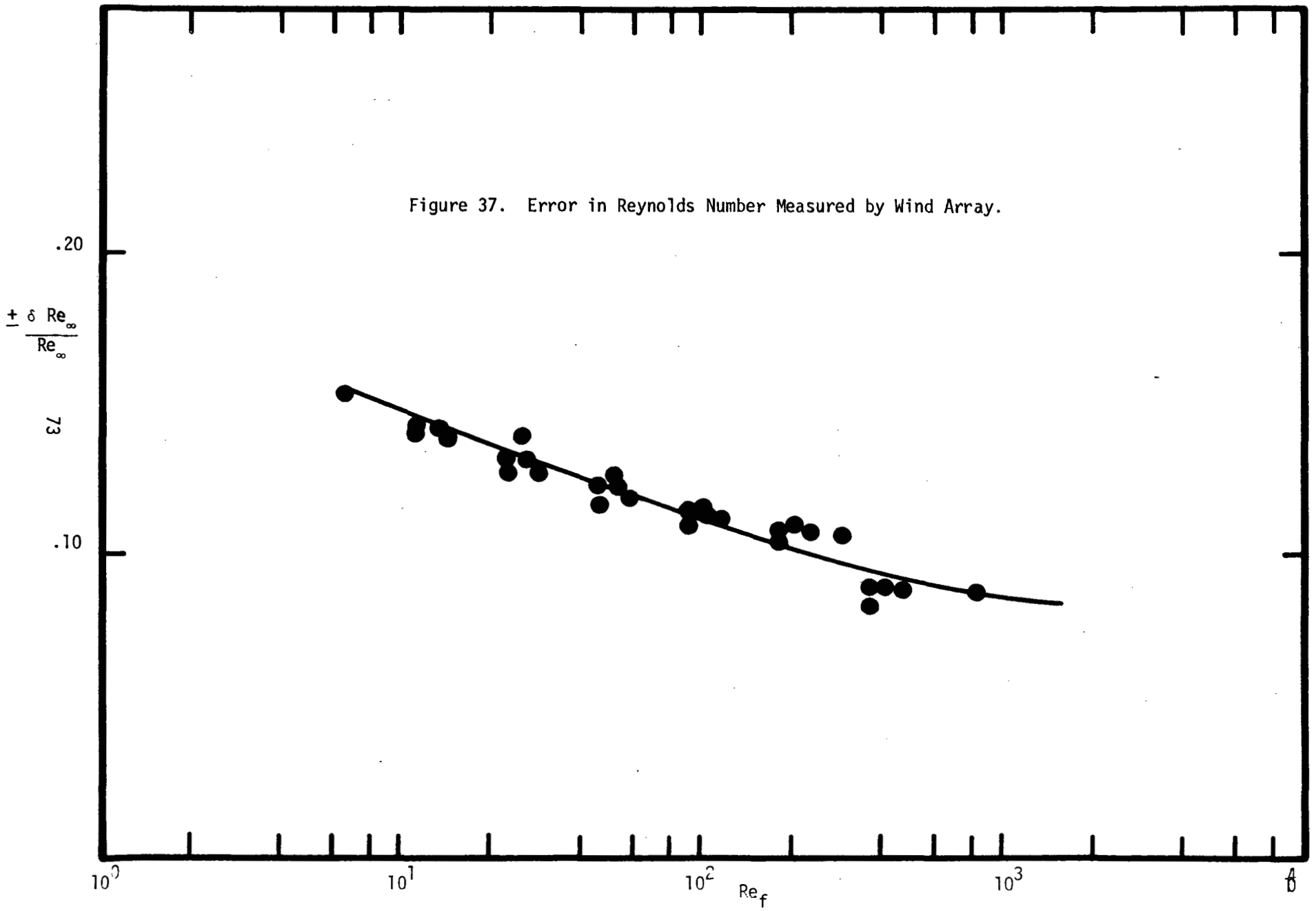

Figure 37. Error in Reynolds Number Measured by Wind Array.

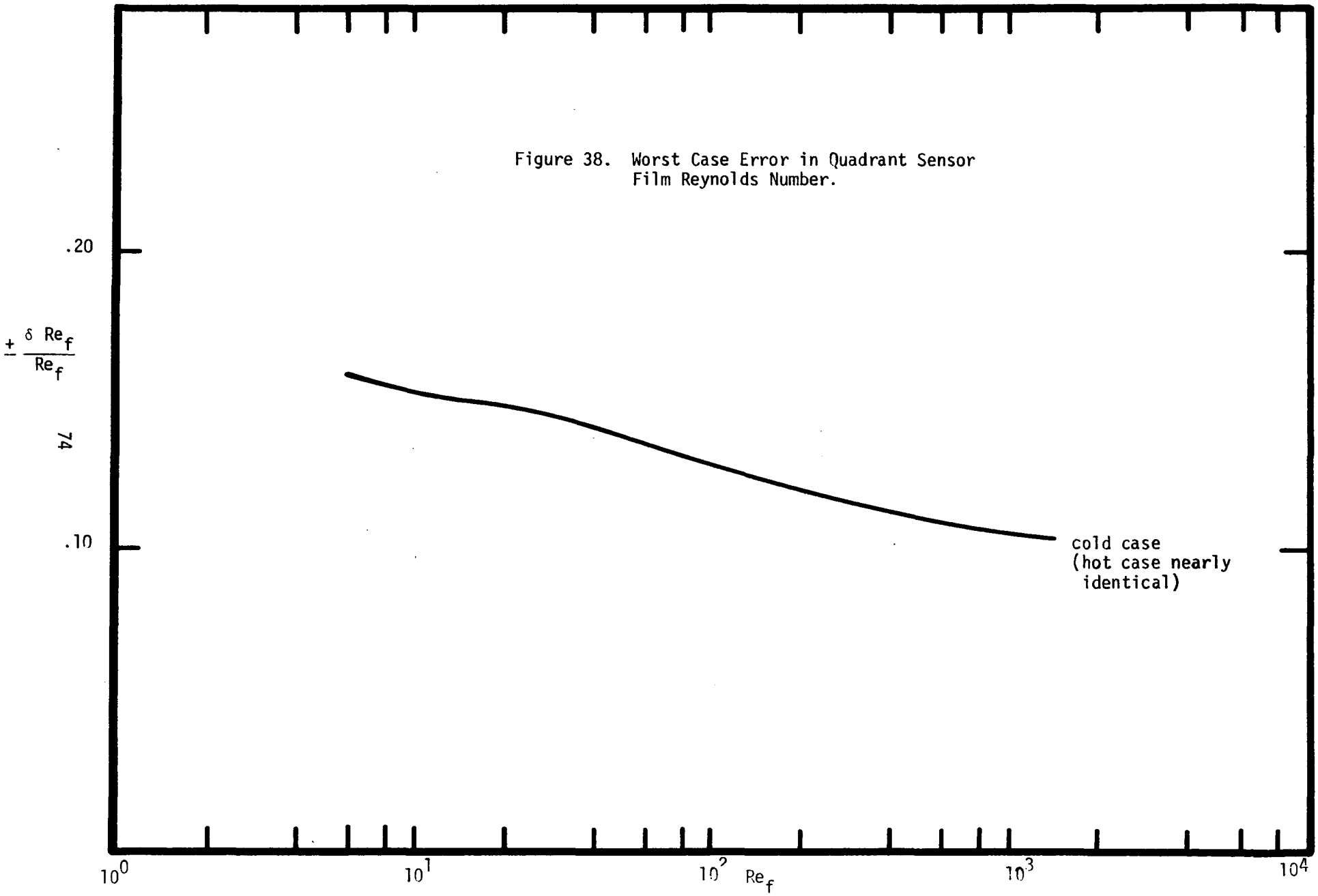

Figure 38. Worst Case Error in Quadrant Sensor Film Reynolds Number.

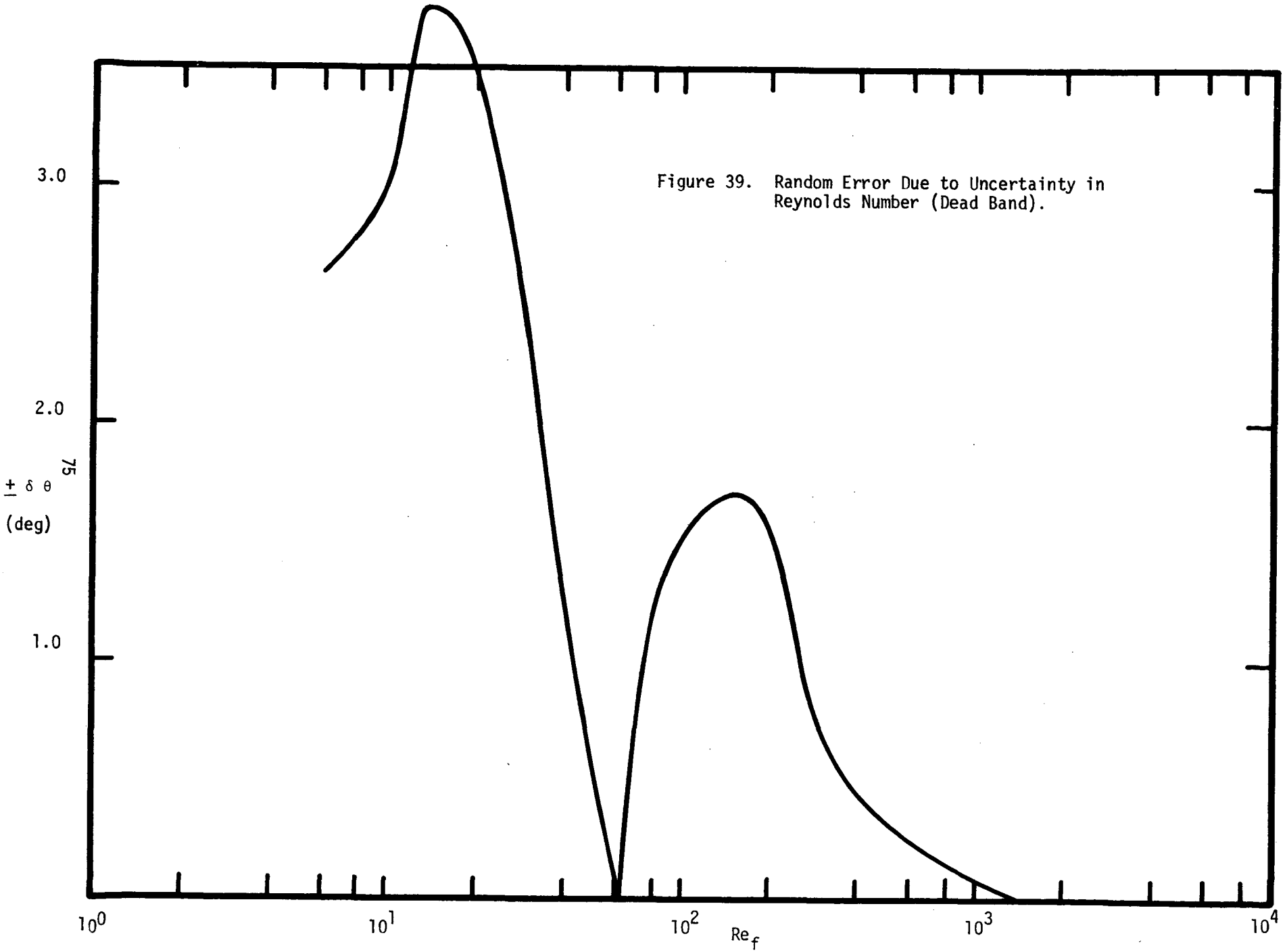

Figure 39. Random Error Due to Uncertainty in Reynolds Number (Dead Band).

Figure 40. Overheat Correction Errors.

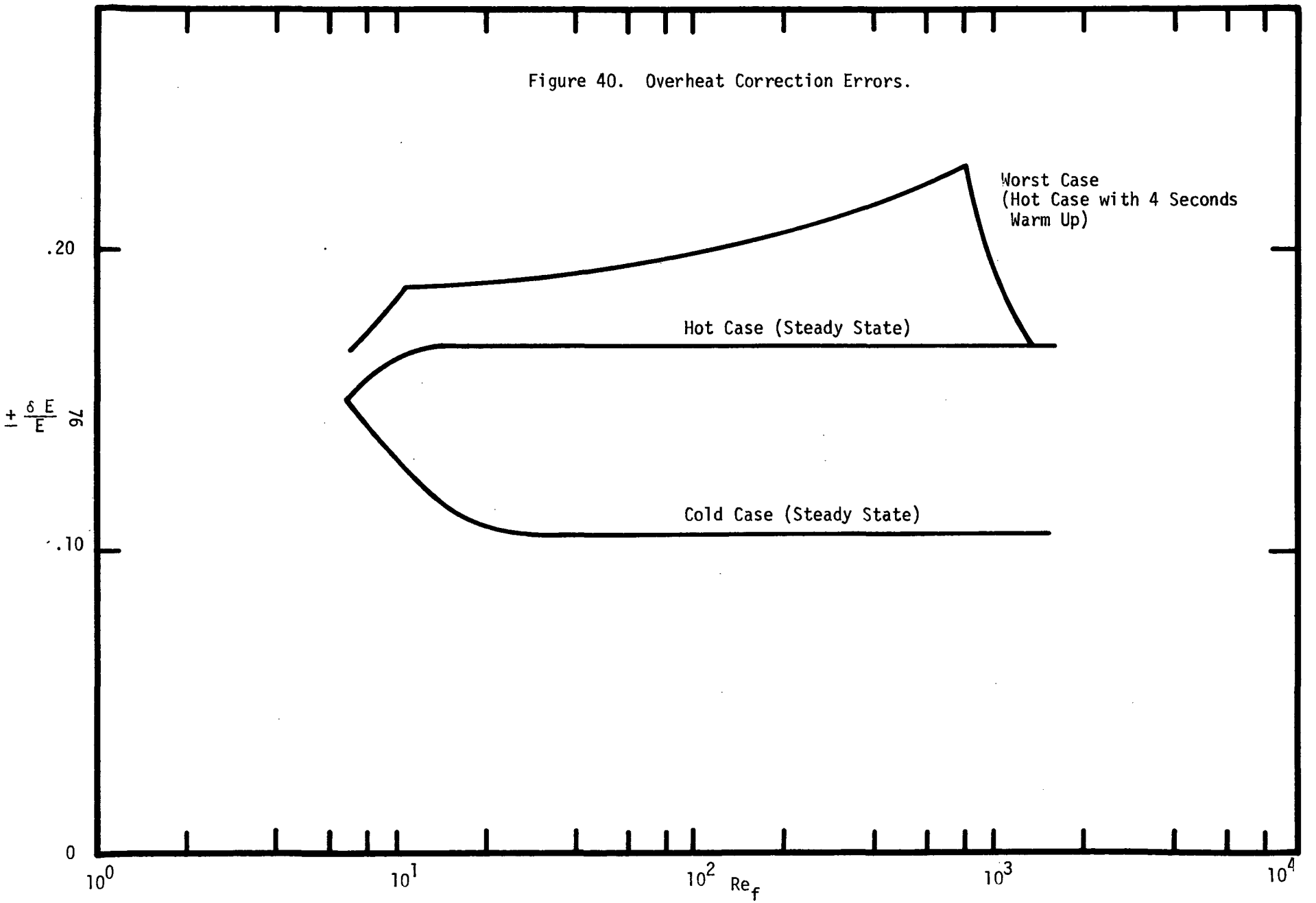

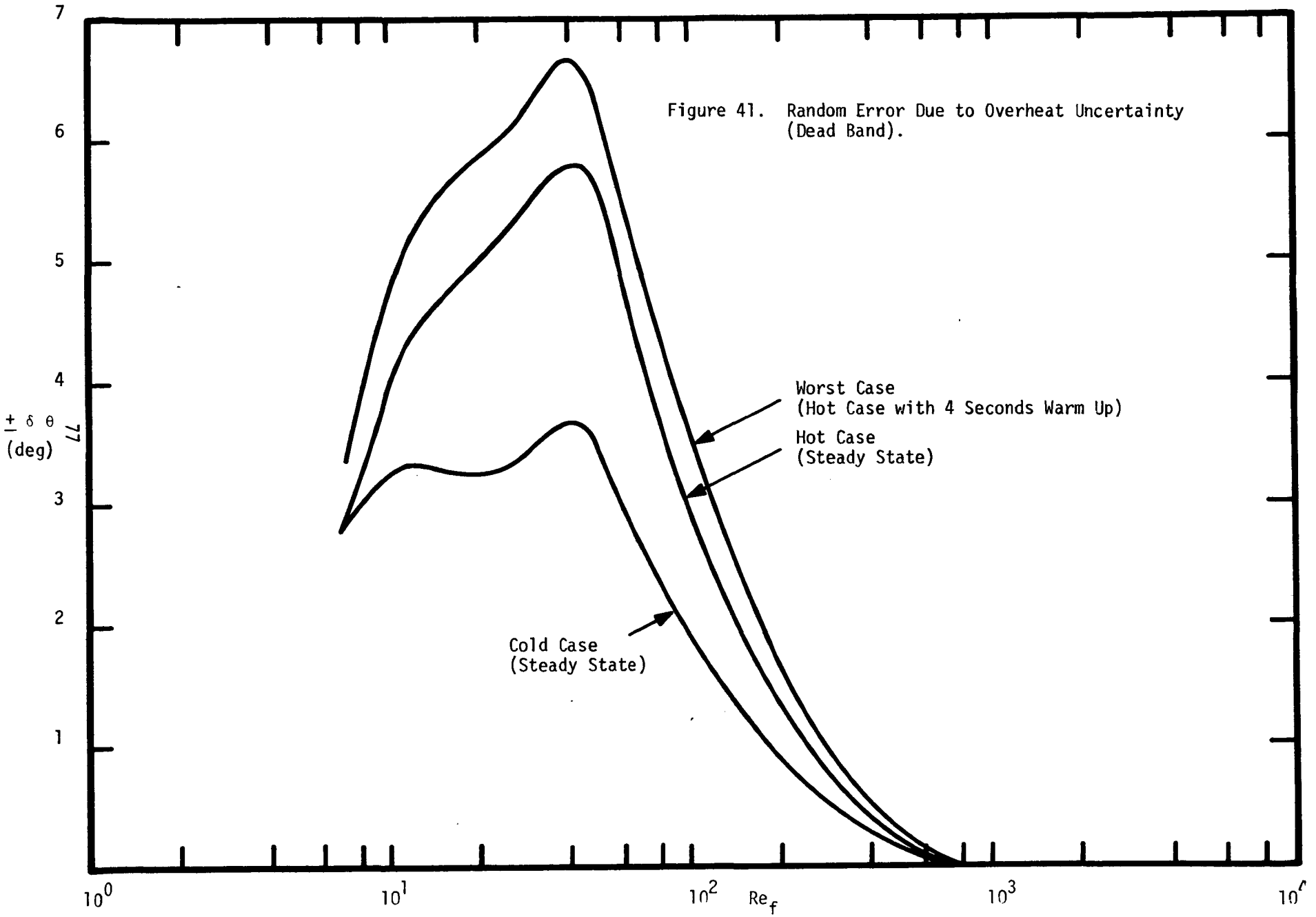

Figure 41. Random Error Due to Overheat Uncertainty (Dead Band).

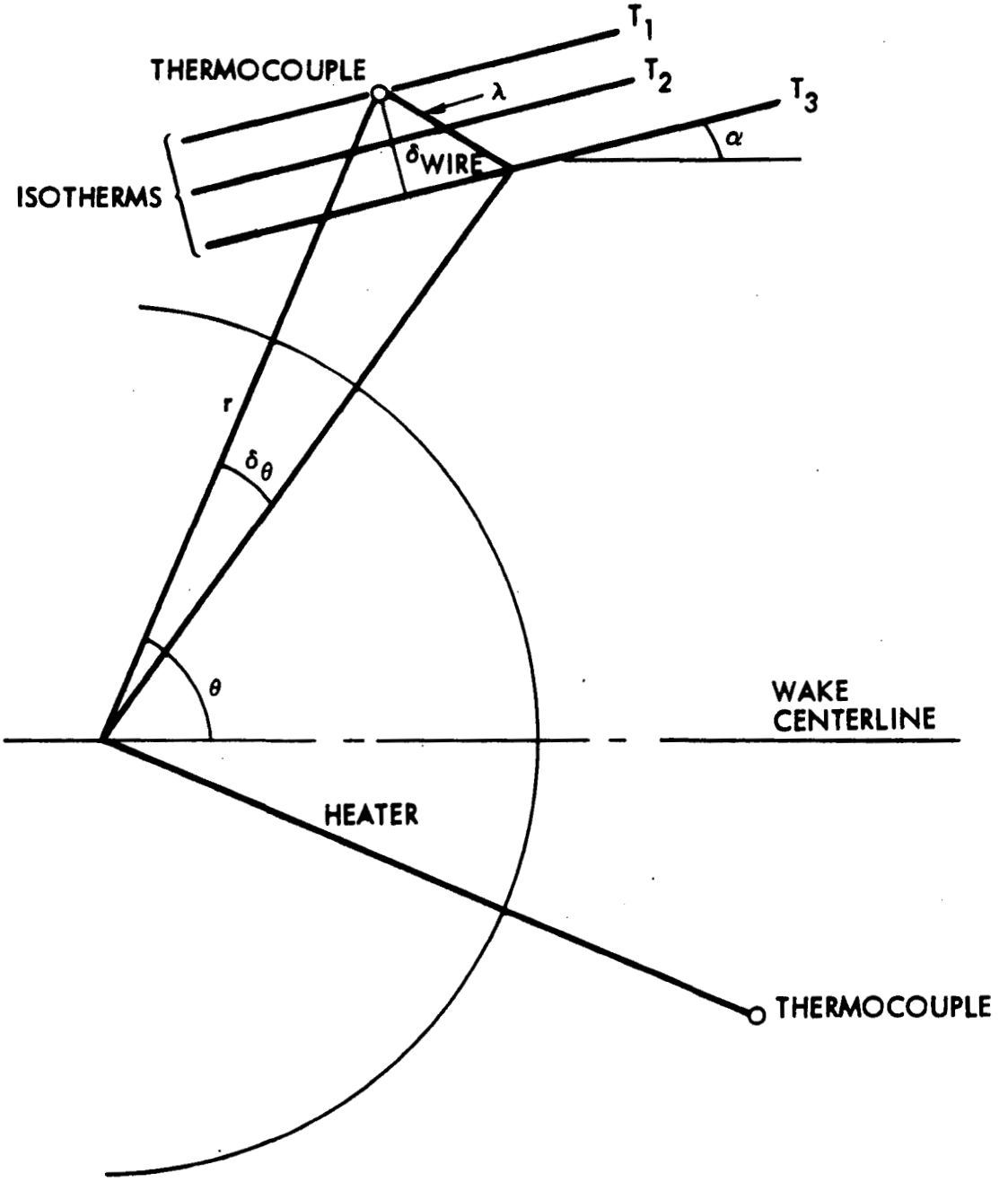

Figure 42. Schematic of Temperature Field Near Wake Edge.

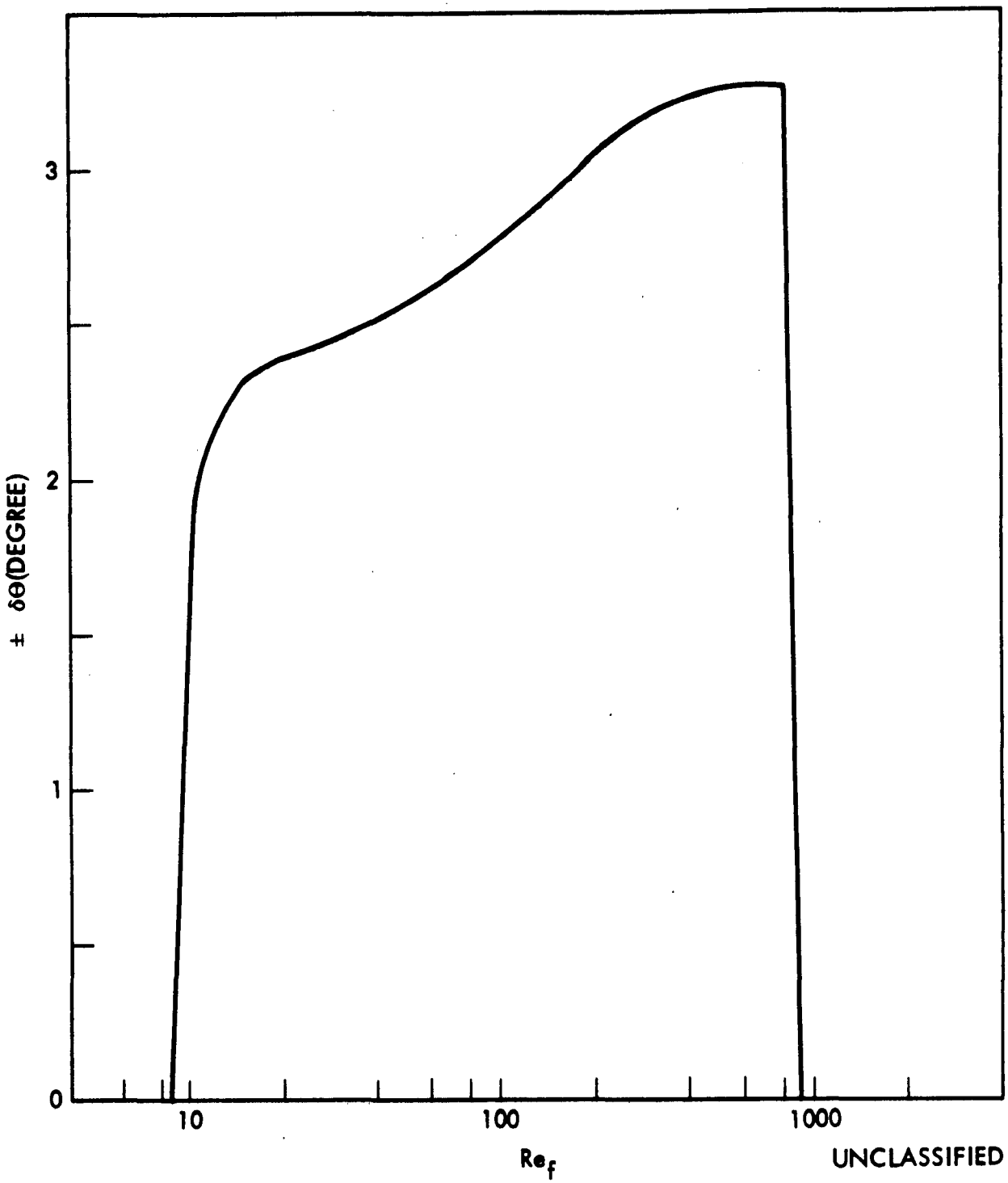

Figure 43. Random Error Due to Movement of Thermocouple Junctions (Dead Band, Hot Case).

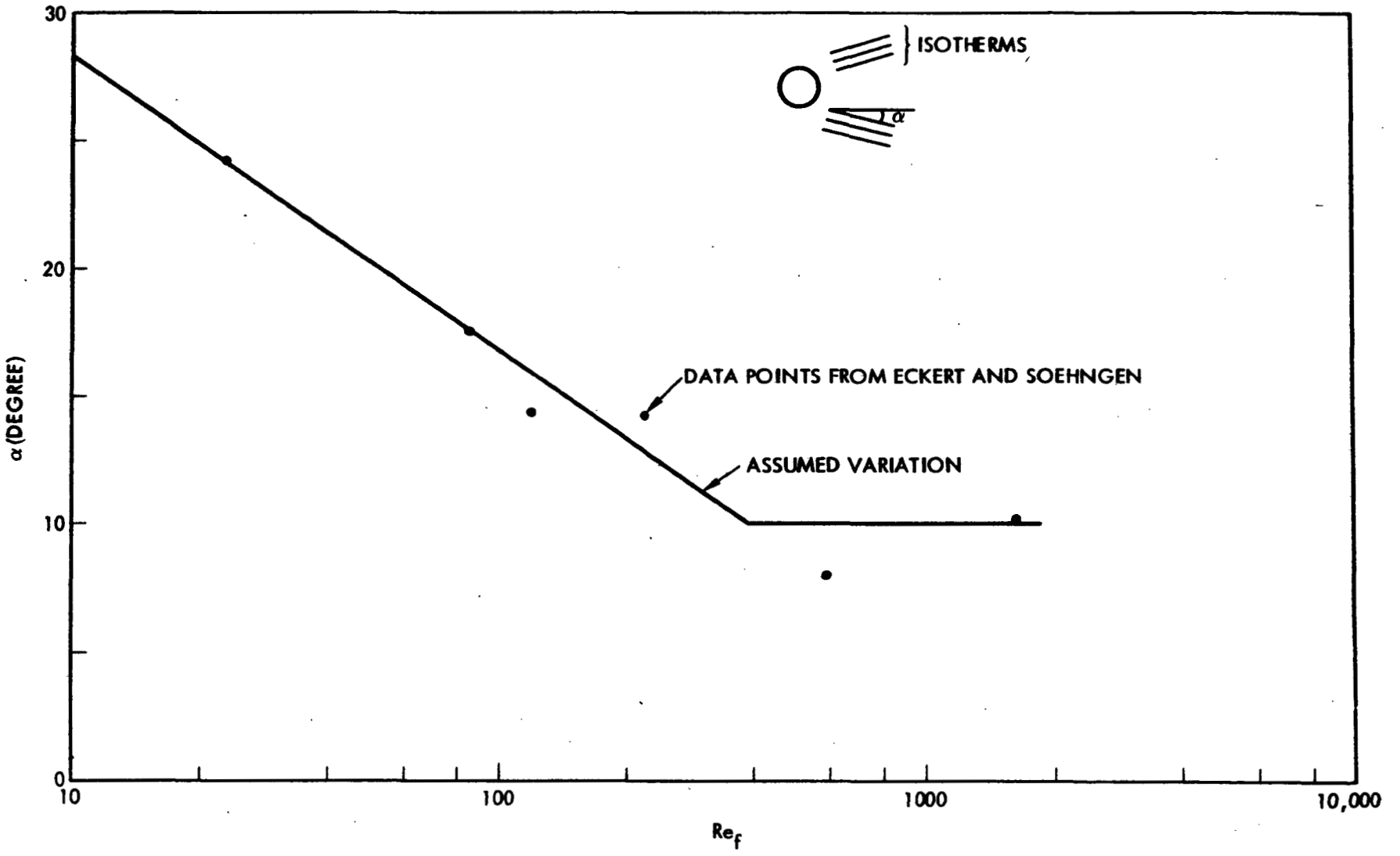

Figure 44. Variation of Isotherm Divergence Angle α with Reynolds Number.

Figure 45. Total Random Error (Dead Band).

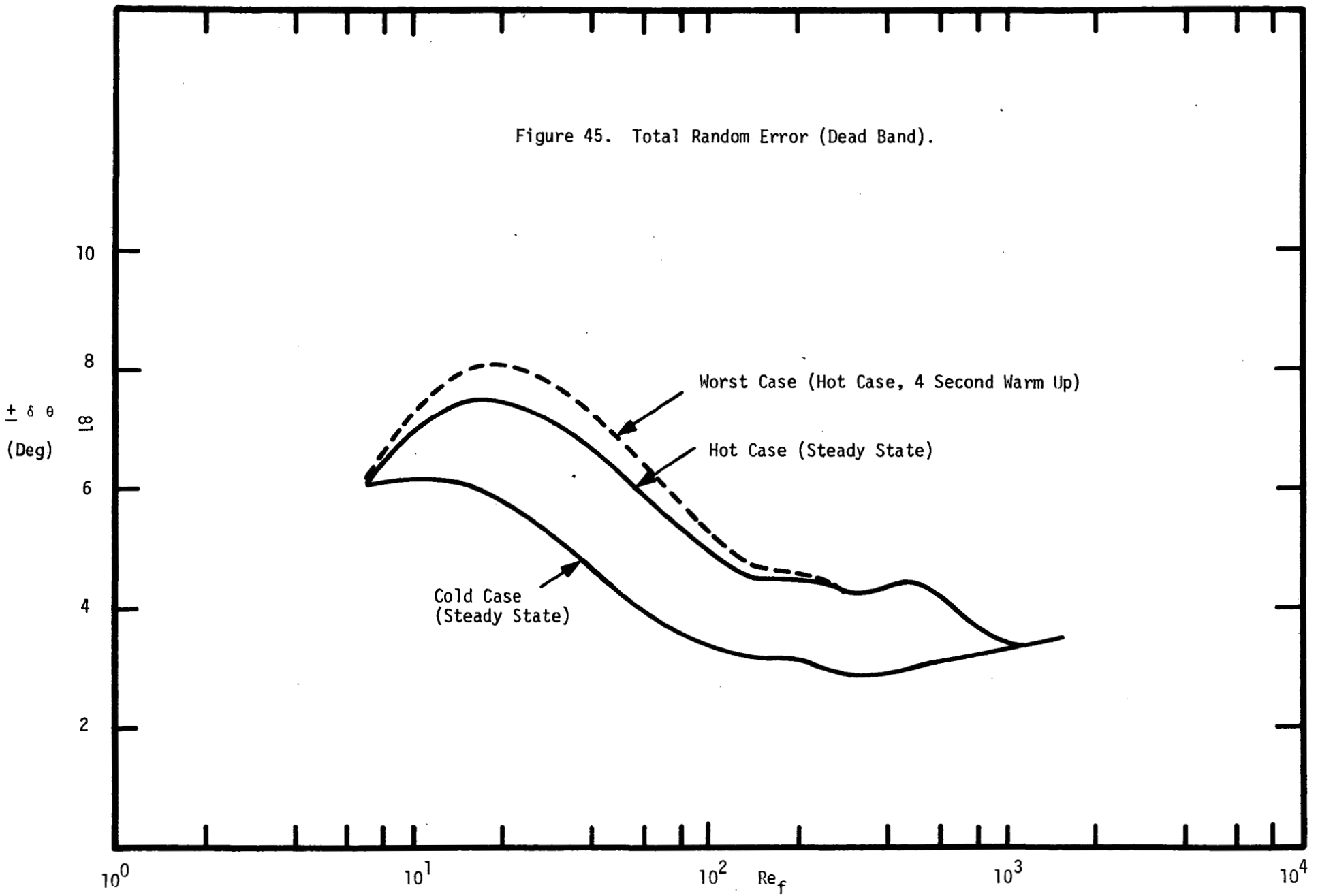

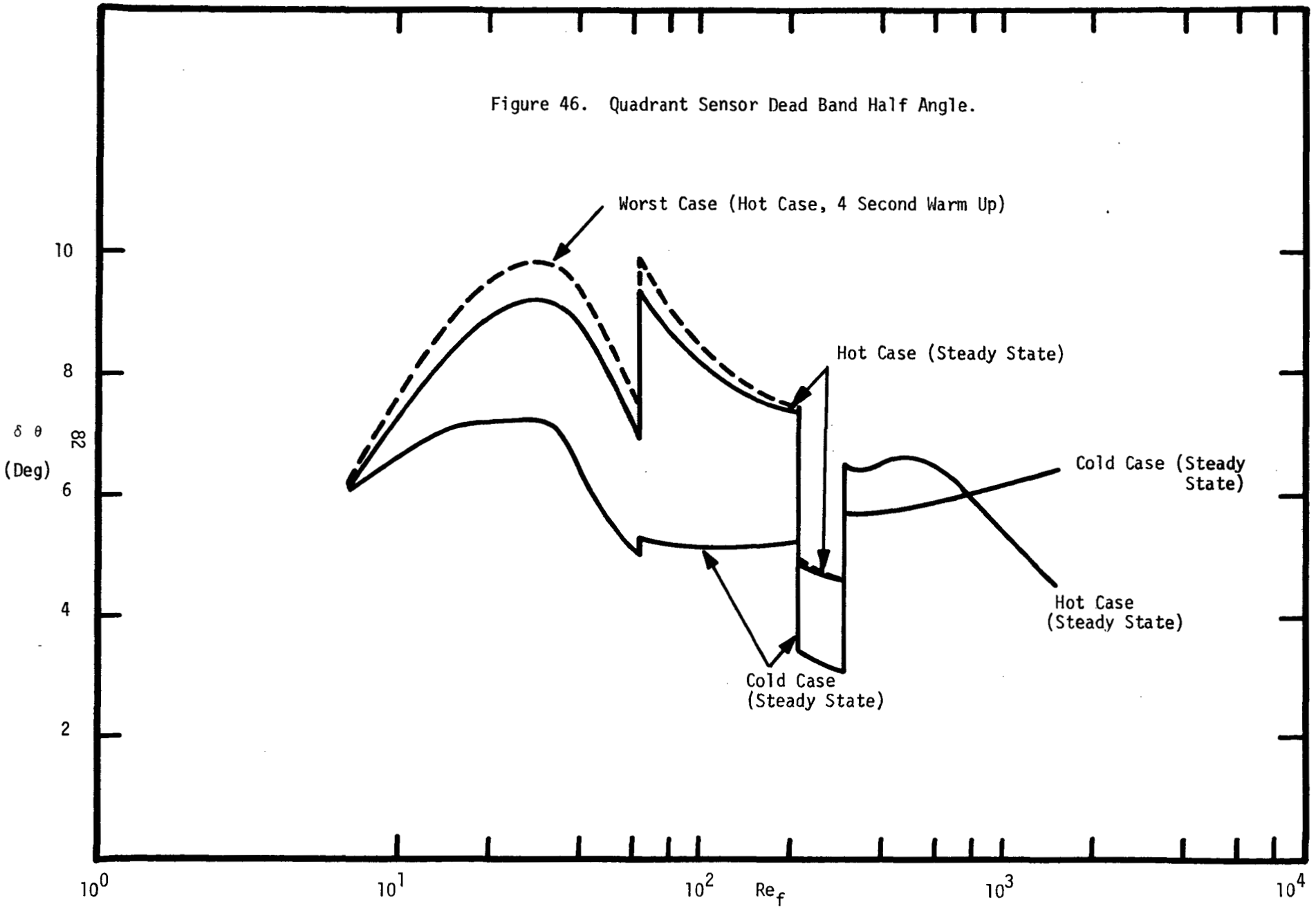

Figure 46. Quadrant Sensor Dead Band Half Angle.

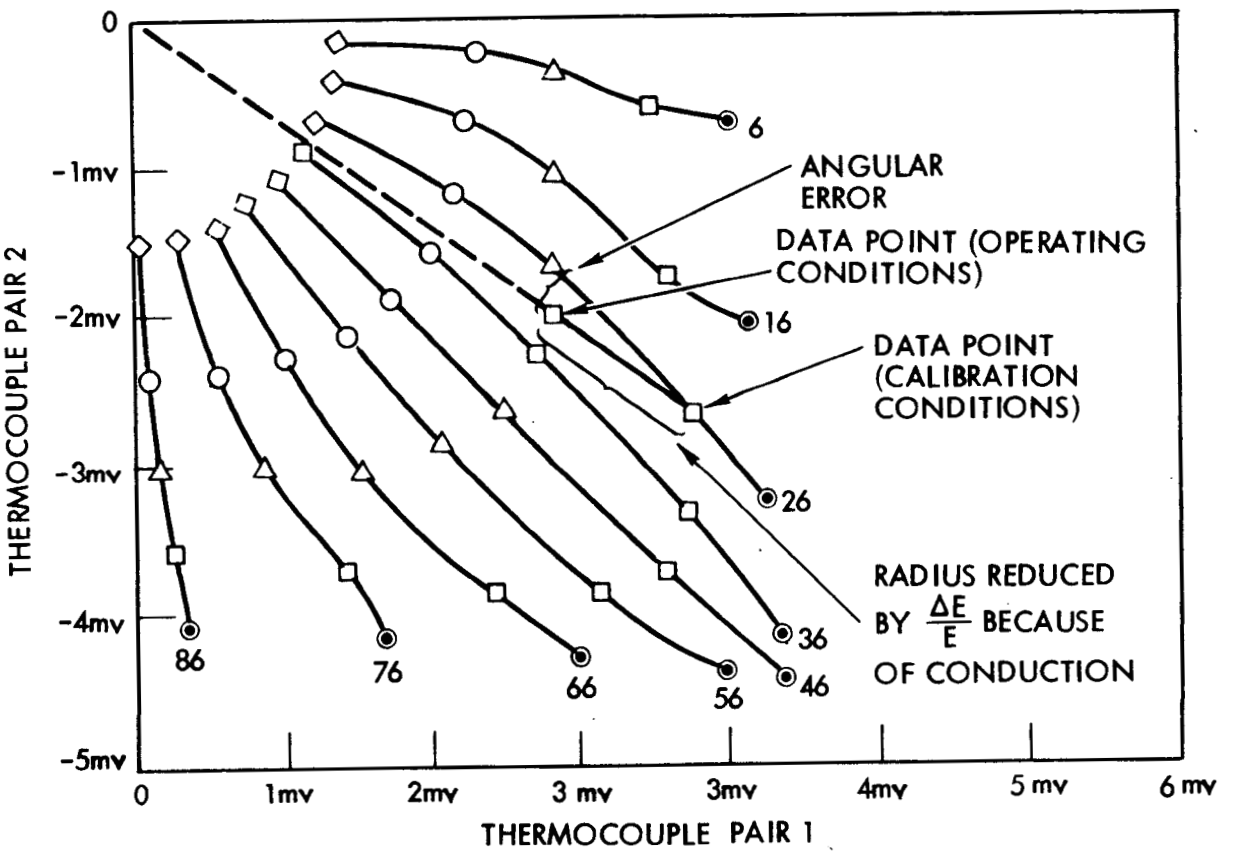

Figure 47. Effect of Heat Conduction on Thermocouple Outputs.

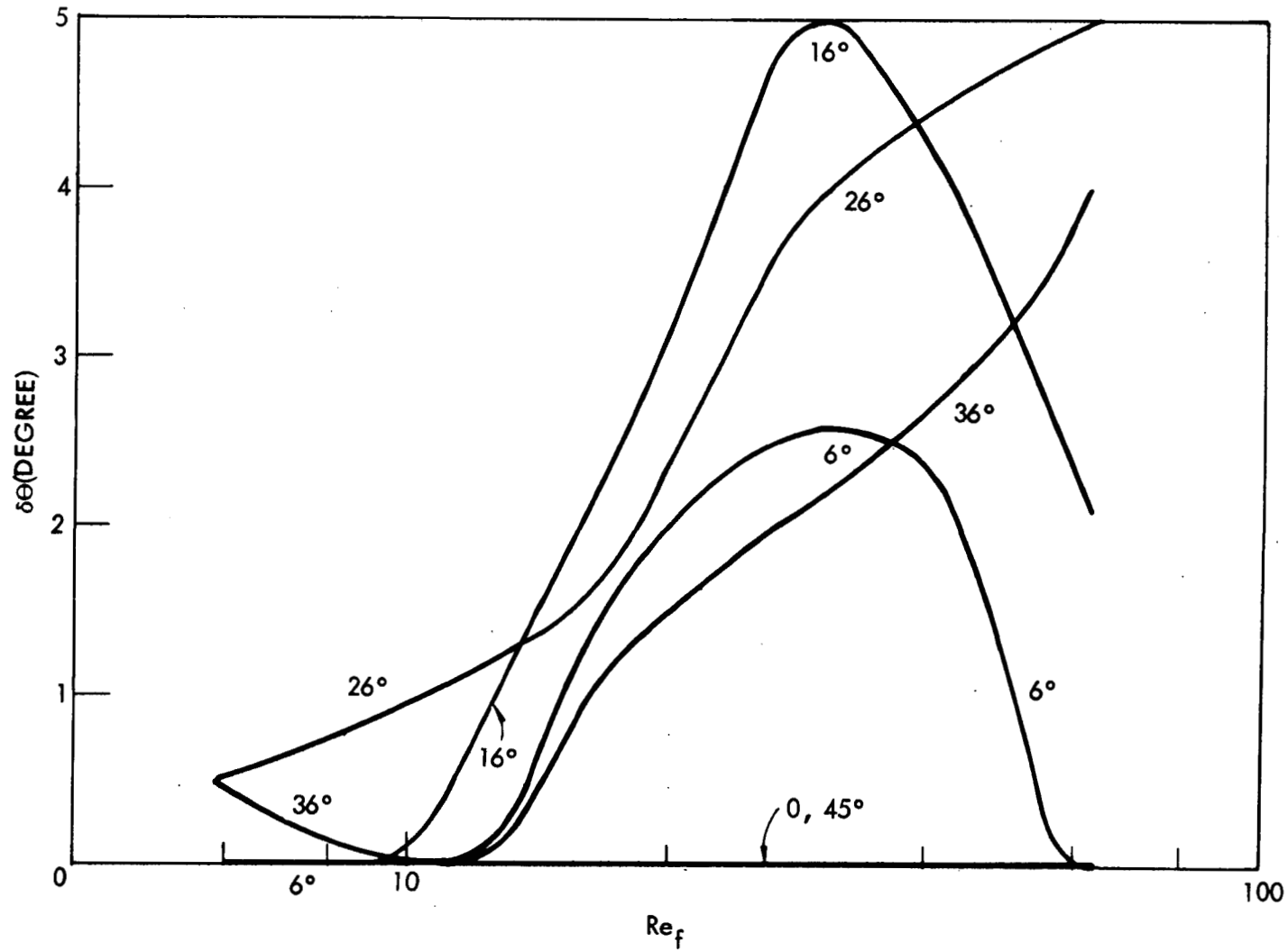

Figure 48. Systematic Error Due to Heat Conduction (Wind Direction, Cold Case).

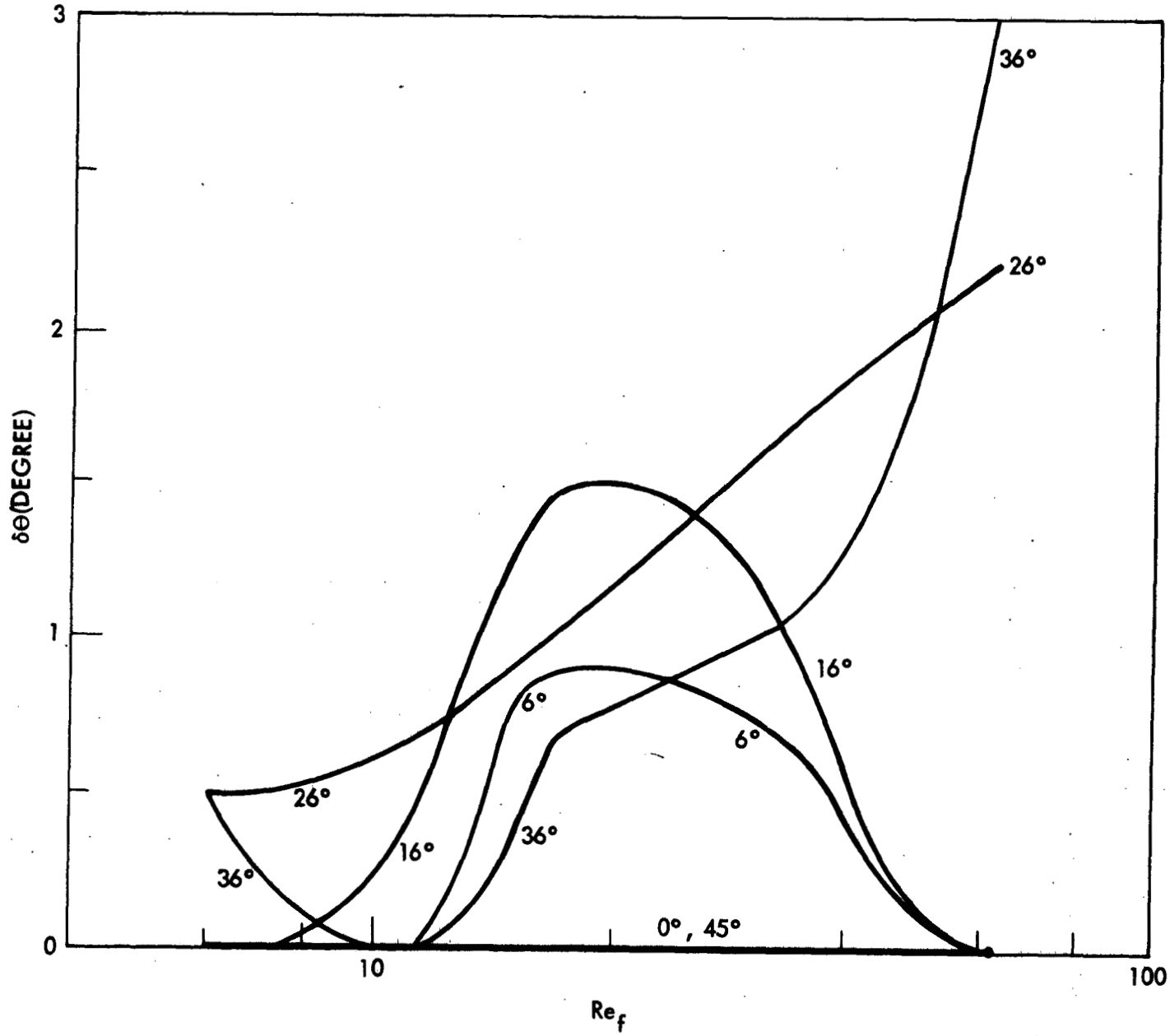

Figure 49. Systematic Error Due to Heat Conduction (Wind Direction, Hot Case).

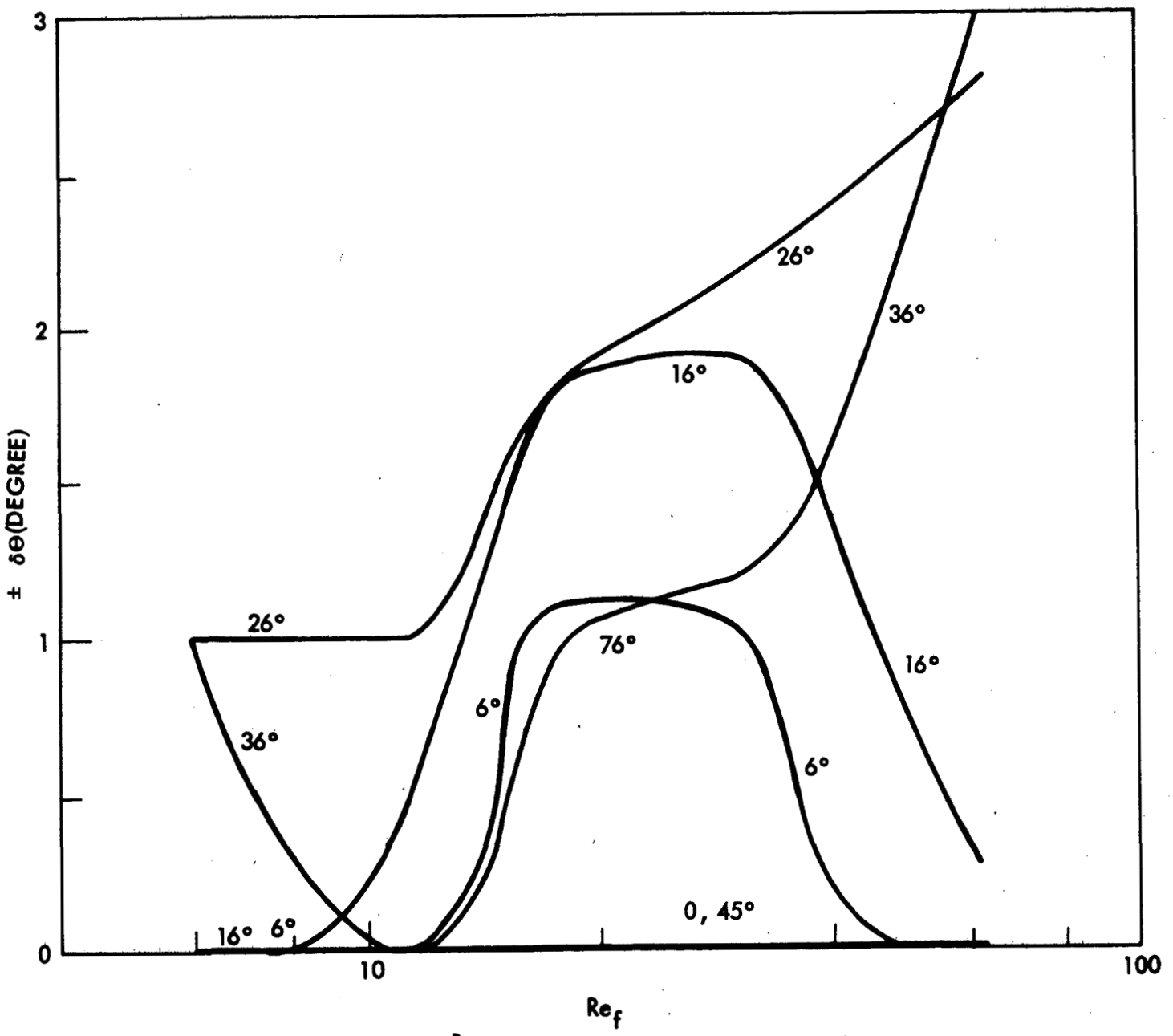

Figure 50. Random Error Due to Overheat Uncertainty (Wind Direction, Cold Case).

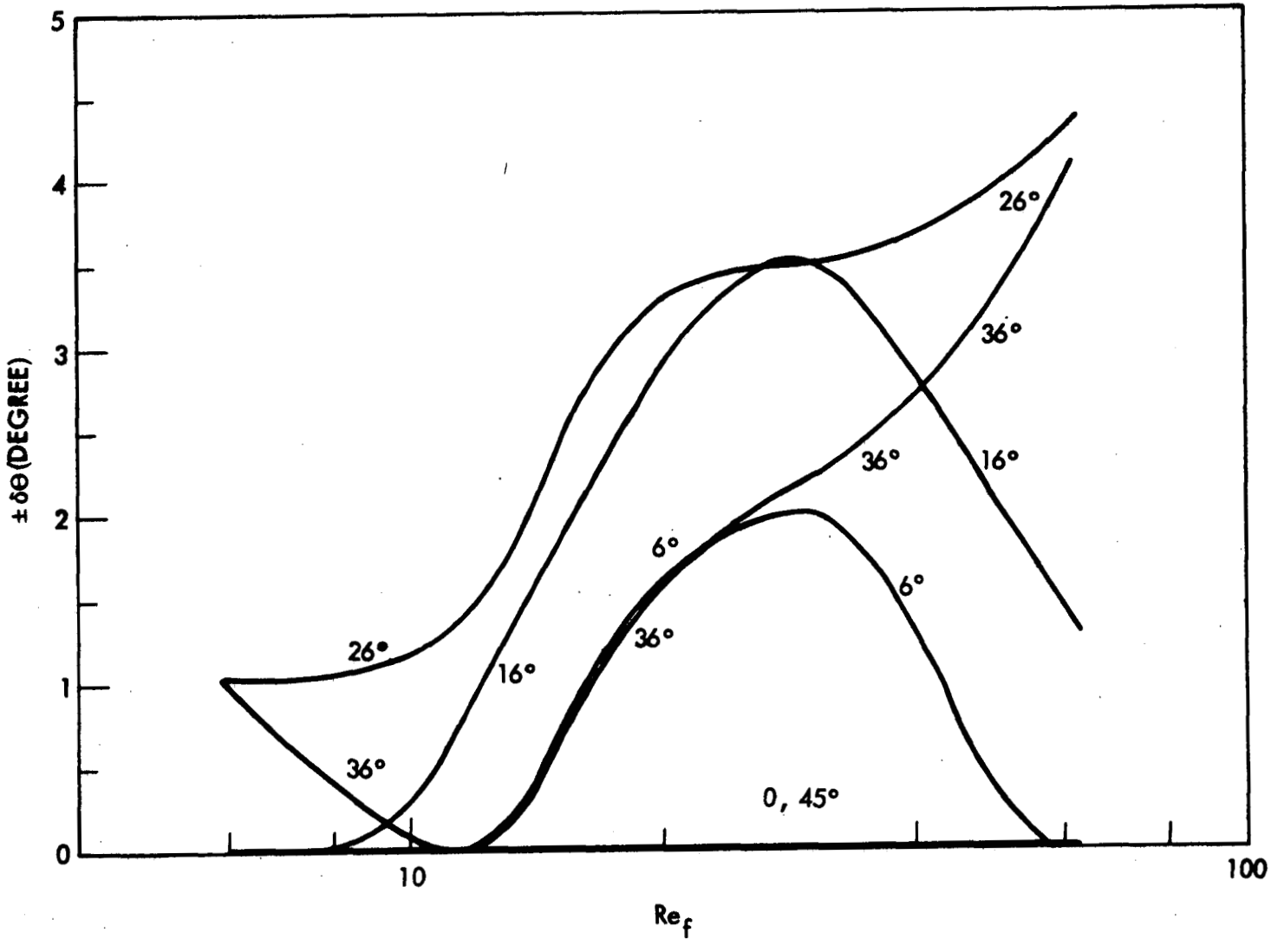

Figure 51. Random Error Due to Overheat Uncertainty (Wind Direction, Hot Case).

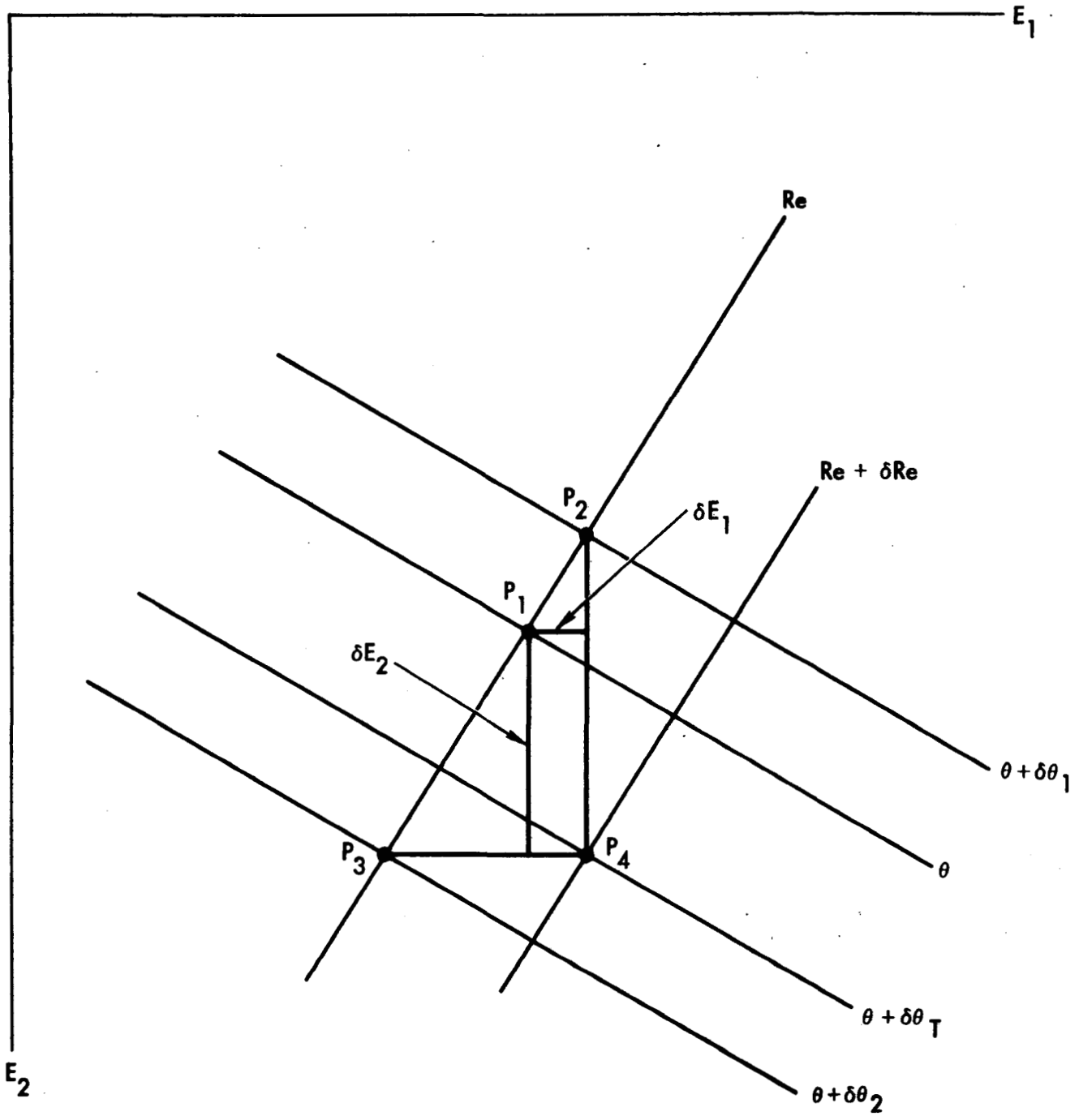

Figure 52. Combination of Single Thermocouple Angle Errors to Give Sensor Wind Direction Errors.

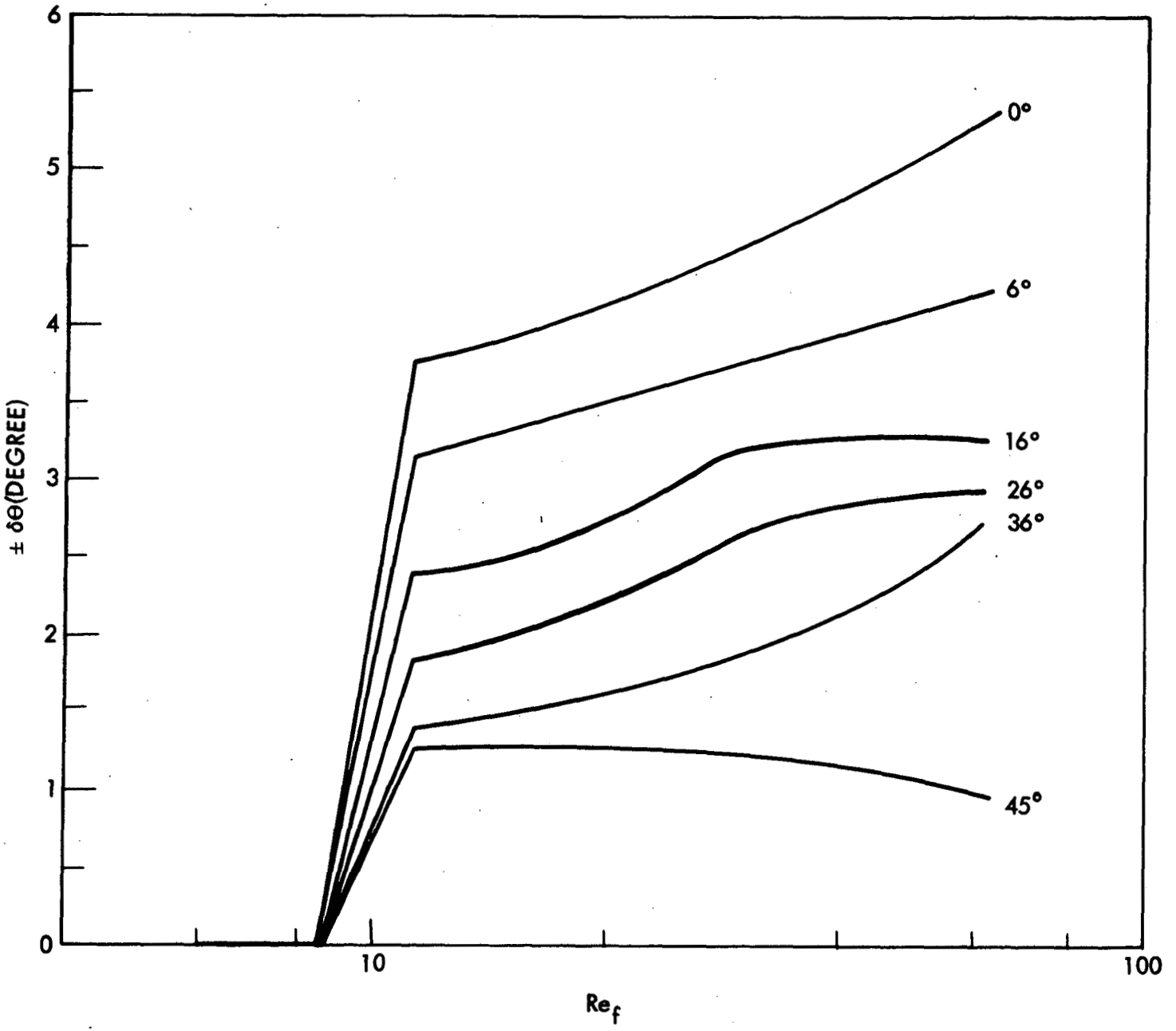

Figure 53. Random Errors Due to Motion of Thermocouple Junctions (Wind Direction, Hot Case).

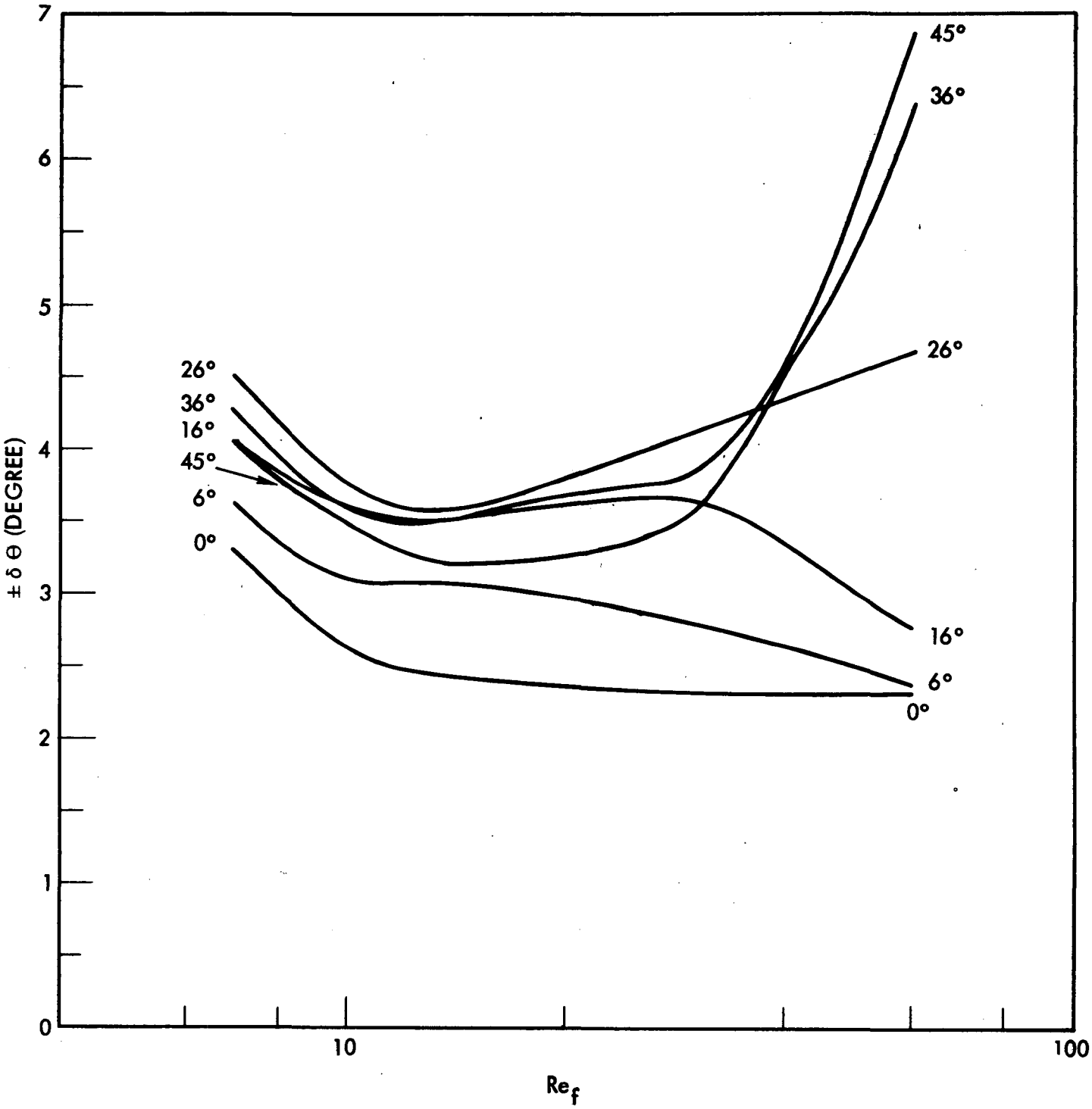

Figure 54. Total Random Error (Wind Direction Measurement, Cold Case).

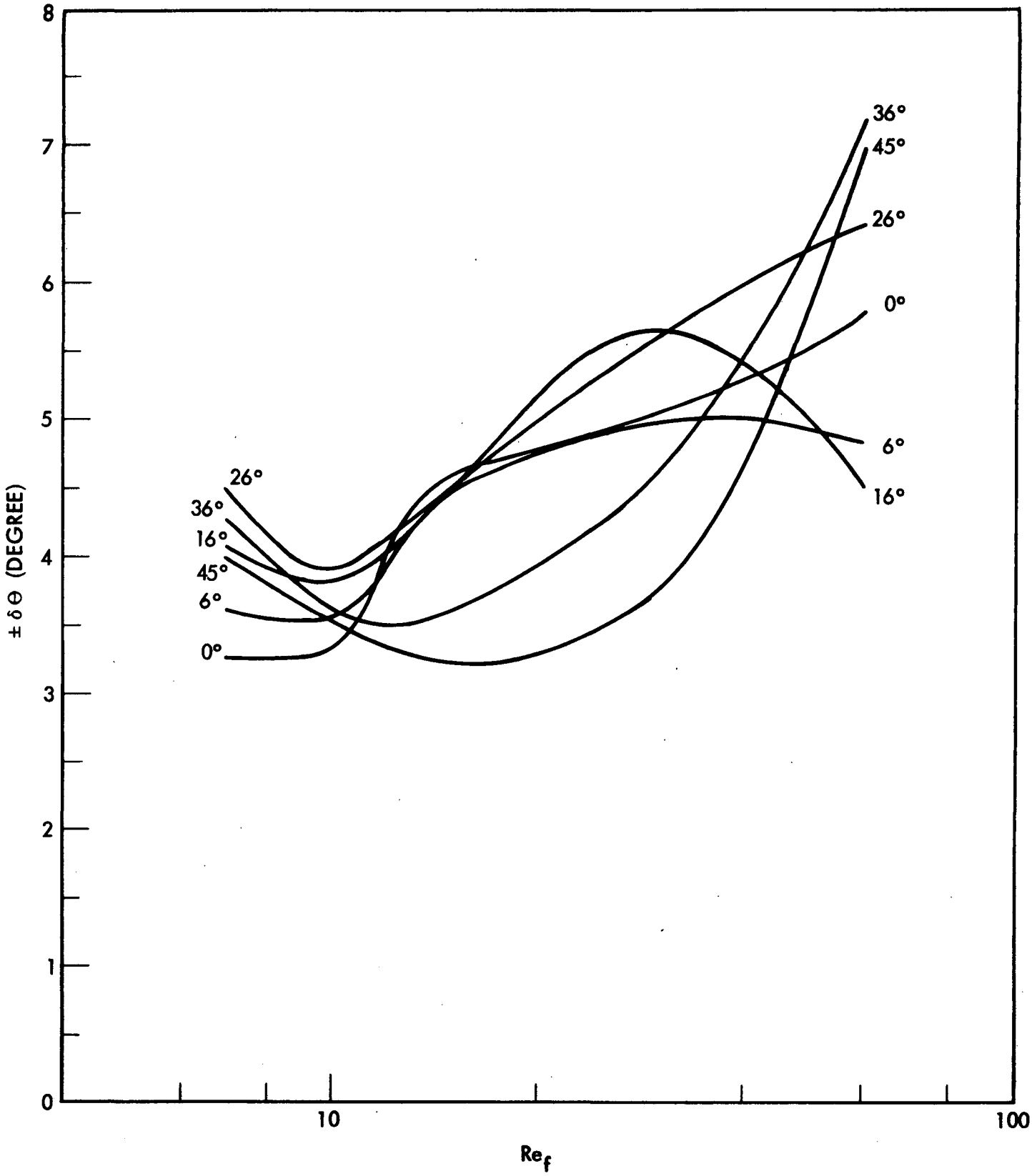

Figure 55. Total Random Error (Wind Direction Measurement, Hot Case).

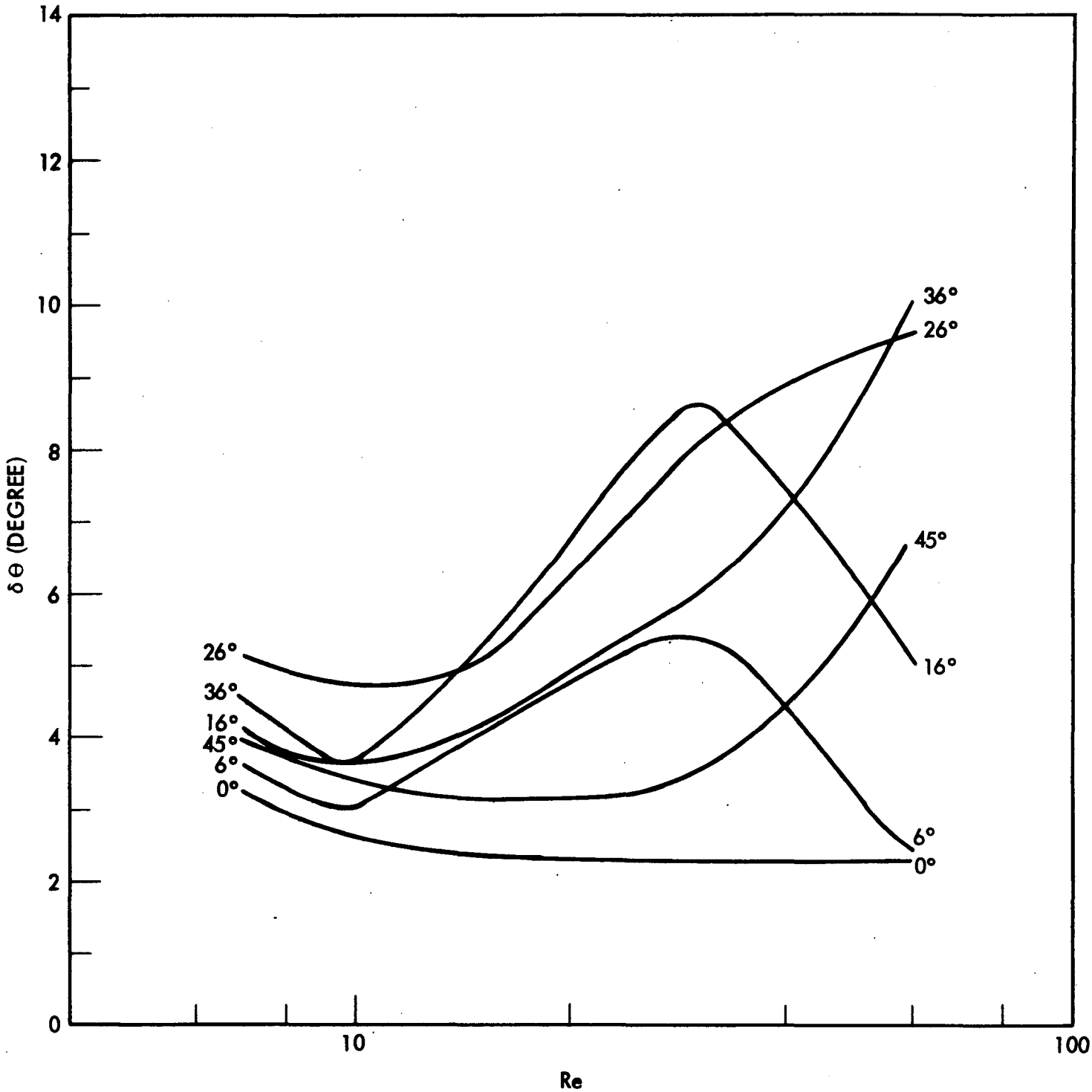

Figure 56. Wind Direction Error Summary (Cold Case).

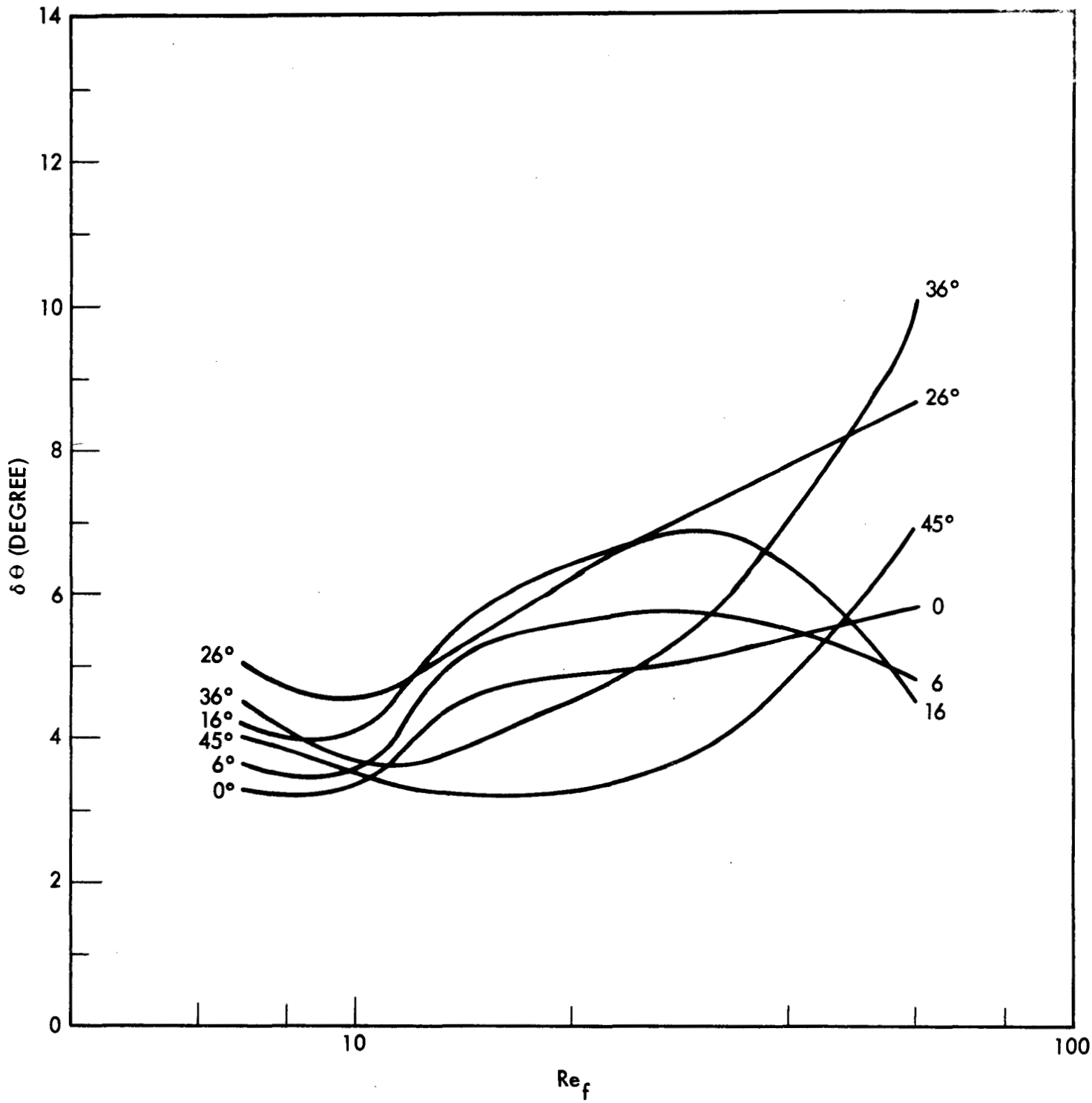

Figure 57. Wind Direction Error Summary (Hot Case).